UNIVERSITY OF LIVERPOOL

Characterization of Neutral Trapped Antihydrogen in the ALPHA Experiment

Mostafa Ahmadi

A thesis submitted in fulfilment of the requirements for the degree of Doctor of Philosophy

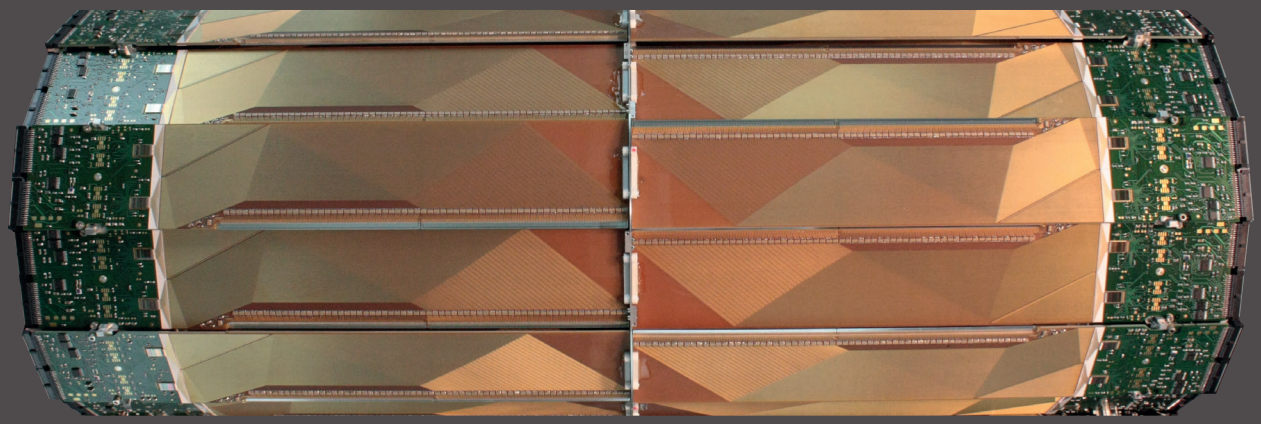

Department of Physics, University of Liverpool

November 2018

Declaration

I confirm that no part of the material offered has previously been submitted by myself for a degree in this or any other university. Where material has been generated through group work, the work of others has been indicated.

Mostafa Ahmadi
Liverpool

Abstract

One of the pivotal principles of physics is the C (charge) P (parity) T (time reversal) (CPT) theorem. One method for testing the CPT symmetry is to investigate the properties of antihydrogen. The Antihydrogen Laser PHysics Apparatus (ALPHA) experiment aims at creating, confining and applying spectroscopic techniques to probe the atomic structure of antihydrogen anti-atom with the same accuracy as that of the hydrogen atom.

There are several non-trivial experimental challenges that must be overcome in antihydrogen studies. One major challenge is the detection of antihydrogen anti-atoms. This is done by identifying the antihydrogen annihilation. This thesis presents both a new method for identifying signal pulses from the background electric pulses of the silicon strips (Alternative Pedestal Analysis (APA), see Appendix A) as well as a completely new and enhanced vertex reconstruction method (Alternative Reconstruction Method (ARM), see Appendix C). The ARM is based on implementing a set of filtration mechanisms to identify the track candidates. Moreover, the reconstruction of the tracks is accomplished by adapting a numerical approach. Combining the APA and the ARM schemes has led to an increase in the vertex reconstruction efficiency by 1.5%.

The alternative approaches for pedestal analysis and vertex reconstruction utilize a considerably more versatile algorithm. This feature allows greater control over variables and selection parameters employed for the reconstruction of vertices. The conclusive verifications of the performances of the new approaches are based on their visualization capabilities, the key aspect in devising the APA and the ARM, see Appendices B and D. The scripts in Appendices A-D haven been written solely by the author and are completely independent of pedestal and even vertex reconstruction algorithms currently implemented in the ALPHA experiment. The full commented versions of the scripts in Appendices A-D are available via the accompanying website at Antimatter[1]

[1] `https://github.com/MosiAhmadi/Antimatter_Detection`

Acknowledgements

I would like to express my special appreciation and thanks to the entire ALPHA collaboration for providing me the opportunity to join their team and gaining access to the ALPHA Silicon Vertex Detector and research facilities. You have encouraged my research and allowed me to grow as a research scientist. My sincere thanks goes to Prof. Jeffrey Hangst, Prof. Niels Madsen and Dr. William Bertsche for having long discussions about my future career. Your advice and motivation for pursing my dream have been priceless and for that I will always be truly grateful. A special thanks to Dr. Joseph McKenna for providing me with the detector data. It would not have been possible to conduct this research without having access to these data.

I would like to acknowledge and thank the Engineering and Physical Sciences Research Council (EPSRC) for funding my PhD scholarship. I would also like to acknowledge the additional financial support from the University of Liverpool physics department provided by Prof. Carsten Welsch and Prof. Paul Nolan.

Last but not the least, I would like to thank my parents. Words cannot express how grateful I am to my father and mother for all the sacrifices they have made on my behalf.

At the end, I would like to express appreciation to all the people on this planet who strive for providing the world with free knowledge, peace and justice. This thesis is dedicated to them.

Dedication

To those who strive for distributing free knowledge, peace and justice.

Publications

The following list includes the scientific papers published by ALPHA collaboration during the author's Ph.D. program and are the outcome of a collaborative work. Based on ALPHA collaboration policy, the authors' names are arranged in alphabetic order.

1. **Observation of the 1S-2P Lyman-α transition in antihydrogen.**

   M. Ahmadi, B. X. R. Alves, C. J. Baker, W. Bertsche, E. Butler, A. Capra,C. Carruth, C. L. Cesar,M. Charlton, S. Cohen, R. Collister, S. Eriksson, A. Evans, N. Evetts, J. Fajans, T. Friesen, M. C. Fujiwara, D. R. Gill, A. Gutierrez, J. S. Hangst, W. N. Hardy, M. E. Hayden, C. A. Isaac, A. Ishida, M. A. Johnson, S. A. Jones, S. Jonsell, L. Kurchaninov, N. Madsen, M. Mathers, D. Maxwell, J. T. K. McKenna, S. Menary, J. M. Michan,T. Momose, J. J. Munich, P. Nolan, K. Olchanski, A. Olin, P. Pusa, C. Ø. Rasmussen, F. Robicheaux, R. L. Sacramento, M. Sameed, E. Sarid, D. M. Silveira, S. Stracka, G. Stutter, C. So, T. D. Tharp, J. E. Thompson,R. I. Thompson, D. P. van der Werf & J. S. Wurtele. *Nature*, volume 561, pages 211–215 (22 August 2018).

2. **Characterization of the 1S-2S transition in antihydrogen.**

   M. Ahmadi, B. X. R. Alves, C. J. Baker, W. Bertsche, E. Butler, A. Capra,C. Carruth, C. L. Cesar,M. Charlton, S. Cohen, R. Collister, S. Eriksson, A. Evans, N. Evetts, J. Fajans, T. Friesen, M. C. Fujiwara, D. R. Gill, A. Gutierrez, J. S. Hangst, W. N. Hardy, M. E. Hayden, C. A. Isaac, A. Ishida, M. A. Johnson, S. A. Jones, S. Jonsell, L. Kurchaninov, N. Madsen, M. Mathers, D. Maxwell, J. T. K. McKenna, S. Menary, J. M. Michan,T. Momose, J. J. Munich, P. Nolan, K. Olchanski, A. Olin, P. Pusa, C. Ø. Rasmussen, F. Robicheaux, R. L. Sacramento, M. Sameed, E. Sarid, D. M. Silveira, S. Stracka, G. Stutter, C. So, T. D. Tharp, J. E. Thompson,R. I. Thompson, D. P. van der Werf & J. S. Wurtele. *Nature*, volume 557, pages 71–75 (6 March 2018).

3. **Enhanced control and reproducibility of non-neutral plasmas.**

   M. Ahmadi, B. X. R. Alves, C. J. Baker, W. Bertsche, E. Butler, A. Capra,C. Carruth, C. L. Cesar,M. Charlton, S. Cohen, R. Collister, S. Eriksson, A. Evans, N. Evetts, J. Fajans, T. Friesen, M. C. Fujiwara, D. R. Gill, A. Gutierrez, J. S. Hangst, W. N. Hardy, M. E. Hayden, C. A. Isaac, A. Ishida, M. A. Johnson, S. A. Jones, S. Jonsell, L. Kurchaninov, N. Madsen, M. Mathers, D. Maxwell, J. T. K. McKenna, S. Menary, J. M. Michan,T. Momose, J. J. Munich, P. Nolan, K. Olchanski, A. Olin, P. Pusa, C. Ø. Rasmussen, F. Robicheaux, R. L. Sacramento, M. Sameed, E. Sarid, D. M. Silveira, S. Stracka, G. Stutter, C. So, T. D. Tharp, J. E. Thompson,R. I. Thompson, D. P. van der Werf & J. S. Wurtele. *Phys. Rev. Lett.*, 120, 025001 (December 2017).

4. **Antihydrogen accumulation for fundamental symmetry tests.**

   M. Ahmadi, B. X. R. Alves, C. J. Baker, W. Bertsche, E. Butler, A. Capra,C. Carruth, C. L. Cesar,M. Charlton, S. Cohen, R. Collister, S. Eriksson, A.

Evans, N. Evetts, J. Fajans, T. Friesen, M. C. Fujiwara, D. R. Gill, A. Gutierrez, J. S. Hangst, W. N. Hardy, M. E. Hayden, C. A. Isaac, A. Ishida, M. A. Johnson, S. A. Jones, S. Jonsell, L. Kurchaninov, N. Madsen, M. Mathers, D. Maxwell, J. T. K. McKenna, S. Menary, J. M. Michan,T. Momose, J. J. Munich, P. Nolan, K. Olchanski, A. Olin, P. Pusa, C. Ø. Rasmussen, F. Robicheaux, R. L. Sacramento, M. Sameed, E. Sarid, D. M. Silveira, S. Stracka, G. Stutter, C. So, T. D. Tharp, J. E. Thompson,R. I. Thompson, D. P. van der Werf & J. S. Wurtele. *Nature Communications*, Article number: 681 (September 2017).

5. **Observation of the hyperfine spectrum of antihydrogen.**

   M. Ahmadi, B. X. R. Alves, C. J. Baker, W. Bertsche, E. Butler, A. Capra,C. Carruth, C. L. Cesar,M. Charlton, S. Cohen, R. Collister, S. Eriksson, A. Evans, N. Evetts, J. Fajans, T. Friesen, M. C. Fujiwara, D. R. Gill, A. Gutierrez, J. S. Hangst, W. N. Hardy, M. E. Hayden, C. A. Isaac, A. Ishida, M. A. Johnson, S. A. Jones, S. Jonsell, L. Kurchaninov, N. Madsen, M. Mathers, D. Maxwell, J. T. K. McKenna, S. Menary, J. M. Michan,T. Momose, J. J. Munich, P. Nolan, K. Olchanski, A. Olin, P. Pusa, C. Ø. Rasmussen, F. Robicheaux, R. L. Sacramento, M. Sameed, E. Sarid, D. M. Silveira, S. Stracka, G. Stutter, C. So, T. D. Tharp, J. E. Thompson,R. I. Thompson, D. P. van der Werf & J. S. Wurtele. *Nature*, volume 548, pages 66–69 (03 August 2017).

6. **Observation of the 1S-2S transition in trapped antihydrogen.**

   M. Ahmadi, B. X. R. Alves, C. J. Baker, W. Bertsche, E. Butler, A. Capra,C. Carruth, C. L. Cesar,M. Charlton, S. Cohen, R. Collister, S. Eriksson, A. Evans, N. Evetts, J. Fajans, T. Friesen, M. C. Fujiwara, D. R. Gill, A. Gutierrez, J. S. Hangst, W. N. Hardy, M. E. Hayden, C. A. Isaac, A. Ishida, M. A. Johnson, S. A. Jones, S. Jonsell, L. Kurchaninov, N. Madsen, M. Mathers, D. Maxwell, J. T. K. McKenna, S. Menary, J. M. Michan,T. Momose, J. J. Munich, P. Nolan, K. Olchanski, A. Olin, P. Pusa, C. Ø. Rasmussen, F. Robicheaux, R. L. Sacramento, M. Sameed, E. Sarid, D. M. Silveira, S. Stracka, G. Stutter, C. So, T. D. Tharp, J. E. Thompson,R. I. Thompson, D. P. van der Werf & J. S. Wurtele. *Nature*, volume 541, pages 506–510 (26 January 2017).

7. **An improved limit on the charge of antihydrogen from stochastic acceleration.**

   M. Ahmadi, B. X. R. Alves, C. J. Baker, W. Bertsche, E. Butler, A. Capra,C. Carruth, C. L. Cesar,M. Charlton, S. Cohen, R. Collister, S. Eriksson, A. Evans, N. Evetts, J. Fajans, T. Friesen, M. C. Fujiwara, D. R. Gill, A. Gutierrez, J. S. Hangst, W. N. Hardy, M. E. Hayden, C. A. Isaac, A. Ishida, M. A. Johnson, S. A. Jones, S. Jonsell, L. Kurchaninov, N. Madsen, M. Mathers, D. Maxwell, J. T. K. McKenna, S. Menary, J. M. Michan,T. Momose, J. J. Munich, P. Nolan, K. Olchanski, A. Olin, P. Pusa, C. Ø. Rasmussen, F. Robicheaux, R. L. Sacramento, M. Sameed, E. Sarid, D. M. Silveira, S. Stracka, G. Stutter, C. So, T. D. Tharp, J. E. Thompson,R. I. Thompson, D. P. van der Werf & J. S. Wurtele. *Nature*, volume 541, pages 506–510 (21 January 2016).

Contents

Declaration

Abstract **i**

Acknowledgements **ii**

Dedication **iii**

List of publications **iv**

Table of Contents **vi**

List of Figures **ix**

List of Tables **xx**

List of Symbols, Acronyms and Abbreviations **xxi**

1 Introduction **1**
1.1 History & Background . . . 3
1.2 Motivation . . . 5
1.2.1 Spectroscopy & CPT symmetry . . . 5
1.3 AD experiments . . . 7
1.4 Thesis overview . . . 8

2 The ALPHA Apparatus **9**
2.1 Apparatus overview . . . 10
2.1.1 ALPHA-I & ALPHA-II . . . 10
2.2 Charged (anti)particle production . . . 14
2.2.1 High-energy antiproton production . . . 14
2.2.2 Low-energy antiproton production . . . 16
2.2.3 Positron accumulator . . . 21
2.2.4 Electron gun . . . 21
2.3 Penning trap for charged particles . . . 23
2.3.1 Theory of confinement . . . 23
2.3.2 ALPHA-I Penning-Malmberg trap . . . 26
2.3.3 ALPHA-II Penning-Malmberg trap . . . 29
2.4 Magnetic neutral-atom trap . . . 31
2.4.1 Theory of confinement . . . 31
2.4.2 ALPHA-I magnetic trap . . . 33
2.4.3 ALPHA-II magnetic trap . . . 37

2.5 Vacuum and cryogenics . . . 39
2.6 Particle detection and diagnostic devices . . . 40
2.6.1 Faraday cup . . . 40
2.6.2 The linear vacuum manipulator . . . 41
2.6.3 Scintillators . . . 45
2.6.4 CsI detectors . . . 46
2.6.5 Flappers . . . 46
2.6.6 Silicon Vertex Detector . . . 46
2.7 Laser access windows . . . 48
2.8 Control system and data acquisition . . . 49

3 Plasma Manipulation & Confinement 50
3.1 Non-neutral plasma confinement in a Penning-Malmberg trap . . . 51
3.1.1 Plasma fundamental properties . . . 51
3.1.2 Theory of confinement . . . 52
3.2 Plasma temperature measurement . . . 53
3.3 Antiproton cooling and trapping . . . 55
3.3.1 The catching trap magnetic field enhancement . . . 59
3.3.2 Rotating wall compression . . . 60
3.3.3 Electron removal . . . 63
3.3.4 Evaporative cooling . . . 66
3.4 Strong Drive Regime Evaporative Cooling . . . 67
3.5 Positron cooling and trapping . . . 68
3.5.1 Manipulation and transfer . . . 70
3.5.2 Adiabatic cooling . . . 71

4 Antihydrogen Synthesis & Confinement 73
4.1 Antihydrogen formation mechanisms . . . 73
4.1.1 Spontaneous radiative recombination . . . 74
4.1.2 Three-body recombination . . . 74
4.2 Antihydrogen synthesis in ALPHA . . . 75
4.2.1 Plasma mixing . . . 75
4.2.2 Antihydrogen accumulation . . . 81
4.2.3 Detection of untrapped antihydrogen . . . 83
4.3 Antihydrogen confinement in ALPHA . . . 85

5 The ALPHA Silicon Vertex Detector 88
5.1 Matter-antimatter interaction . . . 89
5.1.1 Positron-electron annihilation . . . 89
5.1.2 Antiproton-nucleon annihilation . . . 90
5.2 Theory of semiconductors . . . 91
5.2.1 Doped semiconductor . . . 91
5.2.2 *pn* junction . . . 92
5.3 Diode as a charged particle detector . . . 96
5.3.1 Position-sensitive silicon detectors . . . 99
5.4 The SVD design specification . . . 100
5.4.1 The SVD modules . . . 102
5.4.2 VA1TA ASIC read-out chips . . . 103
5.4.3 Data acquisition (DAQ) system . . . 105

6 Pedestal Analysis **108**
6.1 Determining strip background . . . 108
6.1.1 Noise & gain . . . 108
6.1.2 Distinguishing between noise & signal . . . 109
6.2 Strip clustering . . . 119
6.3 Pedestal enhancement . . . 123
6.3.1 Integrating strips . . . 123
6.3.2 Pedestal comparison . . . 124
6.3.3 Integrated-strips enhancement . . . 128

7 Event Vertex Reconstruction **130**
7.1 Overview . . . 131
7.2 Determination of track candidates . . . 134
7.2.1 Tabulating pedestal analysis outcome . . . 134
7.2.2 Identification of a hit . . . 135
7.2.3 Selection criteria . . . 138
7.2.4 Tuning track candidates . . . 145
7.2.5 Pairing track candidates . . . 150
7.2.6 Normalization of pulse heights . . . 151
7.3 Track reconstruction . . . 154
7.4 Vertex reconstruction . . . 158
7.4.1 Distance of closest approach . . . 159
7.4.2 Vertexing . . . 161
7.5 Results . . . 163
7.5.1 Vertex reconstruction enhancement . . . 163
7.5.2 The APA plus ARM enhancement . . . 166
7.5.3 Vertex distribution . . . 168
7.6 Summary . . . 174

8 Conclusion & Future Outlook **177**
8.1 Conclusion . . . 180

Bibliography **188**

Appendices **189**

A Pedestal-Analysis.m **A1**

B Pedestal-Analysis-Visualization.m **B1**

C Event-Vertex-Reconstruction.m **C1**

D Event-Vertex-Reconstruction-Visualization.m **D1**

List of Figures

1.1 Photograph of the first observation of a positron. Blue curved lines (coming from below) illustrate the particle track interpreted as a 63 MeV positron traversing a 6 mm lead plate and later emerging as a positron with an energy of 23 MeV. Image adapted from [14]. 4
1.2 Schematic illustration of atomic and anti-atomic energy levels of hydrogen and antihydrogen. 6

2.1 (a) Schematic illustration of the ALPHA-I apparatus. Procedures for the creation and the subsequent ejection of antiprotons and positrons into the apparatus is described in Sections 2.2.2.2 and 2.2.3, respectively. (b) Trap configuration. (c) Variation of the axial magnetic field. Superimposed on the 1 T external solenoidal field, the blue and red curves represent the fields produced by the 2 T inner solenoid and the two 1.2 T mirror coils of the neutral-atom trap, respectively. Image modified from [22]. 11
2.2 Cross sectional illustration of the ALPHA-II and ALPHA-g apparatus. Credits: the ALPHA Collaboration and Mark Andrew Johnson, private communications. 12
2.3 Flowchart illustrating the steps involved in creating, confining and detecting antihydrogen in the ALPHA apparatus. 13
2.4 (a) Antiproton production cross section versus incident proton momentum. Image adapted from [23]. 15
2.5 Antiproton yield versus collection momentum for a primary beam momentum of 26 GeV/c. Image adapted from [23]. 15
2.6 Antiproton production complex at CERN illustrating the PS along with its associated booster as well as LINACS, the AA–AC facility, and LEAR. 17
2.7 Layout of the AD facility. 19
2.8 Operational cycle of the AD, illustrating the momentum of $\overline{\mathrm{p}}$ versus the time elapsed as well as the prime stochastic, electron and RF cooling mechanisms. 20
2.9 Schematic illustration of the ALPHA positron accumulator. The positrons are guided by the magnetic field lines and follow the green path from the ^{22}Na source on the right to the Penning-Malmberg trap comprising of the segmented electrode to the left where they undergo rotating wall compression (see Sec. 3.3.2) and are subsequently collected as a plasma (blue ellipse). The positrons are eventually transferred to the Mixing Trap (MT), ready for antihydrogen production upon mixing with the antiprotons. 22

2.10 (a) Schematic cross sectional illustration of a hyperbolic Penning trap comprising two endcap electrodes and the ring electrode. The radial and axial confinement of a charged particle are achieved by a magnetic field $\vec{B}$ along the z-axis (trap symmetry axis) and a voltage V_0 applied between the ring and the endcap electrodes, respectively. Image modified from [28]. (b) Illustration of the magnetic and electric field lines of a Penning trap. 24
2.11 (a) Three distinct motions of a charged particle confined in a Penning trap as well as the combined motion (black curve). (b) Projected motion onto the $x - y$ plane (trap mid-plane). Image modified from [28]. 25
2.12 (a) The ALPHA-I apparatus electrode configuration consisting of the Catching Trap (CT), Mixing Trap (MT), Positron Trap (PT) and positron transfer section. (b) Schematic diagram of the ALPHA-II Atom Trap (AT) comprising the Re-Catching Trap (RCT), five mirror coils (green) and the octupole (pink). Also shown are the two booster solenoids (blue) that assist in antiproton and positron preparation. . . 28
2.13 Axial magnetic field strength (the external solenoid responsible for producing the uniform 1 T field is not shown). The dashed blue curve represents the on-axis fields of the two left (RCT) and right (PT) 2 T internal booster solenoids of the AT. The energization of the booster solenoids result in an increase in the field magnitude from 1 to 3 T for enhanced capture, cyclotron cooling and rotating wall efficiency of positron, electron and antiproton plasmas. The solid red curve represents the MT field once the five mirror coils and the octupole magnets are energized. Image modified from [10]. 30
2.14 Radial variation of transverse magnetic field for several multipole magnets. The field and radius have been normalized with their values at the electrode wall. The vertical line denotes the radius of the inner electrode. It is evident that the octupole results in the shallowest trap depth. Image adapted from [32]. 35
2.15 (a) Schematic illustration of three superconducting magnets of the ALPHA-I neutral-atom trap: two magnet mirror coils with the current directions and one octupole coil consisting of 8 eight counter–winding layers (only 2 layers shown here). Antihydrogen is synthesized in the mixing region enclosed by this neutral-atom trap. Image modified from [34] (b) The ALPHA-II cut-way with the surrounding SVD. Five mirror coils of the ALPHA-II neutral-atom trap are shown. Credits: Joseph Tiarnan McKenna, private communications. 36
2.16 The ALPHA-I radial magnetic field profile generated by the octupole magnet at the axial centre of the neutral trap ($z = 0$ mm). 37
2.17 The scalar magnitude of the total magnetic field of the ALPHA-II neutral-atom trap resulted from the five mirror coils, one octupole and the external solenoid is plotted versus position. The radial position is measured from the symmetry axis of the trap, and the axial origin is the centre of the AT. Image adapted from [9]. 38
2.18 Schematic diagram of the Faraday Cup detection system. 40

2.19 The linear vacuum manipulator consisting of the microwave horn, MCP, the pass-through cylinder, an electron source and a microwave mirror. The required component can be positioned in line with the Penning trap electrodes by allowing the entire assembly to move up or down. Image adapted from [22]. 41
2.20 Schematic diagram showing MCP/phosphor screen/CCD camera setup. The electron cascade is created by the incoming particle interacting with the semiconductor material in a small channel. Visible light is generated when the accelerated electrons excite the phosphor screen atoms. The light is then directed towards an external camera using an arrangement of mirrors and a vacuum window. 42
2.21 Images of (a) electron, (b) positron, (c) antiproton, and (d) increased-gain antiproton plasmas obtained by the MCP/phosphor screen detector. The MCP gain voltage has been increased for the antiproton image in (d) to distinguish the annihilation products. The colour implies normalized intensity where red and blue correspond to the highest and lowest intensities, respectively. 43
2.22 Schematic diagram of external scintillators/PMT assemblies in the ALPHA experiment. 45
2.23 (a) Schematic diagram depicting the cross sectional view of the axial centre of the ALPHA apparatus as well as the Silicon Vertex Detector (SVD). The components include: electrode stack, magnet winding form, octupole magnet winding, liquid helium volume, isolation vacuum walls, SVD, and external solenoid magnet. The five mirror coils located at the axial ends of the magnetic neutral-atom trap are not illustrated. Three pions (two charged and one neutral) are produced as a result of an antiproton annihilation on the trap wall. The trajectories of the annihilation products are represented with curved lines while the asterisks and circle markers indicate the position where the particles encounter a silicon module. The annihilation vertex is denoted with the yellow star. The $\pi^0 \rightarrow 2\gamma$ channel arises by the prompt decay of the neutral pion where one of the resulting photons is absorbed in the octupole winding while the other photon has produced an electron-positron pair. (b)-(c) Cross sectional views of reconstructed antiproton annihilation and cosmic events, respectively, generated by the Alternative Reconstruction Method. The electrode surface is depicted by the central black circle surrounded by the SVD modules. The red curved lines are reconstructed charged pions tracks and the blue diamond is an indication of the position of the reconstructed vertex. 47

3.1 Plot demonstrating the number of antiprotons escaping the confining potential versus the on-axis well-depth. The black lines represent the fitted region with the corresponding acquired temperatures of A: 1040 K, B: 325 K, C: 57 K, D: 23 K, E: 19 K, and F: 9 K. The low-energy distributions are magnified in the inset. Image adapted from [42]. . . 54

3.2 Schematic diagram of the antiproton plasma confinement. (a) Extracted antiprotons from the AD are initially decelerated in the degrader. Electrons are pre-loaded into an electrode located at the centre of the CT and are constantly cooled via synchrotron radiation . (b) Prior to the arrival of the antiprotons, a 5 kV barrier is engaged and those with low enough longitudinal kinetic energy are reflected. (c) Approximately 500 ns later, a similar potential barrier close to the entrance of the trap is engaged to prevent antiprotons leaving the trap and the confinement of antiprotons is achieved. (d) After about 20 s, the antiprotons will have cooled via collisions with the pre-loaded cold electrons. 56
3.3 Normalized antiproton capture versus magnetic field strength. Image adapted from [49]. 59
3.4 Schematic representation of a transverse section of the 'Rotating Wall'. A sinusoidal potential is applied to a six-segmented electrode with a phase difference of 60° between each segment. The red circle illustrates the plasma and the blue arrow the direction of rotation. . . 61
3.5 MCP images and the corresponding radial profiles acquired from the application of Rotating Wall technique on antiproton and electron plasmas. This particular analysis uses a $w_{RW}/2\pi$ ∼10 MHz with three compression implication times of 1, 20 and 60 seconds. The red lines represent the Gaussian fits (i.e. $\exp(-|\frac{r}{r_0}|^k)$ where $k \approx 2$) to the radial profiles. Image adapted from [21]. 62
3.8 Various potential wells utilized for evaporative cooling technique resulting in the escape of the most energetic antiprotons along the trap axis to the left. Image adapted from [42]. 67
3.9 Top: the expanded view of the elongated electrode structure of the positron accumulator sub-divided into 8 sections with electrodes of varying diameters resulting in a pressure gradient. Bottom: red curve depicts the variation of the axial electrical potential as a function of position along the trap electrodes. The positron buffer gas cooling is demonstrated by the grey curve. 69

4.1 Schematic illustration of a nested potential well whereby positrons (e^+) are confined in a short well in the middle and antiprotons ($\overline{p}$) in one side of an inverted long well. Red and blue filled regions are an indication of the self-potentials and the physical extents of antiproton and positron plasmas, respectively. 76
4.4 Schematic demonstration of slow merge mixing process. Dashed and solid curves represent electrostatic potentials before and after each step in the process, respectively. (a) Antiproton cloud is confined in the inverted side-well potential adjacent to the central well containing the positron plasma. (b) The simultaneous injection of the two species into each other by the slow merge of the antiproton and positron electrostatic wells. 80

4.5 Plot depicting the antihydrogen stacking. The linear relationship between the number of trapped atoms detected and the mixing cycle is evident. Each mixing/synthesis cycle lasts 4 min and antihydrogen atoms are detected by the ramp down of the magnetic minimum trap subsequent to one or more consecutive mixing cycles. The error bars represent the $\sqrt{N}$ counting statistics. The linear fit to the data implies an average trapping rate of 10.5 ± 0.6 detected antihydrogen atoms per mixing cycle. The detection efficiency is $(73.0 \pm 0.4)\%$. Image adapted from [10]. 82
4.6 (a) The $x - y$ spatial distribution of approximately 2×10^4 antihydrogen atoms projected along the z-axis. The distribution is approximately azimuthally uniform (no angular dependence) and concentrated around the inner electrode surface represented by the white circle. (b) Bare antiprotons annihilate in highly localized hot spots. Image adapted from [48]. 84
4.7 Steps outlining the procedures undertaken to synthesize and confine antihydrogen atoms in the ALPHA experiment. See the text for detailed descriptions. 86

5.1 Diagram illustrating a *pn* junction in thermal equilibrium. An internal electric field created by the uncompensated acceptor and donor impurities prevents the motion of charge carriers in the depletion region. In the absence of an external EMF (zero bias), the diffusion current is balanced by the drift current across the *pn* junction resulting in a zero net current. The energy of the valence, conduction, Fermi and band gap levels are represented with E_V, E_C, E_F and E_g, respectively. 94
5.2 (a) The recombination of the holes and electrons at the junction plane resulting from the electric force of the external EMF on these carriers. A constant net current dominated by a significant diffusion current is established by the continuous replenishment of the supply of the holes on the *p*-side and the electrons on the *n*-side. (b) Reverse bias showing the diversion of the carriers away from the junction, the subsequent increase of the depletion zone width and the virtual cease of diffusion current. Only the very small drift current contributes to the net current. 96
5.3 The mass stopping power of muons in copper as a function of $\beta\gamma$. The solid curve represents the energy loss with all effects added, while the dashed and dotted ones represent the individual contributions. Image adapted from [73]. 98
5.4 Schematic diagram illustrating a basic silicon particle detector where the reverse-biased junction along with a charged particle traversing the depletion region producing electron-hole pairs are highlighted. Approximately 8000 electron-hole pairs are generated per 100 μm in silicon. 99

5.5 Schematic illustration of the positions of hybrids in the ALPHA-I detector (left), comprising of a total of 60 modules, and the ALPHA-II detector (right), consisting of 72 modules. Table 5.2 is a summary of the radial distances of these modules. Image adapted from [77]. . . 101
5.6 Schematic diagram representing a SVD module. The top represents the front view where bond wires, designated as the path of the p-strips signal, connect the silicon sensors to the Application Specific Integrated Circuits (ASICs). The rear view is shown in the bottom where the connection of n-strips to the ASICs is depicted. The silicon wafers, Printed Circuit Board (PCB) and read-out chips are highlighted. 102
5.7 Schematic diagram of a channel of the VA1TA chip. 104
5.8 Schematic diagram of the ALPHA SVD read-out electronics. Low and High Voltages (LV and HV) are provided through Front-end Repeater Cards (FRC) and separate power cards (not drawn) to ASICs and silicon sensors. All signals between Versa Module Europa (VME) crate and the detector are fed through the FRCs. The VME crate contains Timing and Trigger Control (TTC) and IO32 units, eight VF48s and a VME controller. Detector HV, LV, temperatures and humidity are monitored and several trip systems are incorporated to avoid any damage to the sensitive SVD in case of anomalous events. . 106

6.1 Plots illustrating (a) noise measurements in millivolt and (b) gain measurements in milivolt per femto Coulomb obtained from each strip of a particular hybrid. 109
6.2 Flowchart showing the steps undertaken for pedestal analysis of a strip. 110
6.3 Strips raw ADC samples (blue trace) as well mean ADC value of the entire ASIC (dashed red line) for an (a) n-side ASIC, and a (b) p-side ASIC. The vertical axes units are measured in Analog-to-Digital Units (ADU). 112
6.4 Raw ADC values for a particular strip (strip number one) of (a) ASIC_1 and (b) ASIC_3, acquired from a mixing experimental cycle during which 4747 triggers/read-outs have been recored by the detector. . . . 112
6.5 Steps in determining the pedestal of a particular strip of the n-side ASIC shown in Fig. 6.4(a). (a-b) Zeroth pedestal determination and removal of any samples with ADC values outside $\text{p}_0 \pm 3\sigma_0$, (c-d) First pedestal determination and removal of any samples with ADC values outside $\text{p}_1 \pm 2.5\sigma_1$, (e-f) Second pedestal determination and removal of any samples with ADC values outside $\text{p}_2 \pm 2\sigma_2$. 114
6.6 Steps in determining the pedestal of a particular strip of the p-side ASIC shown Fig. 6.4(b). (a-b) Zeroth pedestal determination and removal of any samples with ADC values outside $\text{p}_0 \pm 3\sigma_0$, (c-d) First pedestal determination and removal of any samples with ADC values outside $\text{p}_1 \pm 2.5\sigma_1$, (e-f) Second pedestal determination and removal of any samples with ADC values outside $\text{p}_2 \pm 2\sigma_2$. 115
6.7 Strip pedestal values, p_3, of the same read-out in Fig. 6.3, relative to the ASIC sample mean of an (a) n-side ASIC and a (b) p-side ASIC. The red dashed line is used to guide the eye. 116

6.8 Mean correction of the corresponding strip samples shown in Fig. 6.3 for an (a) n-side ASIC and a (b) p-side ASIC. Also included is the red dashed line representing the mean ADC value. 117
6.9 Final gain normalized pedestal-subtracted strip samples for (a) $ASIC_1$ (b) $ASIC_2$ (c) $ASIC_3$ and (d) $ASIC_4$. The strip samples are represented as blue traces, the $3.75\sigma_3$ signal thresholds are shown as grey traces, and the strips exceeding the signal threshold are highlighted as red traces. 118
6.10 Schematic diagram showing the generation of the signal by two charged particles traversing a silicon detector hybrid. The green solid line depicts a charged particle depositing its charge on one strip due to its small incident angle of θ_1 while the pink solid line is the representation of a charged particle entering the hybrid with a large incident angle of θ_2 and therefore crossing several strips. As a result, signal is distributed among the activated strips. A larger incident angle also results in higher creation of electron-hole pairs. 119
6.11 Plots illustrating the dependence of cluster generation on a defined signal threshold. (a) The expanded view of $ASIC_3$ where the strip gain normalized pedestal-subtracted samples are represented as blue traces, the arbitrary $3.75\sigma_3$ signal threshold is shown as a grey trace, and the strips exceeding the signal threshold are highlighted as red traces. (b) A $3.75\sigma_3$ signal threshold resulting in three clusters (CL1, CL2 and CL3) and two single signal strips (ST1 and ST2). (c) A $4\sigma_3$ signal threshold leading to two clusters and two single signal strips. (d) Five clusters with no single signal strips obtained from a $2.75\sigma_3$ signal threshold. 120
6.12 Spatial representation of an example event where the intersections of p- and n-side signal strips of the hybrids result in the 3-D set of position data for the hits. 121
6.13 Histograms depicting (a) the calculated weighted average strips (blue bars) of the clusters (green bars) and (b) the integration of strips (orange bars) with single strips as well as clusters. 121
6.14 Histograms of the ADC values for four ASICs (a-d) obtained from an entire experimental run. The red illustrates the samples that have exceeded the $3.75\sigma_3$ signal threshold while the dark blue represents the values that did not pass the threshold. The vertical axis is logarithmic scale. 122
6.15 Relative vertex reconstruction efficiency comparing the SPA with various APA two-round filtering threshold scan parameters for a defined n- and p-side signal thresholds of $3.75\sigma_3$. The SPA outperforms the APA scan parameter of $2.5\sigma_0$-$1.5\sigma_1$ by only 0.1% when considering two rounds of filtering. 126
6.16 Relative vertex reconstruction efficiency comparing SPA with various APA three-round filtering threshold scan parameters for a defined n- and p-side signal thresholds of $3.75\sigma_3$. 127

6.17 Relative vertex reconstruction efficiency comparing the SPA with various APA signal threshold scan parameters of the n- and p-side strips. Relative to the SPA, a slight enhancement of only 0.02% is obtained at a scan parameter of $3.6\sigma_3$. 128

7.1 Flowchart demonstrating the procedures in reconstructing a vertex by the Alternative Reconstruction Method. 132
7.2 Four different views of a reconstructed vertex (black stars) where the outcome of the Alternative Pedestal Analysis has been fed into Alternative Reconstruction Method. The vertex has resulted from the annihilation of an antiproton on the trap wall (black circle) during a particular mixing event. Blue curves represent the reconstructed tracks. 133
7.3 Four different views of a vertex reconstructed (black plus symbols) where the outcome of the Standard Pedestal Analysis for the same mixing event in Fig. 7.2 has been fed into the Standard Reconstruction Method. Blue circle represents the trap surface. Credits: the ALPHA Collaboration. 133
7.4 Reconstructed vertex (black stars) corresponding to the same mixing event in Fig. 7.3 where the outcome of the Standard Pedestal Analysis has been fed into the Alternative Reconstruction Method. 134
7.5 Left: the distribution of hybrids on the AD-side. Right: the distribution of hybrids on the POS-side. 136
7.6 Two projections illustrating the AD-side of the detector containing all the 19 hits generated during the mixing event illustrated in Fig. 7.4. 137
7.7 Vertex X-Y projection 139
7.8 The purple cone with a vertex at the centre of the detector and subtending a cone angle of 35° on each side of the inner layer hit on hybrid 4 (the dark blue cross and the red circle marker). Any middle layer hits residing within the purple cone have passed the cone angle selection criterion. The angular separations of the two middle layer hits on hybrids 13 and 22 relative to the inner layer hit on hybrid 4 are represented by the corresponding dark-brown and green projected cones. The middle layer hit on hybrid 13 meets the cone angle filtering condition while the one on hybrid 22 fails. 141
7.9 X-Y projection 142
7.10 Hits of set A surviving cone angle and $z - r$ normal filtration mechanisms. 143
7.11 Illustration of the dot product filtering mechanism applied to the 3-hit combinations of set A where two unit vectors are created from hits on three different layers of the detector. (a-b) A 3-hit combination failing the dot product selection criterion. (c-d) A 3-hit combination meeting the dot product filtering condition. The unit vectors have been scaled for clarity. 145

7.12 Outcome of the various selection criteria applied to all the 19 hits (both sets of A and B) of the example mixing event. (a-b) All the 3-hit combinations meeting the selection criteria (track candidates) in 3-D and projected $x-y$ plane views, respectively. (c) An expanded view of the track candidates arising from hits on hybrid 4. (d) Final hits of set A meeting all the selection criteria. See the text for the explanation of the usage of various markers and colours for the 3-hit combinations. 146
7.13 The $x-y$ projections of the helical tracks for the nine track candidates of the example mixing event. Only six circles are visible since some of the 3-hit combinations have shared hits and their reconstructed circles are superimposed when projected onto the $x-y$ plane. 148
7.14 $x-y$ projection 149
7.15 (a) The final four best 3-hit combinations (track candidates). (b) Four circles constructed by the $x-y$ projections of the helices to the best three-hit combinations. The best 3-hit combination of Set A is shown by the hits having orange markers and reconstructed circle. . . 150
7.16 (a) $z-r$ projections of the best four track candidates. Each circle marker represents the (z,r) coordinate of a hit of a particular track candidate. A star is the (z,r) coordinate of the intersection of the two-paired tracks. (b) Unit vectors of the 3-D best lines of fit projected onto the $x-y$ plane. The unit vectors have been scaled for clarity. . 151
7.17 Visual representation of the dot product between the unit vectors of the inner hybrids' normal (black arrows) and the line of best fit to the 3-hit combinations (red arrows) for the best four track candidates. Also included on each line of best fit is the position of the centroid (blue star with green outline). The unit vectors have been scaled for clarity. 153
7.18 The visual representation of reconstructing a track resulted from a track candidate. Top: the three hits (dark blue crosses and the circle markers) of the track candidate and the $x-y$ projected helix (dark red circle) employed to reconstruct the track through these hits. Bottom: an expanded view of the three hits and the track dots. See the text for descriptions of the parameters. 155
7.19 Reversed process of the helical motion of the charged particle giving rise to the track candidate. 156
7.20 (a) $x-y$ and (b) $x-z$ projections of the reconstructed track subsequent to being subjected to the track length cut. 157
7.21 The reconstructed tracks of the best four track candidates presented in (a) 3-D and (b) $x-y$ projection views. 158

7.22 Spatial illustration of the Point Of Closest Approach (POCA) between (a) two tracks and (b) three tracks. The dotted curves represent the reconstructed tracks. The midpoint along the dark blue line, the smallest distance between two helices, is indicated by the asterisk enclosed by the circle and corresponds to the point two tracks pass closest to each other, the POCA. The POCA is the vertex position in the case of a two-track event as in (a). The vertex position in the case of the three-track event in (b) is represented with a black star. The colour choice for the circle and the asterisk representing a POCA matches that of the paired tracks resulting in the POCA. 160
7.23 Visual representation of the reconstructed vertex (black star) shown in four different views, (a) partial view only illustrating the hybrids containing the hits, (b) full detector view of all the hybrids, (c) $x-y$ projection of hybrids containing the hits and (d) the expanded view of the reconstructed vertex. 162
7.24 (a) Absolute values of vertex efficiency for the Standard Reconstructed Method (SRM) (red plane) and various filtering-angle scan parameters of the Alternative Reconstruction Method (ARM). The SRM has an absolute vertex efficiency of 83.5% while the ARM with a filtering-angle scan parameter of 40°-50° results in a vertex efficiency of 84.8%. (b) Relative vertex efficiency comparing the Standard and Alternative Reconstruction Methods. The filtering-angle scan parameter of 40°-50° leads to a vertex efficiency enhancement of 1.5%. . . . 165
7.25 Reconstructed tracks comparison between the Standard Reconstruction Method (SRM) and various combined filtering angles scan parameters of the Alternative Reconstruction Method. The two-number combinations of the legend correspond to the cone angle and the dot product filtering angles (in degrees). The red indicates the filtering-angles scan parameter resulting in the highest vertex reconstruction efficiency. The ARM performs superior to the SRM for vertex reconstruction of six, seven and higher-tracks events. 166
7.26 (a) Absolute vertex efficiency comparison between the Standard Pedestal and Reconstruction methods (SPA + SRM) as well as the Alternative Pedestal and Reconstruction methods (APA + ARM). Combining the best pedestal parameter, namely $3.5\sigma_0$-$2.5\sigma_1$-$1.5\sigma_0$ combined with the n- and p-side strip signal thresholds of $3.6\sigma_3$, with the best vertex reconstruction parameter of 40°-50° (corresponding to the cone and dot product filtering angles, respectively) leads to an overall increase in the vertex reconstruction efficiency by 1.5% compared with the combined SPA and the SRM. (b) Reconstructed tracks comparison between the Standard and Alternative Methods. Alternative Pedestal and Reconstruction methods reconstruct vertices more efficiently for events with six, seven and higher tracks. 167

7.27 Vertex distribution of bare antiproton annihilations during the mixing phase where antihydrogen atoms are formed while the neutral trap magnets are energized. (a) The $x - y$ projection of the vertex distribution, with the colour palette indicating the number of vertices in each bin. The dashed white circle shows the position of the electrode wall. (b) The z distribution of vertices with the unhatched region representing the extent of the electrodes producing the confining electric potential. The zero position corresponds to the centre of the atom trap. The plots have been obtained from the Standard Reconstruction Method during the operation of the ALPHA-I SVD. Image adapted from [31]. 169
7.30 Distributions of vertex radial position for (a) the Standard Reconstruction Method and (b) the Alternative Reconstruction Method. . . 173
7.31 Histogram depicting the difference between the radial position of the reconstructed vertices by the SRM and the ARM. 173

List of Tables

2.1 Opertional oscillation frequencies for a $B_0 = 1$ T, $V_0 = 10$ V and d = 1 cm in the ALPHA trap. 26

5.1 Tabulated data for branching ratios corresponding to pion final states for antiproton-proton [69] and antiproton-neutron [70] annihilations occurring at rest. The k represents multiple π^0 channels grouped together. An approximate 2% contribution due to kaons has not been included. 91
5.2 Tabulated data of the radial distances of the SVD layers for the ALPHA-I and the upgraded ALPHA-II designs. 101
5.3 Summary of the measured values of the sensor parameters. 103

6.1 Summary of the cosmic and mixing sampling data. The reconstruction of the vertices has been performed by the Standard Reconstruction Method. 125

7.1 Tabulated data representing the parameters characterizing the hits on hybrids 1 and 4 of Fig. 7.6. 138

List of Acronyms, Symbols and Abbreviations

ACRONYMS

AA	Antiproton Accumulator
AC	Antiproton Collector
ACE	Antiproton Cell Experiment
ACOL	Antiproton COLlector
AD	Antiproton Decelerator
ADC	Analog-to-Digital Converter
ADU	Analog-to-Digital Units
AEGIS	Antihydrogen Experiment: Gravity, Interferometry, Spectroscopy
ALPHA	Antihydrogen Laser PHysics Apparatus
APA	Alternative Pedestal Analysis
ARM	Alternative Reconstruction Method
ASACUSA	Atomic Spectroscopy And Collisions Using Slow Antiprotons
ASIC	Application Specific Integrated Circuit
AT	Atom Trap
ATHENA	AnTiHydrogEN Apparatus
ATRAP	Antihydrogen TRAP
BASE	Baryon Antibaryon Symmetry Experiment
CCD	Charged Coupled Device
CERN	European Organization for Nuclear Research
CPT	Charge, Parity and Time reversal
CL	Cluster
CsI	Cesium-Iodide
CT	Catching Trap
ELENA	Extra-Low ENergy Antiproton ring
EMF	ElectroMotive Force
EVC	EVaporative Cooling
FC	Faraday Cup
FPGA	Field Programmable Gate Array
FRC	Front-end Repeater Cards
GBAR	Gravitational Behavior of Antihydrogen at Rest
GR	General Relativity
HV	High Voltage
LEAR	Low-Energy Antiproton Ring
LINAC	LINear ACcelerator
LV	Low Voltage
MATLAB	MATrix LABoratory
MCP	MicroChannel Plate
MIDAS	Multi Instance Data Acquisition System
MT	Mixing Trap
NI	National Instruments

OVC	Outer Vacuum Chamber
PCB	Printed Circuit Board
PET	Positron Emission Tomography
PH	Pulse Height
PMT	Photo-Multiplier Tube
PS	Proton Synchrotron
PSB	Proton Synchrotron Booster
PT	Positron Trap
QED	Quantum ElectroDynamics
QPS	Quench Protection System
RCT	Re-Catching Trap
RF	Radio Frequency
RFQD	Radio Frequency Quadrupole Decelerator
RW	Rotating Wall
SDR	Strong Drive Regime
SDREVC	Strong Drive Regime EVaporative Cooling
SPA	Standard Pedestal Analysis
SRM	Standard Reconstruction Method
SRR	Spontaneous Radiative Recombination
SVD	Silicon Vertex Detector
TPC	Time Projection Chamber
TBR	Three-Body Recombination
TTC	Timing and Trigger Control
UHV	Ultra High Vacuum
WAS	Weighted Average Strip
VME	Versa Module Europa
WEP	Weak Equivalence Principle

(x, y, z)	Coordinates in a Cartesian reference system
(R, ϕ, z)	Coordinates in a cylindrical reference system
Z	Nucleus charge
$p/\overline{p}$	Proton/antiproton
$\mathrm{H}/\overline{\mathrm{H}}$	Hydrogen/antihydrogen
e^-/e^+	Electron/positron
s	Unit of time (second)
Q	Charge
σ	Standard deviation
ms	Millisecond
ns	Nanosecond
mm	Millimeter
MeV	Mega electron-volt
GeV	Giga electron-volt
E	Energy
^{22}Na	Sodium-22
$^{22}\mathrm{Ne}^*$	Excited Neon-22
β^+	Beta-plus
GBq	Gigabecquerel
ν_e	Neutrino
w_c	Cyclotron frequency
q	Particle charge
B_0	Magnetic field z-component
m	Particle mass
$\phi(r)$	Static electric potential
V_0	Applied voltage
r_0	Ring electrode radius
d	Penning trap length parameter/ normal residual
D	Sum of normal residuals
c	Intercept of the line of best fit
w_z	Axial angular frequency
w_+	Modified cyclotron frequency
w_-	Magnetron frequency
T	Tesla/temperature
$\vec{\mu}_{\bar{\mathrm{H}}}$	Antihydrogen magnetic dipole moment
$\vec{\mu}_{\mathrm{S}}$	Spin magnetic dipole moment
g_J	Landé g-factor
μ_B	Bohr magneton
$\vec{J}$	Total angular momentum
$\vec{L}$	Orbital angular momentum
$\vec{S}$	Spin angular momentum
$\vec{\tau}$	Torque
U	Interaction energy
ΔU	Trap depth

$B_{\max}$	Maximum magnetic field
$B_{\min}$	Minimum magnetic field
$B_{\min,\text{axial}}$	Minimum axial magnetic field
$B_{\max,\text{axial}}$	Maximum axial magnetic field
ΔB	Difference between the maximum and minimum field magnitudes
s	Order of the multipole
B_w	Transverse field magnitude at the trap wall
r_w	Radius at the trap wall
$B_{\min,\text{radial}}$	Minimum radial magnetic field
$B_{\max,\text{radial}}$	Maximum radial magnetic field
$I(\vec{r})$	Radial profile density
$a/R/\vec{r_0}/n$	Plasma fit parameters
γ	Gamma
$\pi^-/\pi^+/\pi^0$	Charged and neutral pi mesons
ϕ	Angular displacement of a hit from $+x$ axis
L	The detector layer which the hybrid containing a hit resides on
H	The hybrid containing a hit
n-PH	The pulse height of the n-side strip of a hit
p-PH	The pulse height of the p-side strip of a hit
K	Kevlin degrees
$s_{cluster}$	Weighted average strip number
η_{SPA}	The SPA absolute vertex efficiency
η_{APA}	The APA absolute vertex efficiency
$\eta_{\text{rel.}}$	The relative vertex efficiency
θ_{out}	The angular position of the outer layer hit
θ_{in}	The angular position of the inner layer hit
$\Delta\theta$	Angular displacement between the outer and inner hits
n	Principal quantum number
l	Angular momentum quantum number
keV	Kilo electron volt
w_{rot}	Plasma rotational frequency
k_B	Boltzmann constant
ϵ_0	Vacuum permittivity
w_p	Plasma frequency
τ_p	Plasma period
λ_D	Debye length
$\vec{a}$	Acceleration
ϵ_0	Permittivity of space
c	Speed of light
γ_c	Cyclotron cooling rate
v_θ	Azimuthal velocity
B	Axial magnetic field
$E_\parallel$	Axial/parallel energy
P_θ	Canonical angular momentum

Chapter 1

Introduction

The term antimatter was first coined by Arthur Schuster in 1898 when he proposed the idea in a letter to Nature journal [1]. The hypothesis was that there exists anti-atoms giving rise to antimatter solar systems. It further asserted that matter and antimatter annihilate upon coming into contact with each other. The modern concept of antimatter was first proposed by British physicist Paul Dirac. Whereas normal hydrogen consists of an electron and a proton, the antimatter counterpart of hydrogen, antihydrogen ($\overline{\mathrm{H}}$), is composed of an anti-electron (e^+), known as the positron, and an antiproton ($\overline{p}$). High-energy antihydrogen atoms have been artificially created in particle accelerators.

In the early 1980s, low-energy antimatter establishments located at The European Organization for Nuclear Research (CERN) provided a unique opportunity for scientists to perform fundamental physics experiments on anti-atoms. In 2002, the first production of approximately 50,000 cold antihydrogen atoms was achieved by the AnTiHydrogEN Apparatus (ATHENA) collaboration [2] and shortly afterwards by the Antihydrogen TRAP (ATRAP) collaboration [3] at the Antiproton Decelerator (AD) at CERN. Built in 2005, the Antihydrogen Laser PHysics Apparatus (ALPHA) is the successor of ATHENA and has succeeded in conducting the following prominent experiments:

- The successful creation of 38 magnetically confined atoms of antihydrogen for

at least 172 ms in 2010 [4].

- Further trapping of 400 antihydrogen atoms with a confinement time of more than 15 minutes in 2011 [5].
- Resonant quantum transitions in trapped antihydrogen atoms in 2012 [6].
- A direct experimental limit on the charge of antihydrogen of $Q = (-13 \pm 11 \pm 4)$ parts per billion (1σ confidence level) in 2016, a result regarded as a test of the Charge, Parity and Time reversal (CPT) invariance [7].
- The observation of the 1S–2S transition in magnetically trapped atoms of antihydrogen with a frequency of the transition consistent with that expected for hydrogen in the same environment and consistent with the CPT invariance at a relative precision of about 2×10^{-10} in 2017 [8].
- Microwave spectroscopy on trapped antihydrogen consistent with expectations for atomic hydrogen at the level of four parts in 10^4 in 2017 [9].
- An improved synthesis process resulting in a maximum rate of 10.5 ± 0.6 atoms trapped and detected per cycle in 2017 [10].
- A 10-told increase in the antihydrogen trapping rate (the number of trapped anti-atoms per attempt) by applying the "simultaneous control of the density and particle number of non-neutral plasmas confined in Penning-Malmberg" technique to the positron and electron plasmas in 2018 [11].
- The full line-shape measurement of the 1S-2S transition in antihydrogen resulting in the observation of the 1S–2S transition at a relative precision of about 2×10^{-12} in 2018 - two orders of magnitude more precise than the previous determination [12].

The long-term objective of the ALPHA collaboration is to apply spectroscopic techniques to probe the atomic structure of antihydrogen atoms with the same accuracy

as that of the hydrogen atom, paving the way for shedding light on the current observed matter-antimatter asymmetry in our Universe.

The remainder of this chapter is arranged as follows: Section 1.1 contains a brief description on history of antimatter. Next, a review of some of the fundamental motivations for undertaking physics experiments with antihydrogen is presented. Section 1.3 outlines the current AD experiments working towards the magnetic confinement of antihydrogen. The last section describes the overview of this dissertation.

1.1 History & Background

Without doubt, one of the most significant triumphs of the 20th century physics, and in particular relativistic quantum theory, has been the prediction and the discovery of the positron. The existence of the negative-energy states implied by Dirac's equation, was questioned by the foremost scientists of the day and as a result Dirac attempted to propose a physical significance for these states. His prediction in 1931 [13] was that "there would be a new kind of particle, unknown to experimental physics, having the same mass and opposite charge to an electron". Dirac further expressed: "Presumably the protons will have their own negative-energy states, all of which are normally occupied"; a truly extraordinary and prescient vision.

Positrons were first discovered by Anderson in 1932 [14] when they were observed (see Fig. 1.1) during an investigation of cosmic rays in a cloud chamber and thereafter by Blackett and Occhialini [15] who, in addition, discovered the pair production phenomenon. Since then, positrons are routinely utilized in laboratories with applications ranging from fundamental physics, condensed matter physics, chemistry to Positron Emission Tomography (PET) scanners in medical physics.

The establishment of the 6.2 GeV Bevatron at the Lawrence Berkeley Laboratory in the USA led to the discovery of the antiproton by Chamberlain *et al.* in 1955. Regular production of antiprotons is performed at leading particle accelerators, such as CERN and Fermilab.

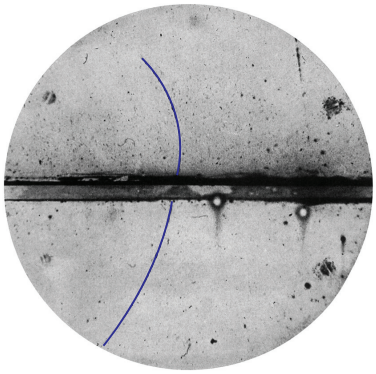

Figure 1.1: Photograph of the first observation of a positron. Blue curved lines (coming from below) illustrate the particle track interpreted as a 63 MeV positron traversing a 6 mm lead plate and later emerging as a positron with an energy of 23 MeV. Image adapted from [14].

The production of 10 antihydrogen atoms was firstly achieved in 1996 at CERN's Low-Energy Antiproton Ring (LEAR) where Baur *et al.* performed an experiment in which a rare interaction (1.1) of an antiproton with an atomic nucleus, Z , was utilized

$$\overline{\mathrm{p}} + \mathrm{Z} \rightarrow \overline{\mathrm{H}} + \mathrm{Z} + \mathrm{e}^{-}. \tag{1.1}$$

Using ordinary matter, detailed study of reactions similar to 1.1 had been conducted and it was known that the cross section for the antihydrogen reaction increases weakly with antiproton kinetic energy and is dependent upon the second power of charge on the target nucleus. As such, xenon gas and antiprotons accelerated to 1.2 GeV, which is close to the maximum energy achieved at LEAR, were selected for a reaction to produce antihydrogen.

The first synthesis of antihydrogen atoms in 1996 has paved the way for scientists in the antimatter research community to pursue the production of antihydrogen atoms at very low energies. Methods for slowing down the positrons and antiprotons must be initially deployed in order to facilitate the capture and subsequent confinement of these charged particles in specialized traps, which will be described in Chapter 2. These methods rely on the collisional loss of the kinetic energy of antiparticles with normal matter due to the fact that the cross sections for annihilation in flight are much lower than those for the equivalent energy loss processes.

1.2 Motivation

1.2.1 Spectroscopy & CPT symmetry

An underlying property of quantum field theories dictated by the central necessity of the Lorentz invariance is the CPT theorem. It states that under the simultaneous change of signs of charge, spatial coordinates and time, the physical laws must be invariant and consequently the physical system is symmetric. The pivotal implication of this symmetry is the existence of a mirror-image of our Universe with particles and their counterpart antiparticles possessing equal lifetimes and inertial masses, as well as equal but opposite electric charges and magnetic moments. In particular, the prediction of identical fine structure, hyperfine structure, and Lamb shifts of atoms with those of anti-atoms (see Fig 1.2) is a direct consequence of the CPT symmetry. A direct verification of CPT theorem would be the comparison of an extremely precise measured quantity of either a particle or atom with its corresponding antiparticle or anti-atom. It is this proposal that laid the foundation of many of the AD experiments to probe antihydrogen structure.

Prior to 1996, high precision tests to confirm CPT symmetry had been conducted exclusively on elementary particles. For instance, a precision of 10^{-9} for the difference between the proton and antiproton charge-to-mass ratios [16] as well as 10^{-12} for the difference between the magnitudes of the magnetic dipole moments of positron and the electron [17] were achieved. Albeit the attainment of the comparison between neutral kaon and neutral anti-kaon masses with staggering accuracy of 10^{-18} has provided the most stringent CPT test thus far, this limit has arguably resulted based on the assumption of the validity of the Standard Model, which itself provides no mechanisms for CPT violation. Nevertheless, these measurements revealed statistically insignificant differences between the matter and antimatter properties under consideration and as such can be regarded as a validation of the CPT theorem pertaining to subatomic particles.

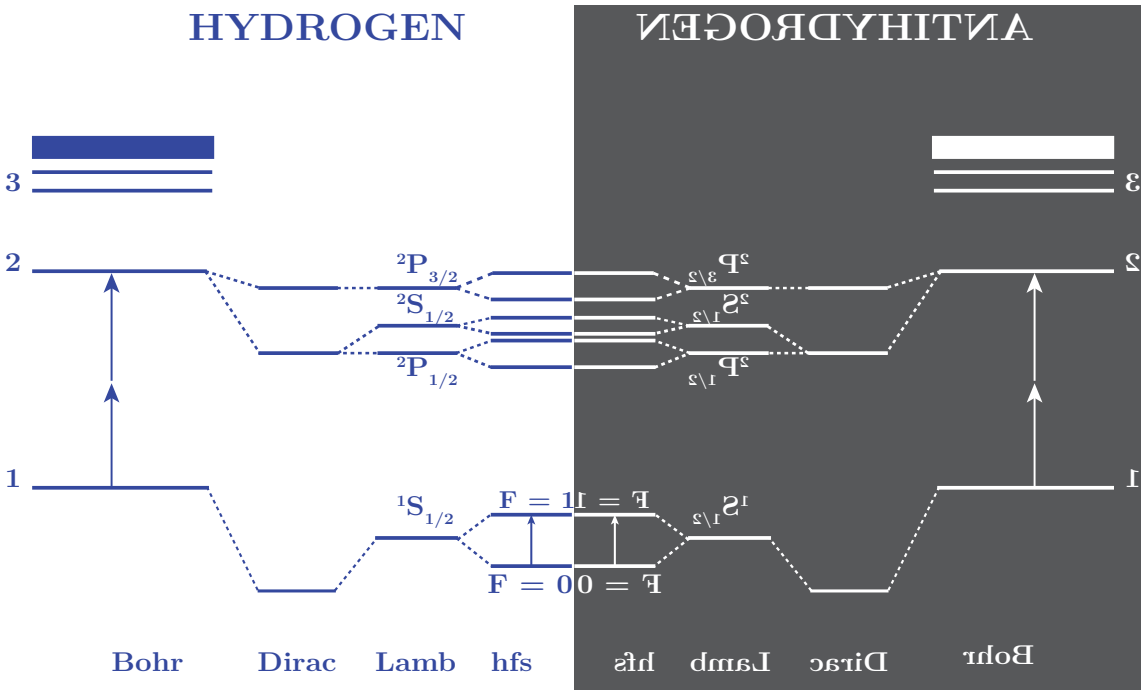

Figure 1.2: Schematic illustration of atomic and anti-atomic energy levels of hydrogen and antihydrogen.

In principle, it is plausible to investigate and attain a comparison of atomic and anti-atomic properties as a further and more concrete verification of the CPT symmetry. The 2S excited state of hydrogen possesses a lifetime of 122 ms, and hence a natural linewidth of five parts in 10^{16}. Consequently, in principle, the 1S-2S quantum transition is capable of providing scientists with a direct comparison of antimatter and matter at a level of one part in 10^{18}. Furthermore, alternative quantities which could be exploited include the hyperfine structure splitting of the ground state of antihydrogen atom. In particular, since measurements such as the ground state hyperfine structure splitting [18] and the 1S-2S two-photon Doppler-free quantum transition [19] of the hydrogen atom have been determined to a very high accuracy of 6 parts in 10^{13} and approximately 4 parts in 10^{15}, respectively, a tremendously precise comparison between hydrogen and antihydrogen can be performed.

Probing antihydrogen with laser light poses extreme technological challenges since firstly the antihydrogen atoms do not occur naturally and as a result they must be synthesized. Secondly, antihydrogen annihilations with normal matter must be prevented by confining anti-atoms in a vacuum. Furthermore, compared to spec-

troscopy on 10^{12} atoms of trapped hydrogen, due to the very small trapping rate of ~ 10, working with only a few anti-atoms at a time is a further challenge that needs to be addressed. To meet these technological challenges, ALPHA has devised various experimental and computational techniques that aim to both enhance the antihydrogen formation and trapping rates, as well as increase the detection efficiency of antihydrogen atoms. The prime diagnostic tool for the detection of antihydrogen in the ALPHA experiment is the Silicon Vertex Detector (SVD), which is the key component for analysing experimental results regarding the antihydrogen investigations.

The detection efficiency and spatial resolution of the SVD is determined by how effectively the statistical, pattern recognition and track reconstruction methods are implemented. The objective of this thesis is to provide a set of new, robust and enhanced software algorithms which both examine the generation of electric pulses due to the passage of charged pions resulted from the annihilation of an antiproton, and estimate the annihilation location (the vertex), see Chapter 6, Chapter 7 and Appendices A-D.

1.3 AD experiments

The function of the AD is to produce low-energy antiprotons for the purpose of antimatter investigations. These cold antiprotons are then ejected into various experiments located inside AD, one of which is ALPHA and will be described in detail in the coming chapters. Other experiments include Atomic Spectroscopy And Collisions Using Slow Antiprotons (ASACUSA), ATRAP, Antiproton Cell Experiment (ACE) and Baryon Antibaryon Symmetry Experiment (BASE). Antihydrogen Experiment: Gravity, Interferometry, Spectroscopy (AEGIS) and Gravitational Behavior of Antihydrogen at Rest (GBAR) experiments have the objective of investigating the gravitational interaction between antimatter and the Earth. GBAR will be utilizing the antiprotons prepared by Extra-Low ENergy Antiproton (ELENA)

ring, the new generation of the AD. The experiments at the AD are based on very low energy anti-matter physics and this thesis addresses the improvement of single anti-atom detection techniques used in the ALPHA experiment.

1.4 Thesis overview

Chapter 2 provides an overview of the ALPHA apparatus, including the upgrade of its original design (ALPHA-I) to ALPHA-II with the objective of highlighting the similarities and differences between the two, its prime procedures and the new techniques designed to trap and study antihydrogen atoms. The confinement and manipulation of the non-neutral plasmas along with various techniques aimed at preparing antiproton and positron plasmas for antihydrogen formation are presented in Chapter 3. Chapter 4 describes methods utilized in the ALPHA experiment to create, trap and detect antihydrogen atoms. The design of the SVD as well as the theory of semiconductors are presented in Chapter 5. The key contributions of the author are presented in Chapters 6 and 7 where an alternative method resulting in a 1.5% increase in the vertex reconstruction efficiency is presented in detail. The new and improved pedestal analysis and event reconstruction methods have laid the foundations for several future investigations, such as the rejection of cosmic background, the comparison with the simulation of reconstructed vertices, the determination of the correlation between the n- and p-side pulse heights of the hits associated with the tracks contributing to the vertex reconstruction, and the analyses of the extant data from the past experiments (observations of the 1S-2S and 1S-2P Lyman-α transitions in antihydrogen at wavelengths of 243 and 121.6 nanometers, respectively) and data to be acquired from the future experiments (measurement of the gravitational acceleration of antihydrogen).

Chapter 2

The ALPHA Apparatus

Antihydrogen formation requires the capture, manipulation, cooling and trapping of its charged constituents, antiproton and positron. In addition, high precision investigation of neutral antihydrogen atoms further relies on devices capable of manipulating, confining and identifying neutral (anti)atomic species. The ALPHA scientists have devised and implemented methods from various disciplines, such as plasma, particle, detector and atomic physics to meet these requirements.

This chapter provides an overview of the ALPHA apparatus, including the upgrade of its original design (ALPHA-I) to ALPHA-II with the objective of highlighting the similarities and differences between the two, its prime procedures and new techniques designed during the past twenty five years to trap and study antihydrogen atoms. A discussion regarding the machines used for creation and accumulation of antiproton, positron and electron plasmas will be presented. Sections 2.3 and 2.4 focus on the theoretical background of the confinement of charged antiparticles and neutral anti-atoms as well as the corresponding devices designed and utilized by the ALPHA collaboration to realize these theoretical concepts. The last section is allocated to the description of devices used for particle detection and diagnostic assessments. Unless stated otherwise, all the discussions in this thesis refer to the ALPHA-II apparatus.

2.1 Apparatus overview

2.1.1 ALPHA-I & ALPHA-II

The ATHENA experiment succeeded in the production but not the confinement of cold antihydrogen atoms in 2002 [2]. The ALPHA experiment is a successor of ATHENA and was assembled in 2005, known as ALPHA-I. This machine was subsequently upgraded as the ALPHA-II experiment in late 2011.

Figures 2.1 and 2.2 display the designs of ALPHA-I and ALPHA-II. Fig. 2.3 summarizes the following prominent steps in creating, confining and detecting antihydrogen atoms in both the ALPHA-I and ALPHA-II machines.

Step 1: Antiprotons are produced by energetic protons injected from the Proton Synchrotron (PS) (Sec. 2.2.1) and then diverted to the Antiproton Decelerator (AD) (Sec. 2.2.2.2). The AD's objective is to decelerate and deliver 30×10^6 antiprotons with an average energy of 5.3 MeV at 100 s intervals to various experiments. Positrons are created inside the positron accumulator (Sec. 2.2.3). The continuous accumulation and the subsequent cooling of the positrons from a radioactive source is accomplished by a Surko-type apparatus [20].

Step 2: The accumulated positrons and antiprotons are manipulated and confined in a Penning-Malmberg trap [21] (Sections 3.3 and 3.5), which utilizes a combination of electric and magnetic fields.

Step 3: The charged anti-particles are ejected into the neutral-atom magnetic trap (Sec. 2.4) located within the mixing section of the Penning-Malmberg trap. This magnetic trap includes a set of superconducting magnets in the form of mirror coils and an octupole magnet. This particular magnetic field configuration along with the axial magnetic field of the external solenoid create a minimum-B field in three-dimensions to trap antihydrogen.

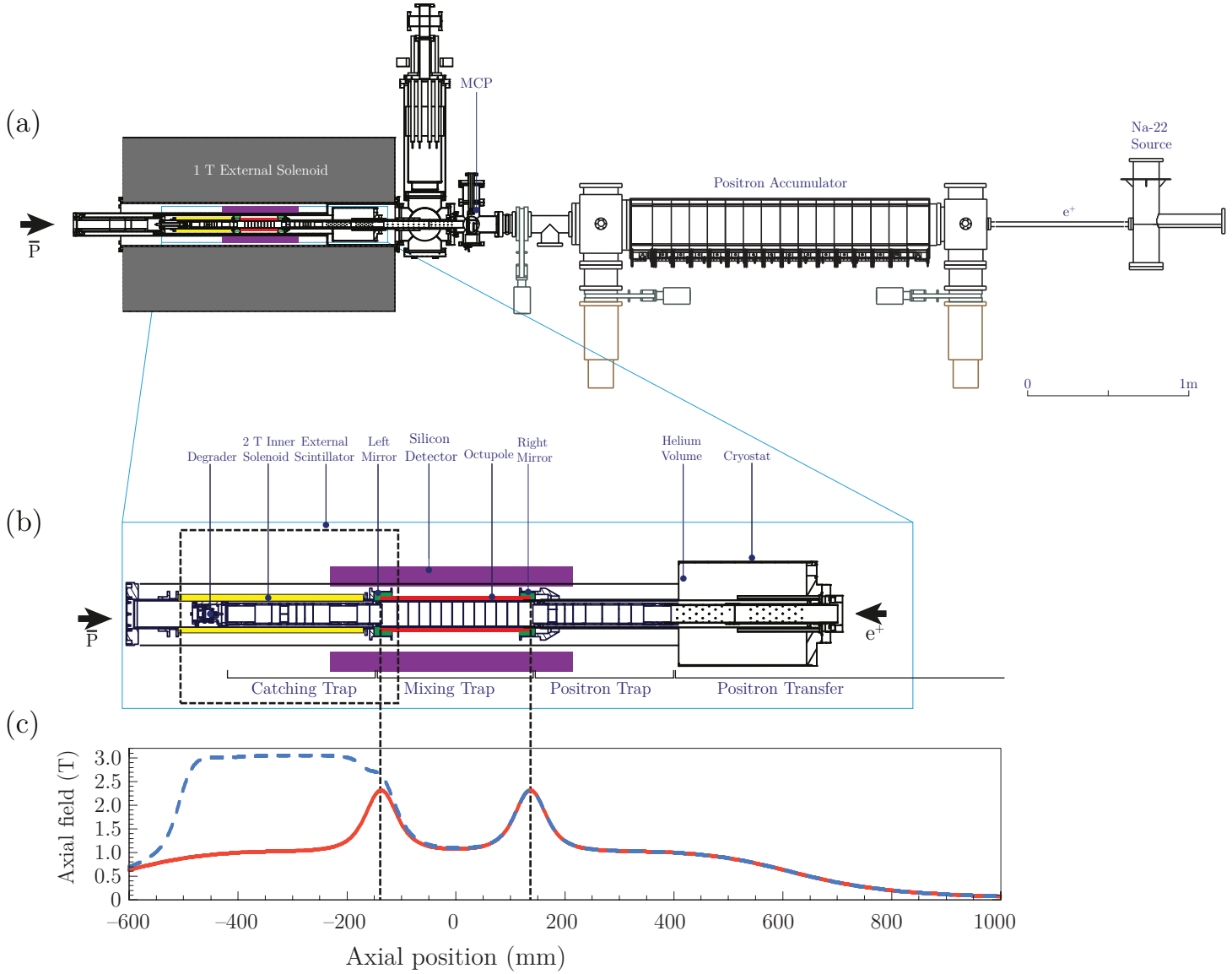

Figure 2.1: (a) Schematic illustration of the ALPHA-I apparatus. Procedures for the creation and the subsequent ejection of antiprotons and positrons into the apparatus is described in Sections 2.2.2.2 and 2.2.3, respectively. (b) Trap configuration. (c) Variation of the axial magnetic field. Superimposed on the 1 T external solenoidal field, the blue and red curves represent the fields produced by the 2 T inner solenoid and the two 1.2 T mirror coils of the neutral-atom trap, respectively. Image modified from [22].

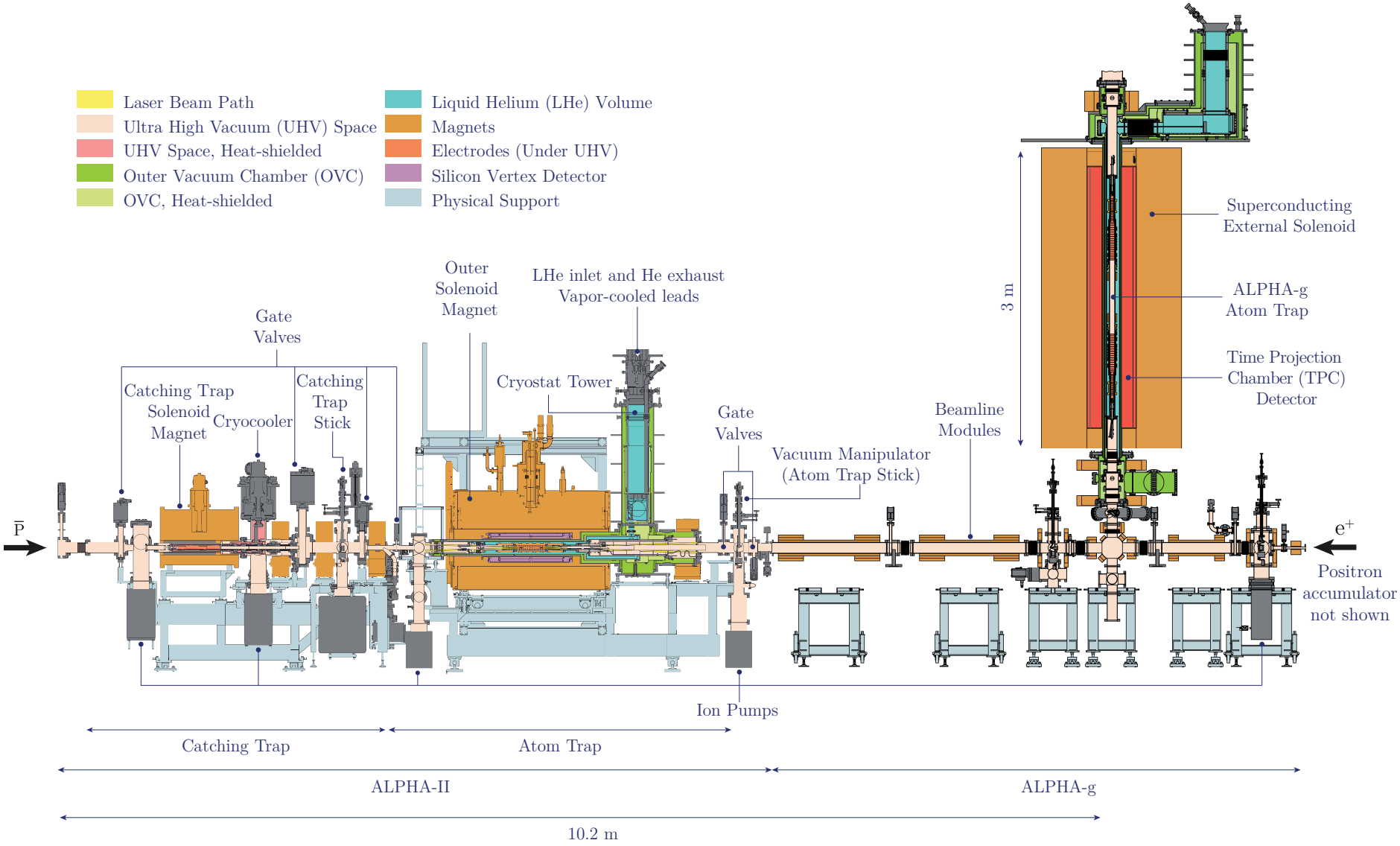

Figure 2.2: Cross sectional illustration of the ALPHA-II and ALPHA-g apparatus. Credits: the ALPHA Collaboration and Mark Andrew Johnson, private communications.

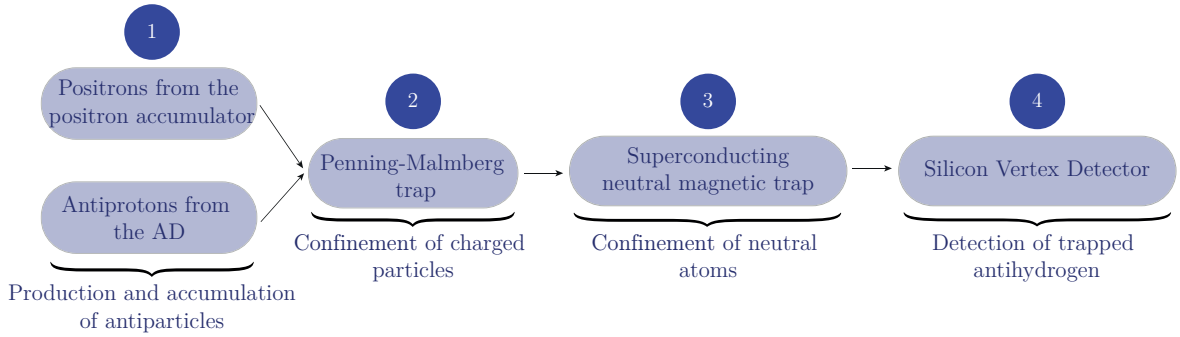

Figure 2.3: Flowchart illustrating the steps involved in creating, confining and detecting antihydrogen in the ALPHA apparatus.

Step 4: Antihydrogen atoms with energies less than the trap-depth of the neutral trap are magnetically confined. The antihydrogen atoms escape the magnetic trap and are detected by the Silicon Vertex Detector once the neutral trap is promptly de-energized. Additional detection and diagnostic devices are employed in the ALPHA apparatus, which assists with acquiring critical information regarding the condition and the particle parameters of the plasma such as density, temperature and size.

Several techniques have been devised by the ALPHA collaboration in order to optimize the manipulation of antiproton and positron plasmas with the objectives of both producing and enhancing the confinement of antihydrogen atoms. A number of these mechanisms include:

The Rotating Wall (RW): Provides the radial compression of charged (anti) plasmas resulting in denser plasmas (Sec. 3.3.2).

EVaporative Cooling (EVC): Utilizing electrons, this mechanism aims at further cooling of antiprotons and positrons (Sec. 3.3.4).

The Strong Drive Regime EVaporative Cooling (SDREVC): Performing the simultaneous evaporative cooling and the rotating-wall compression on the non-neutral plasma in the Strong Drive Regime (SDR) (Sec. 3.4).

Adiabatic cooling: Reducing the axial energy (and the corresponding temperature) of the particles of a plasma by slowly extending the confining potential

well (Sec. 3.5.2).

Autoresonant injection: A technique applied to inject antiprotons into the positron plasma during the mixing phase of the experiment to produce antihydrogen atoms (Sec. 4.2.1.2).

Slow merge mixing: The slow merge ($\sim$ 1 s) of the antiproton and positron electrostatic potential wells permitting the two species to flow into each other (Sec. 4.2.1.3).

The confinement of cold antihydrogen was achieved by the ALPHA-I apparatus in 2010 [4] and as a result the first experimental investigation probing the internal structure of the antihydrogen was conducted in 2012 [6].

Similar to the ALPHA-I apparatus, the ALPHA-II design incorporated additional key features such as the capability of prolonged confinement of antihydrogen as well as performing spectroscopic measurements on trapped antihydrogen. In particular, ALPHA-I and ALPHA-II differ from one another in two prime aspects: (1) laser inclusion for the spectroscopy of antihydrogen (2) the addition of a separate antiproton Penning-Malmberg trap for capturing and manipulating the extracted antiprotons from the AD.

2.2 Charged (anti)particle production

2.2.1 High-energy antiproton production

Various antiproton factories throughout the world, such as CERN and Fermilab, create antiprotons by colliding high-energy protons with a target. Due to the baryon number conservation, the antiproton production threshold energy for the mentioned process is 5.6 GeV and, due to Fermi motion, $\sim$ 4.3 GeV for a nuclear target, indicating that acquiring sufficient number of antiprotons relies on primary beam energy being greater than this threshold. A glance at Fig. 2.4 reveals that the antiproton

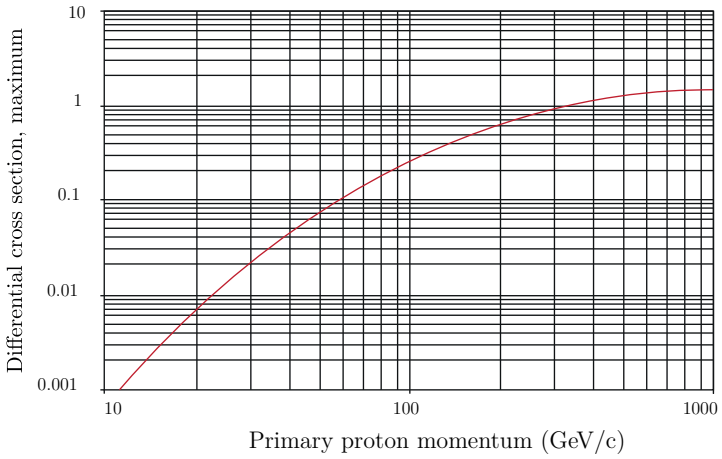

Figure 2.4: (a) Antiproton production cross section versus incident proton momentum. Image adapted from [23].

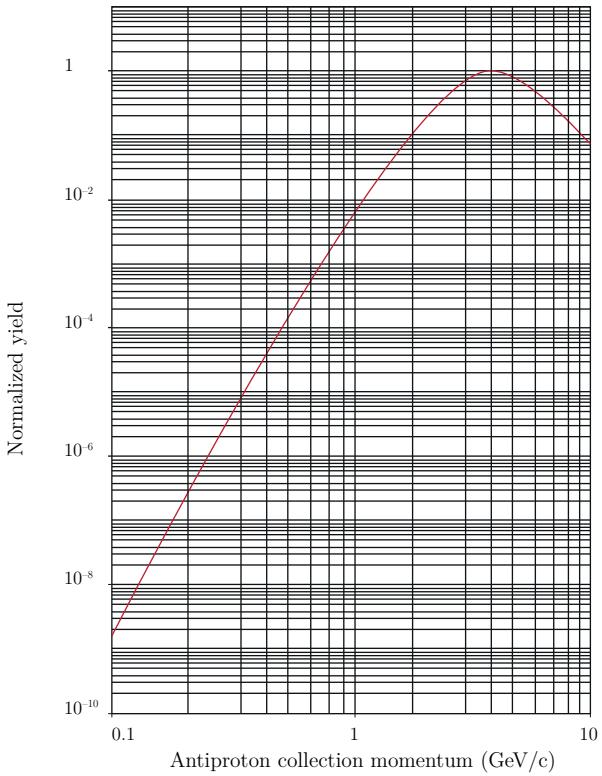

Figure 2.5: Antiproton yield versus collection momentum for a primary beam momentum of 26 GeV/c. Image adapted from [23].

production cross section as a function of primary proton beam momentum follows a gradual growth up to approximately 1000 GeV/c.

Fig. 2.5 is an illustration of selecting a particular primary beam momentum of 26 GeV/c of the CERN antiproton source and observing the change in antiproton yield as a function of antiproton collection momentum. It is noted that the vertical (yield) axis of the plot is scaled logarithmically. The figure depicts that the yield

undergoes through a sharp increase of several orders of magnitude prior to reaching a peak value at typically 10% of the primary beam energy.

In addition, the normalization is performed by assigning the maximum value of the yield (for a corresponding antiproton collection of momentum of 4 GeV/c) to be unity. This maximum yield is greater than the corresponding yield at 100 MeV/c by nine orders of magnitude; it is of profound importance to obtain the antiprotons from the target at the optimal momentum. This explains why the AD at CERN functions at 3.5 GeV/c resulting in a yield of about 3.5×10^{-6} antiprotons for every incoming proton. Equivalently, a typical production primary beam pulse of about 1.5×10^{13} protons yields approximately 5×10^{7} antiprotons.

2.2.2 Low-energy antiproton production

2.2.2.1 The LEAR

The exploitation of antiprotons for physics studies was solely possible by incorporation of a low-energy facility, the so-called The Low Energy Antiproton Ring (LEAR), into the antiproton production complex at CERN in 1982. LEAR's objective was to decelerate and collect antiprotons for experiments and was in operation until 1996. The collection, cooling and deceleration of antiprotons were the interplay of four accelerators at the antiproton production complex: (1) the Proton Synchrotron (PS), an Antiproton Collector (AC) ring, the Antiproton Accumulator (AA) ring and the LEAR, see Fig. 2.6.

The antiproton production procedure is as follows: initially an electric field is applied to a bottle of hydrogen gas to remove hydrogen atoms' electrons as to isolate and produce bare protons. LINear ACcelerator (LINAC)-II is the first accelerator in the complex chain which accelerates the protons to an energy of the 50 MeV/c and subsequently inject them into the Proton Synchrotron Booster (PSB). The protons obtain an acceleration of 1.4 GeV/c by the PSB. The final increase in acceleration of the protons beam to 26 GeV/c is provided by the Proton Synchrotron (PS). The

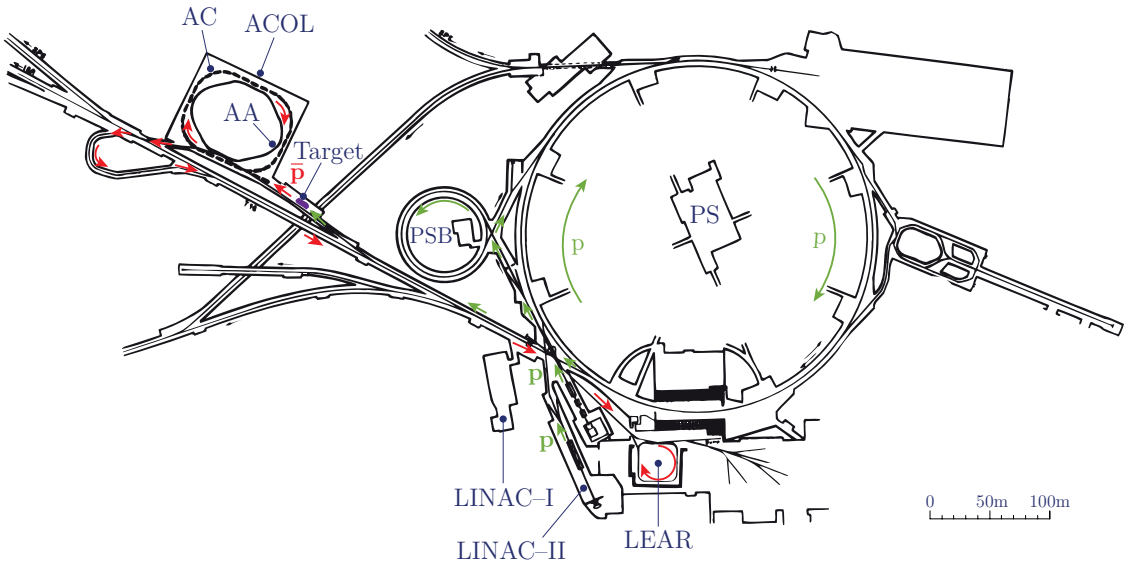

Figure 2.6: Antiproton production complex at CERN illustrating the PS along with its associated booster as well as LINACS, the AA–AC facility, and LEAR.

PS then diverts the proton beam towards the ACOL (Antiproton COLlector). Prior to the ACOL, an iridium target cooled to air temperature was positioned whereby upon contacting with the incoming protons a collision is resulted. In a small fraction of the collisions, one per million, subject to the conservation requirements of energy, momentum, and nucleon number reaction 2.1 occurs

$$\mathrm{p(beam)} + \mathrm{p(iridium)} \rightarrow \mathrm{p} + \mathrm{p} + \mathrm{p} + \overline{\mathrm{p}}. \tag{2.1}$$

This reaction requires the incoming protons to have a minimum kinetic energy of $\mathrm{E} \sim 6$ GeV, whereas the resulting antiproton and three protons have laboratory energies of $\mathrm{E} \sim 1$ GeV. In order to increase the production yield of antiprotons, the PS-AC combination utilizes higher energies of $\mathrm{E} \sim 3.6$ GeV optimized for the large AC ring. The AA ring is capable of stacking multiple production cycles for further prolonged periods of time. The designated antimatter experiments capture the antiprotons into their charged traps by invoking the dynamical switching of the potential walls of the trap (see Sec. 3.3). This requires the charged antiprotons to be delivered to the experiments in the form of short pulses, around $1 - 4 \times 10^8$ particles for a bunch length of 200 ns. To meet this requirement, LEAR was further

incorporated with a fast extraction capability in 1986, allowing antiprotons with momentum of as low as 100 MeV/c to be produced and delivered.

2.2.2.2 The Antiproton Decelerator (AD)

Following the closure of LEAR in 1996, Baird *et al* first introduced a scheme for the simplification of the production of pulsed antiproton beams. The basic concept established the utilization of the original production and the subsequent capture of the 3.57 GeV/c antiprotons in the AC. However, in the proposed scheme, the AC would not only collect but further provide features such as deceleration, electron cooling and stochastic cooling of the antiprotons. The addition of this new feature resulted in the elimination of the three cooling machines and their corresponding beam transfer lines required during the LEAR period. The final design report for the manufacturing of a new machine, the AD, was approved on 7 February 1997. The AD began operating in 2000 and is now the prime provider of cold antiprotons.

Fig. 2.7 is a schematic illustration of the AD. Important cooling components such as stochastic cooling kicker, Radio Frequency (RF) cavities and electron cooler are shown. At first, the reaction 2.1 between the iridium target and an extracted beam from the PS containing 1.5×10^{13} protons with a momentum of 26 GeV/c occur about every minute.

During the reaction, the capture of the produced antiprotons is enhanced by the utilization of a 'lithium lens' consisting of a solid rod of lithium with a diameter and length of 1 cm and 10 cm, respectively. A current of approximately 1 MA is directed along the rod, producing a high magnetic field wrapped around the current. The field magnitude is small at the centre and increases radially towards the edge of the lens. Antiprotons moving close to the centre of the lens are unaffected by the field whereas those moving away from the axis and close to the edge experience a magnetic force towards the axis of the lens. Therefore, the high magnetic field maintains the axial momentum of the antiparticles in order to reduce their divergence, leading to the enhanced capture of the produced antiproton [24]. The resultant antiprotons

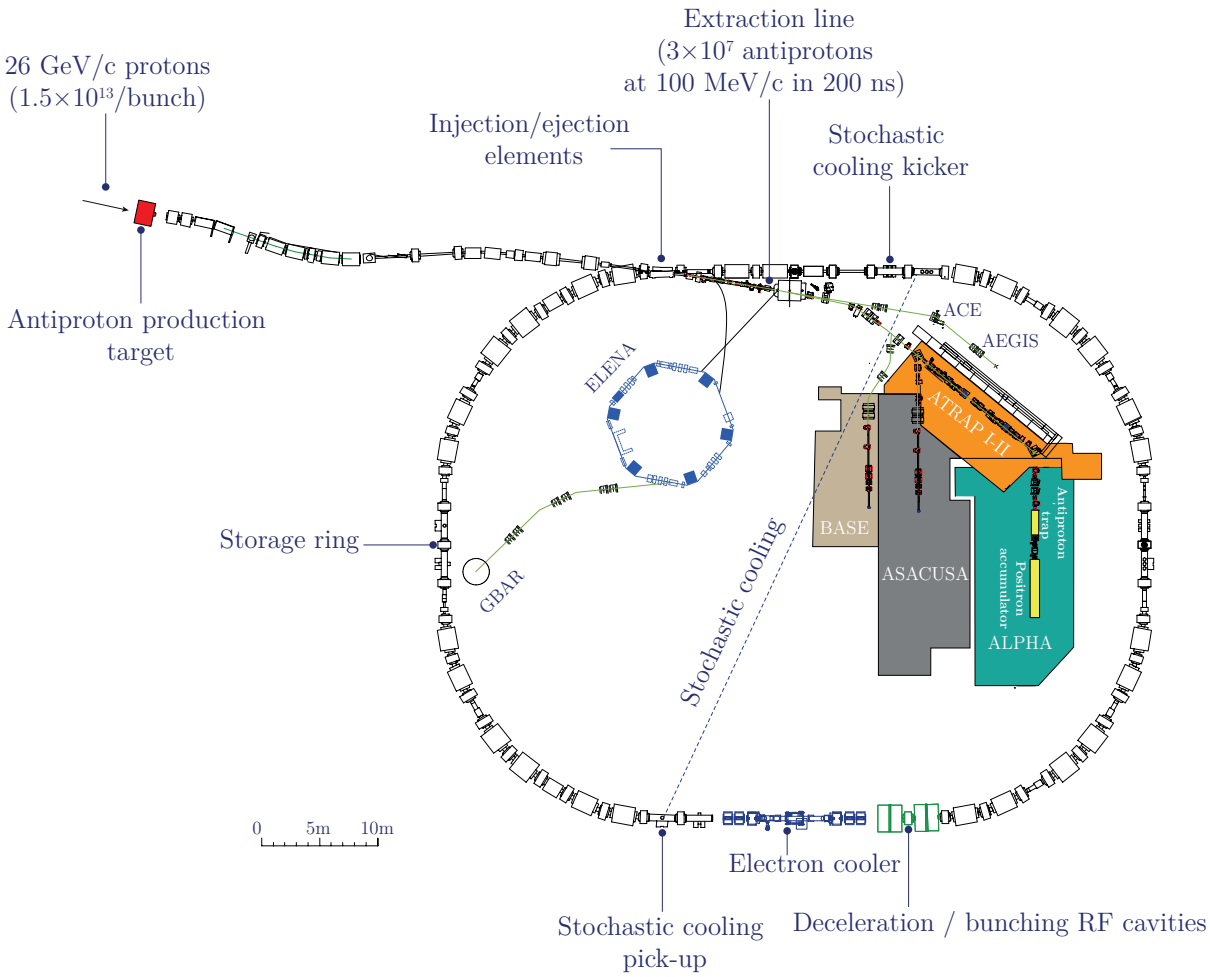

Figure 2.7: Layout of the AD facility.

with a momentum of 3.57 GeV/c are deflected into the AD ring and subsequently cooled and decelerated to a momentum of 100 MeV/c. Afterwards, the low-energy antiprotons are promptly diverted towards one of the experimental beam lines.

Fig. 2.8 shows a 90-second four-step operational cycle of the AD beginning with the injection of 5×10^7 antiprotons at 3.57 GeV/c and ending with the delivery of 3×10^7 antiprotons at 100 MeV/c in a pulse as short as 90 ns.

Step 1 begins by focusing the antiprotons into a manageable beam using a method knowns as 'stochastic cooling' [25][26]. This sort of cooling involves acquiring the measurements of the beam at a particular side of the ring by the kicker. This information is then sent to the pick-up across the middle of the ring in order to provide the required adjustments to the AD prior to the arrival of the beam from the other side. Once the beam is sufficiency refined, the deceleration process begins

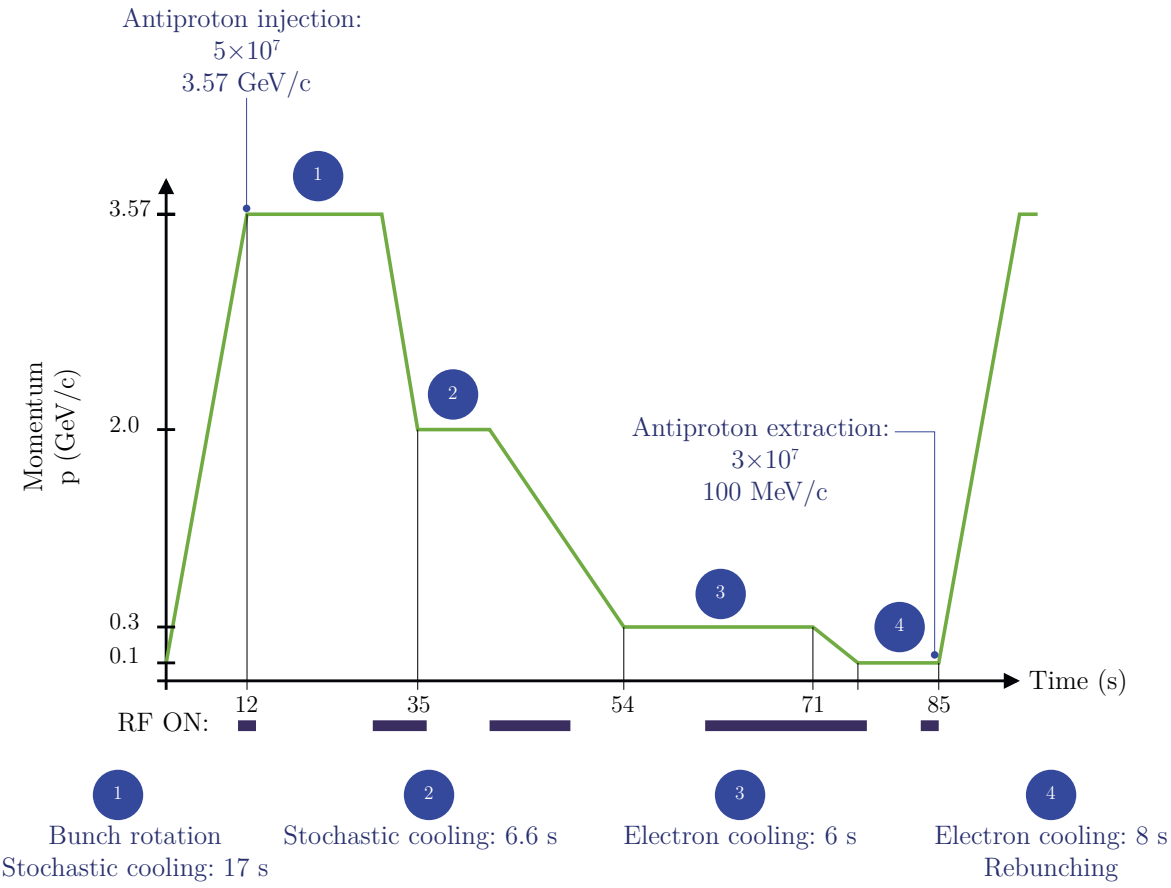

Figure 2.8: Operational cycle of the AD, illustrating the momentum of $\overline{\mathrm{p}}$ versus the time elapsed as well as the prime stochastic, electron and RF cooling mechanisms.

and an antiproton momentum reduction from 3.57 GeV/c to 2 GeV/c is achieved. This cooling is done by employing electric fields inside Radio Frequency (RF) cavities. As it does so, the beam tends to expand. As a result, a combination of dipole and quadropole magnets is used to maintain the beam bend and focus, respectively. Performing the same methods results in a momentum reduction to 0.3 GeV/c at the end of the step 2. Once at 0.3 GeV/c, the antiprotons have been slowed enough for a more rapid cooling mechanism, called electron cooling [27], to be applied during both step 3 and prior to the extraction at 0.1 GeV/c at the end of step 4. The electron cooling provides further cooling by the integration of a dense and cold cloud of electrons traversing in the same direction as the antiprotons. In addition, it assists antiprotons with maintaining their direction of motion and therefore undergoing less divergence.

2.2.3 Positron accumulator

Positrons are emitted by spontaneous β^+ decay of many radioisotopes. The preferred radioactive source in the ALPHA experiment is an isotope of sodium, ^{22}Na, with an activity of 2.7 GBq undergoing the decay process given by

$$^{22}\mathrm{Na} \rightarrow {}^{22}\mathrm{Ne}^* + \beta^+ + \nu_\mathrm{e}. \tag{2.2}$$

The nucleus ^{22}Na is chosen for its high β^+ branching ratio (90%) and its half-life of approximately 2.6 years, thereby reducing the need to change sources frequently. However, ^{22}Na emits positrons with a wide spectrum of energies, reaching a maximum kinetic energy of 544 keV. Synthesizing antihydrogen with high-energy, 'hot', positrons is extremely difficult and so the positrons must be decelerated.

Access to an intense reservoir of low-energy positrons plays a vital role in the formation of atomic antimatter. A significant number of investigations on the implementation of such sources have been carried out for the past three decades, leading to development of better methods for the controlled production of low-energy positron beams. A brief discussion of these methods as well as some of the underlying physics governing the cooling and confinement of positrons are presented in Sections 3.1 and 3.5. A schematic diagram of the positron accumulator is shown in Fig. 2.9.

2.2.4 Electron gun

Various experimental mechanisms in the ALPHA apparatus utilize electrons for plasma manipulations, measurement of the magnetic field in the trap, diagnostic assessment of the trapping apparatus, and the capturing, cooling and compression of the antiproton plasma.

The device providing the apparatus with the required electrons is known as the electron gun [22]. It consists of a barium-oxide filament, which heats up upon the flow of current and the thermionic emission of the electrons follows. Thermionic ele-

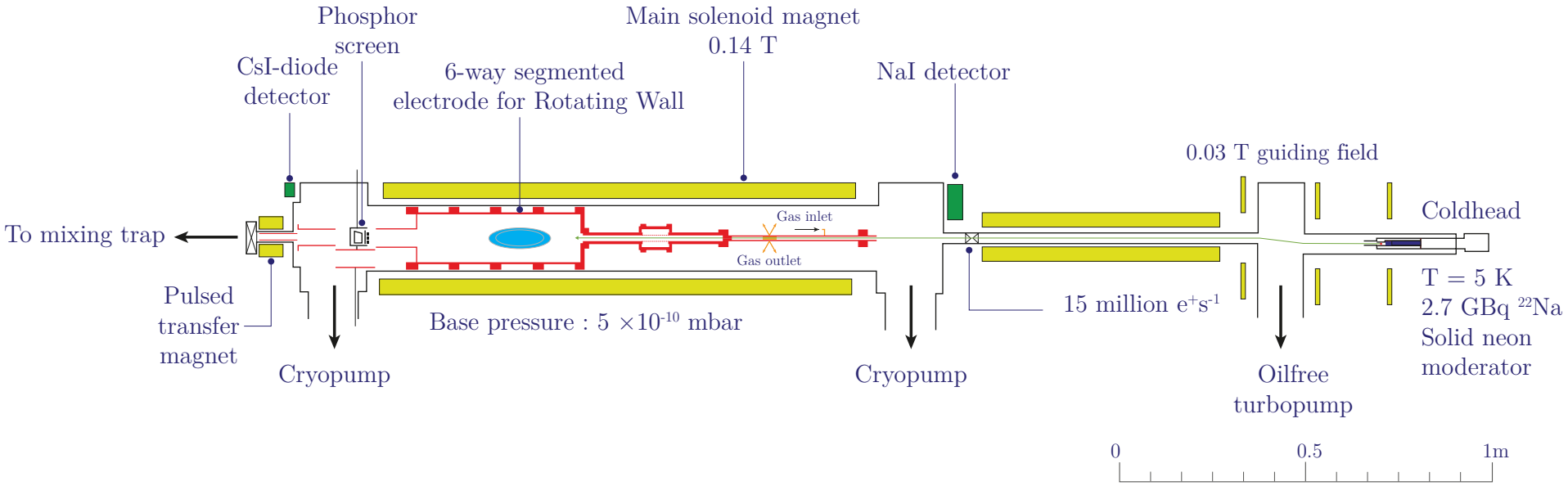

Figure 2.9: Schematic illustration of the ALPHA positron accumulator. The positrons are guided by the magnetic field lines and follow the green path from the ^{22}Na source on the right to the Penning-Malmberg trap comprising of the segmented electrode to the left where they undergo rotating wall compression (see Sec. 3.3.2) and are subsequently collected as a plasma (blue ellipse). The positrons are eventually transferred to the Mixing Trap (MT), ready for antihydrogen production upon mixing with the antiprotons.

ctrons are accelerated by the application of an electric field and guided towards the trap by the magnetic field lines. Two electron guns are incorporated into the ALPHA apparatus, one for the Atom Trap (AT) and one for the Catching Trap (CT).

2.3 Penning trap for charged particles

Antihydrogen production requires the capture, cooling and manipulation of its charged constituents, antiproton and positron. For further diagnostics to be undertaken with no external influences, these antiparticles must be confined for relatively long periods of time. A well-understood and suitable device for this purpose is a Penning trap capable of storing and prolonged continuous manipulation of charged (anti)particles in a controlled fashion. This type of trap is frequently employed in the ALPHA apparatus. The Penning trap operating principle is presented in the following section.

2.3.1 Theory of confinement

A charged particle with a charge-to-mass ratio of q/m traversing perpendicular to a spatially uniform strong magnetic field $\vec{B} = B_0\hat{z}$ undergoes a circular motion in the $x - y$ plane. This oscillatory motion has a free cyclotron angular frequency w_c given by 2.3 and results in the confinement of the charged particle in the plane perpendicular to the magnetic field.

$$w_c = \frac{qB_0}{m}, \tag{2.3}$$

where q, B_0 and m are the charge, magnitude of the z-component of magnetic field and mass of the charged particle, respectively. The axial, along the z direction,

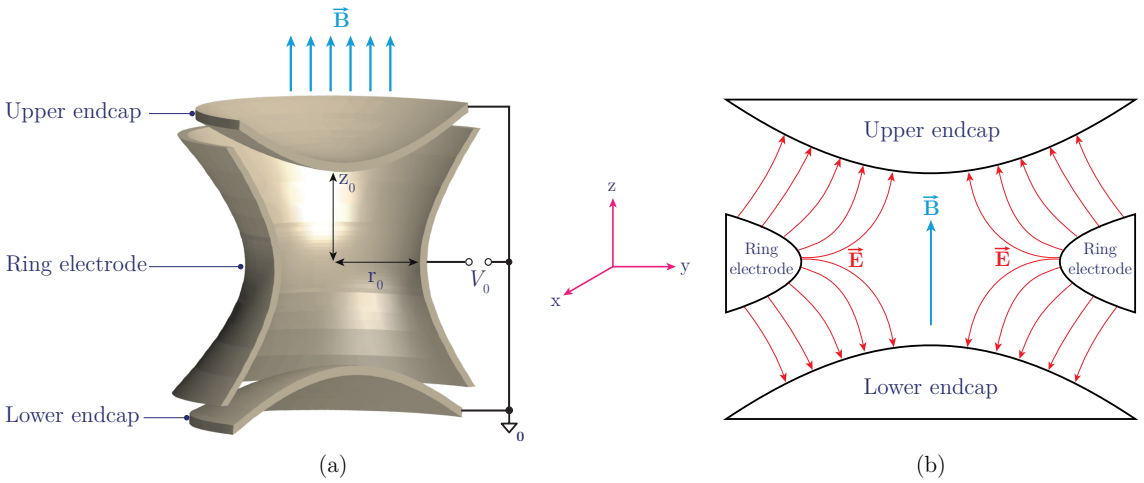

(a) (b)

Figure 2.10: (a) Schematic cross sectional illustration of a hyperbolic Penning trap comprising two endcap electrodes and the ring electrode. The radial and axial confinement of a charged particle are achieved by a magnetic field $\vec{B}$ along the z-axis (trap symmetry axis) and a voltage V_0 applied between the ring and the endcap electrodes, respectively. Image modified from [28]. (b) Illustration of the magnetic and electric field lines of a Penning trap.

confinement is obtained by applying a static electric potential in the form of

$$\phi(r,z) = \frac{V_0}{2d^2}\left(z^2 - \frac{r^2}{2}\right), \tag{2.4}$$

where d is a parameter characterized by the trap geometry, and V_0 is the applied voltage to the electrodes (see Fig. 2.10(a)). The superposition of a weak electric field and a strong magnetic field constitutes a Penning trap (see Fig. 2.10(b)).

Fig. 2.10(a) is a schematic illustration of a Penning trap where the electrodes produce equipotential lines of the form 2.4 with a characteristic trap parameter of

$$d = \sqrt{\frac{1}{2}\left(\frac{r_0^2}{2} + z_0^2\right)}. \tag{2.5}$$

In this figure, r_0 and the distance $2z_0$ between the two endcaps characterize the geometry of the trap. Ideally, a perfect quadrupole potential is obtained by having electrodes of infinite length. The resultant electric field leads to an oscillatory axial motion along the magnetic field lines, purple two-sided arrow in Fig. 2.11(a), with

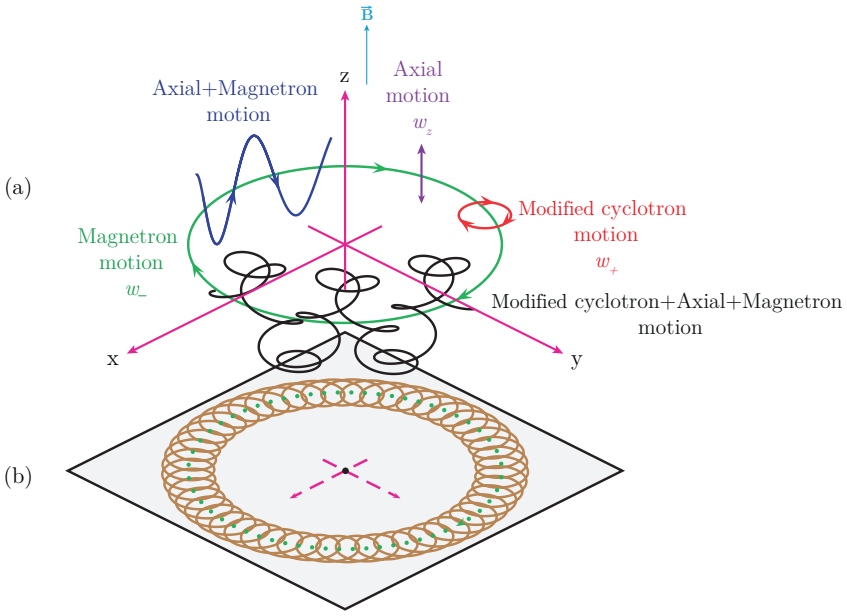

Figure 2.11: (a) Three distinct motions of a charged particle confined in a Penning trap as well as the combined motion (black curve). (b) Projected motion onto the $x-y$ plane (trap mid-plane). Image modified from [28].

an angular frequency of

$$w_z = \sqrt{\frac{qV_0}{md^2}}. \tag{2.6}$$

A particle with mass m and charge q in magnetic and electric fields of a Penning trap is acted on by the Lorentz force given by

$$m\ddot{\vec{r}} = q\Big(-\nabla\phi + \dot{\vec{r}} \times \vec{B}\Big), \tag{2.7}$$

where $\vec{r} = (x, y, z)$. Solving the following three Cartesian components of Eq. 2.7 [29]

$$\begin{aligned} \ddot{x} - w_c\dot{y} - \frac{1}{2}w_z^2 x = 0, \\ \ddot{y} + w_c\dot{x} - \frac{1}{2}w_z^2 y = 0, \\ \ddot{z} + w_z^2 z = 0, \end{aligned} \tag{2.8}$$

yields two distinct modes of radial motion with angular frequencies w_- and w_+ given by

$$\begin{aligned} w_+ &= \frac{1}{2}\Big(w_c + \sqrt{w_c^2 - 2w_z^2}\Big), \\ w_- &= \frac{1}{2}\Big(w_c - \sqrt{w_c^2 - 2w_z^2}\Big). \end{aligned} \tag{2.9}$$

Table 2.1: Opertional oscillation frequencies for a $B_0 = 1$ T, $V_0 = 10$ V and d = 1 cm in the ALPHA trap.

Particle	Modified cyclotron frequency w_+	Axial frequency w_z	Magnetron frequency w_-
Electron	28 GHz	21 MHz	8 kHz
Positron	28 GHz	21 MHz	8 kHz
Antiproton	15 MHz	500 kHz	8 kHz

A confined oscillatory motion requires $w\pm$ to be real which, in turn, implies that $w_c^2 > 2w_z^2$. Providing that $w_c \gg w_z$, $w_+ \simeq w_c$ and the positive root with a larger frequency (compared to the axial frequency) is defined as the modified cyclotron frequency, which represents a cyclotron motion with a small circular orbit (red curve in Fig. 2.11(a)). In addition, having $w_+ w_- = w_z^2/2$, the negative root can be written as $w_- \simeq w_z^2/(2w_c)$. This root is known as magnetron frequency, possesses a smaller frequency and can be characterized as a slow $\vec{E} \times \vec{B}$ drift motion with a large circular orbit (green curve in Fig. 2.11(a)). Fig. 2.11(a) is a graphical representation of the three distinct and decoupled motions with a hierarchy $w_+ \gg w_z \gg w_-$. Fig. 2.11(b) is a projection of these motions onto the trap mid-plane. Nominal oscillation angular frequencies in the ALPHA Penning trap are tabulated in Table 2.1. A detailed description of the particle motion in a Penning trap can be accessed via [29].

In practice, the ALPHA experiment utilizes a Penning-Malmberg trap in which the hollow cylindrical electrodes replace the conventional hyperbolic electrodes of a Penning trap. This is due to the fact that the Penning-Malmberg trap allows inclusion of various instruments at both ends of the cylindrical electrode stack and consequently the trap volume can be accessed more readily. Furthermore, a segmented electrode stack provides a more precise manipulation of the confined charged particles since the axial electric field can be altered (see Sec. 3.3.2).

2.3.2 ALPHA-I Penning-Malmberg trap

In the ALPHA experiment the simultaneous axial and radial confinement and manipulation of charged (anti)particles are performed using an axial electric field of a

Penning-Malmberg trap and a strong axial magnetic field, respectively. The static axial magnetic field of 1 T is provided by an external superconducting solenoid and the electrostatic axial potentials are created by a set of 36 gold-plated and voltage-biased cylindrically symmetric electrodes (see Figures 2.12(a) and 2.1(a)-(b)).

There are a few electrodes providing high voltages up to 5 kV. Based on their prime functions and positions relative to the incoming antiprotons from the AD (the upstream end), the set of electrodes constitute three types of traps (see Fig. 2.12(a)):

Antiproton trap: Known as the CT, this trap is designed for the antiprotons directed from the AD to be first captured (using two high voltage electrodes), cooled (using a pre-loaded electron plasma) and subsequently compressed (using six-segmented electrodes), see Sec. 3.3. Surrounding the CT and superimposed on the 1 T axial external magnetic field, an internal superconducting solenoid (the 'inner' solenoid) with a maximum local magnetic field of 2 T allows the CT to acquire an overall magnetic field of 3 T, vital for enhancement of antiproton catching and cooling (see Sec. 3.3.1). The axial magnetic field profile of the ALPHA-I apparatus is demonstrated in Fig. 2.1(c).

Positron Trap (PT): Located on the downstream end (with respect to the positron accumulator), this trap functions in a similar manner to the CT by manipulating positrons directed from the accumulator. The PT also features an azimuthally segmented electrode to radially compress or expand the positron plasma.

Mixing Trap (MT): Consisting of thirteen electrodes where four of them are filtered by means of low-noise amplifiers, the central 'mixing' trap section of the ALPHA-I Penning trap is where the antihydrogen formation occurs when the antiproton and positron plasmas are mixed. By incorporating larger inner diameter and the minimal thickness aspects into the design of the MT electrodes, antihydrogen atoms can acquire the maximum radial motion (due

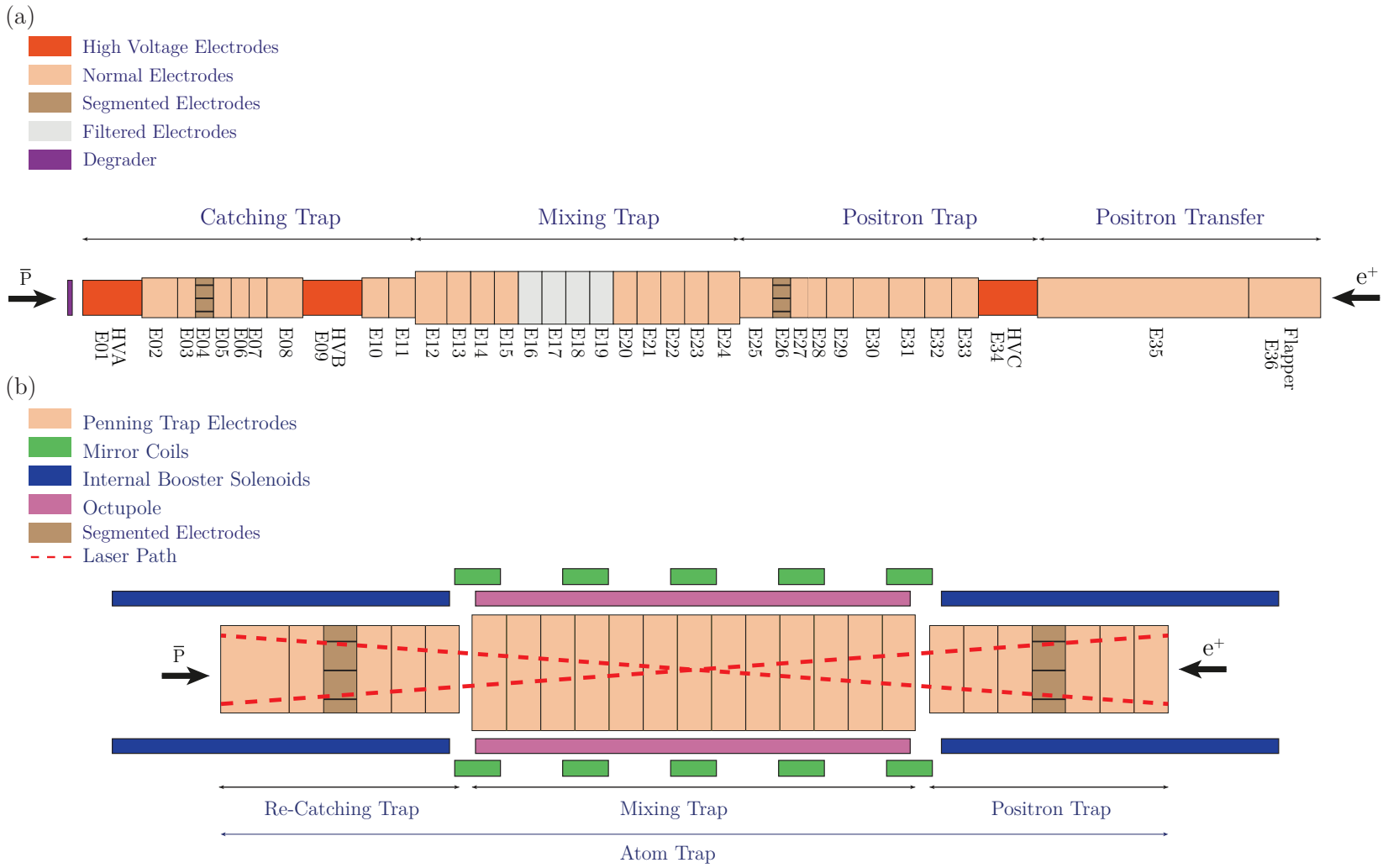

Figure 2.12: (a) The ALPHA-I apparatus electrode configuration consisting of the Catching Trap (CT), Mixing Trap (MT), Positron Trap (PT) and positron transfer section. (b) Schematic diagram of the ALPHA-II Atom Trap (AT) comprising the Re-Catching Trap (RCT), five mirror coils (green) and the octupole (pink). Also shown are the two booster solenoids (blue) that assist in antiproton and positron preparation.

to the maximization of the magnetic trap well-depth) (see Sec. 2.4) and the antiproton annihilation products encounter the minimum amount of scattering material prior to traversing the silicon detector.

Most of the electrodes provide potentials in the range of −140 V to +140 V with a precision of 4 mV while the specially filtered electrodes voltages are in a ±72 V range within 2 mV. High voltage electrodes operate without filters.

2.3.3 ALPHA-II Penning-Malmberg trap

The ALPHA-II apparatus uses two separated Penning-Malmberg traps. In order to conduct independent experiments, the antiproton CT is separated from the main AT, see Figures 2.2 and 2.12(b). This separation of the CT from the AT allows the laser beam to be directed into the AT without being obstructed by the antiproton degrader.

Many features of the ALPHA-II CT resemble the original apparatus. The core objective of the CT is to capture, cool and stack several antiproton bunches and accumulate them at the downstream side of the trap, ready to be first transferred into the ReCatching Trap (RCT) section of the AT for further manipulation and then into the MT section of the AT for producing antihydrogen upon mixing with the positron plasma. The CT consists of twenty electrodes surrounded by an external 3 T solenoid magnet giving rise to a field along the trap axis. The trap is cooled to cryogenic temperatures by a helium gas compressor and two segmented electrodes are incorporated at each end of the CT for compressing the antiproton clouds.

The ALPHA-II AT is demonstrated in Fig. 2.12(b) and is utilized for further precise manipulation of antiproton and positron plasmas as well as the formation and trapping of antihydrogen atoms. It includes twenty-seven electrodes surrounded by an external solenoidal magnetic field of 1 T directed along the trap axis. The AT consists of three different traps:

Re-Catching Trap: Located towards the upstream end of the AT, the antipro-

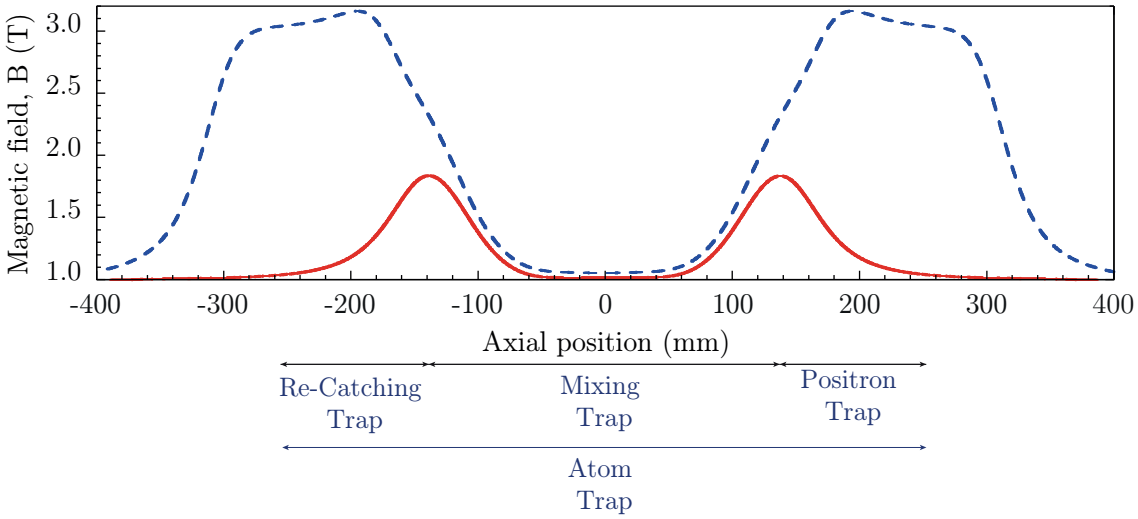

Figure 2.13: Axial magnetic field strength (the external solenoid responsible for producing the uniform 1 T field is not shown). The dashed blue curve represents the on-axis fields of the two left (RCT) and right (PT) 2 T internal booster solenoids of the AT. The energization of the booster solenoids result in an increase in the field magnitude from 1 to 3 T for enhanced capture, cyclotron cooling and rotating wall efficiency of positron, electron and antiproton plasmas. The solid red curve represents the MT field once the five mirror coils and the octupole magnets are energized. Image modified from [10].

ton RCT is where the transferred antiprotons from the CT are re-captured, re-cooled and re-compressed. It consists of seven electrodes with an inner diameter of 29.6 mm where one them is an azimuthally segmented electrode used for compressing and expanding the antiproton plasmas. The RCT includes an internal booster solenoid that is responsible for a maximum axial field of 2 T. Therefore, combined with the 1 T field of the external solenoid, this section of the AT can acquire an overall axial field of 3 T, see Fig. 2.13.

Mixing Trap: The trap at the central region of the AT and is composed of thirteen electrodes where the antiprotons combine with the positrons to form antihydrogen. Same as its original ALPHA-I MT design, the inner diameter of the mixing electrodes are intended to be as large as possible to maximize the trap well-depth. These electrodes are filtered in order to prevent electronic noise.

Positron Trap: Positioned towards the downstream side of the AT, this trap has a function similar to the RCT where the transferred positrons from the positron accumulator are re-captured, re-cooled and re-compressed. Utilizing the 2 T axial field of an internal booster solenoid in the PT and the 1 T field of the external solenoid, the overall axial magnetic field can peak at 3 T in this region, see Fig. 2.13.

2.4 Magnetic neutral-atom trap

In the ALPHA apparatus, subsequent to the formation of antihydrogen, a neutral-atom trap superimposed on the Penning-Malmberg trap is utilized to trap the anti-hydrogen atoms. This section provides the physics theory behind confining neutral antihydrogen in a magnetic trap and the comparison between the ALPHA-I and ALPHA-II magnetic atom traps.

2.4.1 Theory of confinement

Neutral antihydrogen atoms are unable to be confined with Penning-Malmberg traps. However, a small magnetic dipole moment ($\vec{\mu}_{\bar{\mathrm{H}}}$) associated with the total angular momentum ($\vec{J}$) of the neutral-atoms can be used to trap them in a magnetic field. For antihydrogen atom, $\vec{\mu}_{\bar{\mathrm{H}}}$ is given by

$$\vec{\mu}_{\bar{\mathrm{H}}} = -g_J \mu_B \frac{\vec{J}}{\hbar}, \tag{2.10}$$

where g_J is the Landé g-factor, $\mu_B = e\hbar/2m_e$ is the Bohr magneton, and $\vec{J} = \vec{L} + \vec{S}$ is the total angular momentum, with the terms in the sum denoting orbital, $\vec{L}$, and spin, $\vec{S}$, angular momentum.

Antihydrogen in the ground state has no orbital angular momentum ($\vec{L} = 0$) and therefore its magnetic moment is only determined by the spin angular momentum of its constituent antiparticles, antiproton and positrons

$$\vec{\mu}_{\mathrm{S}} = -g\frac{q}{2m}\vec{S}, \tag{2.11}$$

where the magnitudes of g for positron and antiproton are 2.0023 and 5.586, respectively. Eq. 2.11 implies that the spin magnetic moment is inversely proportional to the mass, and therefore, due to the large difference in masses of positron and antiproton, $m_{e^+}/m_{\bar{p}} \simeq (1800)^{-1}$, the positron magnetic moment dominates and the magnetic dipole moment of antihydrogen can then be stated as

$$\vec{\mu}_{\bar{\mathrm{H}}} \simeq \vec{\mu}_{S,e^+} = g_{e^+}\mu_B\frac{\vec{S}}{\hbar}. \tag{2.12}$$

The magnetic moment tends to align with a magnetic field due to experiencing a torque $\vec{\tau} = \vec{\mu}_{\bar{\mathrm{H}}} \times \vec{B}$ determined by the orientation of the dipole moment. With $J_z = S_z = \pm\hbar/2$ and $g_{e^+} \simeq 2$, the ground-state antihydrogen atom positioned in an external magnetic field can possess two quantum states: $\mu_{\bar{\mathrm{H}}_z} = \pm\mu_B$. A positive dipole moment ($+\mu_B$) represents a dipole parallel to the field while a negative dipole moment ($-\mu_B$) denotes a dipole orientated anti-parallel to the magnetic field.

The interaction energy (U) between an external magnetic field and the antihydrogen's magnetic dipole moment is

$$\begin{aligned} U &= -\vec{\mu}_{\bar{\mathrm{H}}} \cdot \vec{B}, \\ &= \mp\mu_B\vec{B}. \end{aligned} \tag{2.13}$$

Eq. 2.13 implies that for antihydrogen atoms in quantum states with their magnetic moments aligned with the field ($\mu_{\bar{\mathrm{H}}_z} = +\mu_B$), the interaction energy decreases in the direction of increasing magnetic field (minimizing U). As a result, the atoms are attracted to regions of high magnetic field and are known as 'high-field seekers'. On contrary, for those atoms with their magnetic moments anti-aligned with the field ($\mu_{\bar{\mathrm{H}}_z} = -\mu_B$), the interaction energy decreases in the direction of decreasing magnetic field. These atoms are consequently attracted to the regions of low magnetic field and are known as 'low-field seekers'.

Establishing a static magnetic field in vacuum with a maximum is not possible [30] and therefore the high-field seeking atoms are unable to be confined. However, a 3-D local magnetic minimum (or 'magnetic bottle') can be constructed such that the magnetic field is at its minimum in the trapping regions and increases radially. Accordingly, the antihydrogen atoms in their 'low-field seeking' ground states can be magnetically trapped if their kinetic energies are smaller than the magnetic potential difference. The trap depth, giving rise to the maximum kinetic energies of the trapped anti-atoms, is determined by

$$\Delta U = \mu_B(B_{\max} - B_{\min}) = \mu_B \Delta B, \tag{2.14}$$

where $B_{\max}$ and $B_{\min}$ are the magnitudes of the maximum and minimum trap magnetic field, ΔB denotes the difference between the maximum and minimum field magnitudes in units of Tesla, respectively. By dividing by the Boltzmann's constant (k_{B}), Eq. 2.14 can be expressed in units of temperature,

$$\frac{\Delta U}{k_{\mathrm{B}}} = \frac{\mu_B \Delta B}{k_{\mathrm{B}}} = \frac{9.3 \times 10^{-24}\,[J/T]\,\Delta B\,[T]}{1.4 \times 10^{-23}\,[J/K]} = 0.67 \Delta B\,[\mathrm{K}]. \tag{2.15}$$

2.4.2 ALPHA-I magnetic trap

Three superconducting magnets (two mirror coils and one octupole coil, see Fig. 2.15(a)) coupled with one external solenoid provide the magnetic field for the ALPHA-I neutral-atom trap. Two superconducting cylindrical coils, also known as mirror coils, separated by $\sim$ 280 mm are positioned at each side of the MT and have a nominal current of 600 A. The axial field component of the mirror coils increases directly within the coil extent. The mirror coils also has a small radial component and fringe fields. The external 1 T magnet provides both the minimum axial magnetic field of the MT as well as establishing the radial confinement of the charged positron and antiproton plasmas prior to the synthesis of antihydrogen.

Once the two mirror coils are energized, the combination of the external solenoid

and each mirror coil produce a minimum axial magnetic field with a magnitude of $B_{\text{min,axial}} = 1.06$ T at the axial centre of the neutral trap, $z = 0$ (which is the combination of the 1 T Penning-Malmberg trap solenoidal field and the 0.06 T fringe field of the mirror coil at the axial centre of the neutral trap). The maximum longitudinal field has a magnitude of approximately $B_{\text{max,axial}} = 2.2$ T at the axial centre of the mirror coil, located either at $z = -140$ mm or $z = +140$ mm (which is the combination of the 1 T Penning-Malmberg trap solenoidal field and the 1.2 T mirror coil field at the axial centre of the mirror coil). The magnetic field gradient between the axial centres of the neutral trap and the mirror coils leads to the axial confinement of antihydrogen atoms. The on-axis field magnitude of the ALPHA-I neutral-atom trap is represented by the red curve in Fig. 2.1(c) whereby the two large bumps at $z = \pm 140$ mm are due to the contributions of the mirror coils fields superimposed on the field of the external Penning-Malmberg solenoid [31].

According to Eq. 2.15, an axial magnetic field difference of $\Delta B = B_{\text{max,axial}} - B_{\text{min,axial}} = 1.14$ gives rise to a corresponding axial well-depth of 0.78 K or equivalently 67 μeV [22].

The 3-D magnetic minimum required to provide both the axial and radial confinements of antihydrogen atoms is completed with the further construction of a transverse multipolar field. A radially increasing magnetic field is created by an ideal multipole magnet of order s that scales with radius as

$$B(r) \propto r^{s-1}, \tag{2.16}$$

where s represents the order of the multipole with $s = 2$, 3 and 4 corresponding to quadrupole, sextupole and octupole fields, respectively. The comparison of the radial variations of the transverse magnetic field magnitudes for various multipole magnets is plotted in Fig. 2.14 where both the transverse field magnitudes and the radii have been normalized with respect to their corresponding maximum values at the electrode surface, represented with B_w and r_w.

The choice of the order of the multipolar field is a prime concern since the in-

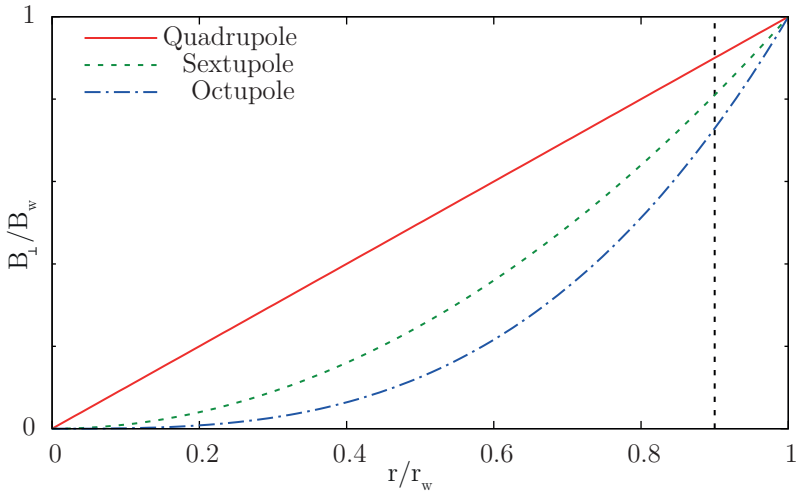

Figure 2.14: Radial variation of transverse magnetic field for several multipole magnets. The field and radius have been normalized with their values at the electrode wall. The vertical line denotes the radius of the inner electrode. It is evident that the octupole results in the shallowest trap depth. Image adapted from [32].

clusion of a multipolar transverse magnetic field breaks the azimuthal symmetry of the Penning-Malmberg trap which, in turn, affects the stability of the plasma confinement [33]. For this reason, the higher order octupole coil has been incorporated into the design of the neutral-atom trap due to its lower near-axis magnetic field (see Fig. 2.14) and therefore much smaller perturbations compared with those of the lower order multiple fields.

A total of eight layers of the octupole windings are utilized in the ALPHA-I mixing trap to produce a strong magnetic field. Two layers of the octupole windings along with the directions of the current have been illustrated in Fig. 2.15(a). When the octupole operates at a current of 900 A, a maximum transverse magnetic field of 1.55 T is generated at the inner radius of the electrodes. The octupole and the mirror coils are wound directly onto the vacuum chamber wall where they are immersed in a liquid helium at a temperature of 4.2 K. The ALPHA-I radial magnetic field profile generated by the octupole at the axial centre of the neutral trap ($z = 0$ mm) is illustrated in Fig. 2.16.

The minimum radial magnetic field magnitude at the centre of the well is $B_{\text{min,radial}} = 1.06$ T, which is the combination of the Penning-Malmberg trap axial solenoidal field and the fringe field of the mirror coils at the axial centre of the

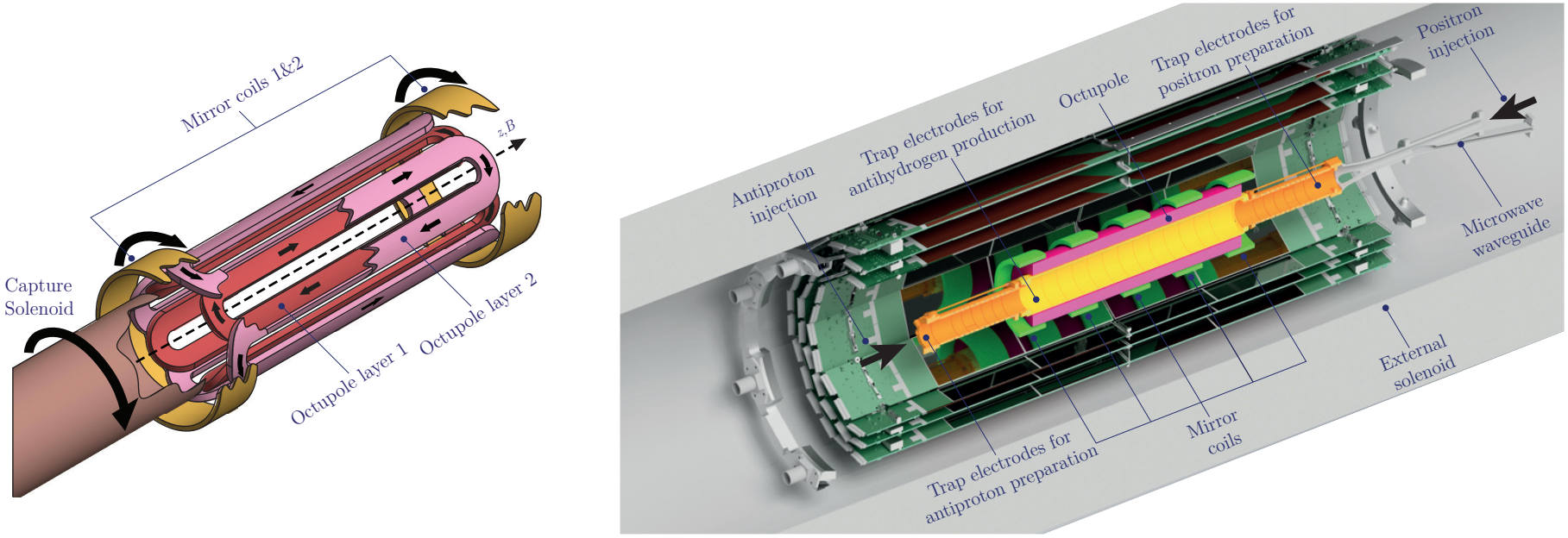

(a) (b)

Figure 2.15: (a) Schematic illustration of three superconducting magnets of the ALPHA-I neutral-atom trap: two magnet mirror coils with the current directions and one octupole coil consisting of 8 eight counter–winding layers (only 2 layers shown here). Antihydrogen is synthesized in the mixing region enclosed by this neutral-atom trap. Image modified from [34] (b) The ALPHA-II cut-way with the surrounding SVD. Five mirror coils of the ALPHA-II neutral-atom trap are shown. Credits: Joseph Tiarnan McKenna, private communications.

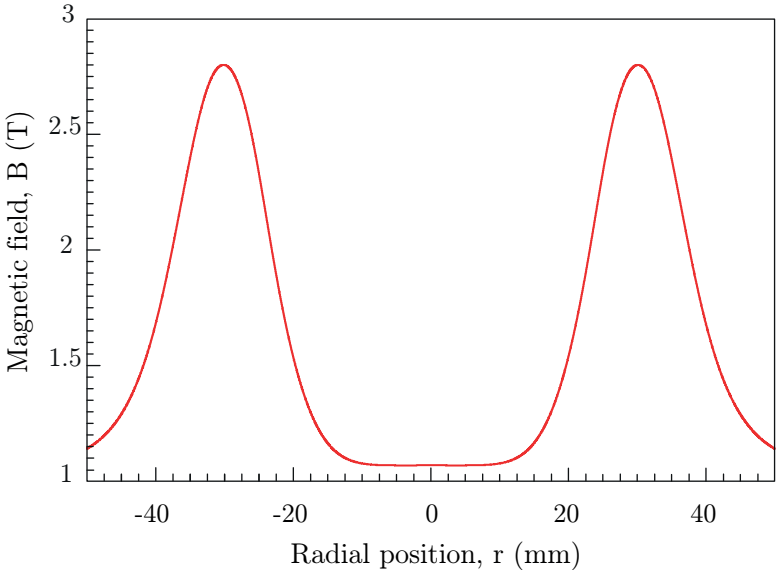

Figure 2.16: The ALPHA-I radial magnetic field profile generated by the octupole magnet at the axial centre of the neutral trap ($z = 0$ mm).

neutral trap, $z = 0$ mm. With the octupole magnet operating at a nominal current of approximately 880 A and since the transverse magnetic field of the octupole and the Penning-Malmberg trap axial solenoidal field at the electrode wall are orthogonal to each other, the quadrature sum of these two fields gives rise to the maximum radial magnetic field of $B_{\text{max,radial}} = 1.82$ T at the electrode wall. As a result, the radial trap depth is determined as $0.67 \times \Delta B = 0.67 \times (B_{\text{max,axial}} - B_{\text{min,axial}}) = 0.5$ K or 44 μeV. Therefore, antihydrogen atoms with kinetic energies equal to or smaller than 44 μeV are confined while those with higher energies escape the magnetic trap.

2.4.3 ALPHA-II magnetic trap

The ALPHA-II magnetic atom trap consists of nine superconducting magnets, which are listed below:

External solenoid: With a nominal field of 1 T, it provides both the radial confinement of the antiproton and positron plasmas, and the minimum magnetic field of the AT.

Two booster solenoids at each end of the AT: Operating at a current of 250 A, a magnetic field of 2 T is produced by each of these solenoids for further

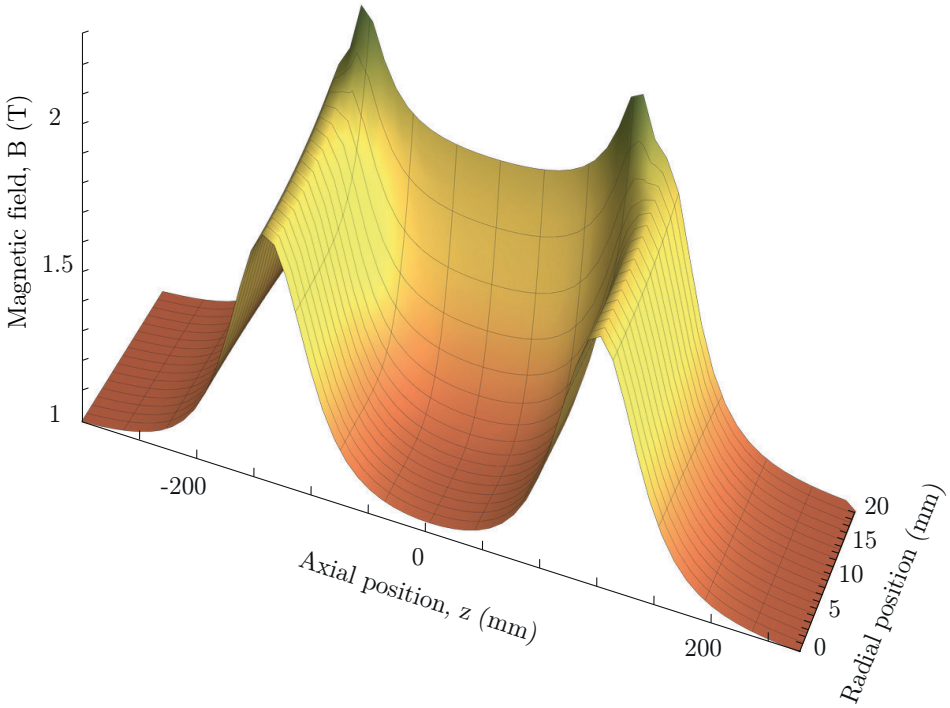

Figure 2.17: The scalar magnitude of the total magnetic field of the ALPHA-II neutral-atom trap resulted from the five mirror coils, one octupole and the external solenoid is plotted versus position. The radial position is measured from the symmetry axis of the trap, and the axial origin is the centre of the AT. Image adapted from [9].

manipulation of charged plasmas such as reducing the cooling time and further enhancement of the radial confinement inside the AT. Prior to antihydrogen formation, these solenoids are de-energized.

One octuple: The ALPHA-I octupole is utilized in the ALPHA-II apparatus for radial trapping of antihydrogen atoms. Once energized to a nominal current of 900 A, the octupole results in a magnetic field of 1.55 T.

Five mirror coils: Each coil operates at a current of 600 A and generates a maximum longitudinal field of 1.2 T, providing the axial confinement of the antihydrogen atoms. Various axial length and trap depths can be acquiring during the experiments because each coil can operate independently, see Fig. 2.15(b).

The 3-D scalar magnitude of the total magnetic field of the ALPHA-II neutral-atom trap resulted from the superposition of the magnetic fields of the five mirror

coils, one octupole magnet and the external solenoid is depicted in Fig. 2.17.

A water-cooled Quench Protection System (QPS) is incorporated into the ALPHA-I and ALPHA-II designs to protect the magnets during a quench. The quench procedure requires the transition of the superconducting wires to the normal conducting state followed by the release of a significant amount of heat capable of damaging the coils. The objective of QPS is the prompt shutdown of the magnetic neutral-atom trap (with a decay time constant of 9 ms) for maximizing the detection of antihydrogen atoms (during a 30 ms time window from the initiation of the shutdown) by reducing the background arising from the cosmic rays.

2.5 Vacuum and cryogenics

The cryostats, filled with liquid helium at a temperature of 4.2 K, maintain the apparatus at cryogenic temperatures and the magnets of the AT in the superconducting state. The helium-filled volume resides between the Ultra-High Vacuum (UHV) vessel and the Outer Vacuum Chamber (OVC). The UHV chamber contains the electrode assembly and is cooled by the helium in the adjacent cryostat vacuum pipe to ~ 8 K. The superconducting magnets immersed inside the helium-filled volume are wound directly to the outer surface of the UHV chamber.

Manipulating antiparticles/anti-atoms requires the minimization of the annihilation with any background atoms or molecules. Hence, maintaining very low pressures is of profound importance. In the ALPHA experiment, the cold surfaces of the UHV volume function as a cryopump, which assists with freezing the background gases. Using the antiproton annihilation rate, a pressure ranging from 10^{-13} to 10^{-14} mbar has been estimated inside the trap [32]. The cryostat is insulated from the room temperature part of the apparatus by a heat shield. The SVD surrounds the OVC and is maintained at room temperature, see Figures 2.2 and 2.23(a).

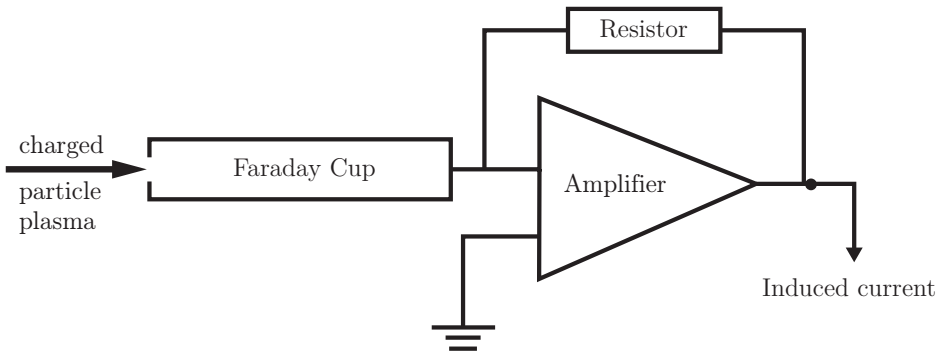

Figure 2.18: Schematic diagram of the Faraday Cup detection system.

2.6 Particle detection and diagnostic devices

2.6.1 Faraday cup

The ALPHA Faraday Cup (FC) is a thin layer of conducting material that measures the number of particles in a positron or an electron plasma confined in the Penning trap. The FC, see Fig. 2.18, is connected to electrical ground via an amplifier that is equipped with a high ohmic resistor (10^{11}-$10^{12}\,\Omega$). A charged-induced voltage due to the potential drop across the resistor is measured when a plasma is directed to the FC. The number of the particles associated with the plasma is subsequently determined by the amount of charge accumulated and the capacitance of the conductor. In order to acquire a measurement above the noise level of the FC, at least 10^6 electrons/positrons are required.

A 165 μm thick beryllium layer acts as the FC in the ALPHA-II apparatus and is placed adjacent to the antiproton CT (see Fig. 2.22). The charge of an antiproton plasma, and therefore the actual number of its constituent, cannot be measured with the FC since the plasma promptly undergoes annihilation in the conductor resulting in the production of several secondary particles. Instead, plastic external scintillators (see Fig. 2.22) are employed to detect these secondary particles and the number of annihilated antiprotons is deduced, allowing the possibility of counting a

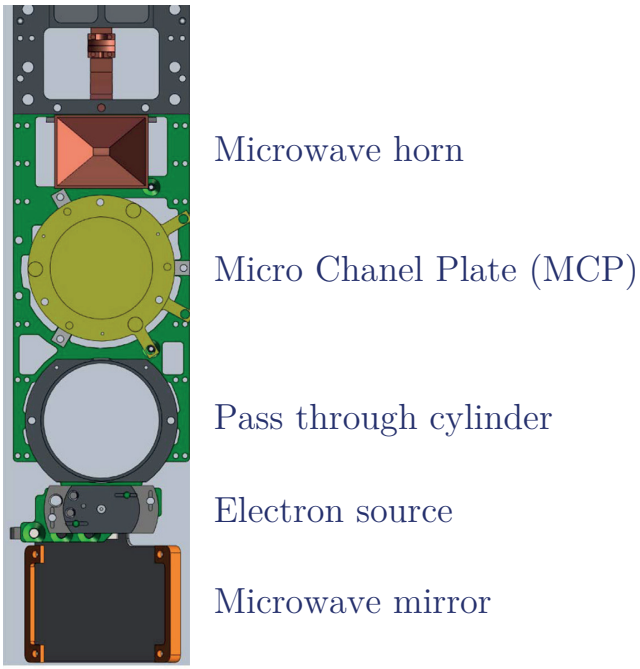

Figure 2.19: The linear vacuum manipulator consisting of the microwave horn, MCP, the pass-through cylinder, an electron source and a microwave mirror. The required component can be positioned in line with the Penning trap electrodes by allowing the entire assembly to move up or down. Image adapted from [22].

significantly smaller number of antiprotons in comparison with the FC.

2.6.2 The linear vacuum manipulator

The linear vacuum manipulator, also known as 'the stick', is a movable instrument consisting of a multitude of tools that can be positioned in line with the trap axis by a stepper motor during an experiment. The stick is shown in Fig. 2.19 and composed of the following components:

Microwave horn: The horn antenna is used for injecting microwave radiation to the trap centre. Its objective was to perform microwave experiments such as the spin flip of antihydrogen [35].

Micro-channel plate / Phosphor screen detector: A charged-particle detector consisting of a MicroChannel Plate (MCP), a phosphor screen, and a Charged Coupled Device (CCD) camera is one of the prime tools in the ALPHA apparatus and used to measure both the size (the radial density profile) and the

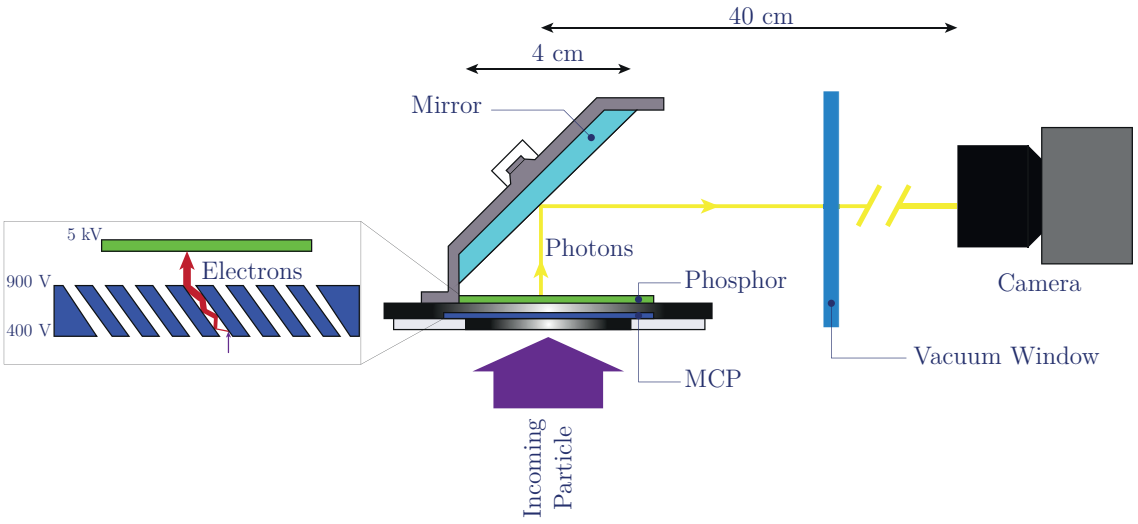

Figure 2.20: Schematic diagram showing MCP/phosphor screen/CCD camera setup. The electron cascade is created by the incoming particle interacting with the semiconductor material in a small channel. Visible light is generated when the accelerated electrons excite the phosphor screen atoms. The light is then directed towards an external camera using an arrangement of mirrors and a vacuum window.

temperature of charged plasmas (see Sec. 3.2). The MCP is a 2-D sensor that amplifies the detected signal and consists of a semiconducting material with an array of miniature channels positioned parallel to each other. The assembly setup as well as its basic operation is presented in Fig. 2.20.

When an incoming particle interacts with one of the MCP channels, secondary electrons are produced which then are accelerated upon the application of a potential difference between the front and rear surfaces of the MCP. The front-back potential difference regulates the gain of the detector and varies between 400V to 900V, depending on the number of particles required to be created. The accelerated secondary electrons, in turn, collide with the wall, resulting in more secondary electrons and the subsequent creation of a cascade. A further potential difference of 5 kV between the rear of the MCP and the phosphor screen is used to accelerate and guide the secondary electrons that exit the MCP channel onto the screen that produces visible light when excited by the electrons. A 45° mirror is finally used to guide the emitted light towards the CCD camera outside the vacuum chamber.

The MCP in the ALPHA experiment possesses an active diameter of 41.5 mm

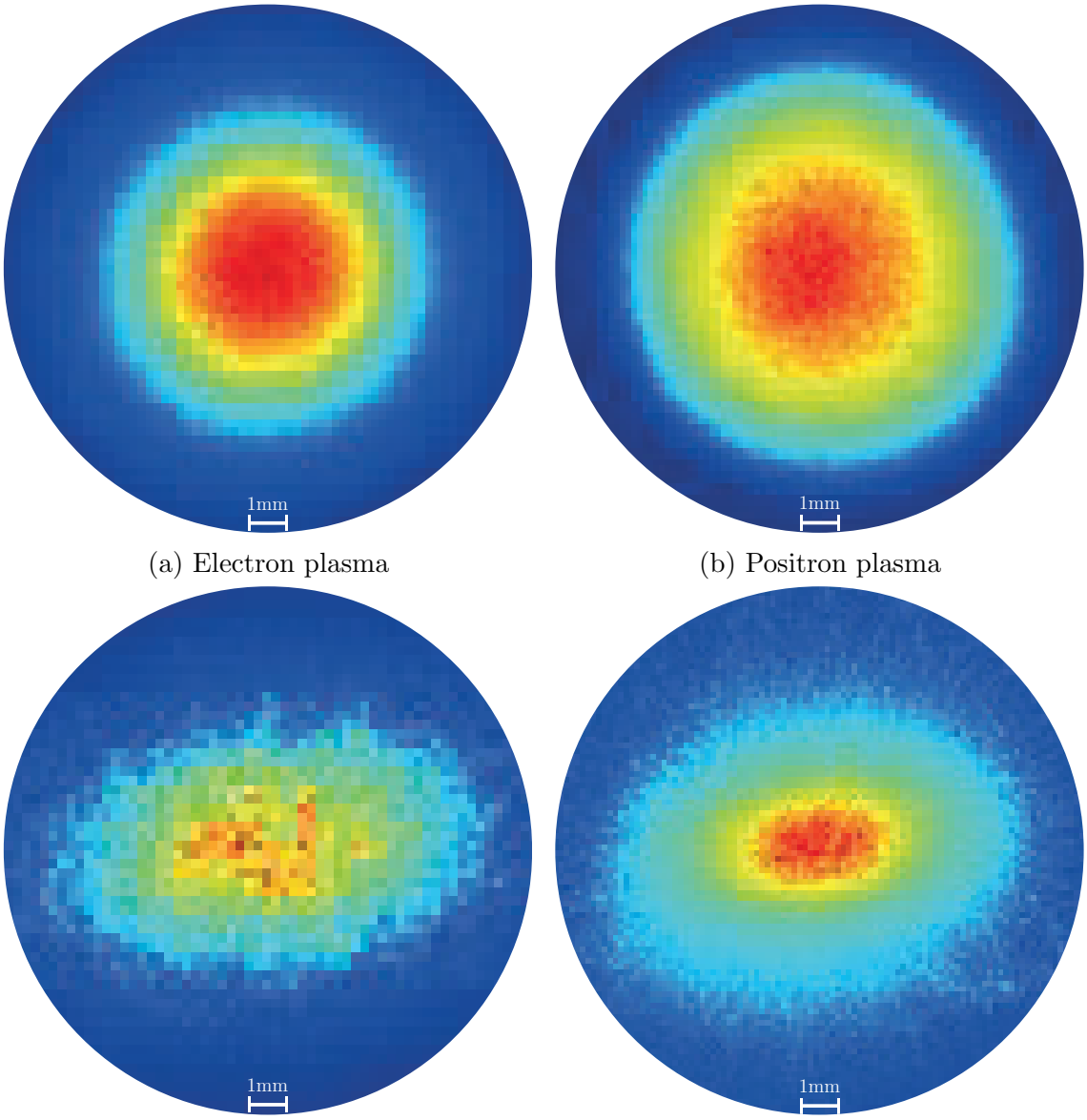

(a) Electron plasma (b) Positron plasma

(c) Antiproton plasma (d) Increased-gain antiproton plasma

Figure 2.21: Images of (a) electron, (b) positron, (c) antiproton, and (d) increased-gain antiproton plasmas obtained by the MCP/phosphor screen detector. The MCP gain voltage has been increased for the antiproton image in (d) to distinguish the annihilation products. The colour implies normalized intensity where red and blue correspond to the highest and lowest intensities, respectively.

with each channel having a diameter of 10 μm and separated by 15 μm in a hexagonal array. Fig. 2.21 demonstrates some example images of various plasmas obtained from the MCP/phosphor screen detector.

The size of a plasma can be determined by fitting the measured intensity

distribution with a 2-D generalized Gaussian function

$$I(\vec{r}) = a \ \exp\left(-\left(\frac{|\vec{r}-\vec{r_0}|}{R}\right)^n\right), \tag{2.17}$$

where $I(\vec{r})$ is the radial profile density, R is the plasma radius and a, R, $\vec{r_0}$ and n are fit parameters [36]. When a plasma is dumped to the MCP/phosphor screen from the Penning trap, a 2-D image is obtained. Positron and electron plasma images exhibit a circular distribution while the antiproton plasma image appears elliptical, caused by the decrease in the magnetic field to 0.024 T at the position of the MCP located 1.3 m from the trap centre. Magnetic field lines allow the electrons and positrons to be tightly bound whereas antiprotons do not follow the field lines tightly and result in the observed elliptical image [37].

Pass-through cylinder: A cylindrical electrode providing the passage of antiprotons from the CT and positrons from the accumulator to the AT.

Electron source: Electrons are required to cool antiprotons. An electron beam is thermionically emitted by a barium-oxide filament placed inside an electron gun and guided by the magnetic field to the antiproton CT.

Microwave mirror: The second microwave injection system consists of a pair of metal mirrors which allow the microwave photons to be injected by the external horn and be subsequently directed towards the central of the AT. This particular microwave configuration has provided the measurement of the magnetic field by determining the cyclotron frequency of an electron plasma.

The ALPHA-II apparatus utilizes two movable sticks, the antiproton CT stick and the AT stick (see Fig. 2.2). Both sticks can be moved along their vertical axes in order for a desired component to be positioned in line with the Penning trap electrode.

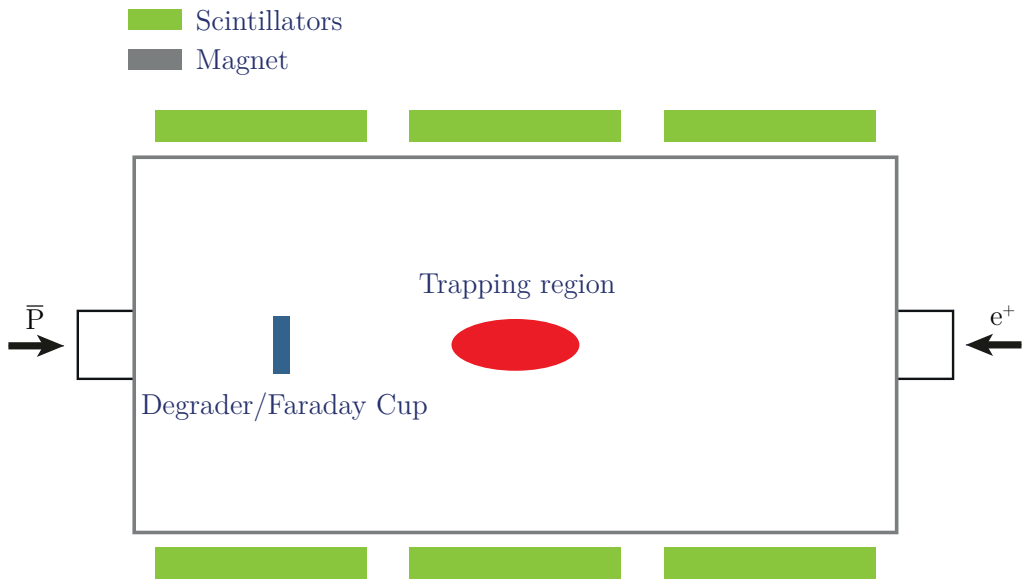

Figure 2.22: Schematic diagram of external scintillators/PMT assemblies in the ALPHA experiment.

2.6.3 Scintillators

In the ALPHA experiment plastic scintillators are used to detect the by-product of antiproton annihilations. When a charged particle traverses the scintillator, electronic excitations of the atoms/molecules proceeds and as a result of the de-excitations of atomic electrons light is emitted. The scintillator is coupled with a Photo-Multiplier Tube (PMT), which converts and amplifies the guided light into a detectable electrical signal.

There are twelve 40 × 60 × 1 cm plastic scintillating paddles in the ALPHA experiment that are placed at three positions on each side of the Faraday cup/degrader, central mixing region, and the positron side of the apparatus (see Fig. 2.22).

The scintillators sensitivity to the passage of cosmic rays are minimized by firstly manufacturing the paddles with minimal thickness and secondly placing the scintillating paddles vertically and normal to the floor. The paddles are paired and providing that both of the scintillators of a pair detect a signal exceeding a voltage threshold during a defined time interval, a 'count' is registered. A GEANT4 simulation is further utilized to translate the registered counts to the total number of annihilated antiprotons.

2.6.4 CsI detectors

The detailed characterization of the positron plasma within the PT section of the AT is accomplished using the MCP and the FC detectors. Several compact Caesium-Iodide (CsI) detectors are positioned along the accumulator and the transfer sections of the apparatus to monitor the efficient accumulation and transfer of positrons from the positron accumulator to the AT. CsI crystals are scintillating detectors made of much denser material and they, therefore, provide 511 keV gamma rays produced from the positron annihilation with a more enhanced sensitivity.

2.6.5 Flappers

Two beam line shutters, also known as 'flappers', are placed at their respective ends of the AT cryostat and act as heat sinks. The flappers utilize a small coil to open and close in the 1 T magnetic field of the external solenoid and are still in the final phases of testing. The black body radiation from the section of the beam line maintained at room temperature is prevented from entering the trap by the closed flappers.

2.6.6 Silicon Vertex Detector

In the ALPHA apparatus, when the magnetic neutral-atom trap is shut down, the antihydrogen is released from the trap and subsequently annihilates on the electrodes of the trap wall. The annihilation process can follow either the positron meeting an electron or the antiproton annihilating a proton of the gold atom of the trap, producing charged particles. The Silicon Vertex Detector, see the photograph on the cover page, is the prime device in detecting and determining the position of the antihydrogen annihilation and is the focus of this thesis.

Fig. 2.23(a) is a schematic representation of an antiproton annihilation inside the apparatus. The passage of the charged particles through the detector triggers

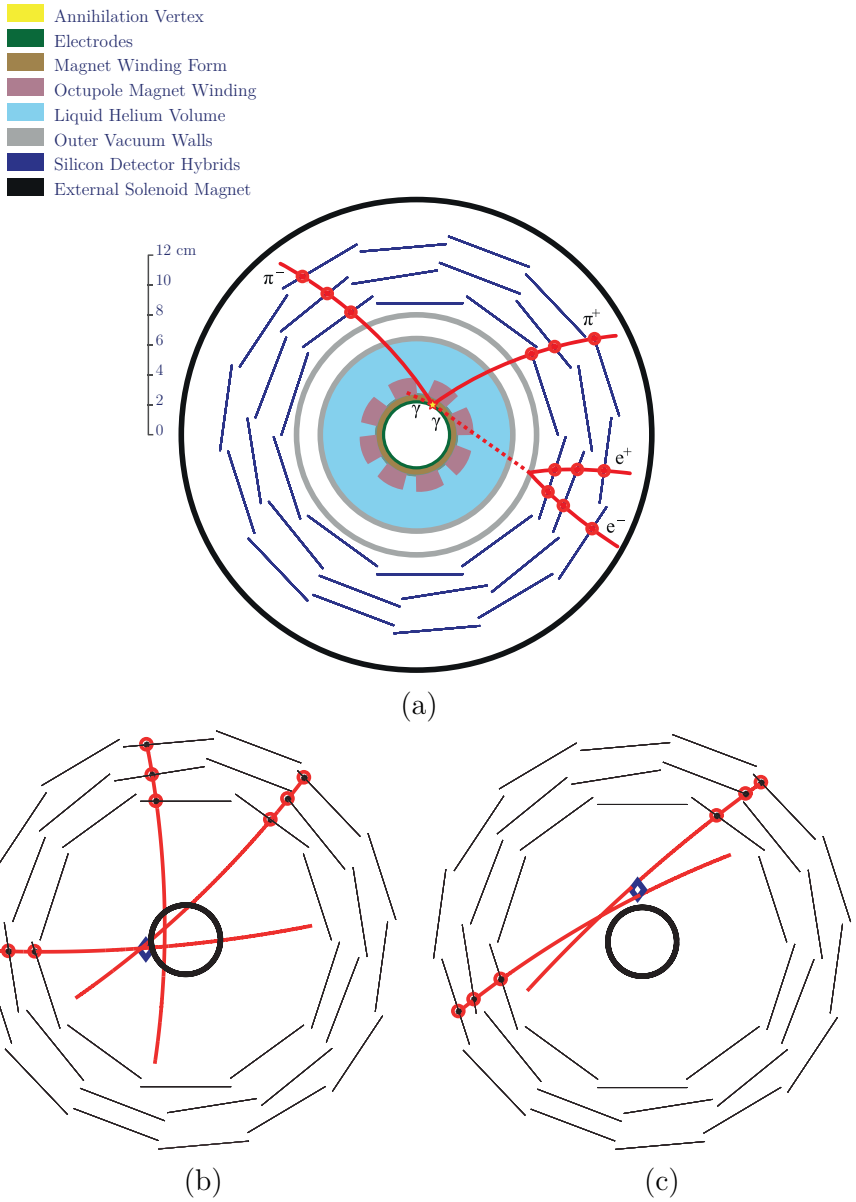

Figure 2.23: (a) Schematic diagram depicting the cross sectional view of the axial centre of the ALPHA apparatus as well as the Silicon Vertex Detector (SVD). The components include: electrode stack, magnet winding form, octupole magnet winding, liquid helium volume, isolation vacuum walls, SVD, and external solenoid magnet. The five mirror coils located at the axial ends of the magnetic neutral-atom trap are not illustrated. Three pions (two charged and one neutral) are produced as a result of an antiproton annihilation on the trap wall. The trajectories of the annihilation products are represented with curved lines while the asterisks and circle markers indicate the position where the particles encounter a silicon module. The annihilation vertex is denoted with the yellow star. The $\pi^0 \rightarrow 2\gamma$ channel arises by the prompt decay of the neutral pion where one of the resulting photons is absorbed in the octupole winding while the other photon has produced an electron-positron pair. (b)-(c) Cross sectional views of reconstructed antiproton annihilation and cosmic events, respectively, generated by the Alternative Reconstruction Method. The electrode surface is depicted by the central black circle surrounded by the SVD modules. The red curved lines are reconstructed charged pions tracks and the blue diamond is an indication of the position of the reconstructed vertex.

each layer of the detector and an analogue and a digital signal are produced. The annihilation position (vertex) is determined by combining the registered signals and the detector geometry. The SVD is enclosed within the 1 T external solenoid and therefore the trajectories of the charged particles follow helical paths.

Events detected by the SVD are mostly due to cosmic rays. The reconstructed tracks due to the passage of high energy $\mu^{\pm}$ through the apparatus consists of two tracks with very large radius of curvature, implying that the tracks are nearly straight. It is evident from Figures 2.23(b) and 2.23(c) that the annihilation and cosmic events exhibit striking different topology, which can be further utilized to discriminate cosmic rays from the true annihilation signal by incorporating variables associated with the reconstructed vertex.

Using Monte Carlo simulation, the average resolution of the SVD is estimated to be (0.67 ± 0.04) cm in the axial (z) direction, (0.68 ± 0.04) cm in the radial (R) direction and (0.82 ± 0.04) cm in the azimuthal (ϕ) direction at the trap wall. The ALPHA-II detector background rate is (0.042 ± 0.001) events/s and the event reconstruction efficiency (the ratio of the number of events identified as antiproton annihilations to the number of detector triggers) is (73.0 ± 0.4)%. The overall annihilation event efficiency is (66 ± 7)%, when combined with the (90 ± 10)% trigger efficiency [22].

2.7 Laser access windows

Eight windows have been incorporated into the ALPHA-II apparatus which provide the optical access to the AT. Each side of the trap accommodates 4 windows with direct path to the trap centre. The laser access has been utilized to perform 1S-2S two-photon and Lyman-α laser spectroscopy as well as other experiments. In addition, a cavity aimed at enhancing the laser power has been built inside the apparatus.

2.8 Control system and data acquisition

The control of all the ALPHA apparatus devices presented in this chapter is attained using a set of FPGA-based sequencers that coordinate the timing and reproducibility of experiments. The sequencers are incorporated with National Instruments (NI) PXI-6733 cards to regulate the timing and amplitude of the Penning trap voltages. The management of the input and output triggers to external hardware is done using NI PXI- 7811R cards.

Programmable sequences are created using custom-made LabVIEW software by National Instruments and permits an experimental sequence to be written by creating a series of 'states' to be executed sequentially. A state can consist of input and output triggers to an external device or a voltage manipulation of the Penning trap electrodes. The timing of the states can be maintained to within 500 ps while the response to external triggers can be performed with a timing of about 100 ns, resulting in the simultaneous execution and a superior reproducibility of complex operations in the ALPHA experiment.

All the acquired data from triggers, detectors and environment regulators are logged with the Multi Instance Data Acquisition System (MIDAS) software and subsequently analysed with custom C++ algorithms and ROOT data analysis framework. The analysis in this thesis has been conducted with MATrix LABoratory (MATLAB).

Chapter 3

Plasma Manipulation & Confinement

The collection of charged particles results in a charged cloud that exhibits various collective behaviours when its density increases. A 'quasi-neutral' plasma is defined as an equal number of positive and negative charges created by the ionization of a neutral gas. The charged clouds produced in ALPHA are entirely composed of a single sign of charge and are non-neutral plasmas sharing many collective features prevalent in neutral plasmas. Since antihydrogen formation is performed by mixing charged antiproton and positron plasmas, understanding the underlying physics of non-neutral plasmas is of vital importance.

The direct mixing of the captured antiproton plasma from the AD and the positron plasma from the positron accumulator would result in high-energy antihydrogen atoms at an extremely low rate and incapable of being trapped. Even though the collective behaviour of the charged plasma can lead to detrimental consequences such as plasma heating and instabilities, utilizing the collective behaviour of the plasmas, the ALPHA collaboration has devised sophisticated and powerful optimization methods to characterize the density, number and temperature of the antiproton and positron plasmas prior to their mixing and the formation and trapping of the antihydrogen atoms.

This chapter begins with providing the theory of non-neutral plasmas in Penning traps, including the confinement of non-neutral plasmas and the plasma temperature diagnostics. The sections following describe various techniques aimed at preparing antiproton and positron plasmas for antihydrogen formation.

3.1 Non-neutral plasma confinement in a Penning-Malmberg trap

3.1.1 Plasma fundamental properties

Perturbed by a small charge displacement, the plasma undergoes an oscillatory motion characterized by a frequency given by

$$w_p = \sqrt{\frac{ne^2}{\epsilon_0 m}}, \tag{3.1}$$

where ϵ_0 is the vacuum permittivity, m the mass of the particle, e is the elementary charge and n is the number density. The plasma frequency (w_p) is inversely dependent on the mass of its constituent particle. For a given density, the electron plasma exhibits the highest plasma frequency. The plasma period, $\tau_p = 1/w_p$, is the distinctive timescale over which the plasma oscillation can be observed.

Likewise, the characteristic length, called the Debye length and given by Eq. 3.2, over which the plasma behaviour is observed is set by the distance travelled by the plasma particle in time τ_p , i.e. $\tau_p \times v$ where v is the speed of the particle

$$\lambda_D = \sqrt{\frac{\epsilon_0 k_B T}{ne^2}}, \tag{3.2}$$

where n is the density of the plasma, k_B is the Boltzmann constant and T is the temperature. The Debye length, λ_D, is independent of the mass of the plasma constituent particle and is generally equivalent for all plasma types. The Debye

length must be smaller than the overall size of the cloud L ($L \gg \lambda_D$) for a cloud of charged particles to be regarded as a plasma. In addition, the Debye length sets the scale over which the collective interactions of plasma particles lead to the cancellation or the shielding of an extra charge introduced to the plasma, a phenomenon known as Debye shielding [38].

3.1.2 Theory of confinement

Analogous to the magnetron frequency of a single charged particle in a Penning-Malmberg trap (see Sec. 2.3.1), the self-charge of the non-neutral plasma results in a self-electric field ($\vec{E}$). The plasma subsequently rotates azimuthally about the trap axis due to the $\vec{E} \times \vec{B}$ circular drift. For a plasma with uniform density, the azimuthal velocity of the plasma is given by

$$v_\theta = \frac{enr}{2\epsilon_0 B} = w_{rot}\, r, \tag{3.3}$$

where n is the plasma number density, e is the elementary charge , B is the axial magnetic field and r is the plasma radius. Eq. 3.3 implies that the plasma rotational frequency w_{rot} is independent of the plasma constituent's mass, charge and radial coordinate. As a result, the plasma rotates like a rigid rotor in steady state with all particles possessing the same rotational frequency [39].

The axial confinement of a non-neutral plasma with a total of N equal charges in a cylindrically symmetric Penning trap is acquired by the static voltages applied to the electrodes on either end of the plasma. The radial confinement of the plasma is provided by the strong axial magnetic field ($\vec{B} = B\hat{z}$) and is governed by the conservation of the total canonical angular momentum of the plasma. In a cylindrical coordinate system with the z axis directed along the axis of symmetry of the trap, the canonical angular momentum can be written as [40]

$$P_\theta = \sum_{j=1}^{N} \Big(m v_{\theta j} r_j - |e| A_\theta(r_j) r_j \Big), \tag{3.4}$$

where e is the elementary charge, $v_{\theta j}$ is the azimuthal velocity, m is the mass of the particles, r_j is the distance from the axis of symmetry (radius) of the jth particle and A_θ is the azimuthal component of the vector potential, i.e. $\vec{A} = A_\theta(r)\hat{\theta}$.

For an axial uniform magnetic field, the vector potential is $A_\theta(r_j) = Br_j/2$ and noting that for a strong magnetic field the second term in Eq. 3.4 dominates and reduces to

$$P_\theta \approx -\frac{|e|B}{2}\sum_{j=1}^{N}(r_j)^2. \tag{3.5}$$

The conservation of angular momentum for a Penning-Malmberg trap with rotational symmetry ensures that the following constraint is placed on a single species plasma in a strong magnetic field

$$P_\theta \approx -\frac{|e|B}{2}\sum_{j=1}^{N}(r_j)^2 \approx -\frac{|e|B}{2}\langle r^2\rangle N = \text{const}, \tag{3.6}$$

where $\langle r^2\rangle$ is the constant mean-square radius of the plasma. The constancy of the mean-square radius prevents the contraction or the expansion of the plasma radius without a corresponding change in the angular momentum, thereby resulting in the confinement of the constituent plasma particles [35].

3.2 Plasma temperature measurement

Antihydrogen formation and trapping is extremely dependent on the temperature of the charged plasmas prior to their mixing and therefore characterizing the temperature of the plasma in a systematic way is critical. In ALPHA, this is achieved by direct sampling of the energy distribution where the constituent particles of the plasma are released along the trap axis by gradual lowering of one side of the confining axial potential well and extracting the particles to either the MCP (for positrons) or the scintillators (for antiprotons). The axial (parallel) kinetic energy distribution is consequently expected to follow a one-dimensional Maxwell-Boltzmann distribu-

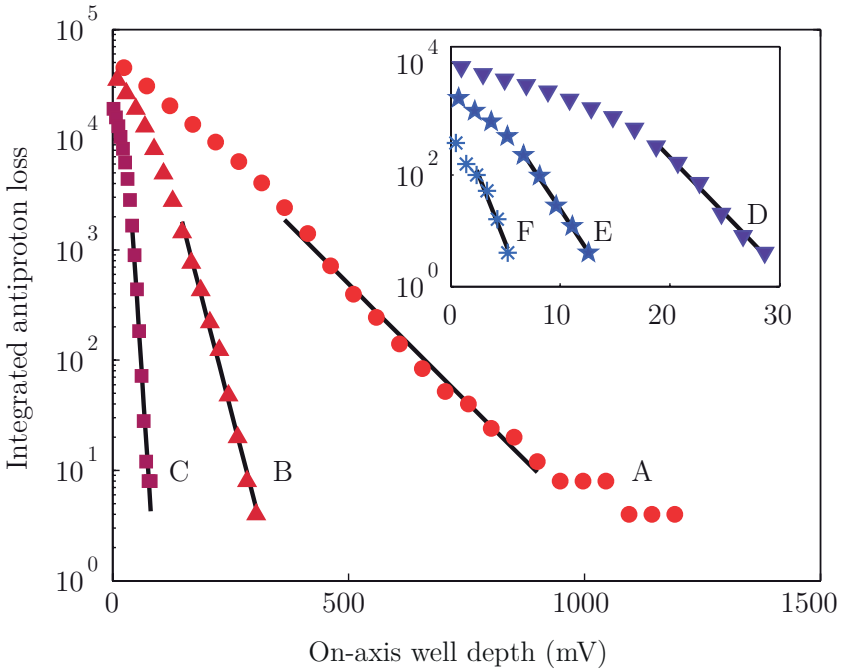

Figure 3.1: Plot demonstrating the number of antiprotons escaping the confining potential versus the on-axis well-depth. The black lines represent the fitted region with the corresponding acquired temperatures of A: 1040 K, B: 325 K, C: 57 K, D: 23 K, E: 19 K, and F: 9 K. The low-energy distributions are magnified in the inset. Image adapted from [42].

tion [41]

$$f(E_{\parallel}) \propto \exp\left(-\frac{E_{\parallel}}{k_B T}\right), \tag{3.7}$$

where $E_{\parallel}$ is the parallel energy, k_B is the Boltzmann's constant and T is the temperature.

Assuming the trapped cloud charge/plasma to be in a state of thermal equilibrium, the correlation between the number of particles (N) escaping the potential well and the change in the confining potential (V_C) is given by [41]

$$\frac{\partial \ln(N)}{\partial V_C} \simeq -\frac{|q|}{k_B T}, \tag{3.8}$$

where q is the charge of escaped particle. Eq. 3.8 indicates that one is able to obtain the temperature of the plasma by fitting a straight line on the semi-log plot and subsequently determining the slope of this line. Fig. 3.1 demonstrates examples of temperature measurements for antiproton.

3.3 Antiproton cooling and trapping

Prior to the synthesis of the antihydrogen atoms by the AD experiments, the confinement and cooling of the constituent antiprotons is to be achieved in Penning-Malmberg traps (see Sec. 2.3.2). The open geometry of this particular type of Penning trap permits the antiprotons to enter the trap axially. The trapping procedure of the ALPHA-I Catching Trap (CT) is schematically illustrated in Fig. 3.2 (ALPHA-II follows the same process). The electrostatic voltages applied to the two end electrodes, E01 and E09 in Fig. 2.12(a), determine the most energetic antiprotons that can be captured by the trap. These two applied voltages are limited to a few kV in order to eliminate the electrical discharges that might occur within the confined volume of the superconducting magnetic solenoid.

The incoming antiprotons from the AD must be decelerated to keV energies prior to their injection into the CT since their kinetic energies (5.3 MeV) are significantly greater than the applied high voltages. To reduce the kinetic energies of the incoming antiprotons, an inefficient cooling mechanism of atomic collision, also known as degrading, is employed. The mechanism is shown in Fig. 3.2(a) and is established by including a thin layer of aluminium, the so-called 'degrader', prior to the trap entrance and allowing the extracted antiprotons from the AD to pass through it. Nevertheless, this energy loss mechanism is associated with range-straggling effects. These effects lead to a considerable fraction of the antiprotons (99%), and hence an inefficient mechanism, undergoing either annihilation in the degrader or departing with energies higher than 10 keV, making them untrappable by the applied high voltages. As a result, adjusting the degrader thickness in order to maximize the antiproton capture efficiency is vital. In ALPHA-I, the degrader is a foil composed of stainless steel and aluminum with thicknesses of 12.5 μm and 218 μm, respectively, whereas ALPHA-II utilizes layers of aluminum and beryllium.

Those antiprotons that exit the foil with degraded energy of less than 10 keV encounter a negative voltage of -5 kV applied to the electrode positioned at the

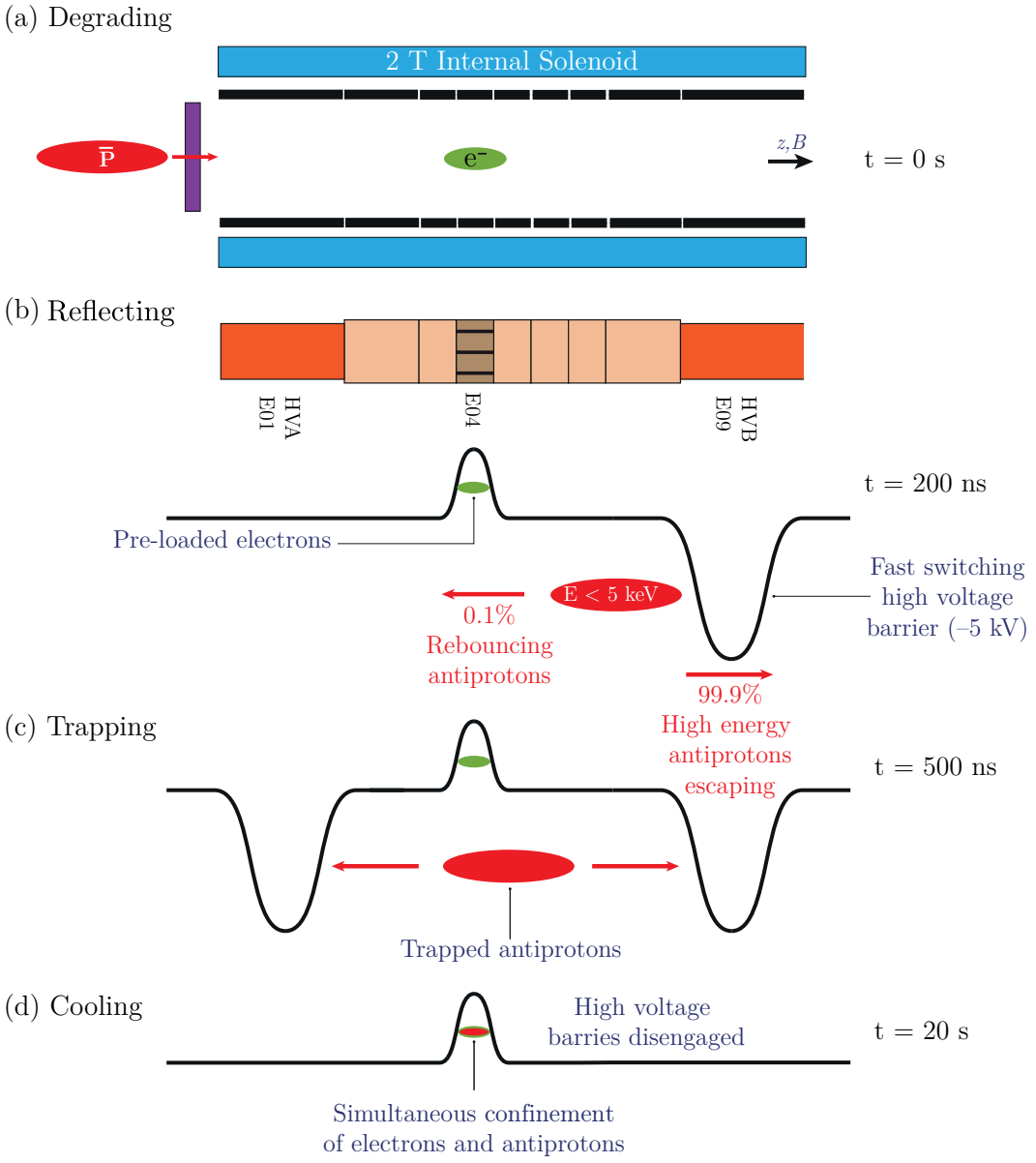

Figure 3.2: Schematic diagram of the antiproton plasma confinement. (a) Extracted antiprotons from the AD are initially decelerated in the degrader. Electrons are pre-loaded into an electrode located at the centre of the CT and are constantly cooled via synchrotron radiation . (b) Prior to the arrival of the antiprotons, a 5 kV barrier is engaged and those with low enough longitudinal kinetic energy are reflected. (c) Approximately 500 ns later, a similar potential barrier close to the entrance of the trap is engaged to prevent antiprotons leaving the trap and the confinement of antiprotons is achieved. (d) After about 20 s, the antiprotons will have cooled via collisions with the pre-loaded cold electrons.

downstream end of the trap (electrode number E09, see Fig. 3.2(b)). A significant number of the antiprotons (99.9%) overcome the barrier and a small fraction (0.1%) with kinetic energies below 5 keV undergo a 180-degrees reflection towards the trap entrance, see Fig. 3.2(b). About 500 ns later, a second negative potential of the same magnitude is promptly raised by the electrode close to the trap entrance (E01) to prevent the reflected antiprotons from escaping the trap, allowing the antiprotons to be dynamically confined between the two potential barriers as illustrated in Fig. 3.2(c).

Once trapped, the keV antiprotons are further cooled using a technique known as 'sympathetic cooling' [43]. This mechanism involves pre-loading approximately 85×10^6 electrons with a radial size of ~ 9 mm (see Sec. 3.4) in a central and shallow well of the CT where they perform cyclotron motion in the strong axial magnetic field. Providing that any heating sources due to the induced noise on the electrodes, space-charge and plasma effects can be eliminated, the pre-loaded electrons self-cool by emitting synchrotron radiation. The electrons will subsequently reach thermal equilibrium (T = 4.2 K) with the cryogenic environment on a timescale of a second or so.

The rate of change of energy resulting from the radiation of a non-relativistic charged particle undergoing acceleration is given by the Larmor's equation [44]

$$\frac{dE}{dt} = -\frac{q^2}{6\pi\epsilon_0 c^3}|\vec{a}|^2, \tag{3.9}$$

where $\vec{a}$ is the acceleration of the charged particle. The dominant mode of motion of a charged (anti)particle in a Penning-Malmberg trap is the cyclotron (see Sec. 2.3.1) and the resultant acceleration is $\vec{a} \simeq \vec{w}_c \times \vec{v}$. Considering the fact that the total energy of the system is entirely kinetic, $E = \frac{1}{2}mv^2$, Brown and Gabrielse [29] have calculated the change in the energy of such a non-relativistic charged (anti)particle as

$$\frac{dE}{dt} = -\gamma_c E. \tag{3.10}$$

In Eq. 3.10 γ_c is the cyclotron cooling rate given by

$$\gamma_c = \frac{q^2 w_c^2}{3\pi\epsilon_0 m c^3} = \frac{q^4 {B_0}^2}{3\pi\epsilon_0 m^3 c^3}. \tag{3.11}$$

The exponential solution, $E(t) = E_0 e^{-\gamma_c t}$ where E_0 represents the initial kinetic energy, implies that the charged particle undergoes self-cooling in a magnetic field. Therefore, with an overall axial magnetic field of 3 T utilized during the antiproton capture in ALPHA-I (see Fig. 2.1(c) and Sec. 3.3.1) and ALPHA-II, the antiproton cyclotron cooling constant, $1/\gamma_{c,\bar{p}}$, is estimated to be $\sim 2 \times 10^9$ s. Such a prolonged cooling time is implausible to be used in practice. However, since the cyclotron cooling rate is inversely proportional to the cubed mass and $m_e/m_{\bar{p}} \sim 1/2000$, the electron cyclotron cooling constant is $1/\gamma_{c,e} = 1/\gamma_{c,\bar{p}}(m_e/m_{\bar{p}})^3 \sim 0.3$ s. This much shorter and therefore practical cooling constant explains the motive behind the utilization of electrons as the cooling medium for antiprotons. As the confined antiprotons undergo backwards and forwards motion within the trap while traversing the electron cloud, they experience elastic scattering off the electrons, which themselves radiate away the excess energy. Consequently, the antiprotons are subsequently cooled and collected in the shorter potential well containing the electron cloud, see Fig. 3.2(d) [31]. A review of the methods developed in order to trap, cool and stack antiprotons can be found in [45].

A model for the temperature evolution of a system constituting electrons and antiprotons has been devised [46]. Implementing this model on 10^4 antiprotons with energies on the order of keV while interacting with an electron cloud possessing a density of $\sim 10^8$ cm^{-3} results in a cooling in the eV range with a timescale on the order of several hundred milliseconds [47]. In principle, the antiprotons should acquire the 4.2 K temperature of the self-cooled electrons. Despite the considerable attempts to eliminate the ALPHA traps' external heating sources arising from the outside environment coupled to the both end electrodes and through the electrode cables, a thermalized antiproton temperature of 358 ± 55 K [48] has been measured.

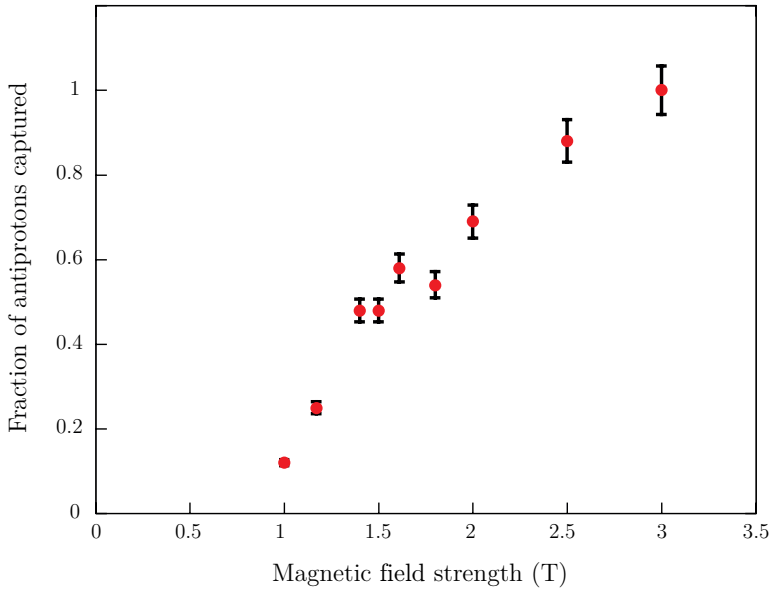

Figure 3.3: Normalized antiproton capture versus magnetic field strength. Image adapted from [49].

3.3.1 The catching trap magnetic field enhancement

Illustrated in Fig. 3.3 is an increase in the fraction of antiprotons captured as a function of increasing magnetic field strength. The measurements have been normalized with respect to numbers of antiprotons captured at the corresponding 3 T magnetic field. Since the electron cyclotron cooling rate varies quadratically with magnetic field (Eq. 3.11), an increase in the magnetic field results in a rise of this cooling rate. Furthermore, this increase enables antiprotons with greater momentum to be captured. However, the overall neutral-atom trap depth decreases by increasing the magnetic field (see Sec. 2.4.2). A compromise can be reached by superimposing a 2 T field generated by an internal solenoid surrounding only the CT (see Fig. 2.1(c)) on the static 1 T axial magnetic field provided by the external solenoid magnet. During the capture process, the inner solenoid is capable of being energized and disengaged with ease and as a result, the catching efficacy can be enhanced. The red curve in Fig. 2.1(c) depicts the axial magnetic field of the Penning-Malmberg trap, while the blue curve is the axial magnetic field with the addition of the inte-

gral solenoid magnet. When energizing all the superconducting magnets, magnetic forces cause stress on the apparatus and the magnetic winding. To avoid this stress, a magnetic field limit of 3 T has been imposed.

3.3.2 Rotating wall compression

A maximum antihydrogen formation efficiency can be acquired by implementing techniques allowing the precise control of radial size of the confined plasma with the objective of optimizing the overlap of the charged clouds during mixing. As described in Sec. 3.1.2, the radial confinement of a plasma for an infinite time is achieved via the conservation of the canonical momentum of the plasma in a perfect trap. In a real trap, nevertheless, a slow expansion and loss of particles can arise from the non-symmetric static fields and the drag exerted by the background gases on the plasma. The radial control of the non-neutral plasma and its subsequent radial compression is accomplished by the application of a torque to the plasma, a technique known as 'Rotating Wall' (RW). The torque is created by a rotating electric field and increases the plasma's rotational frequency. As the plasma density is directly proportional to its rotational frequency, the density also increases.

When a positive torque created by the RW is applied to the plasma, from Eq. 3.6 follows that

$$\tau = \frac{dP_\theta}{dt} > 0, \tag{3.12a}$$

$$\tau \approx -\frac{|e|B}{2}\frac{d\langle r^2\rangle}{dt}N > 0, \tag{3.12b}$$

$$\frac{d\langle r^2\rangle}{dt} < 0, \tag{3.12c}$$

and, as implied by the 3.12(c), the positive torque results in the decrease of the radius of the plasma. Fig. 3.4 depicts an arrangement for producing such torques. The rotating electric field is generated by an electrode split into six azimuthally

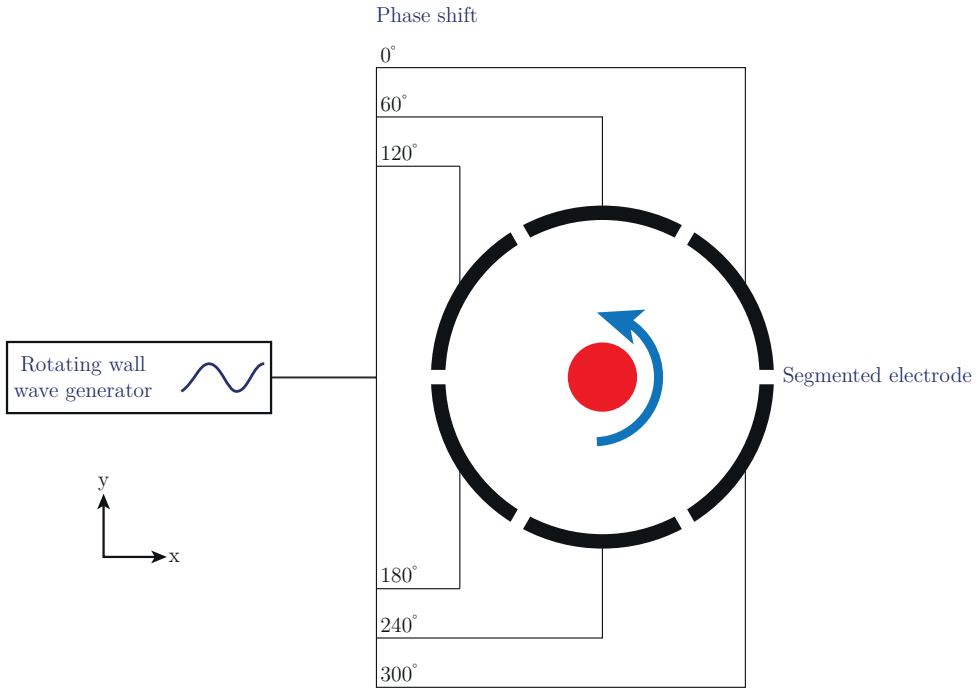

Figure 3.4: Schematic representation of a transverse section of the 'Rotating Wall'. A sinusoidal potential is applied to a six-segmented electrode with a phase difference of 60° between each segment. The red circle illustrates the plasma and the blue arrow the direction of rotation.

isolated sections with each segment provided with a voltage

$$V_i = V_0 \sin(w_{RW} t - \theta_i). \tag{3.13}$$

The ith segment (θ_i) is shifted from its neighbour by $2\pi/N$, where N is the number of segments. The plasma rotational frequency synchronizes with the applied rotating wall frequency w_{RW} if the drive amplitude V_0 is large enough, known as the Strong Drive Regime [50].

Frequent compression of antiproton, electron and positron plasmas is conducted in ALPHA by utilizing the Rotating Wall technique. In contrast with positron and electron charged clouds, however, the antiproton plasma is not directly affected by the Rotating Wall. The radial compression of the antiproton cloud is attained by using a mixed electron-antiproton plasma where both the electron and antiproton plasmas are placed inside the potential well at the position of the segmented electrode and the rotating potential is subsequently applied to both species simul-

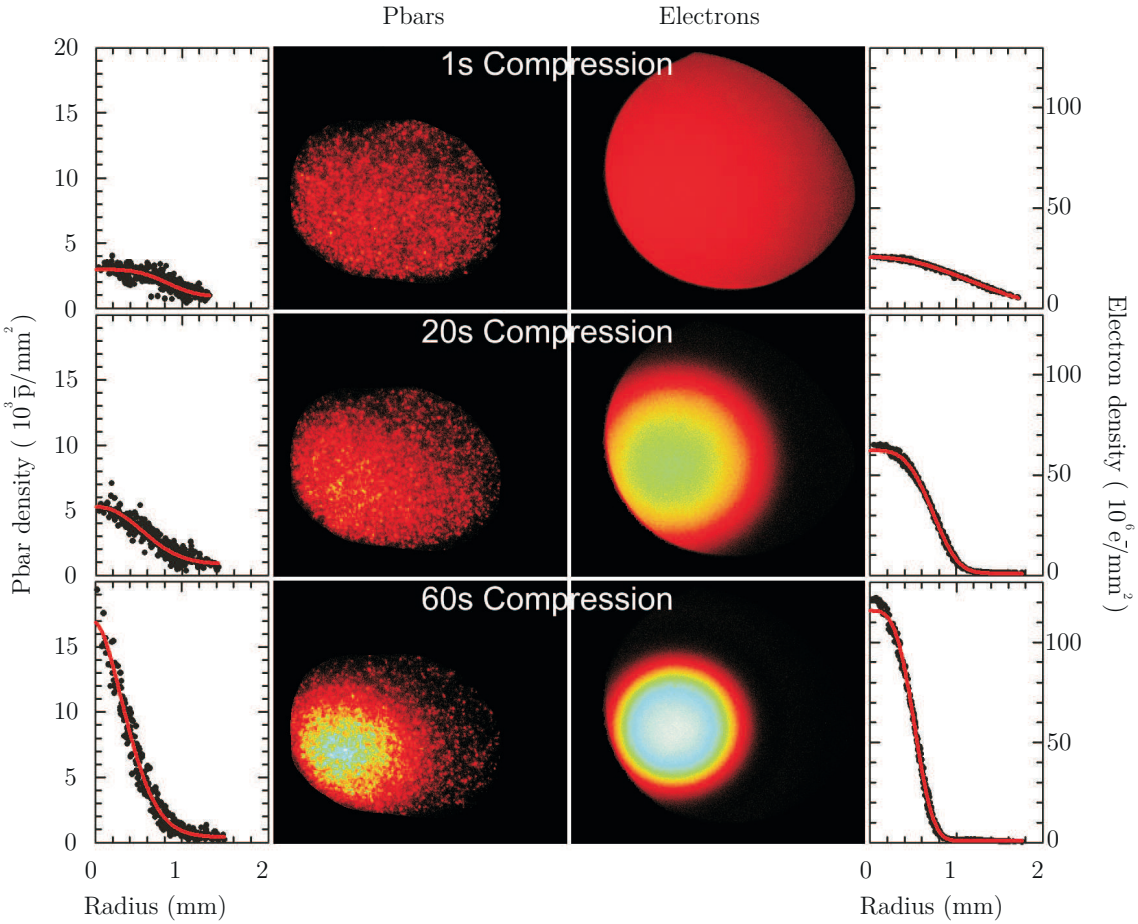

Figure 3.5: MCP images and the corresponding radial profiles acquired from the application of Rotating Wall technique on antiproton and electron plasmas. This particular analysis uses a $w_{RW}/2\pi$ ~10 MHz with three compression implication times of 1, 20 and 60 seconds. The red lines represent the Gaussian fits (i.e. $\exp(-|\frac{r}{r_0}|^k)$ where $k \approx 2$) to the radial profiles. Image adapted from [21].

taneously. The antiproton plasma undergoes through similar compression to that of the electron cloud providing that the electron compression is slow.

The application of the RW technique has the detrimental consequence of heating the plasma, thereby affecting the effectiveness of the compression. The cyclotron cooling counterbalances the generated heat whereby the antiprotons transfer their energy via the collisions with the electrons, which, in turn, radiate away the excess energy in the strong magnetic field. Fig. 3.5 shows the MCP images of the electron and antiproton plasmas as well as their corresponding radial profiles obtained from three Rotating Wall implication times, leading to the attainment of antiproton plasmas with radii of 0.29 mm.

3.3.3 Electron removal

A combined antiproton-electron cloud resulted in obtaining a cold and dense antiproton plasma. The synthesis of antihydrogen requires the removal of the electrons from the antiproton-electron cloud prior to the transfer of the antiprotons to the Re-Catching Trap (RCT) section of the Atom Trap (AT). Any electrons transferred to the Mixing Trap (MT) section of the AT lead to a loss of positrons due to the electron-positron annihilation. In addition, the space-charge/self-charge of the electron cloud has a detrimental effect on the antihydrogen formation and trapping rate.

The mass difference of the electron and antiproton can be employed to remove the electrons from the mixed electron-antiproton cloud, a mechanism known as 'electron kick-out'. The procedure is shown in Fig. 3.6 whereby a voltage pulse is applied to the electrode set creating the confining potential well such that one side of the well containing the mixed cloud is momentarily lowered. This leads to the momentary un-confinement of the constituent species of the cloud. The lighter electrons acquire a higher velocities and escape the confining potential whereas the heavier antiprotons remain temporarily confined by the well, see Fig. 3.6(b). The antiprotons are unable to follow the electrons and escape the trap as long as the confining electrode potential is re-established promptly (of the order of $\sim$ 100 ns). The result is a pure antiproton cloud permanently confined by the potential well.

The swift change in the electric potential wells as well as the prompt removal of the electron space-charge give rise to the unwanted heating of the antiproton plasma. This heating can be minimized by an optimized version of the electron kick-out whereby the removal is performed in two steps. The first step entails removing at least 90% of the electrons, leaving behind the confined electron-antiproton cloud possessing temperature of approximately 1000 K. The remaining electrons of the cloud act as the cooling medium, allowing the antiprotons to be sympathetically cooled by transferring their energies via Coulomb collisions with the electrons.

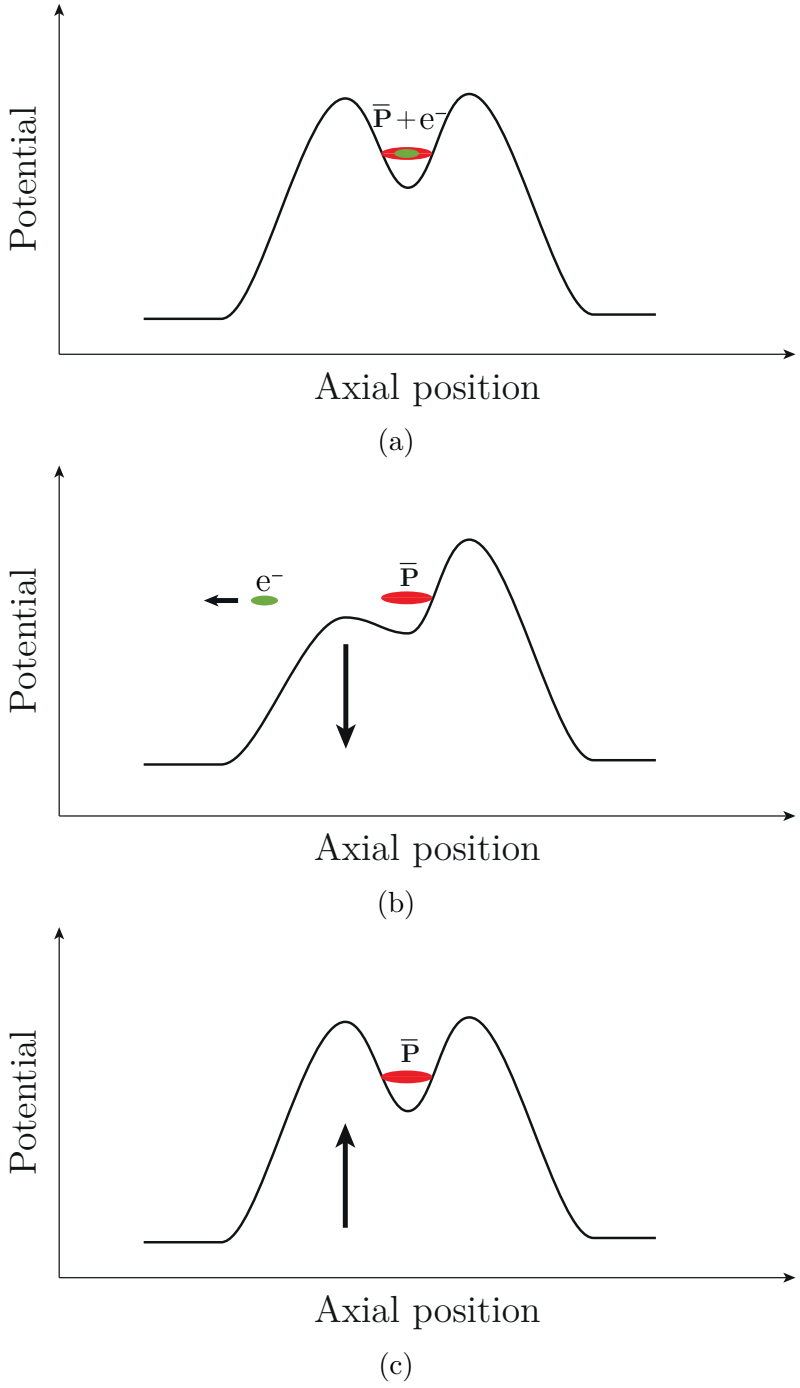

Figure 3.6: Schematic demonstration of the electron kick-out procedure. (a) A mixed antiproton-electron cloud is confined by a potential well. (b) One side of the well is momentarily lowered. Electrons acquire higher axial kinetic energies and escape the well whereas the heavier antiprotons lack sufficient axial kinetic energies to escape the confining well and remain temporally trapped. (c) Subsequent to the removal of the electrons, the lowered side of the well is re-established promptly (on the order of $\sim$ 100 ns) resulting in the permanent confinement of antiprotons.

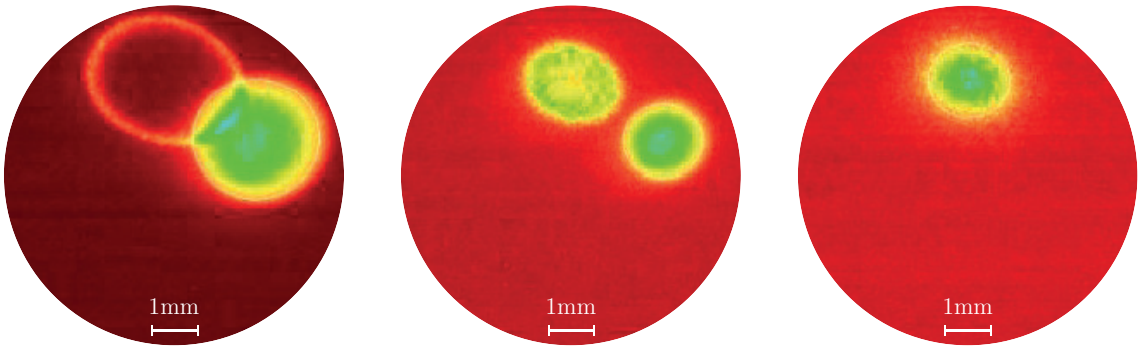

(a) (b) (c)

Figure 3.7: (a) The centrifugal separation [51] of the antiproton cloud (left) and the electron cloud (right) subsequent to the initial/first Rotating Wall compression prior to the application of the first electron kick-out. (b) Further/second compression of the antiproton cloud after the first electron kick-out resulting in the removal of 90% of electrons. (c) The removal of the remaining electrons by the second kick-out leading to a cold and confined antiproton plasma ready to be transfered into the RCT section of the AT for further manipulation and cooling. Due to a small misalignment between the magnetic field and the electrode stack, the images for antiprotons and electrons map to different locations on the MCP.

The electrons, in turn, cool via cyclotron radiation. Furthermore, Rotating Wall is applied to acquire further compression of the mixed plasma. The inclusion of an intermediate electron kick between the two plasma compressions (the first RW compression, see Sec. 3.3.2, is applied before the first electron removal) allows more compressed antiprotons to be obtained as the minimum radial size of the plasma is determined by the maximum density attainable with the Rotating Wall method, see Fig. 3.7. Therefore, removing the majority of the electrons during the first kick-out assists the RW compression with resulting in a denser cloud. Subsequent to the second compression, the second electron kick-out requires a much smaller magnitude as the amount of space charge subsequent to the first kick is significantly reduced, leading to the minimization of antiproton heating compared to the first kick. Utilizing such electron removal techniques has allowed ALPHA to acquire approximately 110,000 antiprotons with a temperature of $\sim$ 400 K and a radial size of 0.2 mm. The overall process takes approximately 100 s to complete. Fig. 3.7 illustrates MCP images of antiproton and electron plasmas at various stages of preparation prior to the transfer of the antiproton plasma to the RCT section of the AT.

The transfer of the antiprotons to the RCT is performed by promptly ($\sim 2\mu$s)

removing the confining potential, permitting the antiproton charged cloud to be sent ballistically to the RCT and cooled with pre-loaded electrons. The RCT booster solenoid (see Figures 2.12(b) and 2.13) is then energized and the mixed antiproton-electron plasma is subjected to similar treatments occurring in the CT, following the sequence of Rotating Wall compression, electron kick-out, further compression, and two more electron kick-outs, taking approximately 100 s and resulting in a pure, cold ($\sim$ 100 K) and dense (0.4 mm) plasma consisting of $\sim$ 110,000 antiprotons. The final manipulation of the antiproton plasma involves de-energizing the booster solenoid and shuffling the antiproton cloud from the RCT to the MT where further evaporative cooling (see the next Section) occurs over 10 s [42]. At this stage, ALPHA has acquired $\sim$ 90,000 antiprotons with a radius and temperature of 1 mm and 40 K, respectively, ready to be mixed with positrons to synthesize cold and trappable antihydrogen.

3.3.4 Evaporative cooling

The formation of antihydrogen atoms requires positron and antiproton plasmas to be at sufficiently low temperatures. For a particle distribution, the average kinetic energy of the system defines the temperature of the system. If the most energetic particles of the system are removed from the potential confining the particles, the average kinetic energy of the remaining distribution decreases and the system becomes colder, a technique known as EVaporative Cooling (EVC). An analogy is the cooling of a cup of coffee where the most energetic molecules escape as steam, allowing the remaining coffee to be cooled. Atomic physicists routinely utilize the evaporative cooling to both cool a collection of gas atoms to the ground state and establish the Bose-Einstein condensates [52].

EVC is routinely employed in ALPHA to reduce the temperature of the antiproton and positron plasmas for antihydrogen formation in the MT section of the AT [42]. The evaporative cooling of antiprotons is illustrated in Fig. 3.8 with antiproton charged cloud initially confined in a potential well set at 1500 mV in the Penning-

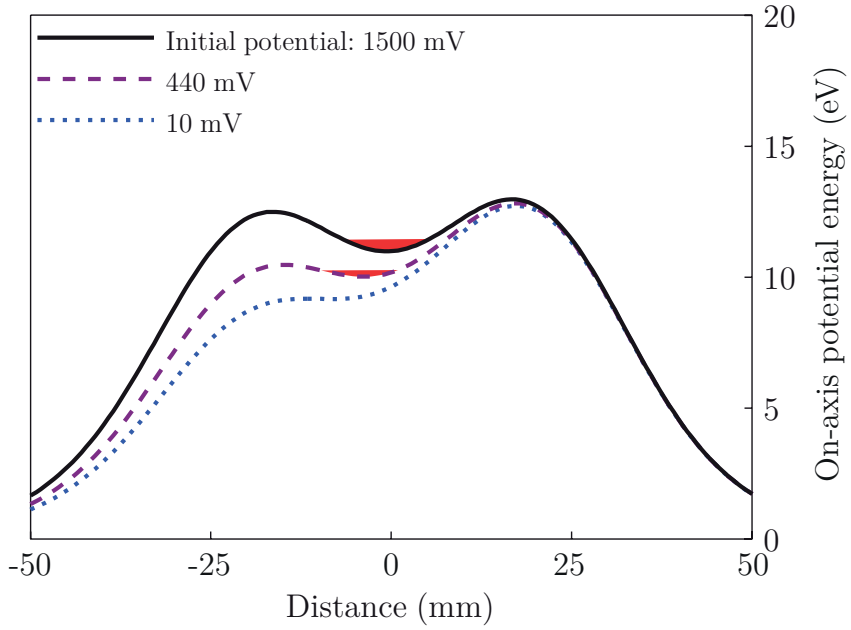

Figure 3.8: Various potential wells utilized for evaporative cooling technique resulting in the escape of the most energetic antiprotons along the trap axis to the left. Image adapted from [42].

Malmberg trap. The potential at one side of the well is subsequently slowly lowered, permitting the particles with the highest energy to escape (an evaporative boil-off) along the trap axis. The depth of the potential well determines the reduced temperature of the re-thermalized remaining distribution. EVC is exploited in a new technique known as Strong Drive Regime EVaporative Cooling (SDREVC) and will be discussed in the next section.

3.4 Strong Drive Regime Evaporative Cooling

The SDREVC is a technique devised by the ALPHA collaboration to acquire plasmas of required number and density subject to a variety of initial plasma parameters. It entails simultaneous applications of Rotating Wall compression in the Strong Drive Regime (SDR) and the EVaporative Cooling (EVC) of the plasma. At its core, the SDREVC relies on the realization that the plasma density is set by the Rotating Wall frequency while its potential is determined by the shape of the confining trap

well and the final electrode potential of the EVC, allowing the full final parameters of the plasma to be distinctively determined.

The first application of the SDREVC was carried out in ALPHA for electron plasmas pre-loaded at the CT before capturing the antiprotons delivered by the AD [53]. The SDREVC resulted in acquiring an electron plasma with final desired density and space charge parameters of 85×10^6 electrons with a radial size of ~ 9 mm. Stable and reproducible positron plasmas required for antihydrogen synthesis were subsequently acquired by the implementation of the SDREVC in the MT section of the AT [9], see Sec. 3.5.1.

3.5 Positron cooling and trapping

In parallel with the preparation of antiprotons in the CT, positrons are being produced and accumulated in the positron accumulator for 150 s, see Sec. 2.2.3. The ALPHA scientists have devised and implemented a unique technique to produce low energy, 'cold', positrons in vacuum. The process of decreasing the kinetic energy of positrons is known as moderation. To fulfil this process, ALPHA utilizes a solid film of condensed neon, the first stage in cooling the positrons. Emitted positrons must be collected, cooled and subsequently accumulated prior to their mixing with antiprotons in the neutral-atom trap. This is accomplished by incorporating an efficient Surko-type positron accumulator [20] into the apparatus. When the positrons leave the solid moderator, they are guided by the accumulator into a buffer gas and confined in a Penning-Malmberg trap.

The right side of Fig. 2.9 demonstrates the moderator and the beam line. The sodium radioactive source is positioned on a coldhead that has been cooled to a temperature of approximately 5 K. On the top of the coldhead is the neon moderator through which positrons rapidly become thermalized and diffuse. A small fraction (0.4%) of the emitted positrons become sufficiently cold to reach the surface of the solid neon and then into the vacuum chamber, amounting to 15×10^6 positrons per

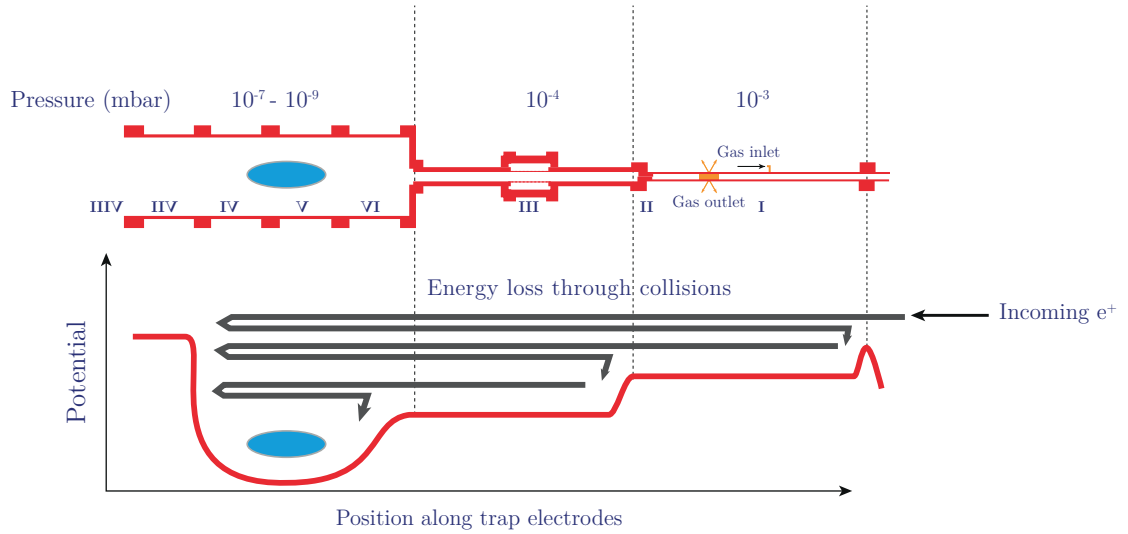

Figure 3.9: Top: the expanded view of the elongated electrode structure of the positron accumulator sub-divided into 8 sections with electrodes of varying diameters resulting in a pressure gradient. Bottom: red curve depicts the variation of the axial electrical potential as a function of position along the trap electrodes. The positron buffer gas cooling is demonstrated by the grey curve.

second possessing energies of approximately 50 eV. These moderated positrons are subsequently formed into a beam and follow the external magnetic field towards the trapping region on the left side of the accumulator.

The trapping region is depicted in Fig. 3.9. It shows a schematic illustration of the variations of the electrical potential and the pressure as a function of position along the trap. Also included is the cylindrically symmetric electrode structure of the trap. The trap is surrounded by an external solenoid magnet producing a 0.14 T magnetic field, see Fig. 2.9.

Within the accumulator trapping region, three cooling mechanisms are performed. The first cooling mechanism makes use of the energy loss via collisions between nitrogen gas molecules and positrons. Initially, the electric potential of the well is raised in order to trap the incoming positrons from the coldhead. Afterwards, the molecular N_2 gas is introduced into region-I of the trap maintained at a pressure of 10^{-3} mbar. By designing axial trap electrodes of varying diameters, a differential pumping between region-I and the rest of the trap results in a pressure gradient in the buffer gas in the vicinity of the electrodes. In addition, a step-wise decreasing electrostatic potential is applied such that the trough of potential well corresponds

to the region with the lowest gas pressure.

Positrons traverse through regions I, II and III. A particular electrode configuration within the region-III gives rise to an electrical potential that reflects the positrons towards the entrance of the trap. During the transit through the three regions, two competing collisional processes between a positron and a nitrogen molecule occur: (1) positron excitation transition (3.14) (2) positron loss channel of positronium (3.15). $\sim 30\%$ of the positrons undergo electronic excitation of the N_2, process (1), and as a result they lose about 9 eV of their kinetic energies.

These positrons are subsequently trapped, oscillating back and forth through regions I to III. Eventually, they are further cooled by exciting vibrational and rotational transitions of the N_2 molecules and thereby dropping deeper and deeper into the electrostatic potential well. After around 1 s, the positrons acquire temperatures on the scale of room temperature and resides in region-III at a pressure of 10^{-4}

$$e^+ + N_2 \rightarrow e^+ + {N_2}^*, \tag{3.14}$$

$$e^+ + N_2 \rightarrow Ps + {N_2}^+. \tag{3.15}$$

3.5.1 Manipulation and transfer

The rapid accumulation of the positrons leads to the increase in size and density of the positron plasma and the subsequent formation of a non-neutral plasma. The desired size and intensity of the plasma prior to its ejection from the accumulator into the AT is achieved using the Rotating Wall technique (see Sec. 3.3.2) within regions VI-IIIV. As shown in Fig. 2.9, one of the trap electrodes has been segmented into six sectors and provides an electric field to produce a torque shrinking the positron plasma and hence increasing the positron density. However, the increase in density is accompanied by an increase in the plasma's temperature. The undesired heat is removed from the plasma by the simultaneous application of RW and the continuous collisional cooling between the plasma and the nitrogen buffer gas with a pressure

of 10^{-7} mbar.

Before the injection of cooled positrons from the accumulator to the PT section of the AT, see Fig. 2.12(b), two cryopumps are in operation to remove the nitrogen gas. The gas removal improves the quality of the vacuum by 4 orders of magnitude from 10^{-5} to about 10^{-9} mbar during a period of 40 s. A valve separating the accumulator and the AT is then opened and a pulsed magnet is engaged, allowing 80×10^6 positrons to follow the magnetic field lines and be ballistically transferred to the Positron Trap of the Atom Trap.

Having a pulse length of 200 ns, the injected positron plasma is dynamically captured and trapped with an efficiency of approximately 10%. Superimposed on the 1 T external solenoid, the 2 T internal booster solenoid of the PT is energized so that this section of the AT acquires an overall magnetic field of 3 T, see Fig. 2.13, where positrons are cooled by cyclotron radiation for 30 s. Due to the significant loss of positrons during the transient to the PT, the density and number of positrons transferred to the AT fluctuates on a shot-to-shot basis. This variation can be reduced by the application of the SDREVC on the positron cloud with typical parameters leading to 3×10^6 positrons. The positrons are further compressed using RW compression and cooled by cyclotron radiation for 20 s in the 3 T axial magnetic field, eventually leading to the production of cold positrons with nominal temperature of 50 K prior to the de-energization of the booster solenoid.

3.5.2 Adiabatic cooling

For a charged particle with mass m in a harmonic confined potential well of a Penning-Malmberg trap, a restoring force acts on the particle and as a result the particle undergoes oscillatory motion with an axial bounce frequency of w_z. The total axial energy of the particle is given by

$$E_z = \frac{1}{2}mv_z^2 + \frac{1}{2}mw_z^2z^2. \tag{3.16}$$

For a given energy, the path the particle traces out in phase-space is an elliptical orbit. The area of the ellipse is calculated as $2\pi\frac{E_z}{w_z}$ and for gradual changes in w_z the area remains unchanged, implying that the ratio representing the area is an adiabatic invariant [54]. In practice, one is able to achieve an adiabatic decrease of w_z by slowly extending the confiding potential well. Consequently, the axial energy (and the corresponding temperature) of the particle is reduced [55], a process known as 'adiabatic cooling'.

The single-particle approximation is valid for plasmas with low density as the Coulomb interactions can be assumed negligible and it can therefore be asserted that the temperature is linearly dependent on the plasma frequency, i.e. $T \sim w_p$. The assumption is no longer applicable for high-density plasmas due to the presence of collisions and space-charge effects. A temperature dependence of the type $T \sim w_p^{\frac{4}{3}}$ has been predicted [56] and verified experimentally [57] using antiprotons.

The positron plasma is transferred to the centre of the Mixing Trap following the de-energization of the booster solenoid in the PT. Engaging the neutral-atom trap leads to the disadvantageous effect of heating up the positrons which is caused by the magnetic field inhomogeneities induced by the octupole magnet. Accordingly, the positron cloud undergoes adiabatic cooling. Positrons can maintain a much longer lifetime without annihilating with the residual gas due to the presence of a very low pressure in the cryogenic surrounding of the MT. This longer lifetime allows further cool-down of the positrons by the evaporative cooling technique, resulting in the attainment of $\sim 2 \times 10^6$ positrons possessing an average temperature of 18 K. At this stage, both the antiproton and positron plasmas are ready to be mixed for antihydrogen synthesis [58].

Chapter 4

Antihydrogen Synthesis & Confinement

Chapter 3 provided various techniques utilized to cool, compress and prepare antiproton and positron plasmas for antihydrogen formation and trapping. The objective of this chapter is to describe detailed procedures undertaken in ALPHA to synthesize and confine antihydrogen atoms. The first part of the chapter covers the mechanisms for production of antihydrogen, various initiatives devised by ALPHA to mix antiprotons with positrons, a new technique whereby antihydrogen can be accumulated, and the detection of untrapped antihydrogen atoms. The second section focuses on the confinement of antihydrogen atoms in the ALPHA apparatus.

4.1 Antihydrogen formation mechanisms

The production of low-energy antihydrogen atoms occurs when positron and antiproton plasmas are mixed together. In this process, the positrons combine with antiprotons and the excess binding energy is carried away by a third particle. Several combining mechanisms are described.

4.1.1 Spontaneous radiative recombination

Spontaneous Radiative Recombination (SRR) is the simple mechanism of combining antiprotons and positrons whereby the excess binding energy is carried away by a photon [27] such that

$$\overline{p} + e^{+} \rightarrow \overline{\mathrm{H}} + h\nu, \tag{4.1}$$

where h is Planck's constant and ν is the frequency of the photon.

In SRR, the densities of the positrons and antiprotons and their relative velocities determine the rate of antihydrogen formation. Considering the formation process in the rest-frame of the antiproton, the rate of formation Γ_{SRR} can be stated in terms of positron density n_{e^+} and temperature T_{e^+} [59]

$$\Gamma_{\mathrm{SRR}} = 3 \times 10^{-17} \left(\frac{4.2\ \mathrm{K}}{T_{e^+}} \right)^{1/2} \left(\frac{n_{e^+}}{\mathrm{m}^{-3}} \right) \mathrm{s}^{-1} \text{ per antiproton.} \tag{4.2}$$

In the ALPHA experiment, for a positron plasma with nominal temperature and density of 20 K and 10^{13} m^{-3}, respectively, Γ_{SRR} is $\sim 10^{-4}$ s^{-1} per antiproton.

4.1.2 Three-body recombination

For a dense and cold positron plasma, a collision between two positrons in close proximity of an antiproton results in one of the positrons losing significant of its kinetic energy, allowing the antiproton to combine with the low-energy positron while the excess binding energy is carried away by the other positron such that

$$e^{+} + e^{+} + \overline{p} \rightarrow \overline{\mathrm{H}} + e^{+}. \tag{4.3}$$

In a strong magnetic field, the formation rate of the Three-Body Recombination (TBR) mechanism for a plasma in steady-state is given by [60]

$$\Gamma_{\mathrm{TBR}} = C(8 \times 10^{-24}) \left(\frac{4.2\ \mathrm{K}}{T_{e^+}} \right)^{9/2} \left(\frac{n_{e^+}}{\mathrm{m}^{-3}} \right)^{2} \mathrm{s}^{-1} \text{ per antiproton,} \tag{4.4}$$

where C is a constant dependent on the magnetic field and temperature. For a positron plasma in a magnetic field of 1 T with nominal temperature and density of 20 K and 10^{13} m^{-3}, respectively, C $\sim$ 0.19 [61]. This gives rise to a Γ_{TBR} of $\sim 10^2$ s^{-1} per antiproton, six orders of magnitude greater than Γ_{SRR}. Therefore, Γ_{TBR} is believed to be the dominant process of antihydrogen formation when merging antiproton plasma with a cold and dense positron plasma. In addition, Eq. 4.4 demonstrates the significant dependence of the Γ_{TBR} on T_{e^+} and n_{e^+}, which explains the motive behind employing the evaporative cooling technique to cool the positron plasma (see Sec. 3.3.4) and the Rotating Wall technique to acquire the radial compression of the plasma (see Sec. 3.3.2), both techniques leading to the optimization of the formation rate of the low-energy antihydrogen atoms.

4.2 Antihydrogen synthesis in ALPHA

4.2.1 Plasma mixing

Once the positron and antiproton plasmas are ready to be mixed for antihydrogen production, they are required to be confined simultaneously in the Mixing Trap of the Atom Trap. As the two plasmas possess opposite charges, a potential configuration known as 'nested potential well' [62] is used to achieve the simultaneous confinement. As shown in Fig. 4.1, the nested well consists of two wells, one well being short and central while the other well is long and inverted, giving rise to two 'side-wells' located on each side of the middle well.

The velocity distribution of antihydrogen atoms subsequent to their formation is dependent on the antiproton velocity due to its heavier mass. Hence, minimizing the kinetic energy of antiprotons during the mixing is vital. One would expect that placing the heavier antiprotons in the central well and, in some manner, increasing the longitudinal energy of the lighter positrons confined in one of the side wells to allow them to overcome their confined potential and interact/overlap with the

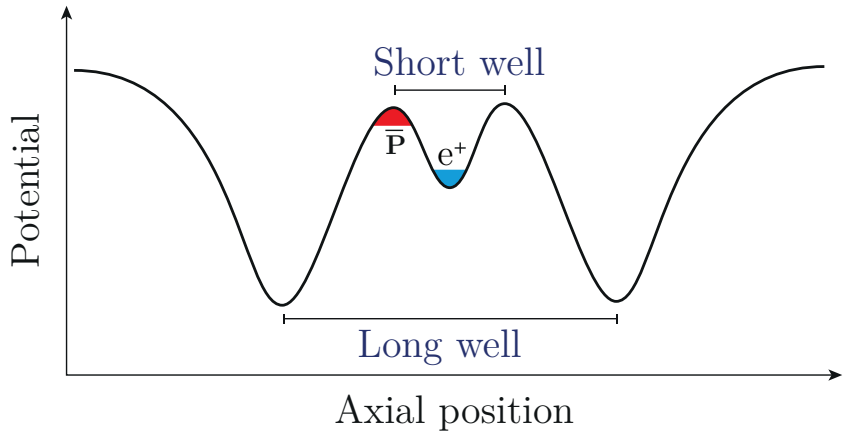

Figure 4.1: Schematic illustration of a nested potential well whereby positrons (e^+) are confined in a short well in the middle and antiprotons ($\overline{p}$) in one side of an inverted long well. Red and blue filled regions are an indication of the self-potentials and the physical extents of antiproton and positron plasmas, respectively.

antiprotons is the optimal technique to achieve the most efficient mixing outcome. However, positrons undergo rapid cyclotron cooling in the strong magnetic field ($\sim$ 4 s at 1 T), and they lose their energy and cool into the side-well, ceasing both the interaction with antiprotons and the subsequent creation of antihydrogen atoms. This explains why the positrons need to be maintained at the central well and antiprotons to be confined in one of the side-wells prior to their injection into the positron plasma at the short well at the centre of the MT.

There are various approaches one can adopt to accomplish mixing antiproton and positron plasmas by means of a nested-well potential, each resulting in an antihydrogen formation with slightly different temperature and kinetic energy distributions. These approaches are described in the following subsections.

4.2.1.1 Simple mixing

The simplest mixing scheme uses a modified version of the nested potential well whereby antiprotons are confined by a higher potential barrier relative to the positron plasma barrier, see Fig. 4.2. The antiproton plasma is subsequently injected into the positron plasma when its confining potential is lowered and the antiprotons have acquired a kinetic energy of 15 eV. The antiprotons launch into the positron plasma, which allows some of the positrons to become bounded to the

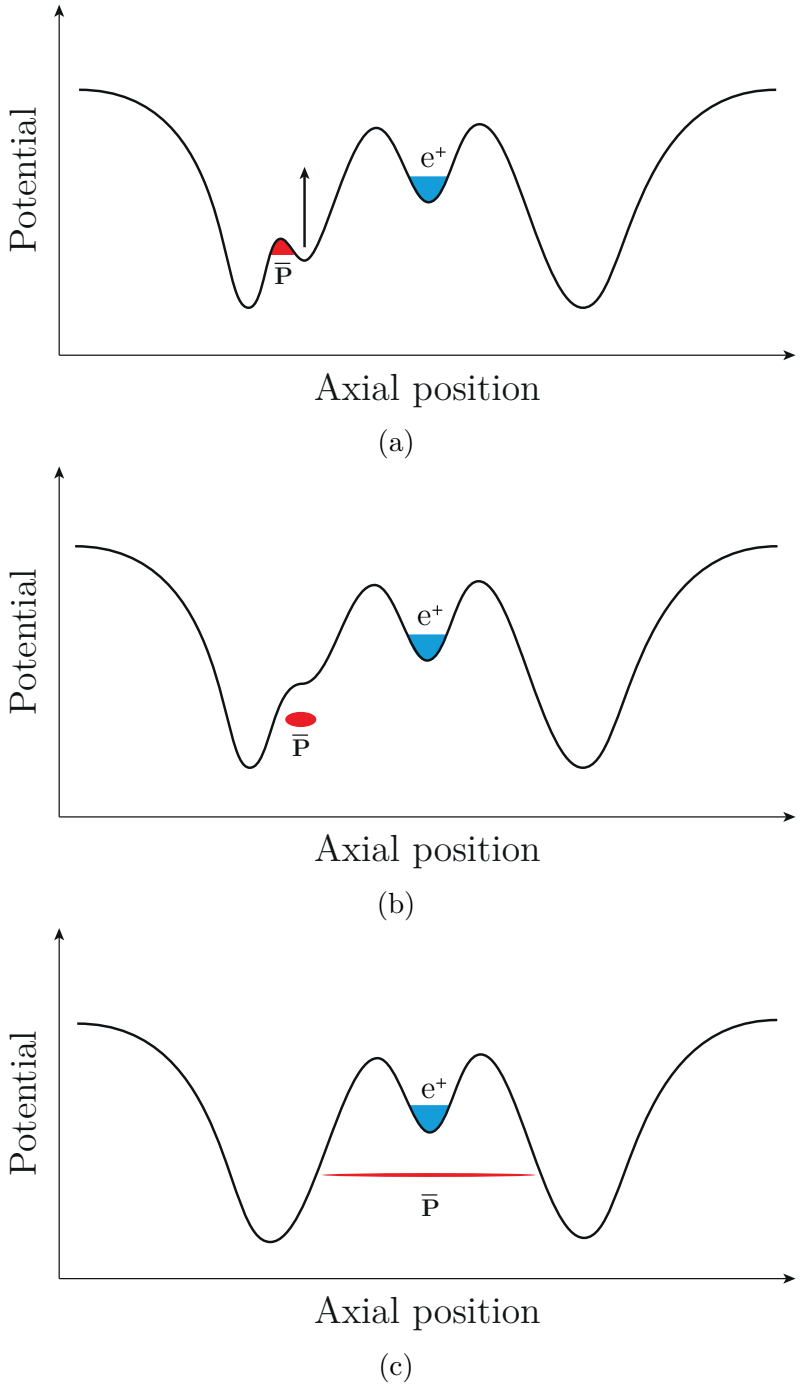

Figure 4.2: Schematic diagram of a simple mixing sequence. (a) An antiproton plasma is confined within a potential barrier higher than the barrier confronted by the positron plasma. (b) Lowering the antiproton barrier allow them to be injected into the positron plasma. (c) Antiproton and positron plasmas are mixed and antihydrogen atoms are created.

incoming antiprotons, giving rise to the formation of untrapped antihydrogen atoms with kinetic energies higher than the magnetic trap depth of 0.5 K. Using this mixing scheme, the first 'cold' production of antihydrogen was demonstrated in 2002 by ATHENA [2] and ATRAP [3].

4.2.1.2 Autoresonant injection

A confined antiproton cloud undergoes an axial oscillatory motion with a bounce frequency related to the oscillation amplitude. Based on this fact, ALPHA has developed a technique, known as 'autoresonant' mixing [63], that upon the application of a swept frequency drive the antiproton cloud axial oscillation matches the drive frequency at every instant. The acquired matching mode further allows the oscillation amplitude to be controlled by varying the driving frequency. This continuous phase-locked response explains the reason behind adopting the name 'autoresonant'.

A schematic diagram illustrating the autoresonant mixing procedure is depicted in Fig. 4.3. Firstly, the cold antiprotons are confined by a side-well potential which prevents them from overcoming the potential barrier. Secondly, a swept frequency is applied, locking the antiproton bounce frequency. Reducing the drive frequency leads to an increase in the axial potential of the phase-locked antiprotons. Providing that the sweeping of the drive is performed slowly, antiprotons eventually acquire sufficient energy (by the increase in their kinetic energy) to overcome the confining potential and are injected into the positron central well. Once in the central well, the antiprotons are no longer locked with the drive and therefore they acquire no additional energy from the drive, resulting in the mixing of the antiprotons having low axial kinetic energies with the positron plasma. The cold antiprotons then thermalize in the positron plasma prior to the formation of antihydrogen atoms. Although the autoresonant drive has no direct impact on the positrons, it has been observed that positrons are heated from 20 K to $\sim$ 50 K once the injection is completed. In addition, an increase in the number of antiprotons leads to further heating of the positron plasma, which has the adverse consequence of lowering the

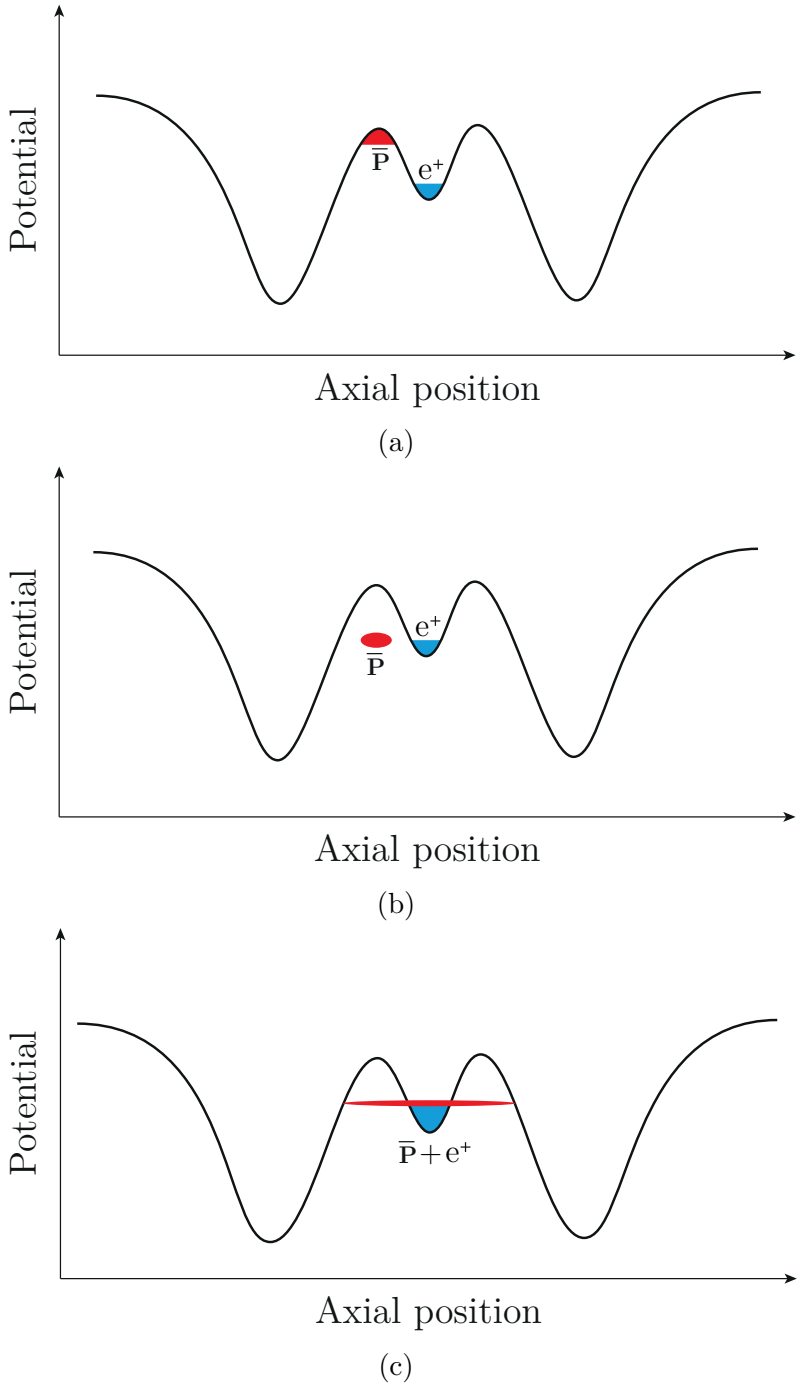

Figure 4.3: Schematic illustration of the autoresonant mixing process. (a) Antiprotons are initially confined in a side-well potential while positrons are trapped in the middle/-central well. (b) An autoresonant drive provides the antiprotons with an axial energy. (c) Antiprotons acquire sufficient axial kinetic energy to overcome the potential barrier and are injected into the positron plasma where they become thermalized. Antihydrogen formation subsequently follows.

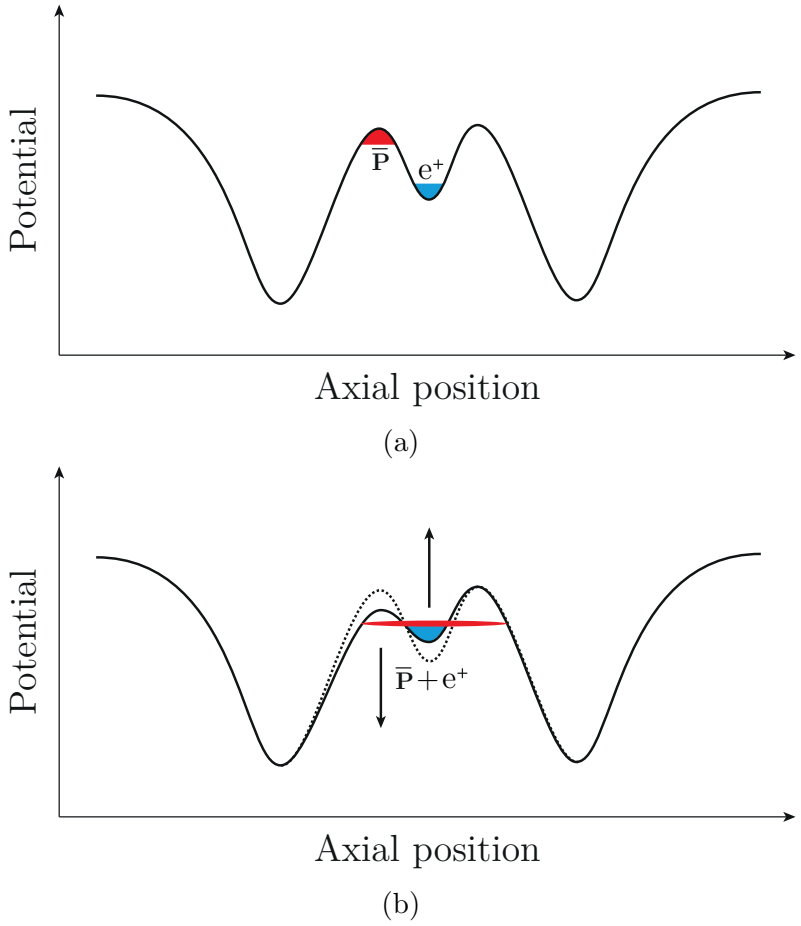

Figure 4.4: Schematic demonstration of slow merge mixing process. Dashed and solid curves represent electrostatic potentials before and after each step in the process, respectively. (a) Antiproton cloud is confined in the inverted side-well potential adjacent to the central well containing the positron plasma. (b) The simultaneous injection of the two species into each other by the slow merge of the antiproton and positron electrostatic wells.

trapping rate (i.e. the number of trapped atoms per attempt).

Utilizing the autoresonant mixing scheme, the first successful confinement of cold antihydrogen was demonstrated by ALPHA in 2010 [4]. Autoresonant-excitation mixing was employed until the end of 2016 where a trapping rate of 2 atoms per trial and a simultaneous detection of a maximum of 4 atoms within the trap (using the standard online analysis method with a detection efficiency of 63.4%) were acquired.

4.2.1.3 Slow merge

The unfavourable heating effect of autoresonant mixing induced by the increased number of antiprotons can be eliminated using a mixing technique called 'slow merge'

and is demonstrated in Fig. 4.4 [10]. Here, similar to the autoresonant scheme, the antiproton and positron plasmas are initially confined by two adjacent potential wells. Antiprotons are confined by an inverted side-well while positrons are confined by the middle well. Antihydrogen formation begins when the simultaneous injection of the two species into each other is accomplished by the slow merge of the antiproton and positron electrostatic wells over a period of over 1 s, see Fig. 4.4(b), while the positron plasma is cooled to below 20 K by evaporative cooling [64].

Employing the slow merge mixing during the 2016 run led to the significant increased trapping rate of 10.6 ± 0.6 atoms per experimental cycle, see Sec. 4.2.2 [65]. It is noted that the record trapping rate achieved by utilizing the potential merge mixing resulted in about an order of magnitude more trapped antihydrogen atoms in a single six-month experimental run than were accumulated over many years using autoresonant injection mixing technique.

4.2.2 Antihydrogen accumulation

The AD delivers antiproton batches every 2 minutes and the antihydrogen formation takes between 3 to 4 minutes. In addition, experiments with antihydrogen atoms can take up to 20 minutes. The relatively long timescale of the overall process of the capture, synthesis and trapping highlights the importance of identifying antihydrogen atoms and the necessity for optimizing the number of antihydrogen atoms utilized during scientific experiments. Furthermore, an improvement in the signal-to-background ratio for the observation of antihydrogen annihilations can be attained by having more confined antihydrogen atoms present during the long exposures to microwave or laser radiation.

Superimposing the transverse octupole trapping field on the uniform axial solenoidal field distorts the axial magnetic field of Penning-Malmberg trap, which results in drifting the particles towards the trap wall. The radial limit, known as critical radius, beyond which the particles traversing through the $\sim$ 30 cm long and fully energized neutral trap will be lost is calculated to be about 4.5 mm [33]. This

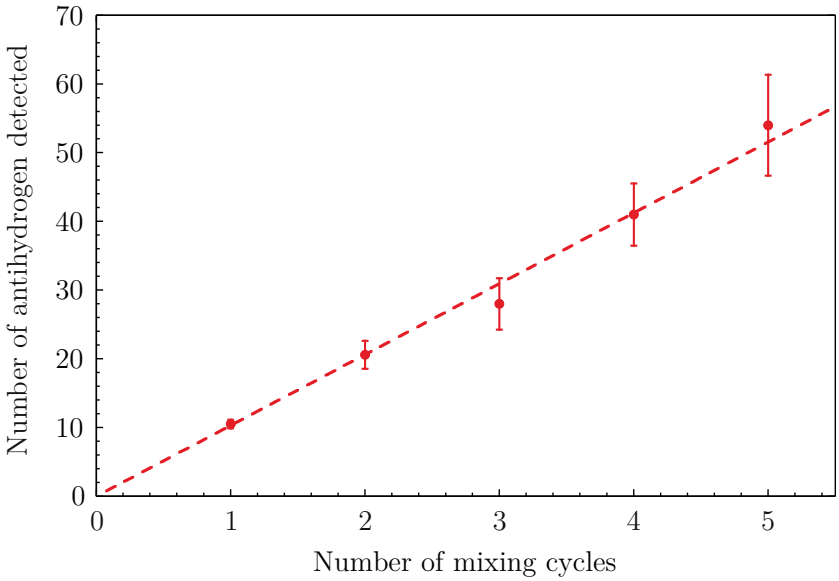

Figure 4.5: Plot depicting the antihydrogen stacking. The linear relationship between the number of trapped atoms detected and the mixing cycle is evident. Each mixing/synthesis cycle lasts 4 min and antihydrogen atoms are detected by the ramp down of the magnetic minimum trap subsequent to one or more consecutive mixing cycles. The error bars represent the $\sqrt{N}$ counting statistics. The linear fit to the data implies an average trapping rate of 10.5 $\pm$ 0.6 detected antihydrogen atoms per mixing cycle. The detection efficiency is (73.0 $\pm$ 0.4)%. Image adapted from [10].

limit is much greater than the radial size of the electron, positron and antiproton plasmas ($<$ 1 mm) prepared in ALPHA. Hence, the critical radius can be regarded as a dynamic aperture for the controlled shuffling of plasmas during the preparation of the charged particle plasmas in the AT while the magnetic minimum trap fields are energized. This has provided the possibility of creating more antihydrogen while the atoms from the previous formation cycle (lasting about 4 min) remain confined. Furthermore, consistent with the dynamic aperture considerations stated above, no adverse effects on plasma preparation were perceived. Due to thermal considerations of the octupole magnet current supply circuit, the antihydrogen accumulation, 'stacking', procedure was repeated for a maximum of five cycles.

The average number of confined and detected anti-atoms as a function of the number of synthesis/mixing cycles is shown in Fig. 4.5. The linear dependence between the number of trapped atoms and the number of stacks is evident. The linear fit implies an average trapping rate of 10.5 $\pm$ 0.6 detected antihydrogen atoms per

mixing cycle, or equivalently a maximum absolute effective trapping rate of 2.6 ± 0.2 detected antihydrogen atoms per minute. Moreover, the five-cycle experiment gave rise to a total of 54 detected antihydrogen atoms, and accounting for the detection efficiency of $(73.0 \pm 0.4)\%$, this indicates that about 74 atoms were simultaneously confined [10].

4.2.3 Detection of untrapped antihydrogen

In ALPHA, the detection of antihydrogen atoms formed during the mixing of antiproton and positron plasmas is achieved by a destructive method where the detection commences by the de-energization/shutdown of magnetic neutral-atom trap. With no magnetic fields due to the octupole or the mirror coils present, the neutral antihydrogen atoms are no longer confined. The anti-atoms escape the trap and annihilate on the trap wall. The annihilation is detected by the SVD (see Sec. 5.1) which provides information regarding the position and timing of the annihilations. The trap shutdown can be performed in two ways: (1) the deliberate triggering of the quench response of the magnets (see Sec. 2.4.3), or (2) the rapid ramp-down of the trap power supplies without initiating the quench response.

The deliberate triggering of the quench response leads to the de-energization of the magnets with a time constant of 9.5 ms, which is sufficiently fast to allow the elimination of false-positive signals arisen from the cosmic background. However, this shutdown technique results in the creation of eddy currents in the electrodes by the quenching magnets which, in turn, heats up the electrodes. A 15-minute wait is required for the electrodes to re-establish the thermal equilibrium with the cryostat before the next mixing cycle can be repeated.

The rapid ramp-down of the trap power supplies without initiating the quench response is performed in 1.5 s and no electrode heating results. The relatively much longer search time window of 1.5 s (compared to 9.5 ms) for annihilation events increases the false-positive signals due to the cosmic rays. Yet, the rate of the false-positive signals is smaller than 0.1 per ramp-down, implying that combining

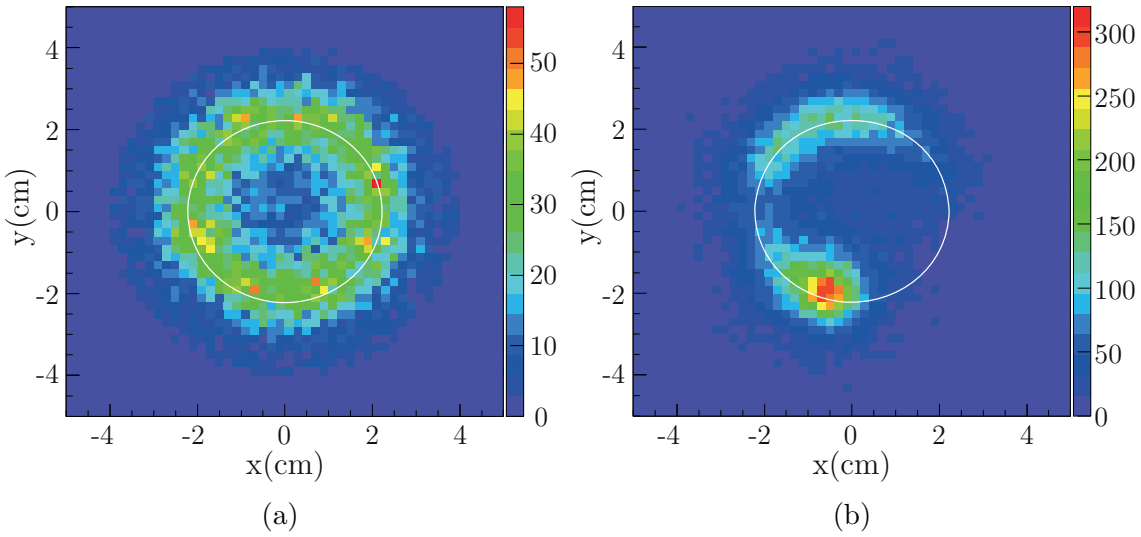

Figure 4.6: (a) The $x-y$ spatial distribution of approximately 2×10^4 antihydrogen atoms projected along the z-axis. The distribution is approximately azimuthally uniform (no angular dependence) and concentrated around the inner electrode surface represented by the white circle. (b) Bare antiprotons annihilate in highly localized hot spots. Image adapted from [48].

a mixing scheme leading to a sufficiently high trapping rate (for example, the slow merge mixing) with the fast ramp-down technique allows the feasibility of conducting experiments with a higher duty cycle without introducing considerable false-positive background signals.

As well as the cosmic events registered as false signals, another source of false-positive background signal is the low-energy bare antiprotons which did not bind with positrons to form antihydrogen during the mixing and remained trapped between the mirror coils. The SVD is sensitive to the charged particles originating from the bound antiproton of the antihydrogen atom annihilating a proton of the gold nucleus of the trap wall but not the gamma rays produced by the positron annihilation. For this reason, extensive investigation has been performed whereby the annihilation of a bare mirror-trapped antiproton is discriminated from that of a bound-antiproton of the antihydrogen atom [66].

After the slow merge mixing of antiprotons and positrons for 1 s, the Penning-Malmberg electrodes are grounded, allowing the remaining charged antiparticles to axially escape the trap. The removal of mirror-trapped antiprotons from the trap (and therefore minimizing their false-positive signal contribution) is achieved by the

application of four pulses of axial electric field (up to 500 V/m). Furthermore, during the magnet trap shutdown a sloped electrostatic potential is applied to deflect the trajectory of antiprotons to one side of the trap, depending on the direction of the electric field. Since the trajectory of the neutral antihydrogen atoms is unaffected by the electrostatic potential, this technique provides a systematic way of discriminating between mirror-trapped bare antiprotons and antihydrogen annihilations.

Fig. 4.6(a) demonstrates an example of the $x - y$ position (projected along the trap axis) distribution of the untrapped antihydrogen annihilation vertices reconstructed by the SVD. It is evident that the majority of the annihilations occur on the inner electrode surface (represented by the white circle) with no angular dependence. A pure antiproton distribution can be acquired by deliberately destabilizing an antiproton plasma, allowing the antiprotons to annihilate on the electrode surface. Fig. 4.6(b) is the outcome of such distribution where the antiprotons influenced by the Penning trap electric and magnetic fields have annihilated in localized 'hot spots'.

4.3 Antihydrogen confinement in ALPHA

The indefinite confinement of low-field seeking antihydrogen atoms with kinetic energies less than the magnetic-trap depth can be attained by establishing a perfect vacuum inside the trap and allowing the magnetic traps to remain energized. In practice, perfect vacuum conditions are unattainable and therefore the confined anti-atoms undergo annihilation on the residual gas particles over time. By implementing the various experimental techniques described thus far, the first confinement of 38 antihydrogen atoms for 172 ms was conducted in the ALPHA-I apparatus in 2010. Enhanced confinement of antihydrogen atoms for up to 1,000 seconds [67] has followed since then. This is a sufficiently long confinement that has paved the way for performing further experiments on antihydrogen atoms [6] [7] [8] [12].

The steps required in conducting a trapping cycle are shown in Fig. 4.7. Recent

	AT			
CT	RCT	MT	PT	Positron Accumulator
• Load ~ 85M e^- with r ~ 9mm using SDREVC. • AD injection of 30M $\bar{p}$ at 5MeV. • Catch $\bar{p}$ from the AD using the HV electrodes. • Cool $\bar{p}$ for 20s to E < 5keV using pre-loaded e^-. • Lower the HV electrodes to eject remaining uncooled $\bar{p}$ (hot dump). • RW compression for 5s. • e-kickout1. • RW compression for 10s. • e-kickout2. • Cyclotron cooling for 10s. • e-kickout3. • Total processing time of ~ 100s results in 110,000 $\bar{p}$ with r = 0.2mm, T ~ 400K and kinetic energy of 25eV. • Transfer $\bar{p}$ to the RCT.	• Load e^-. • Re-catch $\bar{p}$ from CT. • Energize RCT booster solenoid. • RW. • Cool $\bar{p}$ with pre-loaded electrons. • e-kickout1, RW, e-kickout2 and e-kickout3. • Total processing time of 100s results in 110,000 $\bar{p}$ with T ~ 100K and r ~ 0.4mm. • De-energize RCT booster solenoid. • Transfer $\bar{p}$ to MT.	• $\bar{p}$ plasma confined in an inverted side-well. • EVC on $\bar{p}$ for 10s results in ~90,000 $\bar{p}$ with T = 40K and r = 1mm. • e^+ plasma confined in a central well adjacent to the $\bar{p}$ well. • Neutral-atom trap is energized. • Adiabatic cooling and evaporative cooling on e^+ plasma lead to ~ 2M e^+ with T = 18K. • Slow merge of the $\bar{p}$ and e^+ plasmas simultaneously for 1s. • Grounding electrodes to allow the escape of remaining charged particles. • $\bar{p}$ clearing pulses. • Hold/trap $\bar{H}$ for physics. • Rapid ramp-down of AT magnets.	• Re-capture of 10% of e^+ due to the low efficient transfer. • Energize PT booster solenoid. • Cool e^+ for 30s in 3T field. • SDREVC results in ~ 3M e^+. • RW of e^+ plasma. • Cyclotron cooling for 20s. • Thermalization with trap environement gives rise to T ~ 50K. • De-energize the PT booster solenoid. • Transfer e^+ plamsa to MT.	• Emission of e^+ from sodium-22 radiactive source. • Accumulation in the 3-stage Surko-type trap. • Cooling with nitrogen buffer gas. • Positron accumulation results in 80M e^+ in 150s. • Pumping out nitrogen gas from the accumulator to avoid contamination of the AT. • Opening the valves separating the PT and the positron accumulator. • Transfer e^+ to PT.

Figure 4.7: Steps outlining the procedures undertaken to synthesize and confine antihydrogen atoms in the ALPHA experiment. See the text for detailed descriptions.

experiments at ALPHA have demonstrated the synthesis of up to 50,000 antihydrogen atoms per trapping cycle. However, only a small fraction ($\sim$ 0.02%) of these atoms are sufficiently cold (i.e. with kinetic energies less than the magnetic trap depth) to be confined. This small number of trapped antihydrogen atoms implies that the verification of a scientific pursuit (such as CPT) requires significant number of trapping cycles in order to achieve the necessary statistical significance. Improving the precision of existing measurements and the feasibility of future experiments (such as anti-gravity) can be attained in two ways. Firstly, by enhancing the antihydrogen formation and trapping rates. Secondly, by increasing the detection efficiency of antihydrogen atoms. The rest of this thesis is motivated by the latter desire and aims to present a new method capable of increasing the detection efficiency of antihydrogen annihilations.

Chapter 5

The ALPHA Silicon Vertex Detector

Silicon is the most widely utilized semiconductor material and possesses a wide range of applications. Silicon characteristics and fabrication processes have been studied extensively and, as a result, a majority of electronic devices are manufactured using silicon.

The ALPHA experiment utilizes a silicon detector in order to reconstruct the trajectories of antihydrogen annihilation products and determine the position of the annihilation point, which is also known as the vertex. One section of this chapter will describe antihydrogen annihilation processes that are used to generate the antihydrogen signature. Furthermore, since the Silicon Vertex Detector (SVD) and the electronic read-out chips employ silicon as the prime material, a brief theoretical introduction to the key semiconductor properties that affect the performance of a detector will be presented. The final section deals with the technological features, including the design, the assembly and the read-out electronics, that are incorporated into the SVD in order to enable the detection of the annihilation signature.

5.1 Matter-antimatter interaction

When a particle encounters its antiparticle (a particle with the same mass and spin however with opposite charge and quantum numbers) an annihilation occurs. This is followed by the disappearance of both the particle and the antiparticle and the subsequent transformation of their combined energies into other particle/antiparticles. The conservation of momentum and charge will be satisfied through the generation of additional particles/antiparticles in the annihilation. This thesis will focus primarily on the detection and the subsequent analysis of antiproton annihilation products.

Trapped antihydrogen in the ALPHA experiment reaches an upper average kinetic energy of approximately 0.043 meV, an energy dictated by the neutral trap well-depth of 0.5 K. Moreover, positron and antiproton plasmas can acquire temperatures up to approximately 18 K and 40 K corresponding to an average kinetic energy of 1.55 meV and 3.44 meV, respectively. Energies with such small orders of magnitude imply that the annihilation processes can be investigated non-relativistically. For simplicity, in this thesis the particle-antiparticle interactions are assumed to occur at rest.

5.1.1 Positron-electron annihilation

If a positron travelling through normal matter encounters an electron, it undergoes annihilation. The positron survival time is inversely proportional to the electron density of the sample [68]. For low-energy positron-electron annihilation, the process results in the production of two or more gamma-ray photons

$$\mathrm{e}^- + \mathrm{e}^+ \rightarrow \gamma + \gamma. \tag{5.1}$$

The total energy of the process 5.1 amounts to the total rest mass energy of its constituents (e^- and e^+) and it is subsequently shared equally between the two

photons. Since photons cannot be stationary and the process is required to conserve momentum, the two γ-ray photons must travel in opposite directions. The two back-to-back γ-ray photons of energy of 511 keV produced in positron annihilation was the distinct signature ATHENA detector sought to detect as a means of determining the annihilation position [47].

5.1.2 Antiproton-nucleon annihilation

Antiprotons undergo annihilation either upon interacting with protons or neutrons in normal matter. The resultant antiproton-nucleon annihilation is significantly complex compared with that of a positron since the antiproton is a composite system consisting of quarks and gluons. As shown in Table 5.1, charged and neutral pions are the primary products of a low-energy antiproton annihilation.

In the ALPHA experiment, an antiproton annihilation can arise in two ways: (1) antiprotons annihilate on the residual gas. Since the pressure of the residual gas within the atom trap is at a considerably low level better than 10^{-12} mbar, the likelihood of this annihilation mode is small. (2) antiprotons annihilate on the gold electrodes of the trap wall. This annihilation process is more likely to occur, compared to interactions with the residual gas, and leads to the fragmentation of the gold atoms in the trap wall into lighter elements as well as several sub-atomic particles such as charged and neutral pions. The fragmented atoms are absorbed within the apparatus materials and incapable of exiting the apparatus and being detected by the SVD due to their high masses.

Charged pions have lifetimes on the order of 10^{-8} s, which is sufficiently long to allow these particles to survive the scattering through the material and be detected by the SVD. The neutral pions have a lifetime of 10^{-16} s and will promptly undergo a decay resulting in γ rays. The γ-ray photons, in turn, can be converted into e^+e^- pairs within the apparatus material. The distinct attribute of the annihilation signal is provided by the charged pions and the positron-electron pairs traversing radially outwards from the annihilation location.

Table 5.1: Tabulated data for branching ratios corresponding to pion final states for antiproton-proton [69] and antiproton-neutron [70] annihilations occurring at rest. The k represents multiple π^0 channels grouped together. An approximate 2% contribution due to kaons has not been included.

Antiproton-proton [69]		Antiproton-neutron [70]	
Pion final state	Branching ratio	Pion final state	Branching ratio
$2\pi^0$	0.00028	$\pi^-\pi^0$	0.0075
$3\pi^0$	0.0076	$\pi^- k\pi^0 (k > 1)$	0.169
$4\pi^0$	0.03	$\pi^+ 2\pi^-$	0.023
$\pi^+\pi^-$	0.032	$\pi^+ 2\pi^-\pi^0$	0.17
$\pi^+\pi^-\pi^0$	0.069	$\pi^+ 2\pi^- k\pi^0 (k > 1)$	0.397
$\pi^+\pi^- 2\pi^0$	0.093	$2\pi^+ 3\pi^-$	0.042
$\pi^+\pi^- 3\pi^0$	0.233	$2\pi^+ 3\pi^-\pi^0$	0.12
$\pi^+\pi^- 4\pi^0$	0.028	$2\pi^+ 3\pi^- k\pi^0 (k > 1)$	0.066
$2\pi^+ 2\pi^-$	0.069	$3\pi^+ 4\pi^- k\pi^0 (k > 1)$	0.0035
$2\pi^+ 2\pi^-\pi^0$	0.196		
$2\pi^+ 2\pi^- 2\pi^0$	0.166		
$2\pi^+ 2\pi^- 3\pi^0$	0.042		
$3\pi^+ 3\pi^-$	0.021		
$3\pi^+ 3\pi^-\pi^0$	0.019		

5.2 Theory of semiconductors

A semiconductor is essentially an insulator with a comparatively small band gap of approximately a few eV, allowing electrons in the valence band to acquire sufficient energy to reach the conducting band via thermal agitations and the subsequent creation of equal number of holes in the valence band. Under the influence of an electric field, the motion of both the electron and hole charge carriers establish a current. An intrinsic semiconductor has a small number of impurities compared to the number of thermally liberated electrons and holes.

5.2.1 Doped semiconductor

Intrinsic semiconductors are not typically used in the manufacturing of semiconductor devices due to the small number of charge carriers. Instead, impurities are introduced into the crystal structure to obtain additional advantageous electrical

properties in a process known as doping. The effect impurity atoms has on the density of charge carriers can result in either an increase in the number of electrons giving rise to an n-type semiconductor, or an increase in the number of holes producing a p-type semiconductor depending on the valency of the impurity. In the n-type semiconductor, the electrons and holes are known as the majority and minority charge carriers, respectively. Conversely, in the p-type semiconductors, holes act as the majority charge carriers and electrons as the minority.

The introduced impurities designate the type of dopant. For instance, for silicon belonging to the fourth valence group, phosphorus from the fifth valence group has one extra electron in the valence band and can donate it to the silicon lattice conduction band as a free electron. Boron, belonging to the third valence group and known as an acceptor, has one electron less than silicon and can therefore accept one electron from the valence band, dictating the creation of a hole in that band.

In addition to influencing the density of charge carriers, dopants alter the energy band structures of the semiconductor by the addition of further energy levels in the band gap. Donors energy level is close to the bottom of the conduction band while acceptors energy level is close to the top of the valence band.

5.2.2 *pn* junction

The simplest semiconductor device is a *pn* junction, also known as the diode, which is a prominent structure in semiconductor physics since its attributes plays a vital role in creating a wide variety of devices such as particle detectors. It is composed of a single crystal semiconductor doped to make a section of it p-type and the remainder n-type. The *pn* junction has the intriguing feature that it allows the conduction of current in only one direction.

Thermal equilibrium

When an n- and a p-type semiconductor are joined together, in the absence of an external applied potential (zero bias) an electron and a hole density gradient is

formed at the interface of the junction. As a result, by lowering their energy, the electrons of the n-type conduction band diffuse across the junction to fill the hole states in the p-type valence band. In a similar fashion, the holes of the p-type valence band tend to diffuse into the n side. The respective motion of these majority charge carriers, i.e. n-side electrons from the conduction band and p-side holes from the valence band, constitute a diffusion current, see Fig. 5.1. The recombination of the diffused charges on each side *'uncovers'* their ionized donor and acceptor impurities in a region in the vicinity of the junction and results in the formation of a space charge. The charge separation, in turn, produces an exceedingly high local electric field ($\sim 10^6$ V/m), or equivalently an internal potential difference (V_0). This contact potential prevents the diffusion current and leads to the establishment of a depleted region, known as the depletion zone in which virtually no conduction electrons or holes exit.

The formation of minor charge carries is as follows: the conduction band of the p-side contains a very small concentration of electrons that have been thermally agitated from the valence band. Similarly, the valence band of the n-side entails a very small concentration of holes that have been formed due to the thermal activation of electrons from this band to the conduction band. The internal built-in electric field in the depletion region promptly sweeps these minority charge carriers across the junction, creating a drift current. As illustrated in Fig. 5.1, a thermal equilibrium is achieved when the drift and diffusion currents are equal in magnitude, resulting in a zero net current across the junction.

Forward bias

Fig. 5.2(a) is a demonstration of a forward bias where an external potential (V_{ext}) is applied to the pn junction such that the positive terminal is connected to the p-type. The conduction electrons of the n-side and the positive holes on the p-side are driven towards the junction interface by the ElectroMotive Force (EMF) and subsequently recombine, giving rise to a continuous loss of charge carriers. However, the external voltage replenishes the supply of the lost carriers by firstly extracting the electrons

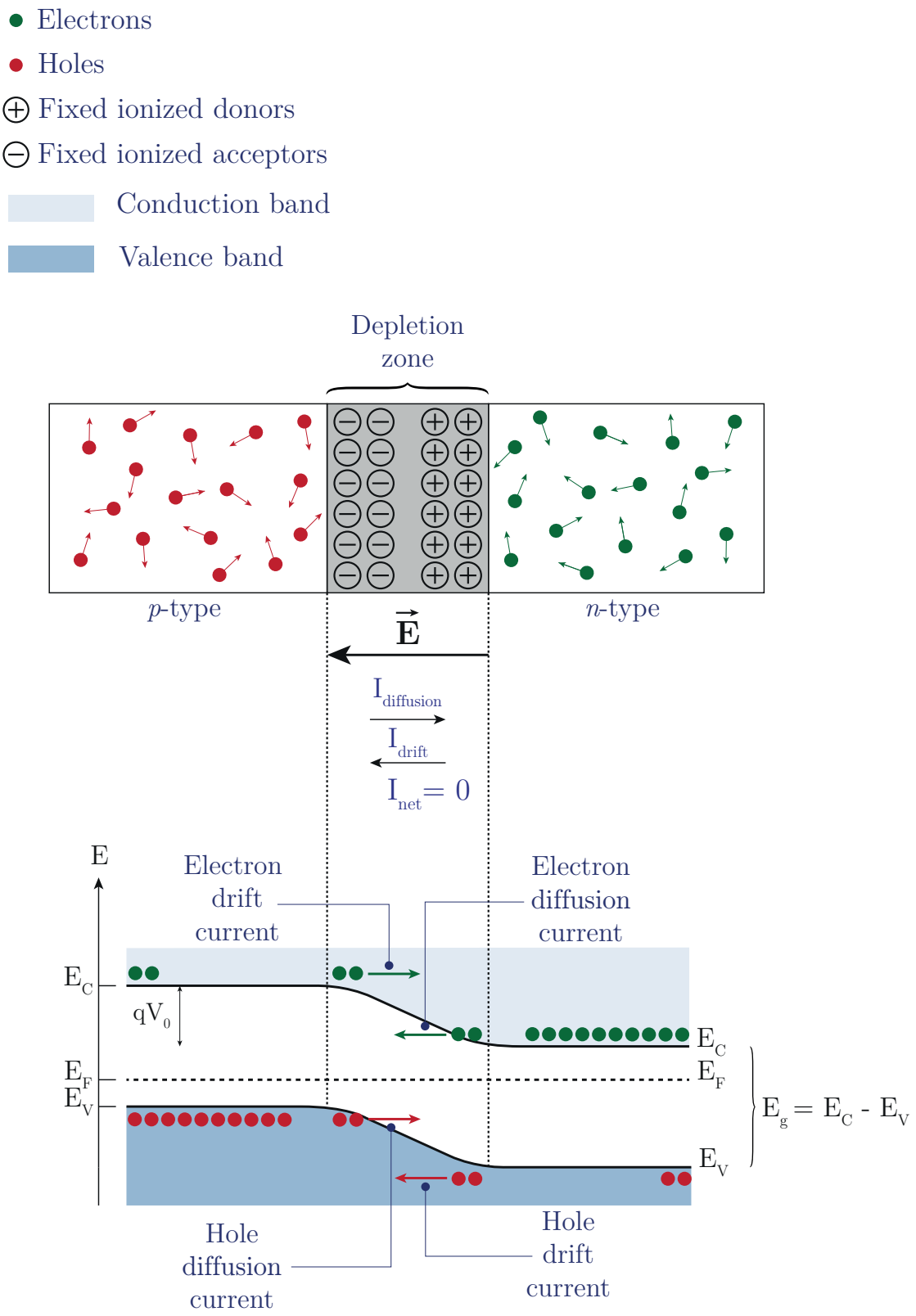

Figure 5.1: Diagram illustrating a *pn* junction in thermal equilibrium. An internal electric field created by the uncompensated acceptor and donor impurities prevents the motion of charge carriers in the depletion region. In the absence of an external EMF (zero bias), the diffusion current is balanced by the drift current across the *pn* junction resulting in a zero net current. The energy of the valence, conduction, Fermi and band gap levels are represented with E_V, E_C, E_F and E_g, respectively.

from the p-side, producing new holes, and secondly by the provision of extra electrons to the n-side. The creation of the new mobile charge carriers initiates a constant current. In terms of the band structure diagram, (lower part of Fig. 5.2(a)), the external applied potential increases the kinetic energies of both the n-side electrons in the conduction band and the holes in the valence band of the p-side, causing the rise of the energy levels of the n-side conduction band and the lowering of the p-side valence band energy levels. As a result, compared with Fig. 5.1, the majority charge carriers of the n- and p-sides encounter a lower energy barrier of magnitude $q(V_0 - V_{ext})$ and, accordingly, the diffusion current is increased. The minority charge carriers, on the other hand, is unaffected by the barrier and consequently the drift current remains unchanged and a net current dominated by a large diffusion current is established.

Reverse bias

A reverse bias is acquired when the positive terminal of an external voltage is connected the n-side of a pn junction. The width of the depletion zone is increased since electrons and holes are diverted away from the junction, see Fig. 5.2(b). The depletion zone width is given by [71]

$$w = \sqrt{\frac{2\epsilon_r \epsilon_0}{q}\left(\frac{1}{N_D} + \frac{1}{N_A}\right)(V_0 - V_{ext})}, \tag{5.2}$$

where ϵ_r is the relative permittivity of the medium (11.9 for silicon), ϵ_0 is the vacuum permittivity, N_A and N_D are the acceptor and donor impurities concentrations, respectively, and V_{ext} is the applied reverse bias voltage. For instance, an applied bias of $V_{ext} = 65$ V with dopant densities of $N_A = N_D = 10^{13}$ cm^{-1} leads to a depletion width of $w \simeq 300$ μm.

As the size of the depletion region increases, so does the internal electric field associated with the fixed donor and acceptor impurities. The internal electric field eventually cancels out the external applied field and the current nearly ceases. With regards to the band structure of the junction, the external potential of the reverse

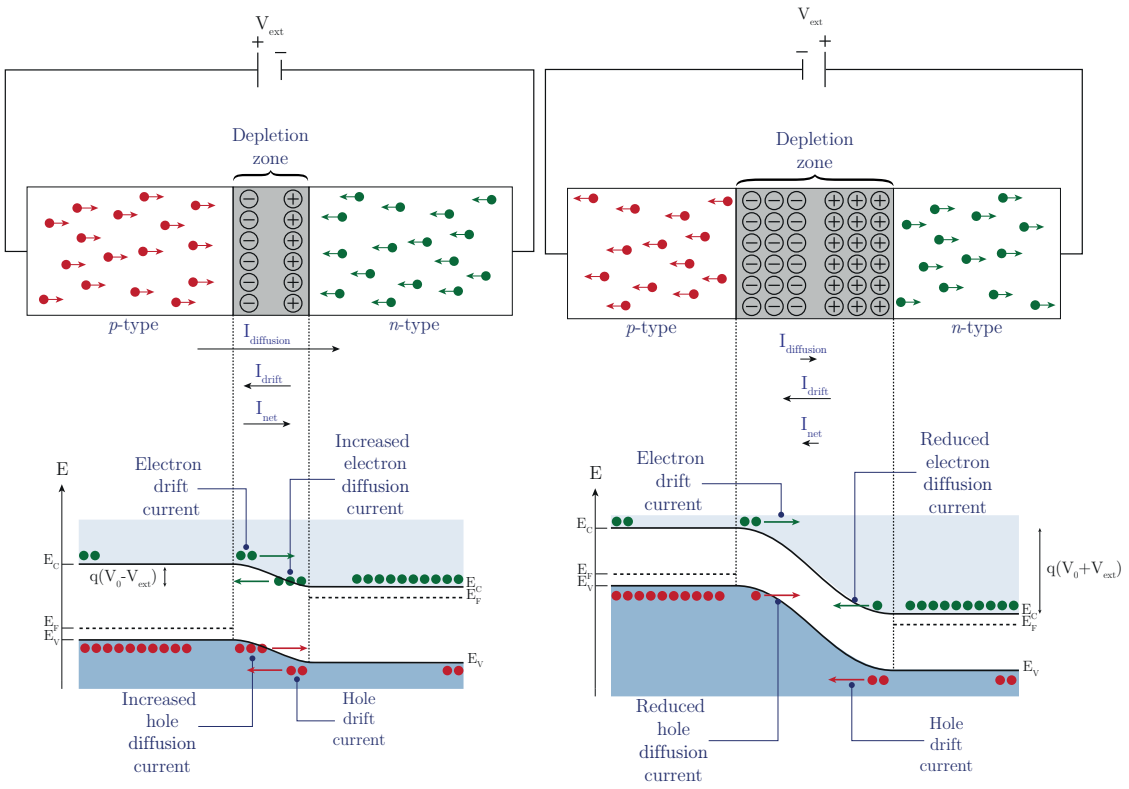

(a) Forward bias (b) Reverse bias

Figure 5.2: (a) The recombination of the holes and electrons at the junction plane resulting from the electric force of the external EMF on these carriers. A constant net current dominated by a significant diffusion current is established by the continuous replenishment of the supply of the holes on the p-side and the electrons on the n-side. (b) Reverse bias showing the diversion of the carriers away from the junction, the subsequent increase of the depletion zone width and the virtual cease of diffusion current. Only the very small drift current contributes to the net current.

bias raises the height of the barrier to $q(V_0 + V_{ext})$, greatly reducing the diffusion current since the carriers must overcome an escalated activation barrier. Similar to the forward bias, the motion of the minority charge carries is independent of the barrier height and the net current across the pn junction is now only dominated by the drift current due to the minority carriers, see Fig. 5.2(b) [72].

5.3 Diode as a charged particle detector

Upon interacting with matter, a charged particle tends to lose its kinetic energy via ionization or excitation of bound electrons. Moreover, the prime loss of energy occurs by the electromagnetic interaction of the charged particle with the electrons

of the material. The average energy loss per unit distance $\langle \frac{dE}{dx} \rangle$ (also known as stopping power) results from ionization of a charged particle traversing the bulk of a material and is described by the Bethe-Bloch formula [73]

$$-\left\langle \frac{dE}{dx} \right\rangle = Kz^2 \frac{Z}{A} \frac{1}{\beta^2} \left[\frac{1}{2} \ln \frac{2m_e c^2 \beta^2 \gamma^2 W_{max}}{I^2} - \beta^2 - \frac{\delta(\beta\gamma)}{2} \right], \tag{5.3}$$

where

K	$4\pi N_A {r_e}^2 m_e c^2 = 0.307075$ MeV cm^2,
r_e	the classical electron radius,
m_e	mass of the electron,
c	speed of light,
z	charge number of incident particles,
Z	atomic number of absorber,
A	atomic mass of absorber,
β	velocity of the traversing particle in units of the speed of light,
γ	Lorentz factor,
W_{max}	maximum kinetic energy which can be transferred to an electron by a charged particle,
I	mean excitation energy,
δ	density-effect correction,

The shape of the curve produced by Eq. 5.3 is illustrated in figure 5.3. It shows the mass stopping power, which is the stopping power per unit density. Details of all the regions and contributions to this curve can be found in [73]. The Minimum Ionising Particle (MIP) is the status attributed to the particle with a $\langle \frac{dE}{dx} \rangle$ close to the minimum of the the Bethe-Bloch formula. The number of electron-holes generated by the passage of a MIP through silicon depends on the average energy required to create an electron-hole pair. For silicon, this energy is 3.6 eV and leads to production of 80 electron-hole pairs per μm [74].

A *pn* junction is immensely appealing as a particle detector since the established

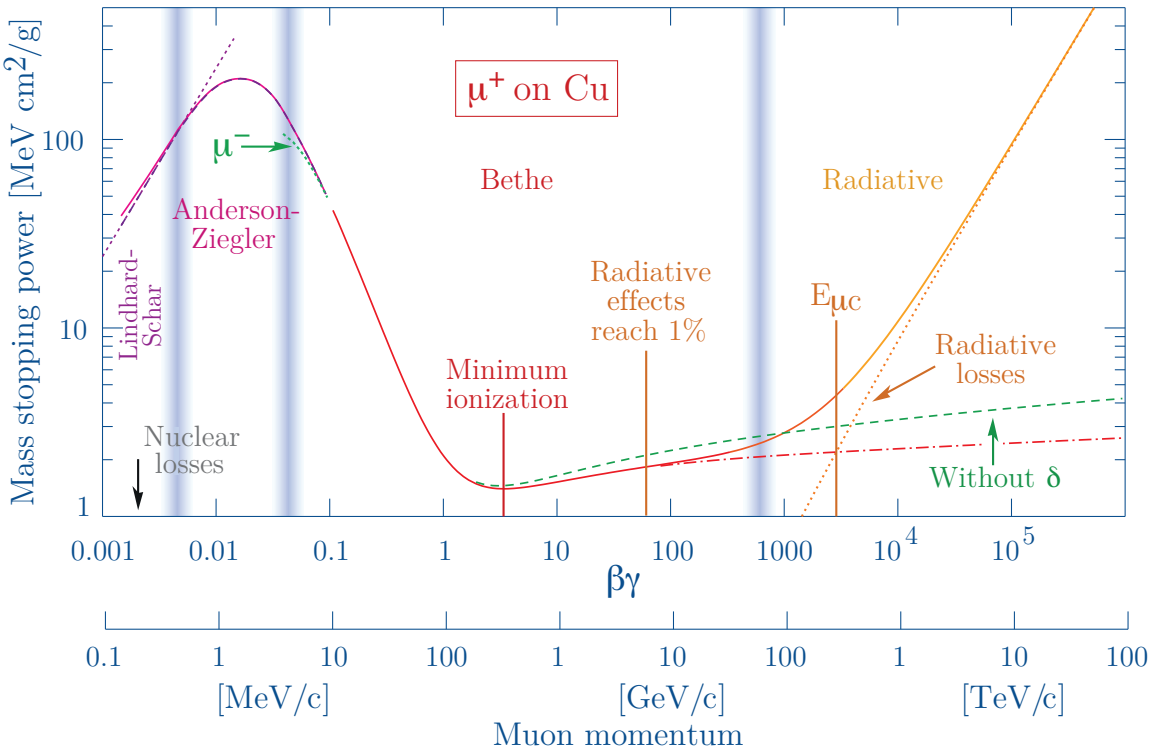

Figure 5.3: The mass stopping power of muons in copper as a function of $\beta\gamma$. The solid curve represents the energy loss with all effects added, while the dashed and dotted ones represent the individual contributions. Image adapted from [73].

electric field in the depletion region of a reversed bias diode can be utilized to collect generated free carriers arising from processes such as ionization by charged particles and thermal agitations that produce a leakage current. In all these processes, an electron-hole pair is created by the liberation of an electron from the valence band to the conduction band. The basic principle of a silicon particle detector is depicted in Fig. 5.4. The silicon bulk is depleted of mobile charge carriers by the reverse bias electric field. Charged particles with sufficient energy traversing the depletion region liberate electrons from the valence band to the conduction band creating electron-hole pairs. The holes and electrons are guided towards the collecting electrodes by the electric field where the collected charge is converted into an electric signal by means of signal amplifying electronics. The signal is subsequently read out and sent to a chip capable of processing and interpreting it. In the ALPHA detector, the chips are manufactured on 300 μm n-type bulk silicon with p-type implants [75].

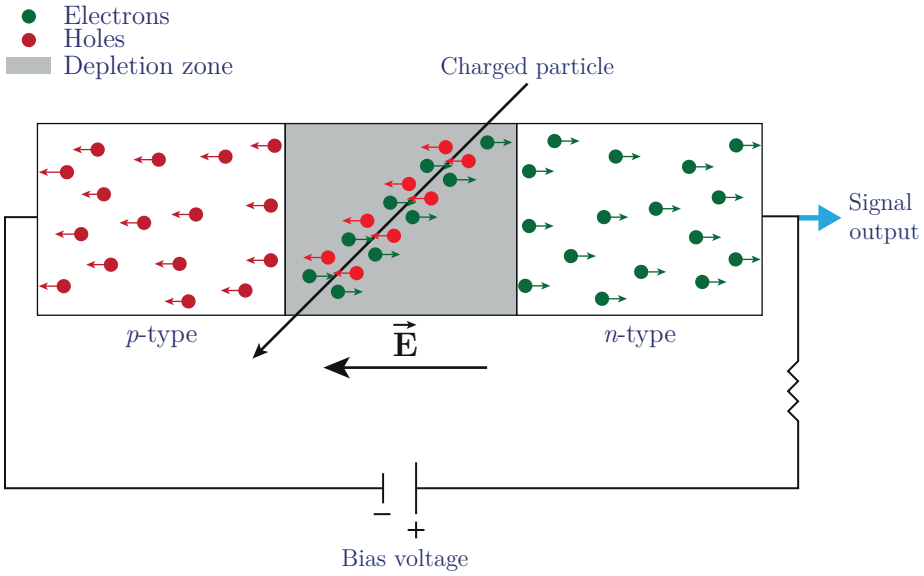

Figure 5.4: Schematic diagram illustrating a basic silicon particle detector where the reverse-biased junction along with a charged particle traversing the depletion region producing electron-hole pairs are highlighted. Approximately 8000 electron-hole pairs are generated per 100 μm in silicon.

5.3.1 Position-sensitive silicon detectors

The passage of a charged particle through silicon can be traced by an array of strips that register the electric signal. By placing the collection electrodes on opposite sides of the applied bias, both generated electrons and holes can be collected. In addition, arranging the strips of the collection electrode in orthogonal directions allows the localization of the position of the charged particle in two dimensions. The detector geometry and its position relative to the centre of atom trap can be incorporated to infer the third dimension.

A double-sided microstrip detector is composed of n-type bulk silicon with one side of the wafer being designated with p-type strips ('p-side') and the opposite side being integrated with orthogonal AC-coupled strips ('n-side'), resulting in creation of the pn junction at the intersection of the p-side strips and the n-type bulk. The generated signal from n-side strips are separated from the DC bias on the silicon backplane by an external AC-coupling, allowing signals arising from electrons and holes to be collected simultaneously on both sides of the sensor [31].

5.4 The SVD design specification

The prime objective of the ALPHA silicon vertex detector is the detection and determination of the position of antiproton annihilations within the apparatus. The SVD is capable of identifying untrapped antihydrogen atoms and the rejection of background events. Furthermore, it has been utilized as a diagnostic tool for investigating plasma and atomic procedures within the ALPHA apparatus [76].

The SVD is located around the central atom trap and the following main constituents have been incorporated within the atom trap:

- A Penning-Malmberg trap generating an axial electric field and a transversal magnetic field to capture, cool and manipulate the charged plasmas.
- An ultra high vacuum minimizing the annihilation of the antiparticles with the residual gas.
- An Ioffe-Pritchard magnetic trap creating a magnetic field with a minimum at the centre and designed to trap antihydrogen atoms formed by the mixing of positron and antiproton plasmas. The magnetic field required to maintain the anti-atoms are established by cryogenically cooled superconducting magnets.

Figures 2.15(b) and 2.23(a) depict the SVD and the prime components residing between the atom trap and the SVD. The amount of material present implies that annihilation products must traverse several layers of material prior to their first encounter with the detector. To compensate for these space constraints, the ALPHA-I silicon detector was positioned coaxially around the neutral-atom trap and composed of two halves, each half containing 30 double-sided silicon microstrip detector modules, also known as hybrids due to having two silicon sensors (wafers) as illustrated in Fig. 5.6. In total, 60 modules were arranged in three concentric layers with the inner, middle and outer layers consisting of 8, 10 and 12 hybrids, respectively, where only the outer layer was staggered into two different radii. This

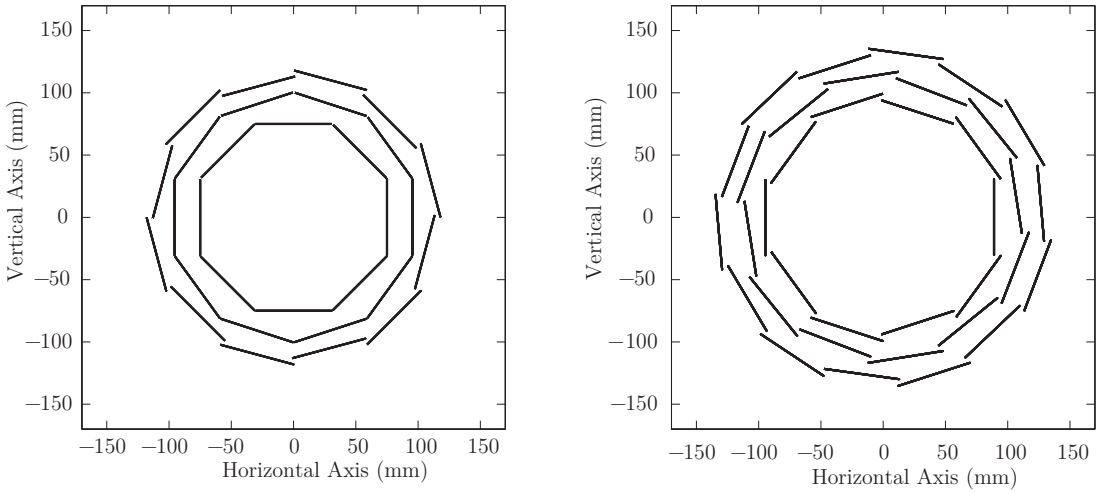

Figure 5.5: Schematic illustration of the positions of hybrids in the ALPHA-I detector (left), comprising of a total of 60 modules, and the ALPHA-II detector (right), consisting of 72 modules. Table 5.2 is a summary of the radial distances of these modules. Image adapted from [77].

Table 5.2: Tabulated data of the radial distances of the SVD layers for the ALPHA-I and the upgraded ALPHA-II designs.

Layer	**ALPHA-I(mm)**	**ALPHA-II(mm)**
Inner	75	89
		94.5
Middle	95.5	108
		113.5
Outer	108	114
	127	132.5

particular configuration of the ALPHA-I detector provided a large solid angle coverage around the atom trap, amounting to covering a solid angle of approximately 90% of the 4π steradians.

Due to the new spatial requirements of the ALPHA-II apparatus, such as the increase in the inner diameter of bore of the external solenoid and the outer diameter of the beam pipe, the SVD was upgraded and the total number of hybrids was increased to 72. In addition, each layer is staggered with inner, middle and outer layers now accommodating 10, 12 and 14 hybrids, respectively, providing further enhancement of the solid angle coverage. Fig. 5.5 and Table 5.2 represent the positions and the radial distances of the ALPHA-I and ALPHA-II detector hybrids.

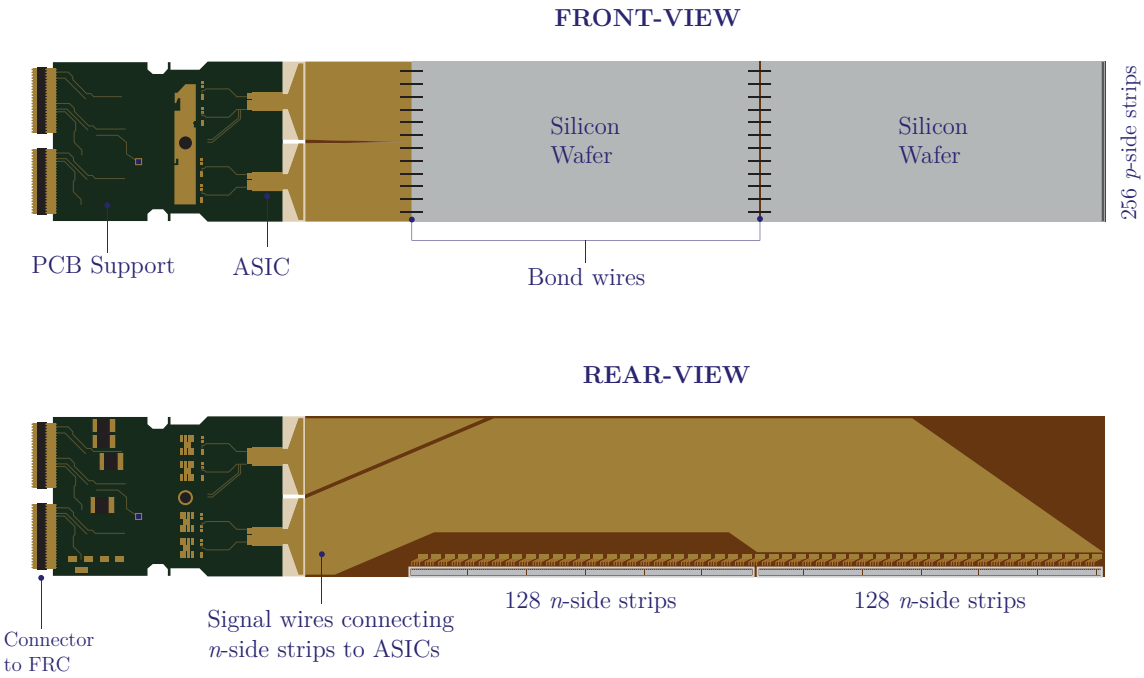

Figure 5.6: Schematic diagram representing a SVD module. The top represents the front view where bond wires, designated as the path of the p-strips signal, connect the silicon sensors to the Application Specific Integrated Circuits (ASICs). The rear view is shown in the bottom where the connection of n-strips to the ASICs is depicted. The silicon wafers, Printed Circuit Board (PCB) and read-out chips are highlighted.

5.4.1 The SVD modules

Fig. 5.6 is a schematic diagram showing a SVD module (hybrid) accommodating four VA1TA Application Specific Integrated Circuits (ASICs) [78], two silicon wafers along with the read-out chips and the corresponding read-out electronics all mounted on a Printed Circuit Board (PCB) support structure. Each silicon wafer (sensor) is a double-sided microstrip detector with the n- and p-strips consisting of $p+$ and $n+$ implants on the two sides of the silicon n-bulk. The n- and p-strips run orthogonal and parallel to the length of the hybrid, respectively. Each sensor contains 128 n-strips and 256 p-strips and covers an area of 5.8 $\times$ 11.2 cm^2. Therefore, with two wafers per hybrid, a single hybrid possesses an active silicon area of 5.8 cm $\times$ 22.4 cm = 129.9 cm^2.

Charges due to the drift of electrons to the n^+ doped strips are collected and subsequently, using an external 1nF capacitor, induced by AC coupling to the charge

Table 5.3: Summary of the measured values of the sensor parameters.

Sensor Parameters	
Physical size	61 × 115 mm
Active area	58.1 × 112.0 mm
Typical bias resistor value	7–15 MΩ
Depletion voltage	40–50 V

Measured Parameters	***p*-side**	***n*-side**
Strip length	112 mm	58 mm
Strip pitch	227 μm	875 μm
Interstrip spacing	50 μm	10 μm
Typical strip leakage current	6 nA	12 nA
Number of strips	256	128

preamplifier of the ASIC. On contrary, the p^+ doped strips are DC coupled to the ASIC's charge preamplifiers.

The 512 strip enumeration corresponds to $ASIC_1$ (n-side strips 1-128), $ASIC_2$ ($n-$side strips 129-256), $ASIC_3$ (p-side strips 257-384) and $ASIC_4$ (p-side strips 385-512). The 256 n-side signal strips of a module are read out by the chips of ASICs 1 and 2 whereas ASICs 3 and 4 are responsible for reading the 256 p-side signal strips, amounting to a total of 512 signal strips (channels) per hybrid. The ALPHA-II SVD has 72 hybrids yielding $72 \times 512 = 36{,}864$ channels. Table 5.3 provides a summary of the sensor parameters and the representative measured values.

Combining the p- and n-side signal information allows one to localize the position of a charged particle traversing the silicon in the plane of the hybrid. Furthermore, the hit positions can be determined in the global reference of the apparatus by incorporating information regarding the 3-D orientation and position of the hybrid.

5.4.2 VA1TA ASIC read-out chips

Each ASIC, a VA1TA read-out chip composed of 128 channels, is responsible for controlling both the trigger signalling and the strip read-out. Each channel consists of two parts: the 'VA' part managing the analogue strip signals and the 'TA' part handling the digital triggers. Fig. 5.7 is the schematic diagram of a single channel of

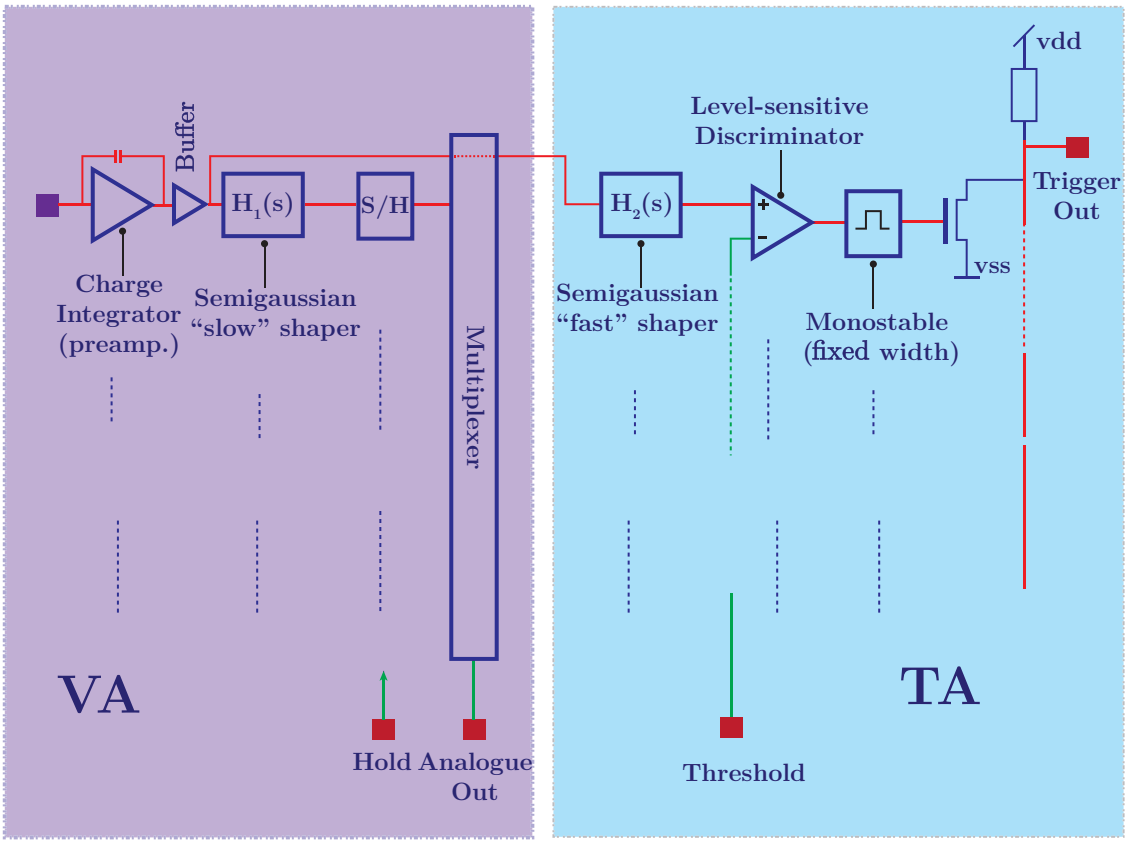

Figure 5.7: Schematic diagram of a channel of the VA1TA chip.

a VA1TA chip demonstrating the interplay between the VA and TA parts and reveals that the channel comprises a preamplifier, slow shaper, fast shaper, discriminator, and monostable circuit. The preamplifier is shared between the VA and TA parts. Subsequently, the VA circuit incorporates a slow ($\sim 1\mu$s) shaper, whereas the TA circuit features a fast (75 ns) shaper. A discriminator threshold is set such that a fast shaper with a pulse height, the amount of charge collected in a silicon strip, exceeding the threshold will be converted to a fixed width (10 ns) trigger pulse by a monostable multivibrator. The 128 digital signals from the TA part of the ASIC are logically processed in coincidence (i.e. logical OR) and therefore only one TA trigger signal will be outputted by an ASIC [31].

Likewise, of all the 128 VA analogue signal strips of each ASIC, only one will be outputted. This is accomplished by multiplexing and the serial read-out of the VA analogue pulse heights, a method – known as 'sample and hold' – where each analogue signal is kept at the shaping peak prior to its multiplexing.

5.4.3 Data acquisition (DAQ) system

Fig. 5.8 is a simplified schematic diagram of the ALPHA-II SVD read-out electronics. The trigger signals of all the 288 ASIC read-out chips arriving from each layer of the detector are delivered to two Timing and Trigger Control (TTC) units, special-purpose VME modules functioning based on Field Programmable Gate Array (FPGA). Being programmed with information regarding the hybrid layering, the TTCs perform two functions on the TA trigger signals. The TTC directs the detector read-out chain by grouping the received trigger signals in accordance with the layers and the half-detector part where they originate. They also compute the signal multiplicity, i.e. determining the number of trigger signals arriving in coincidence. The signals from the silicon p-side pass the shortest distance possible to the charge amplifiers which is reflected in the noise performance of this side. As a result, the trigger decisioning is accomplished by using only the p-side trigger signals due to the superior noise performance.

The communication between the TTCs and the SVD hybrids is provided by Front-end Repeater Cards (FRCs). A total of 20 FRCs, external to the apparatus, provide power to the ASIC chips and are connected to the hybrids by means of two ribbon cables; one cable for the analogue strip read-out signal and one for the digital trigger signal. A single FRC can communicate with four hybrids.

Subsequent to amplification via the FRCs, the 288 VA analogue signals are fed into eight VF48 digitizers, each having a 10-bit Analogue-to-Digital Converter (ADC) Versa Module Europa (VME) module with 48 channels. The sampling clock is provided to the VF48s by the TTCs. In addition, via the FRCs, the TTCs provide the multiplexer clock to the ASICs.

ALPHA-II currently employs a '2-1-1' trigger configuration where each number represents the minimum number of triggers registered on the inner, middle and outer layers, respectively. This trigger configuration is aimed at registering as many events as possible, and therefore a very loose trigger, while dismissing most triggers induc-

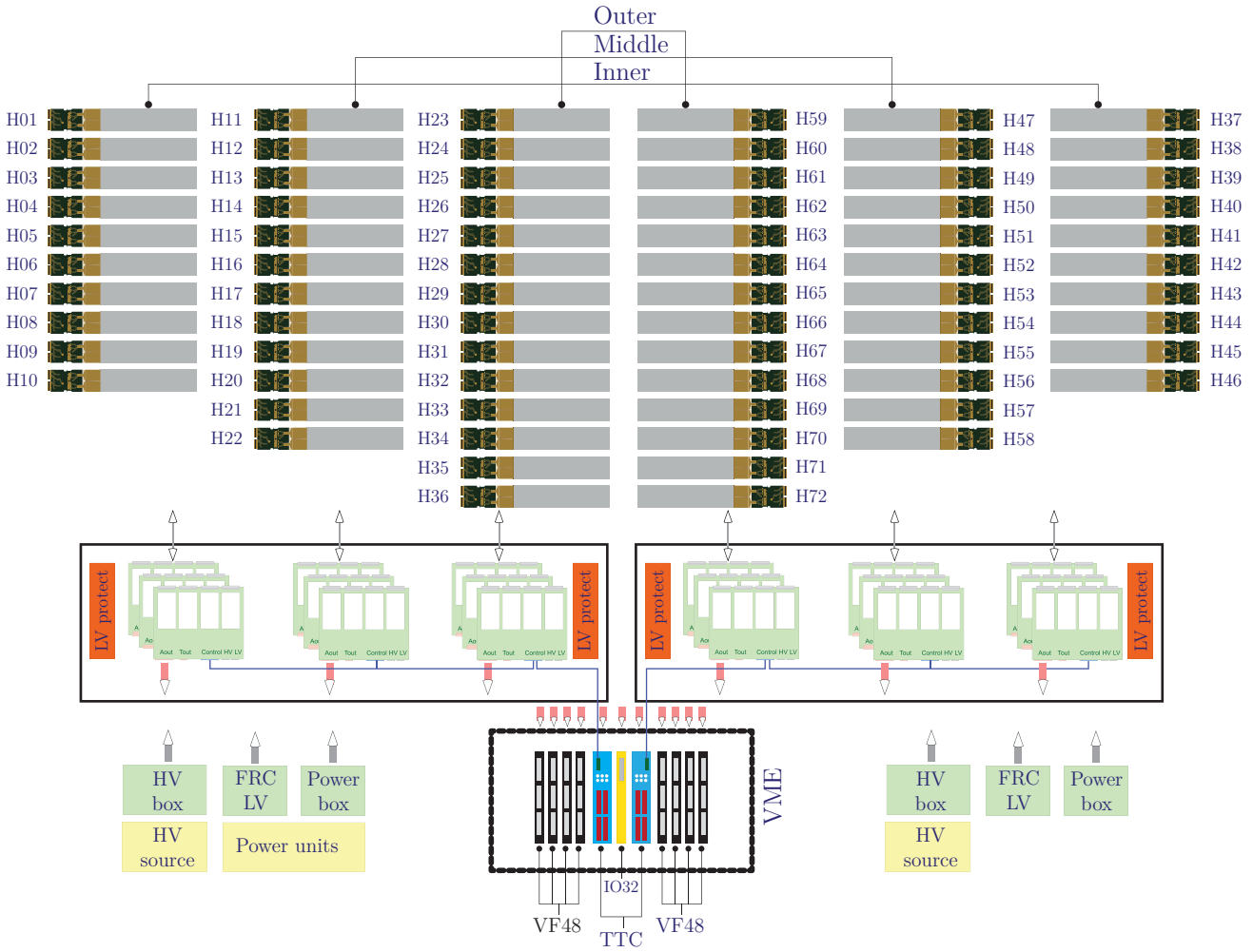

Figure 5.8: Schematic diagram of the ALPHA SVD read-out electronics. Low and High Voltages (LV and HV) are provided through Front-end Repeater Cards (FRC) and separate power cards (not drawn) to ASICs and silicon sensors. All signals between Versa Module Europa (VME) crate and the detector are fed through the FRCs. The VME crate contains Timing and Trigger Control (TTC) and IO32 units, eight VF48s and a VME controller. Detector HV, LV, temperatures and humidity are monitored and several trip systems are incorporated to avoid any damage to the sensitive SVD in case of anomalous events.

ed by noise. A peak rate of $\sim$ 30 kHz is regularly attained by the '2-1-1' trigger during the positron-antiproton mixing phase.

For rates less than $\sim$ 250 Hz, the '2-1-1' trigger is able to infer the presence of a desirable event and the subsequent initiation of the triggering of the full detector read-out follows. Nevertheless, for higher rates, the duration of the digitization of the analogue strip levels might exceed the time between successive triggerable events. Consequently, in order not to disturb a read-out in progress, the '2-1-1' multiplicity trigger is combined with a *'busy'* signal sent by the VF48s to the IO32, a VME FPGA board that receives both the multiplicity triggers from the TTCs and the busy signals from the VF48s as the inputs. The output is a decision made as to trigger the full read-out of the VA signals. If the VF48s are not in the process of reading out the analogue strip levels, a 'Not Busy' signal is initiated. The 'Not Busy' signal then provides the read-out trigger ('RO trigger') to be diverted back to the TTCs to handle the analogue read-out of the strips by sending the hold signals to the VA1TA chips. The maximum read-out rate obtained in the ALPHA-II detector is $\sim$ 500 Hz [31] [79]. A detailed description of the DAQ can be accessed from [31].

Chapter 6

Pedestal Analysis

Reconstructing a charged-particle track through the detector and subsequently determining the position (vertex) of an antiproton annihilation is dependent on how accurately the position information of a hit can be extracted from the analogue read-out of the silicon modules. This chapter describes the procedures undertaken in analysing the raw analogue data with the objective of characterizing the strip background noise (pedestal) by separating the signal from various noise sources. In addition, new pedestal approaches aimed at increasing the vertex reconstruction efficiency will be discussed. The complete algorithm for the Alternative Pedestal Analysis (APA) (see Appendix A) has been devised by the author and is completely independent of Standard Pedestal Analysis (SPA) currently implemented in the ALPHA experiment [31][80]. The results presented in this chapter can serve as a validation and enhancement of the Standard Pedestal Analysis.

6.1 Determining strip background

6.1.1 Noise & gain

The noise associated with strips of a module is acquired by calculating the variance of several output voltage measurements with no input signal. Fig. 6.1(a) illustrates a typical noise measurement for a particular hybrid. Similarly, the strips' gains

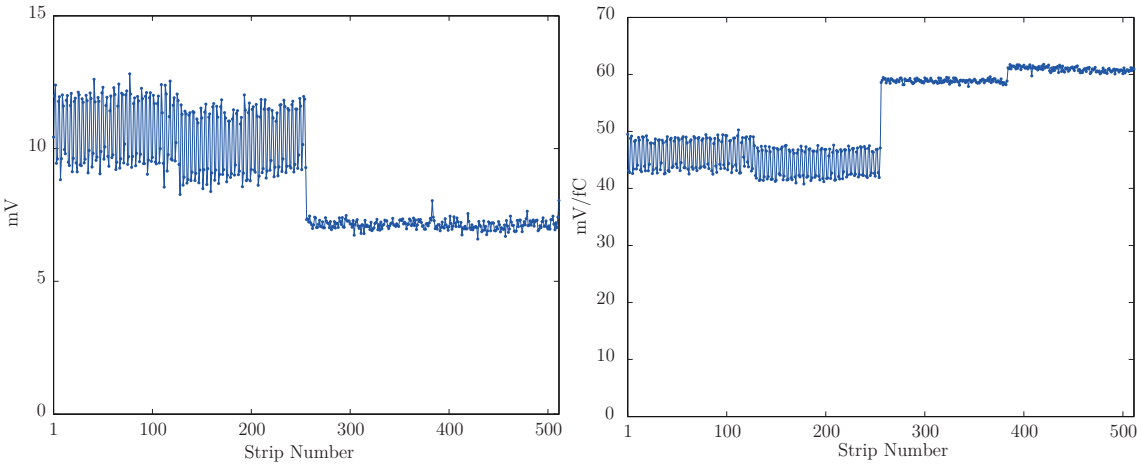

(a) (b)

Figure 6.1: Plots illustrating (a) noise measurements in millivolt and (b) gain measurements in milivolt per femto Coulomb obtained from each strip of a particular hybrid.

are obtained by feeding various test pulses of varying magnitudes into the detector and measuring the voltage outputs from pre-amplifiers. The gain of a silicon strip is subsequently determined by performing a fit to these set of measurements. The acquired gain values are utilized in the normalization of the strip signals during pedestal analysis in the experiment. Fig. 6.1(b) shows an example of a gain measurement for a particular hybrid.

Figures 6.1(a) and 6.1(b) demonstrate that n and p-side strips exhibit considerably different behavior in terms of noise and gain performance. Due to the greater distance travelled by the signals from the silicon n-side, the n-side strips (channels 1-256) are affected by greater noise than the p-side strips (channels 257-512). This noise pattern reflects the bond wire alignment maintained between the ASIC and its inputs. Copper tracks connecting the silicon strips to the capacitors at the rear of a hybrid contribute the most substantial amount of noise to the n-side strips as well as diminishing the gain on these strips.

6.1.2 Distinguishing between noise & signal

Fig. 6.2 shows a flowchart detailing the steps undertaken in determining the pedestal of a strip. Every time the detector read-out is triggered by a charged pion generated

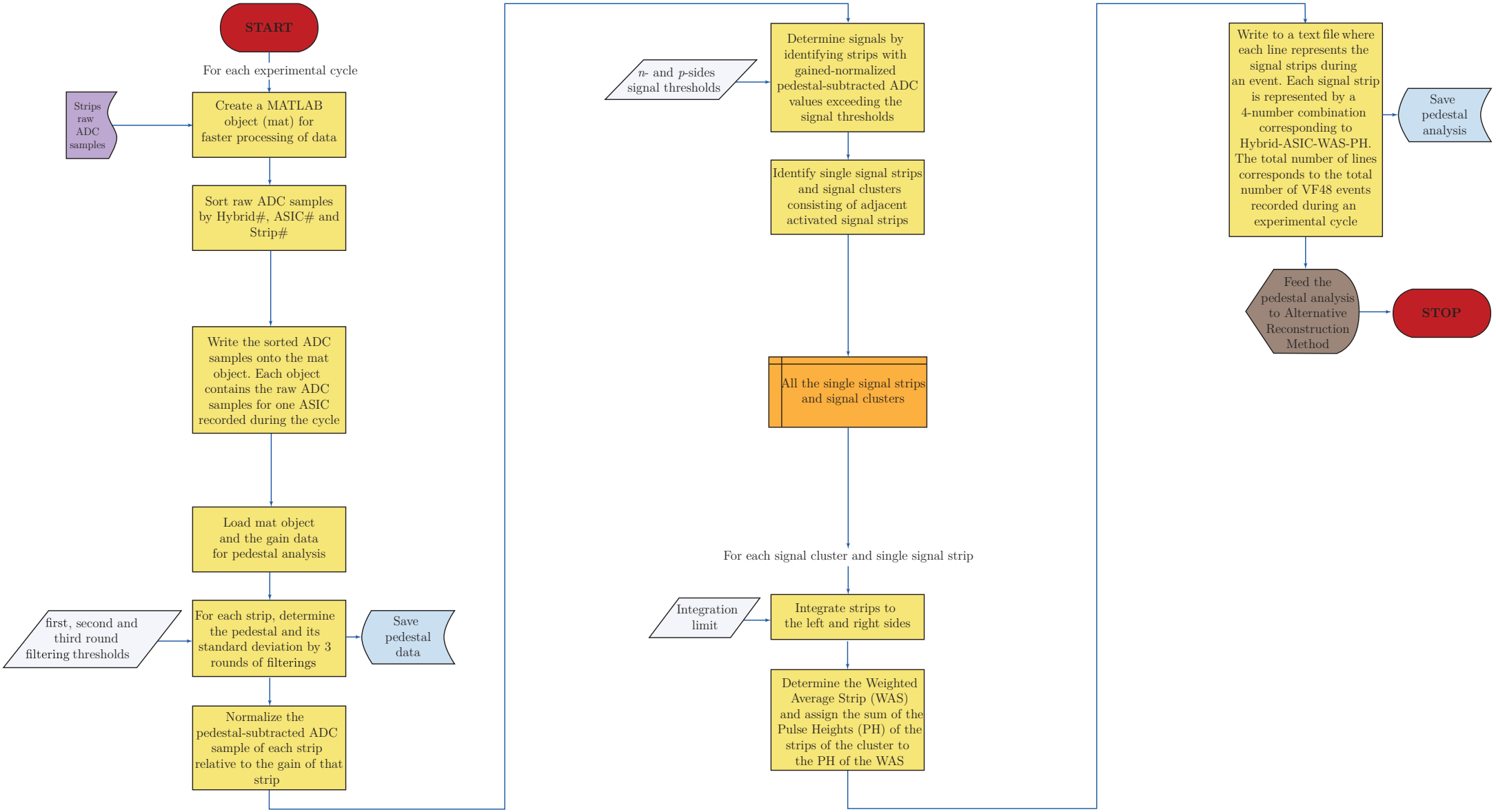

Figure 6.2: Flowchart showing the steps undertaken for pedestal analysis of a strip.

by the annihilation of an antiproton with a proton in the gold nucleus of the atom trap wall, charge is accumulated and an analogue read-out is outputted. This analogue voltage is digitized and an Analogue-to-Digital Converter (ADC) sample is generated for each strip. Each ASIC is responsible for reading 128 strips and therefore each detector read-out outputs 288 sets (72 modules $\times$ 4 ASICs per module) of 128 ADC samples. The ADC sample contains both the signal due to the passage of the charged pions and various noises arising from the leakage current of the silicon, long cables and a noisy environment. The background noise can be represented by an approximate Gaussian function. The determination of strips that accumulate charge due to pion interactions depends on the ability to characterize and remove background noise (pedestal). A pedestal analysis MATLAB script has been devised in order to perform the characterization of the strip background and is included in Appendix A.

A mixing experimental cycle occurs when the positron and antiproton plasmas are mixed and very energetic, 'hot', antihydrogen atoms are produced. The hot antihydrogen atoms are untrappable and undergo annihilations on either the residual gas or the trap wall. Approximately 5,000 detector read-outs (triggers) are recorded during every mixing experimental cycle and each ASIC is read out during each trigger. As a result, there are 5,000 ADC samples generated for each individual strip during one mixing experimental cycle. However, only a small number of strips contain the signal. Fig. 6.3 illustrates raw ADC samples of an n-side and a p-side ASIC for a particular detector read-out. Set by the finite dynamic range of the VF48 digitizers, the ADC samples stored from the VF48s are digitized as 10-bit integers. Therefore, pulse heights have a maximum and minimum ADC values of 1024 and 0, respectively. The signal threshold calculation, the correction of any systematic DC offsets and the determination of the noise width are all obtained from these ADC samples.

The following steps outline the procedures undertaken in order to determine the pedestal of a strip:

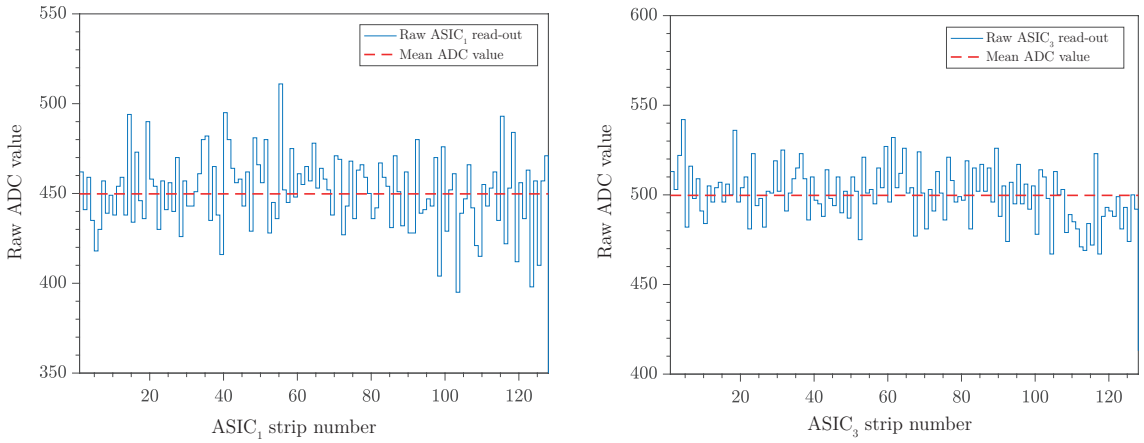

(a) n-side (b) p-side

Figure 6.3: Strips raw ADC samples (blue trace) as well mean ADC value of the entire ASIC (dashed red line) for an (a) n-side ASIC, and a (b) p-side ASIC. The vertical axes units are measured in Analog-to-Digital Units (ADU).

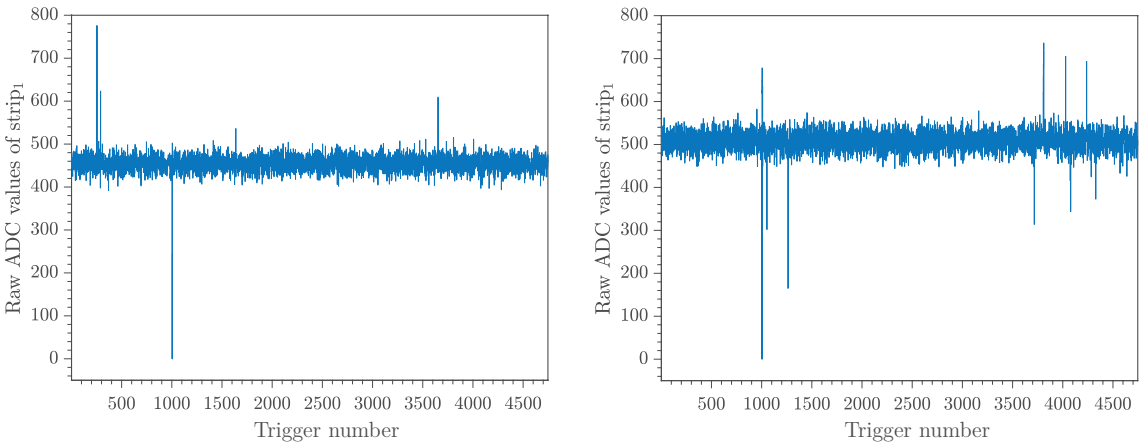

(a) $ASIC_1$ (b) $ASIC_3$

Figure 6.4: Raw ADC values for a particular strip (strip number one) of (a) $ASIC_1$ and (b) $ASIC_3$, acquired from a mixing experimental cycle during which 4747 triggers/read-outs have been recored by the detector.

1. For a particular strip, the raw ADC samples recorded during an experimental cycle are obtained. Fig. 6.4 is a demonstration of the raw ADC samples of a strip for an n-side ASIC ($ASIC_1$) as well as a p-side ASIC ($ASIC_3$).

2. A first run-through of all the read-outs/triggers ($N_{trigger}$) is performed, see Fig. 6.5(a). For a strip, the average ADC value, $\overline{\mathrm{ADC}}_{\mathrm{strip}} \equiv \mathrm{p}_0$, and the standard deviation, $\sigma_{\mathrm{strip}} \equiv \sigma_0$, are calculated as

$$\overline{\mathrm{ADC}}_{\mathrm{strip}} = \frac{1}{\mathrm{N}_{\mathrm{trigger}}} \sum_{t=1}^{\mathrm{N}_{\mathrm{trigger}}} \mathrm{ADC}_{\mathrm{strip},t}, \tag{6.1}$$

$$\sigma_{\mathrm{strip}} = \sqrt{\frac{1}{\mathrm{N}_{\mathrm{trigger}} - 1} \sum_{t=1}^{\mathrm{N}_{\mathrm{trigger}}} (\mathrm{ADC}_{\mathrm{strip},t} - \overline{\mathrm{ADC}}_{\mathrm{strip}})^2}, \tag{6.2}$$

where $N_{trigger}$, t and $\mathrm{ADC}_{\mathrm{strip},t}$ represent the total number of triggers recorded, the trigger number and the ADC value of the particular strip for the t th trigger, respectively.

Due to the absence of signals in a significant number of strips, Eqs. 6.1 and 6.2 are considered to be an estimate of the sample mean and the standard deviation of the pedestal.

3. A signal, induced by the charged particles generating their charges in the silicon strip, is defined as a strip having an ADC value greater than a defined threshold (σ) associated with the strip pedestal. The first run-through (sampling) determination of the pedestal contains the signal and this signal contamination is required to be removed to attain a more accurate estimate of the pedestal. For n-side strips, the signal is defined as an ADC value greater than $+\sigma$ and any ADC value smaller than $-\sigma$ is defined as a read-out anomaly, see Fig. 6.5(a). In contrast, for p-side strips, the signals are defined as ADC values smaller than $-\sigma$ and the read-out anomalies are defined as ADC values greater than $+\sigma$, see Fig. 6.6(a). A set of further filtering mechanisms are required to eliminate any signals from the pedestal determination.

   The first-time filtering involves discarding those samples possessing ADC values outside the $\mathrm{p}_0 \pm 3\sigma_0$, where $3\sigma_0$ is defined as the first-round filtering threshold. Fig. 6.5(b) shows the first-time filtering procedure. The second iteration of the remaining samples calculates new values of mean ADC and standard deviation which are defined as p_1 and σ_1, see Fig. 6.5(c). The second filtering uses a $2.5\sigma_1$ filtering threshold and entails removing samples having ADC val-

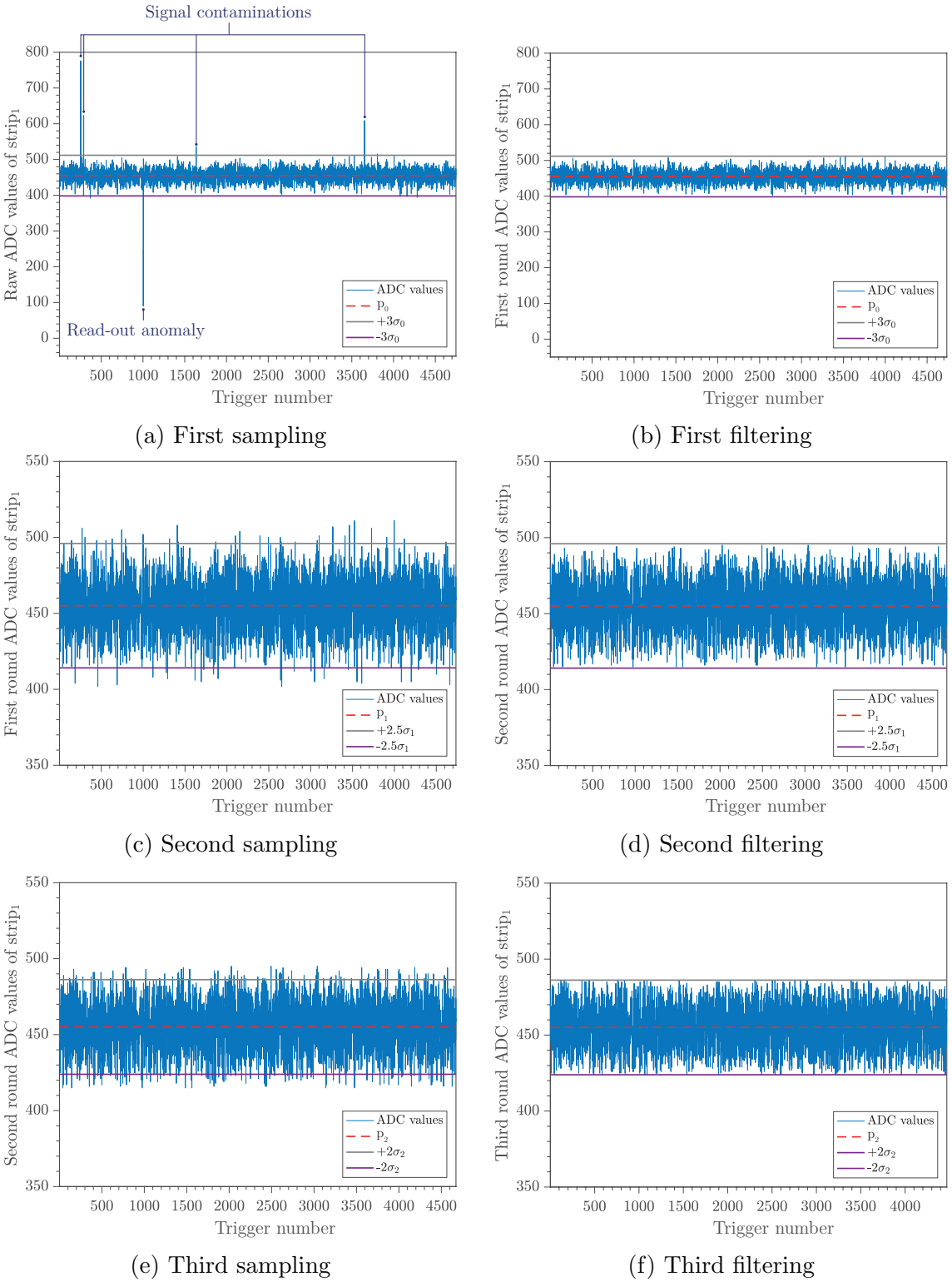

(a) First sampling

(b) First filtering

(c) Second sampling

(d) Second filtering

(e) Third sampling

(f) Third filtering

Figure 6.5: Steps in determining the pedestal of a particular strip of the n-side ASIC shown in Fig. 6.4(a). (a-b) Zeroth pedestal determination and removal of any samples with ADC values outside $p_0 \pm 3\sigma_0$, (c-d) First pedestal determination and removal of any samples with ADC values outside $p_1 \pm 2.5\sigma_1$, (e-f) Second pedestal determination and removal of any samples with ADC values outside $p_2 \pm 2\sigma_2$.

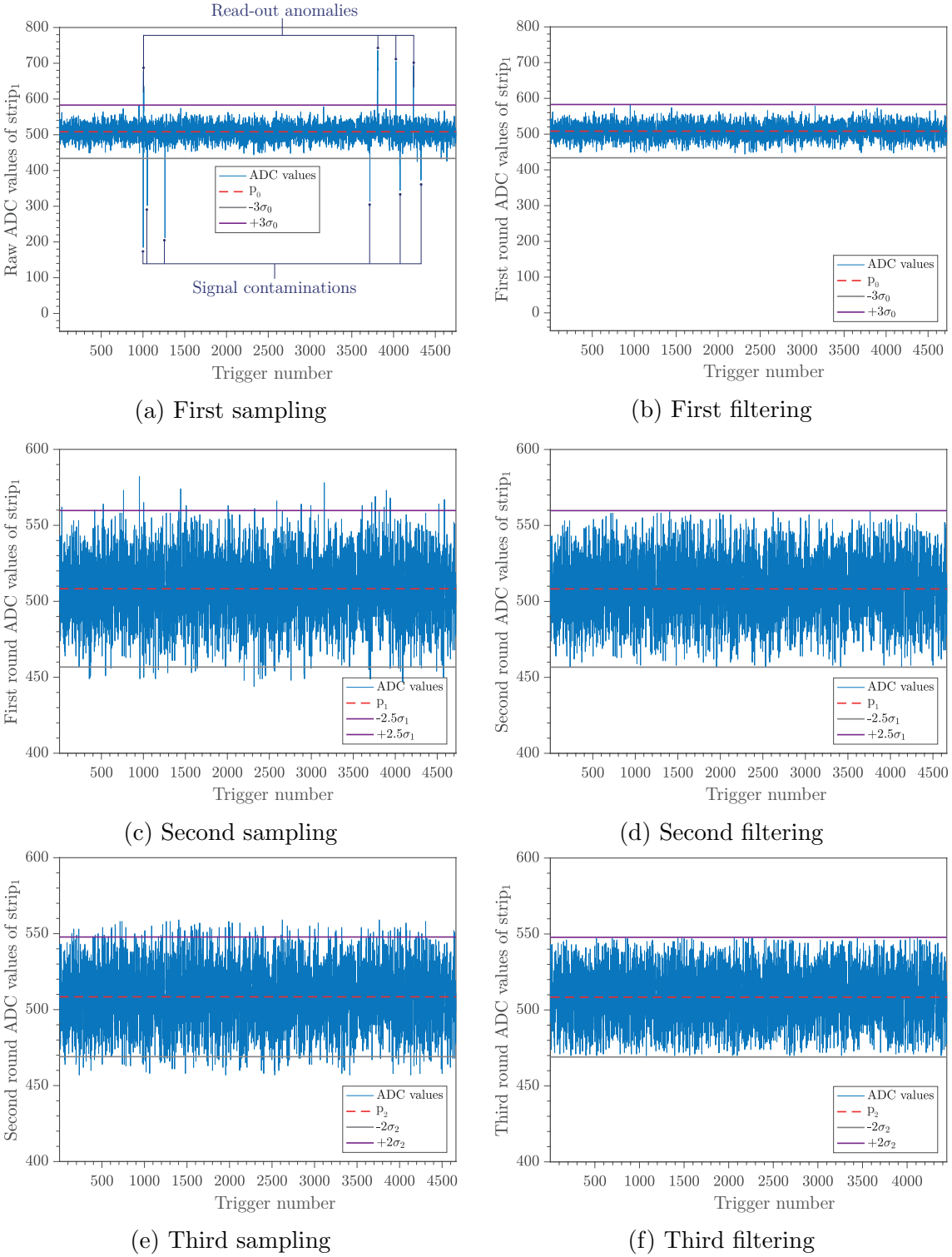

Figure 6.6: Steps in determining the pedestal of a particular strip of the p-side ASIC shown Fig. 6.4(b). (a-b) Zeroth pedestal determination and removal of any samples with ADC values outside $p_0 \pm 3\sigma_0$, (c-d) First pedestal determination and removal of any samples with ADC values outside $p_1 \pm 2.5\sigma_1$, (e-f) Second pedestal determination and removal of any samples with ADC values outside $p_2 \pm 2\sigma_2$.

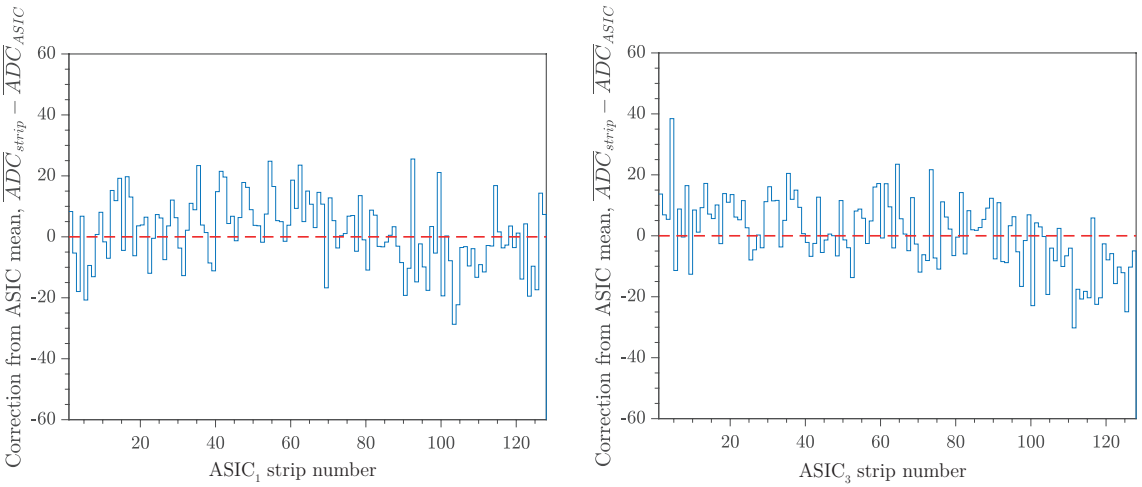

(a) n-side (b) p-side

Figure 6.7: Strip pedestal values, p_3, of the same read-out in Fig. 6.3, relative to the ASIC sample mean of an (a) n-side ASIC and a (b) p-side ASIC. The red dashed line is used to guide the eye.

ues outside $p_1 \pm 2.5\sigma_1$, see Fig. 6.5(d). The third sampling, Fig. 6.5(e), and filtering with a threshold of $2\sigma_2$, Fig. 6.5(f), result in acquiring the p_2 and σ_2 values as well as discarding samples with ADC values outside $p_2 \pm 2\sigma_2$. Subsequent to the third filtering, a final run-through of the remaining ADC samples yields p_3 and σ_3. These two values are considered as the strip pedestal and its standard deviation and are the basis for characterizing the behaviour of the strip baseline. The procedure of determining the pedestal of a p-side strip of ASIC$_3$ in Fig. 6.4(b) is demonstrated in Fig. 6.6 and follows the same method.

All the ADC samples undergo a DC offset caused by an alternation of the reference voltage. Accordingly, it is advantageous to express the strip pedestal, $\overline{\mathrm{ADC}}_{\mathrm{strip}} \equiv p_3$, with respect to the ASIC sample mean, $\overline{\mathrm{ADC}}_{\mathrm{ASIC}}$, which is determined by

$$\overline{\mathrm{ADC}}_{\mathrm{ASIC}} = \frac{1}{128} \sum_{\mathrm{strip}=1}^{128} \overline{\mathrm{ADC}}_{\mathrm{strip}}. \tag{6.3}$$

This provides the correction of the induced DC offset for every event. Fig. 6.7 depicts the relative strip pedestal values of a complete ASIC for both n and p-sides.

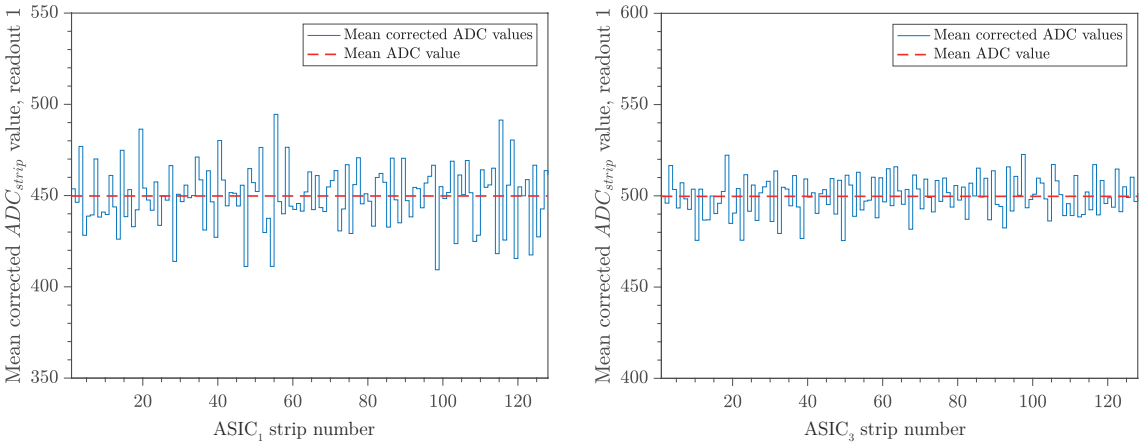

(a) n-side (b) p-side

Figure 6.8: Mean correction of the corresponding strip samples shown in Fig. 6.3 for an (a) n-side ASIC and a (b) p-side ASIC. Also included is the red dashed line representing the mean ADC value.

The correction from ASIC mean values of all the strips of a given ASIC is expected to be distributed within an order of magnitude from zero. However, Fig. 6.7 shows a greater variation of theses values for each strip, which can be corrected by subtracting the correction from ASIC mean values from the raw ADC values. Fig. 6.8 is the outcome of performing the strip mean correction on the corresponding raw strip ADC values of Fig. 6.3.

4. Finally, the ASIC sample mean of a particular trigger, t, is determined using

$$\overline{\mathrm{ADC}}_{\mathrm{ASIC},t} = 1/128 \sum_{\mathrm{strip}=1}^{128} \mathrm{ADC}_{\mathrm{strip},t} \tag{6.4}$$

In order to both normalize the sample mean to zero and compensate any shifting of the baseline of the ADC, each mean-corrected ADC value of Fig. 6.8 is subtracted from $\overline{\mathrm{ADC}}_{\mathrm{ASIC}}$.

The gained normalized pedestal subtraction is shown by blue traces in Fig. 6.9 for four ASICs of a particular event. For simplicity, the polarity of the p-side strips (ASICs 3 and 4) ADC values have been reversed. Therefore, for both the n- and p-side strips, any strip with subtracted ADC value exceeding a defined signal threshold of $+3.75\sigma_3$ (grey traces) is considered to be signal and is represented by red traces.

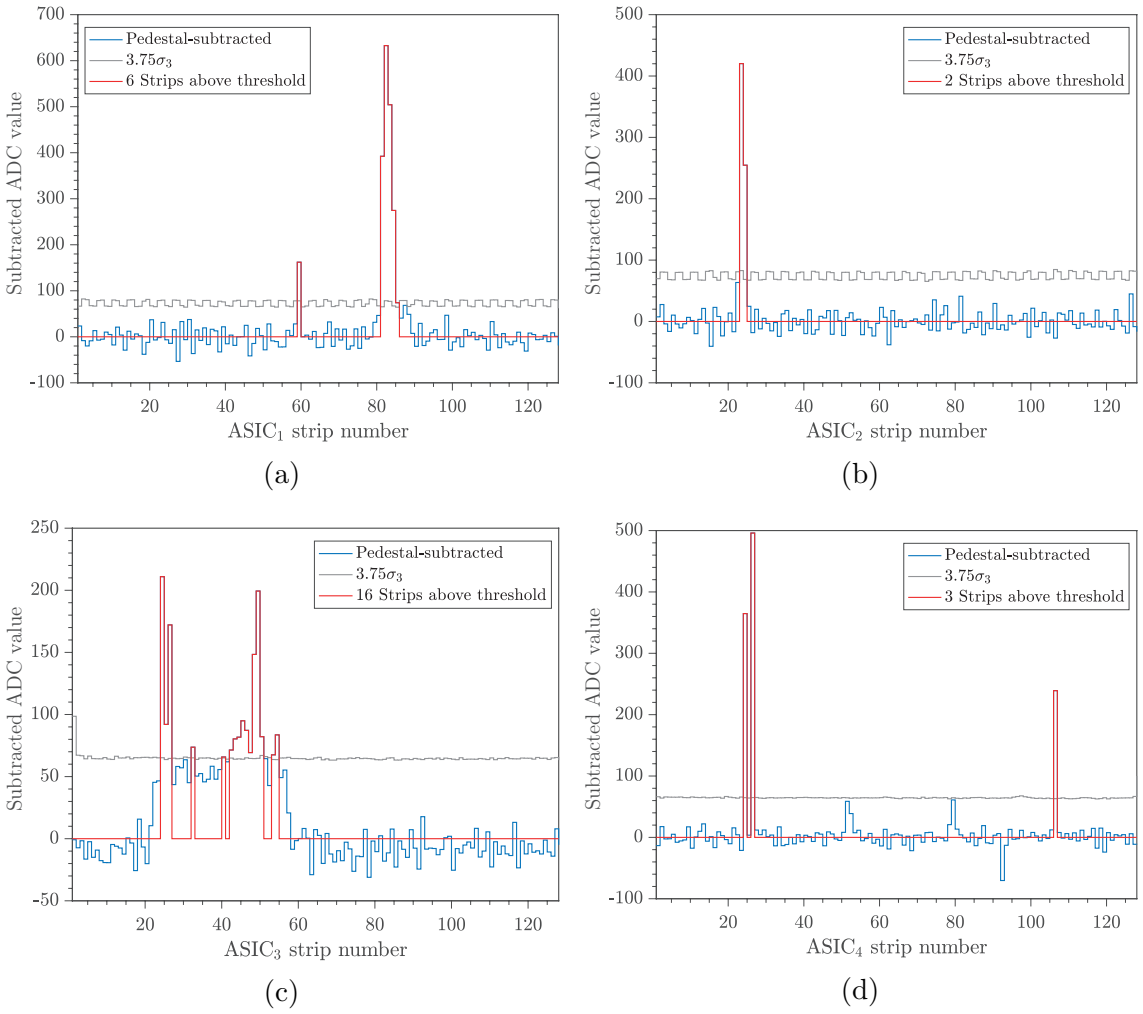

Figure 6.9: Final gain normalized pedestal-subtracted strip samples for (a) $ASIC_1$ (b) $ASIC_2$ (c) $ASIC_3$ and (d) $ASIC_4$. The strip samples are represented as blue traces, the $3.75\sigma_3$ signal thresholds are shown as grey traces, and the strips exceeding the signal threshold are highlighted as red traces.

It can be seen that signal strips can be divided into two groups. Firstly, signal strips consisting of only one strip with subtracted ADC values exceeding the threshold. Secondly, signal strips where multiple adjacent strips have joined to form one *'cluster'*. For example, Fig. 6.9(a) demonstrates that $ASIC_1$ has one single signal strip and one cluster formed by grouping of five adjacent signal strips while $ASIC_2$ in Fig. 6.9(b) has no single signal strip but only one cluster of signal strips. The following section describes grouping of signal strips to form clusters.

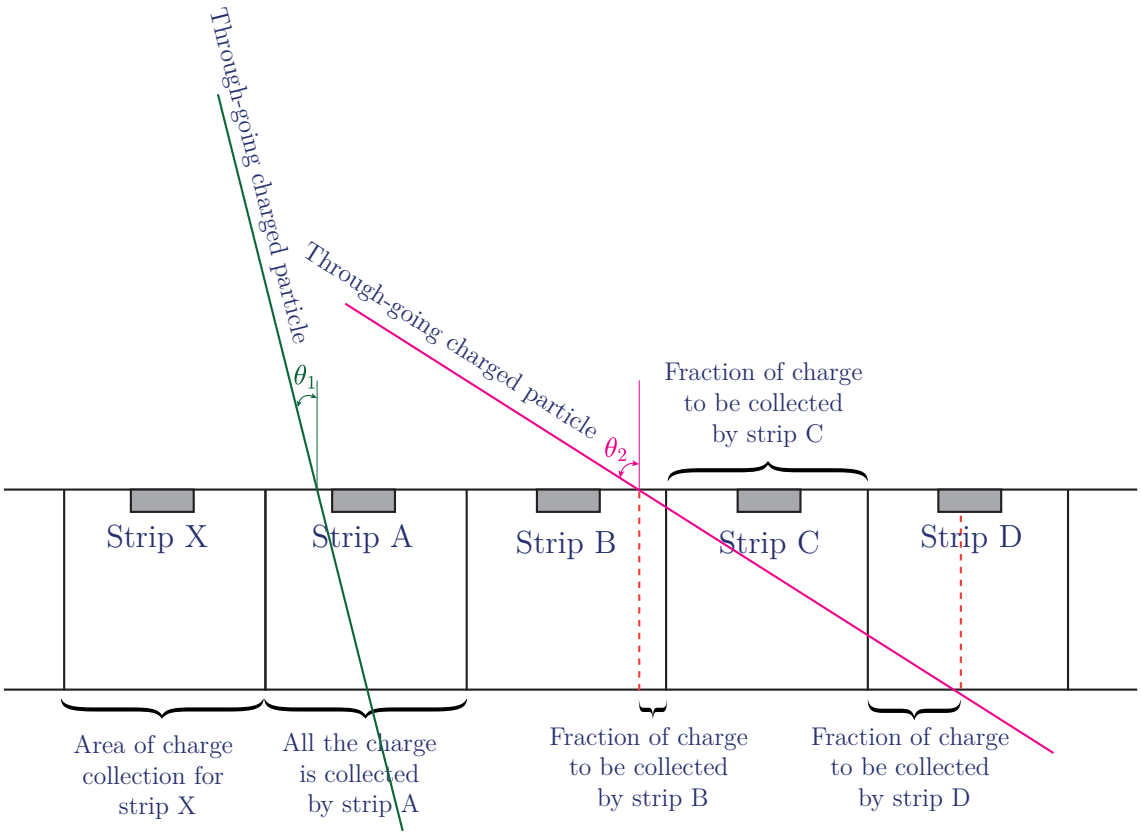

Figure 6.10: Schematic diagram showing the generation of the signal by two charged particles traversing a silicon detector hybrid. The green solid line depicts a charged particle depositing its charge on one strip due to its small incident angle of θ_1 while the pink solid line is the representation of a charged particle entering the hybrid with a large incident angle of θ_2 and therefore crossing several strips. As a result, signal is distributed among the activated strips. A larger incident angle also results in higher creation of electron-hole pairs.

6.2 Strip clustering

The signal recorded by the detector is proportional to the number of electron-hole pairs generated, which in turn is dependent on the amount of energy deposited within the detector volume as a particle passes through it. A signal is generated in solely one strip providing that the incident angle of a charged particle traversing the silicon wafer is small, represented by the green solid line and incident angle of θ_1 in Fig. 6.10. Conversely, a large incident angle, depicted by the pink solid line and θ_2 angle in Fig. 6.10, implies that the particle crosses several strips and the signal distribution will be based on the fraction of the strip over which the particle traveled. As a result, adjacent strips share the generated charge cloud within the

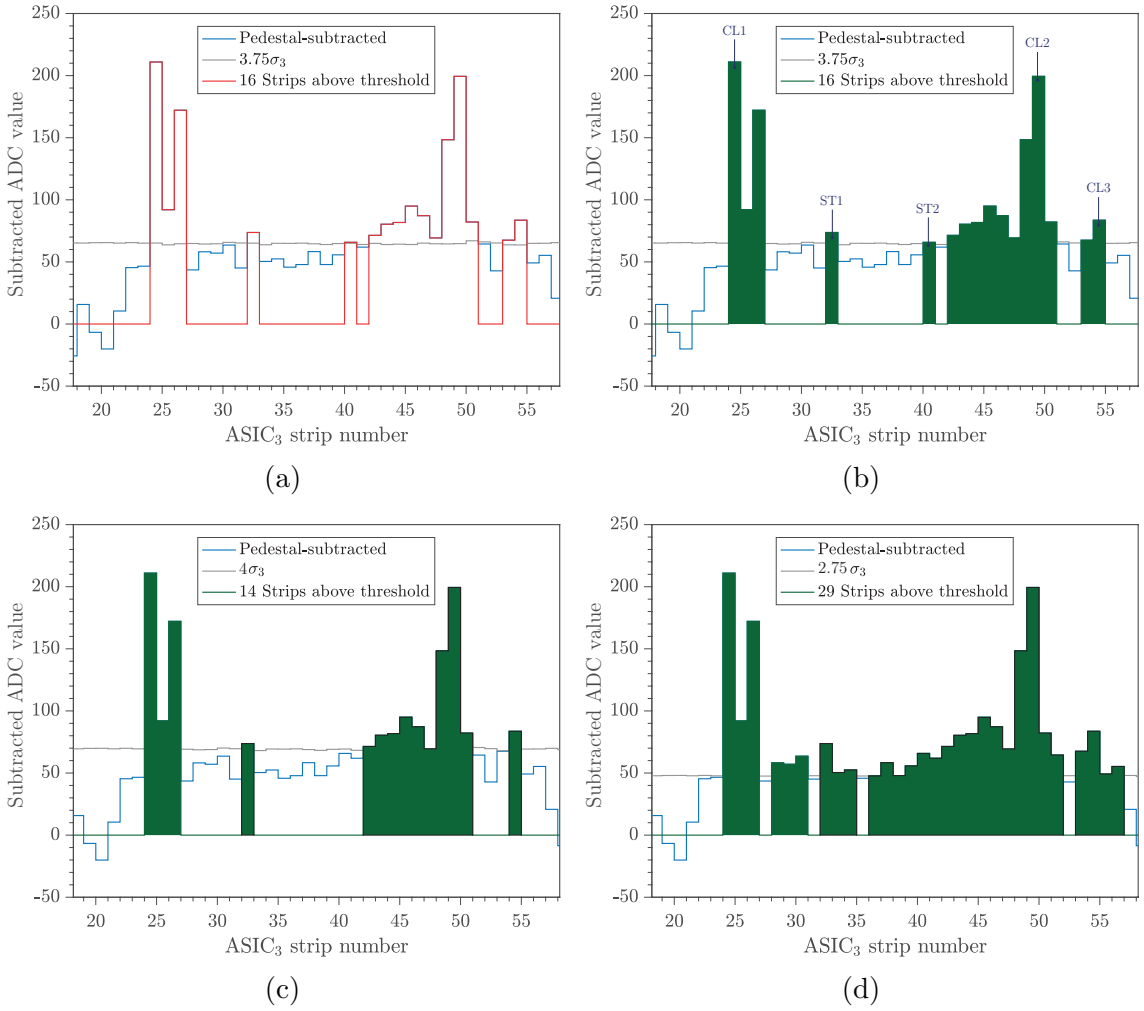

Figure 6.11: Plots illustrating the dependence of cluster generation on a defined signal threshold. (a) The expanded view of $ASIC_3$ where the strip gain normalized pedestal-subtracted samples are represented as blue traces, the arbitrary $3.75\sigma_3$ signal threshold is shown as a grey trace, and the strips exceeding the signal threshold are highlighted as red traces. (b) A $3.75\sigma_3$ signal threshold resulting in three clusters (CL1, CL2 and CL3) and two single signal strips (ST1 and ST2). (c) A $4\sigma_3$ signal threshold leading to two clusters and two single signal strips. (d) Five clusters with no single signal strips obtained from a $2.75\sigma_3$ signal threshold.

silicon depletion layer. These activated adjacent strips are known as strip clusters.

Fig. 6.11 illustrates an expanded region of Fig. 6.9(c) and aims to provide a visual representation of the dependence of the number of generated signal strips on a defined signal threshold. For example, an arbitrary defined signal threshold of $3.75\sigma_3$ in Fig. 6.11(b) leads to a total of 16 signal strips, corresponding to two single strips (ST1 and ST2) and three clusters (CL1, CL2 and CL3 each containing 3, 9 and 2 adjacent activated strips, respectively). Figures 6.11(c) and 6.11(d) demonstrate

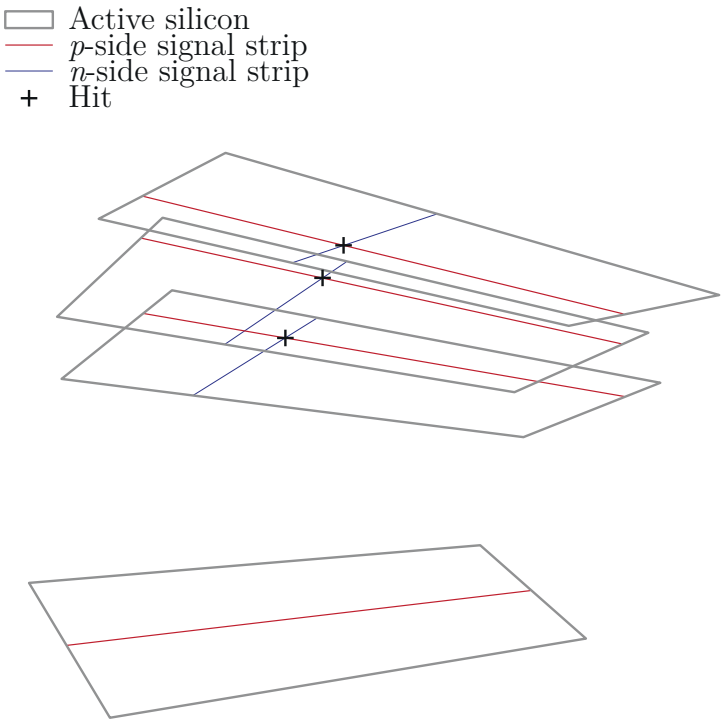

Figure 6.12: Spatial representation of an example event where the intersections of p- and n-side signal strips of the hybrids result in the 3-D set of position data for the hits.

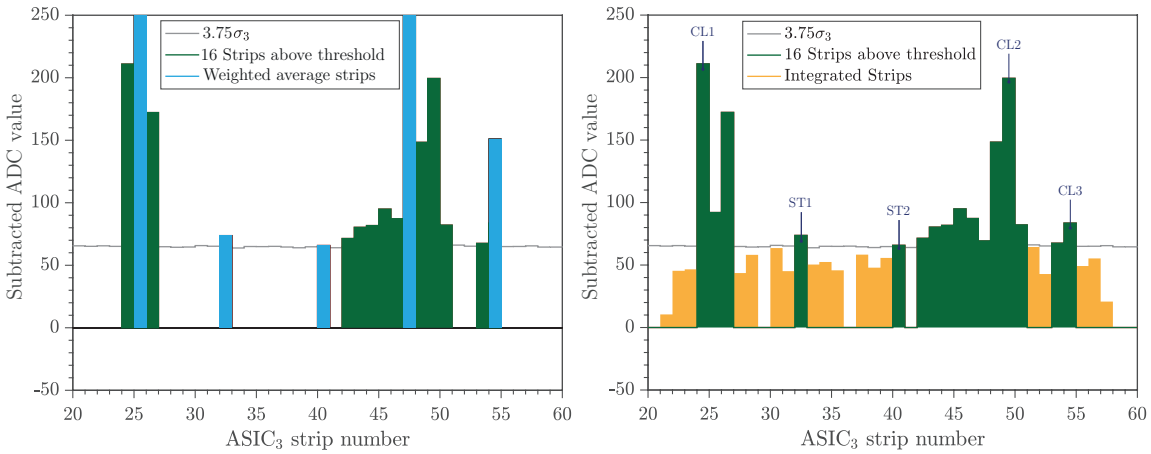

(a) (b)

Figure 6.13: Histograms depicting (a) the calculated weighted average strips (blue bars) of the clusters (green bars) and (b) the integration of strips (orange bars) with single strips as well as clusters.

two alternative pedestal definitions. Using a signal threshold of $4\sigma_3$ results in 14 signal strips corresponding to two single strips and two clusters. Similarly, a pedestal definition with a signal threshold of $2.75\sigma_3$ gives rise to 29 signal strips corresponding to no single strip and five clusters.

Subsequent to the identification of a strip cluster, the position of a hit in the detector reference frame will be determined using the signal strip (see Fig. 6.12 and Sec. 7.2.2.1). For a strip cluster, the central strip is calculated by weighting the strip numbers by the normalized strip energies, or equivalently the strip ADC pulse heights. This weighted average strip number is given by

$$s_{cluster} = \frac{\sum_{i=1}^{N}(E_i)(s_i)}{\sum_{i=1}^{N} E_i}, \tag{6.5}$$

where E_i is the pulse height and s_i is the ith strip. Fig. 6.13(a) is a schematic illustration of the outcome of such weighted average technique. For each cluster, a weighted average strip number is calculated and a pulse height corresponding to the

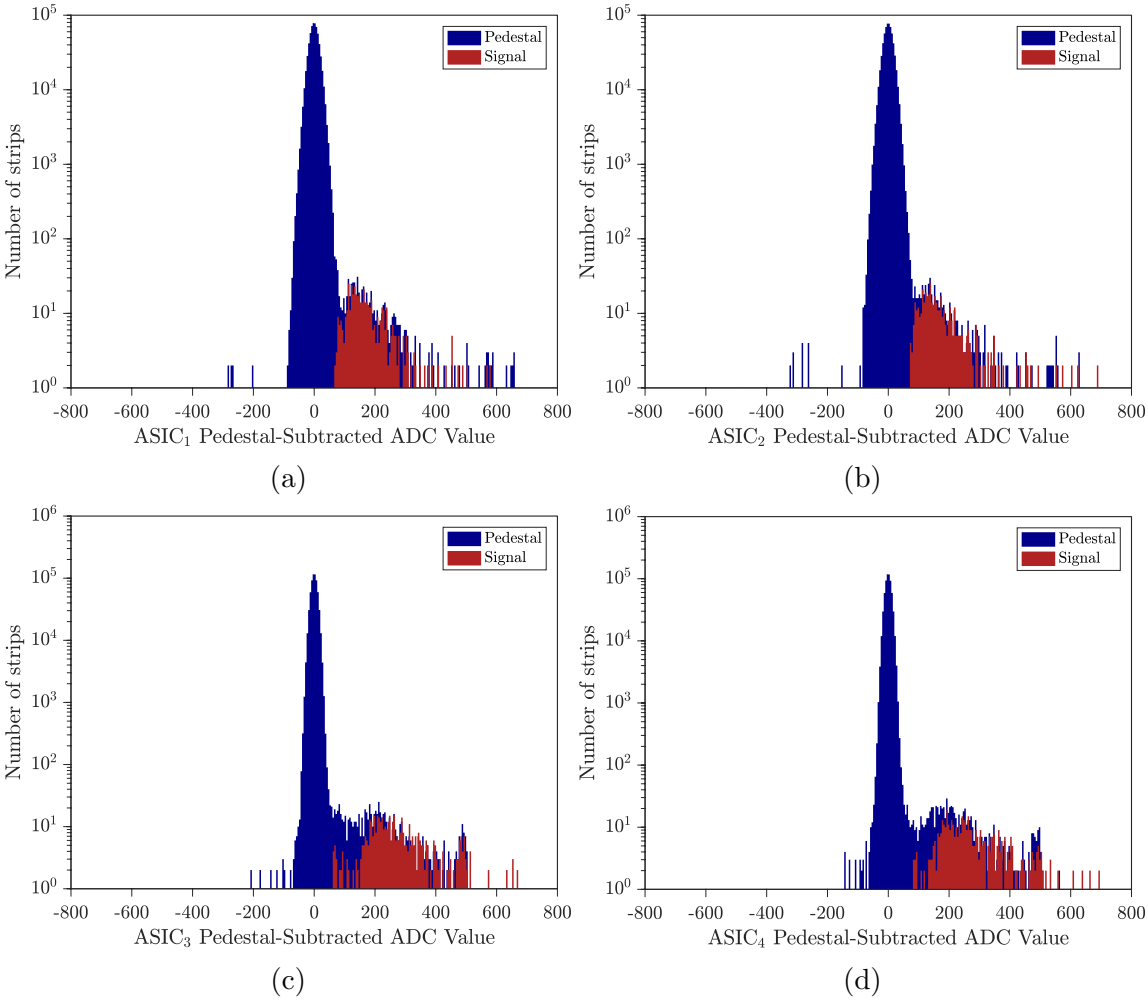

Figure 6.14: Histograms of the ADC values for four ASICs (a-d) obtained from an entire experimental run. The red illustrates the samples that have exceeded the $3.75\sigma_3$ signal threshold while the dark blue represents the values that did not pass the threshold. The vertical axis is logarithmic scale.

sum of all the pulse heights of the strips of that cluster (the height of the blue bars) is assigned to the weighted average strip.

Fig. 6.14 is the distribution of ADC sample values acquired from a complete experimental run. The red illustrates the samples that have exceeded the arbitrary $3.75\sigma_3$ signal threshold while the dark blue represents the values that did not pass the threshold.

The output of the pedestal analysis is a text file where each line corresponds to a particular event occurring during a mixing experimental cycle. The recorded event could be an annihilation, a cosmic or none. For every hybrid strip triggered during the event, a four-number combination corresponding to hybrid number, ASIC number, the weighted average strip and the sum of the pulse heights of the cluster's strips is recorded. This output is subsequently fed into the reconstruction algorithm to determine the position of a possible vertex, see Sec. 7.2.1.

6.3 Pedestal enhancement

6.3.1 Integrating strips

One approach in investigating the enhancement of the vertex reconstruction efficiency is to integrate strips with single signal strips as well as signal clusters. Fig. 6.13(b) is the outcome of an algorithm devised to adopt such an approach.

Firstly, for a given number of integrated strips (Integrating Limit), the code identifies the first and the last clusters, i.e. non-intermediate clusters. The clusters might either possess one single strip or multiple activated adjacent strips. In this case, the non-intermediate clusters CL1 and CL3 consist of multiple activated adjacent strips. For the first cluster (CL1), the algorithm examines the number of non-signal strips to the left of it. If the number of non-signal strips is equal to or greater than the Integrating Limit, the defined number of integrated strips (Integrating Limit = 3 and represented by orange bars in Fig. 6.13(b)) is incorporated

into the left of the first cluster. Similarly, with regards to the last cluster (CL3), the code determines the number of non-signal strips to the left and right of the last cluster. If the number of non-signal strips is equal to or greater than the Integrating Limit, the defined number of integrated strips is added to the left and right of the last cluster.

Secondly, for every intermediate cluster (ST1, ST2 and CL2), the number of non-signal strips between adjacent clusters (Strip Difference) is determined. Providing that the Strip Difference is equal to or greater than twice the Integrating Limit (Strip Difference $\geqslant 2 \times$ Integrating Limit), the defined number of integrated strips is added to the left and to the right of the studied cluster and the preceding cluster, respectively. Otherwise, the number of integrated strips will be half of Strip Difference rounded to the lower integer.

As an illustration, Fig. 6.13(b) reveals that there exist five non-signal strips between CL1 and ST1 (Strip Difference = 5). Since this is smaller than twice the Integrating Limit of three (Strip Difference $< 2 \times 3 = 6$), only 2 - half the Strip Difference rounded to lower integer - strips have been integrated to the right and left of CL1 and ST1, respectively.

Once the strip integration is performed, the weighted average scheme calculates the central strip utilizing the new wider cluster. Since higher number of strips are included within a cluster, the pulse height assigned to the calculated central strip will, therefore, be greater compared to those demonstrated in Fig. 6.13(a).

6.3.2 Pedestal comparison

In order to compare the performances of the Standard and Alternative Pedestal methods, two sets of sampling data have been acquired, one sample representing the background (cosmic) while the other sample a representative of the signal (mixing) and both samples are summarized in Table 6.1.

The background sample has been collected by allowing the SVD to operate with no antiparticles present in the trap. The signal sample is a collection of events which

Table 6.1: Summary of the cosmic and mixing sampling data. The reconstruction of the vertices has been performed by the Standard Reconstruction Method.

Cosmic Sample	
Total Run Time	4383.4 s
Total Number of Events	42430
Number of Reconstructed Vertexes	22900
Vertexes for $N_{helices} = 2$	21720 [95%]
Vertexes for $N_{helices} > 2$	1180 [5%]
Rate	(9.68 ± 0.05)Hz

(a) Cosmic

Mixing Sample	
Total Run Time	49.8 s
Total Number of Events	29965
Number of Reconstructed Vertexes	25017
Vertexes for $N_{helices} = 2$	7305 [29%]
Vertexes for $N_{helices} > 2$	17712 [71%]
Rate	(602 ± 3)Hz

(b) Mixing

have been recorded during the mixing phases of the experiment by the SVD. A mixing phase constitutes a significant number of events in a relatively short period of time and therefore the reason behind acquiring the mixing sampling data. In addition, the knowledge of mixing sampling is not biased by any experiment performed on trapped antihydrogen atoms. As implied by Table 6.1, the mixing sample is associated with a cosmic ray contribution of 1.6%.

Standard Pedestal Analysis (SPA) utilizes two rounds of filtration, each round employing a filtering threshold of $p \pm 3\sigma$ in order to eliminate the signal contamination and determine the pedestal of a strip. Once the pedestal is acquired, the n and p-side strips exceeding an arbitrary pre-defined signal threshold of $3.75\sigma_3$ are identified as signals. SPA has no implementations of integrated strips with clusters.

To compare the performance of the SPA with the APA, 29,965 events were analysed by each pedestal method. The outputs from the SPA and the APA were then fed into the Alternative Reconstruction Method (ARM). The absolute vertex reconstruction efficiencies due to the SPA (η_{SPA}) and APA (η_{APA}) are defined as

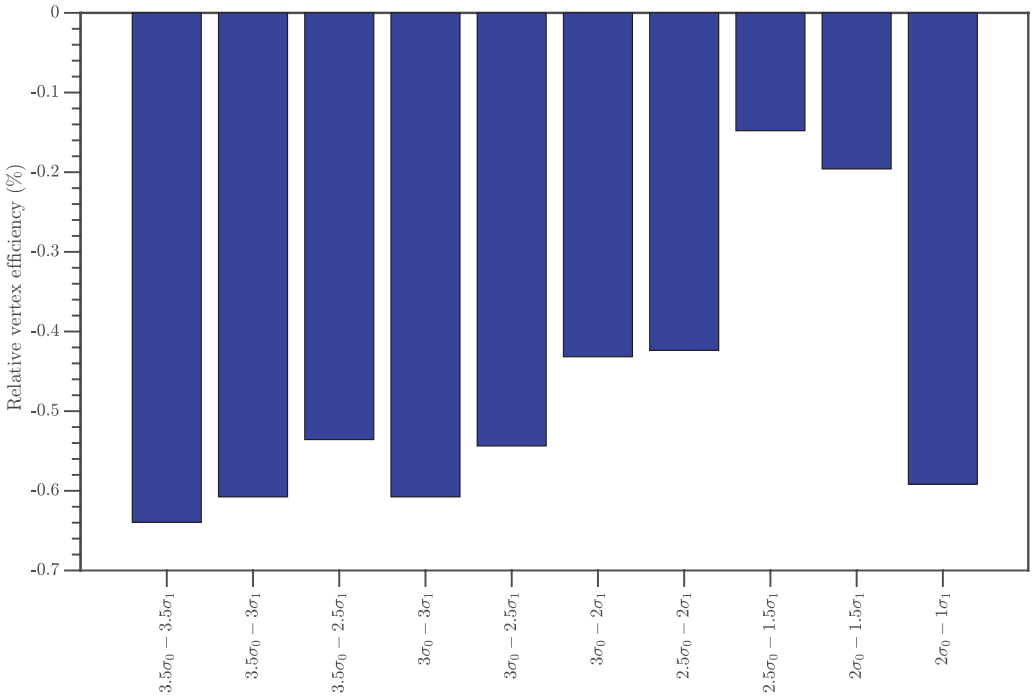

Figure 6.15: Relative vertex reconstruction efficiency comparing the SPA with various APA two-round filtering threshold scan parameters for a defined n- and p-side signal thresholds of $3.75\sigma_3$. The SPA outperforms the APA scan parameter of $2.5\sigma_0$-$1.5\sigma_1$ by only 0.1% when considering two rounds of filtering.

the percentage of the events leading to a reconstructed vertex - or equivalently the percentage of events with two or more tracks. Referring to Table 6.1(b), it can be seen that $\eta_{\text{SPA}} = 25017 \ / \ 29965 = 83.5\%$. The relative vertex reconstruction efficiency ($\eta_{\text{rel.}}$) comparing the absolute vertex efficiencies of the SPA and the APA is defined as

$$\eta_{\text{rel.}} = \frac{\eta_{\text{APA}} - \eta_{\text{SPA}}}{\eta_{\text{SPA}}}. \tag{6.6}$$

The SPA utilizes two rounds of filtering with the corresponding filtering thresholds of $3\sigma_0$ and $3\sigma_1$, respectively. In addition, the n- and p-side strips signal thresholds are set as $3.75\sigma_3$.

As a first attempt to provide a comparison between the performance of the APA and the SPA, a two-round filtering involving the scan of the σ_0 and σ_1 thresholds combined with a defined signal threshold of $3.75\sigma_3$ was acquired. Fig. 6.15 illustrates the relative vertex efficiency comparison between the SPA and various two-round filtering threshold scan parameters of the APA. It is evident from this plot that

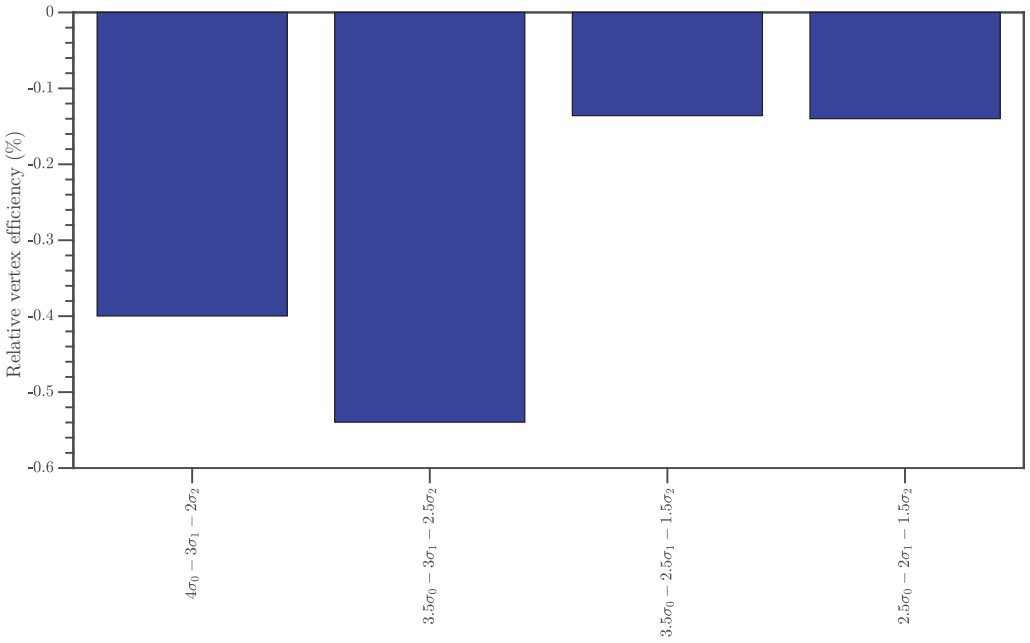

Figure 6.16: Relative vertex reconstruction efficiency comparing SPA with various APA three-round filtering threshold scan parameters for a defined n- and p-side signal thresholds of $3.75\sigma_3$.

the SPA outperforms the APA scan parameter of $2.5\sigma_0$-$1.5\sigma_1$ by only 0.1% when utilizing two rounds of filtering. Furthermore, lowering the first and second round filtering thresholds to $2.5\sigma_0$-$1.5\sigma_1$ leads to reconstruction of higher number of vertices. This is in agreement with the fact that lowering the filtering thresholds results in a more efficient elimination of contaminated signal strips and, accordingly, the acquired strip pedestals and their corresponding standard deviations (σ_3) are lower in magnitude. For a given signal threshold of $3.75\sigma_3$ on both the n- and p-side strips, a lower σ_3 indicates that greater number of strips exceeds the threshold and consequently greater number of hits will be identified, implying that further tracks will be reconstructed. Subsequent decrease of the filtering thresholds has a negative impact on the reconstruction of vertices.

Shown in Fig. 6.16 is the plot demonstrating the relative vertex reconstruction efficiency of the SPA and various APA three-round filtering threshold scan parameters for a defined n- and p-side signal thresholds of $3.75\sigma_3$. The addition of third round filtering threshold leads to the gradual increase in the reconstruction of vertices, resulting in a maximum relative vertex efficiency at $3.5\sigma_0$-$2.5\sigma_1$-$1.5\sigma_0$.

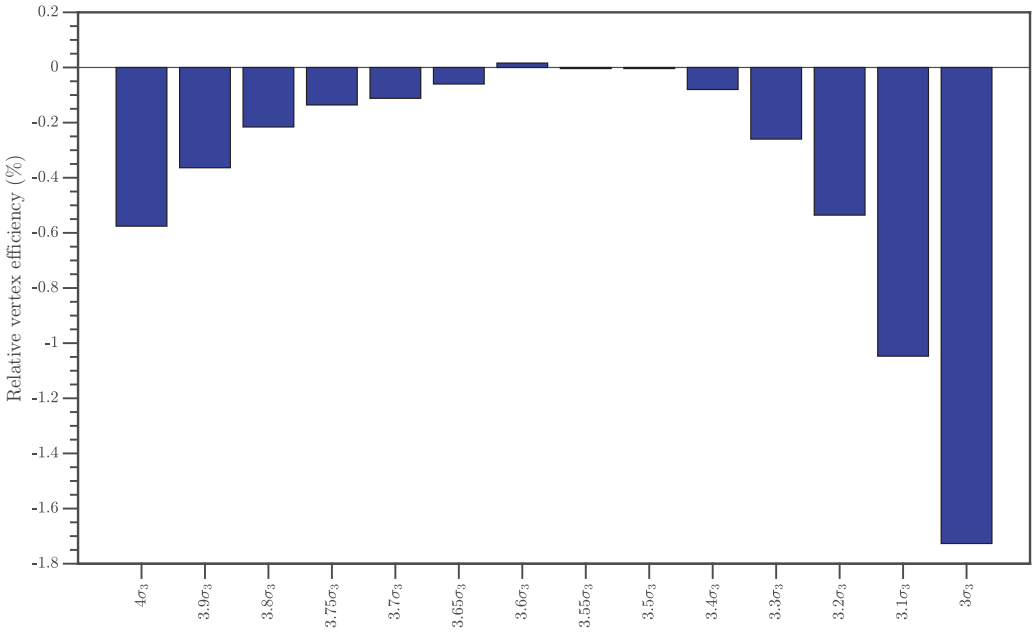

Figure 6.17: Relative vertex reconstruction efficiency comparing the SPA with various APA signal threshold scan parameters of the n- and p-side strips. Relative to the SPA, a slight enhancement of only 0.02% is obtained at a scan parameter of $3.6\sigma_3$.

Having identified the most efficient pedestal scan having three rounds of filtering, namely $3.5\sigma_0$-$2.5\sigma_1$-$1.5\sigma_0$, Fig. 6.17 is the outcome of investigating the effect of lowering the n- and p-side strip signal thresholds on the enhancement of the vertex reconstruction. The plot indicates that a maximum vertex reconstruction efficiency was acquired for a signal threshold of $3.6\sigma_3$, indicating a slight enhancement of only 0.02% relative to the SPA. The vertex reconstruction efficiency declines with any subsequent decrease of the σ_3.

6.3.3 Integrated-strips enhancement

Having identified the most efficient APA scan parameter, an attempt was made to investigate the effect of integrating strips with clusters. The integration of strips with clusters results in no enhancement of vertex reconstruction.

The objective of this chapter was to provide a detailed description of the APA. The improvement which can be applicable to the ALPHA experiment is the investigation of adding a third round filtering to determine the strip pedestal. In addition

to the increase in the vertex reconstruction efficiency, the Alternative Pedestal Analysis script (see Appendix A) has the following remarkable features:

- Considerable amount of effort has been made by the author to produce scripts capable of providing the best visualizations for better understanding of the physics processes being investigated. Alternative Pedestal Analysis involves analysing the pedestal performance of each 36,864 strips (channels) of the detector. A comprehensive additional script has been devised that provides one with a visual representation of the pedestal analysis of every single ASIC and strip, such as the one shown in Fig. 6.9. This script assists with determining any probable software or hardware faults occurring during the readout of the detector and has been of great importance for providing the most accurate results for this chapter (see Appendix B for the Pedestal-Analysis-Visualization.m script)

- Standard Pedestal Analysis and Reconstruction Method are implemented in C++. MATLAB, compared with C++, is slower in terms of processing speed. However, the Alternative Pedestal Analysis written in MATLAB is exceedingly fast, capable of performing the pedestal analysis of the entire 36,846 channels in less than 60 seconds, on average.

- The pedestal analysis script has the great flexibility of being incorporated with further parameters which might enhance the reconstruction of vertices.

Employing the pedestal analysis output from this chapter, in the next chapter a comprehensive description of reconstructing a vertex, either due to the annihilation of an antiproton on the trap wall or the passage of a cosmic through the detector, will be provided.

Chapter 7

Event Vertex Reconstruction

High-energy physics experiments employ silicon tracking detectors to reconstruct the particle trajectories. The ALPHA Silicon Vertex Detector uses the position-sensitive features of the detector hybrids to reconstruct the tracks of charged particles. By investigating the tracks from a number of particles, the common origin (the vertex position) of the particles is determined by the SVD.

The objective of this chapter is to provide a detailed description of an Alternative Reconstruction Method utilized to both characterize an event and determine the position of a reconstructed vertex. By utilizing the outcome of the Standard Pedestal Analysis, detailed steps leading to the reconstruction of the charged particle tracks and the determination of the annihilation position are described. A section will discuss the vertex reconstruction efficiency enhancement and the implication of the Alternative Reconstruction Method in acquiring the distribution of vertices for mixing and cosmic events. The complete algorithm for the Alternative Reconstruction Method (Appendix C) has been solely written by the author and is completely independent of the Standard Reconstruction Method currently implemented in the ALPHA experiment [31][80]. The results presented in this chapter can serve as a validation and enhancement of the Standard Reconstruction Method.

7.1 Overview

The following procedures, outlined with the flowchart in Fig. 7.1, show the steps leading to the reconstruction of a vertex:

1. Enumeration and filtering of track candidates (Sec. 7.2). The total set of hits are identified. Several selection criteria aimed at extracting the best 3-hit combinations, each hit corresponding to a different detector layer, are applied to the set of hits. Hits failing to pass the filtering conditions are rejected. Each 3-hit combination meeting the filtering mechanisms is considered a track candidate.

2. Tuning of track candidates (Sec. 7.2.4). The $x-y$ projections of helices corresponding to the track candidates allows the tuning and the final selection of the best track candidates.

3. Reconstruction of tracks (Sec. 7.3). The $x-y$ projections of the helices corresponding to the best track candidates are utilized to numerically reconstruct the 3-D track for each best track candidate.

4. Reconstruction of a vertex (Sec. 7.4). The reconstructed 3-D tracks are used to determine the vertex position.

The outcome of the Alternative Pedestal Analysis was described in Chapter 6 where a hit was defined as the intersection of the n-side and p-side strips and will be used as a 3-D position in the reference frame of the detector (see Fig. 6.12). As an overview, Fig. 7.2 illustrates a vertex reconstructed by feeding the outcome of the Alternative Pedestal Analysis with scan parameters resulting in the highest attainment of the vertex efficiency (see Fig. 6.17) to the Alternative Reconstruction Method.

In order to provide the best comparison between the Standard Reconstruction Method and the Alternative Reconstruction Method, a particular annihilation event was acquired where the outcome of the Standard Pedestal Analysis had been fed in

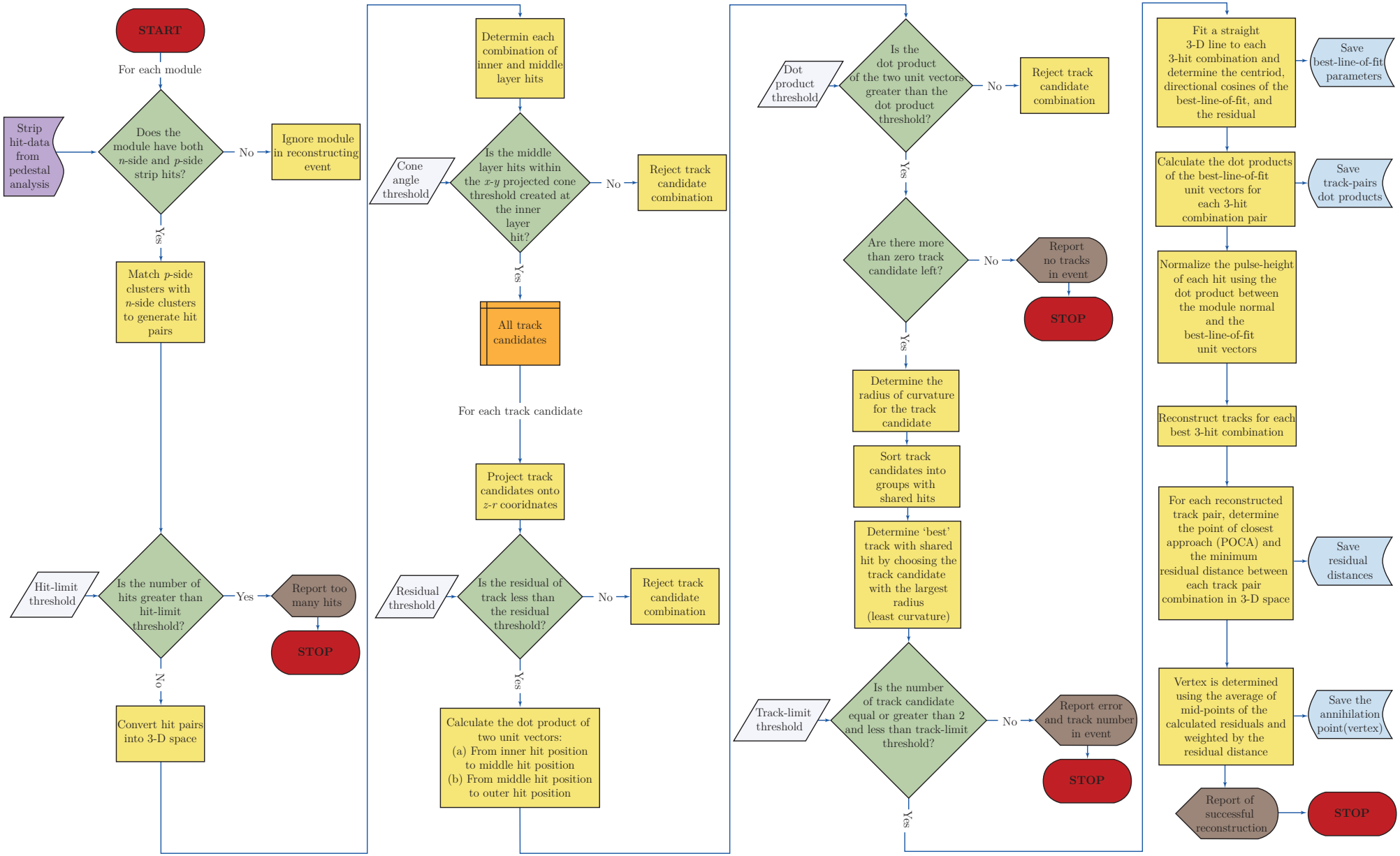

Figure 7.1: Flowchart demonstrating the procedures in reconstructing a vertex by the Alternative Reconstruction Method.

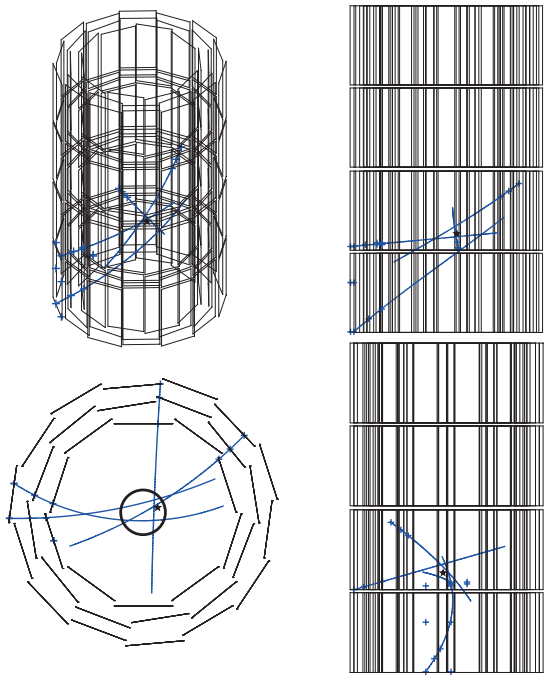

Figure 7.2: Four different views of a reconstructed vertex (black stars) where the outcome of the Alternative Pedestal Analysis has been fed into Alternative Reconstruction Method. The vertex has resulted from the annihilation of an antiproton on the trap wall (black circle) during a particular mixing event. Blue curves represent the reconstructed tracks.

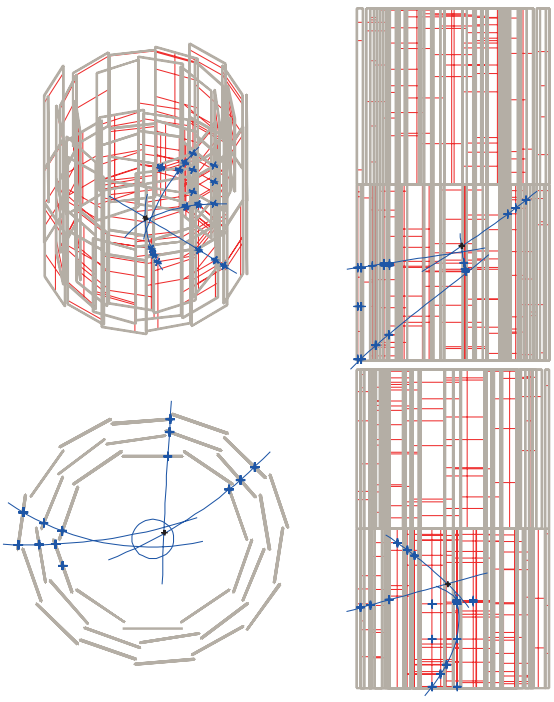

Figure 7.3: Four different views of a vertex reconstructed (black plus symbols) where the outcome of the Standard Pedestal Analysis for the same mixing event in Fig. 7.2 has been fed into the Standard Reconstruction Method. Blue circle represents the trap surface. Credits: the ALPHA Collaboration.

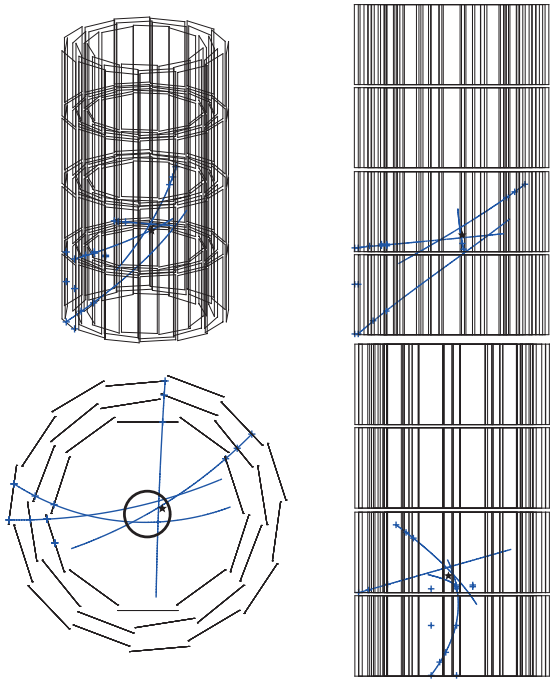

Figure 7.4: Reconstructed vertex (black stars) corresponding to the same mixing event in Fig. 7.3 where the outcome of the Standard Pedestal Analysis has been fed into the Alternative Reconstruction Method.

to the Standard Reconstruction Method, see Fig. 7.3. Subsequently the same Standard Pedestal Analysis outcome was fed into the Alternative Reconstruction Method to obtain a reconstructed vertex corresponding to the same annihilation event. The result is provided in Fig. 7.4 and serves as a visual representation of how well the Alternative Reconstruction Method reconstructs a vertex compared to that of the Standard Reconstruction Method. The following sections describe the steps implemented in reconstructing the tracks and the vertex shown as the blue curves and black star, respectively, in Fig. 7.4.

7.2 Determination of track candidates

7.2.1 Tabulating pedestal analysis outcome

Once the pedestal analysis is conducted, the output is a text file arranged such that each row represents an event where a signal strip is represented with a four-number combination corresponding to the hybrid number, the ASIC number, the

weighted average strip and the pulse height corresponding to the weighted average strip, respectively.

The first step in identification of the track candidates is to determine which hybrids have registered hits during an event. To do this, two tables of 72 (the total number of hybrids) $\times$ 4 (the total number of ASICs per hybrid) are constructed from the four-number combination data of an event. Each ASIC can have one or more signal strips. Hence, for every row (hybrid) of the first table, each column (ASIC) can have one or more elements representing the weighted average strip value of the signal strip. The second table possesses rows with elements representing the corresponding pulse heights of the row elements in the first table. Since the p-side of a hybrid is facing the atom trap, a charged pion ought to first encounter a p-side strip of a hybrid. Therefore, a hybrid with only (an) n-side fired strip(s) will be rejected for track consideration. Only the hybrids with the simultaneous registration of both the n- and p-side signal strips will be considered for track reconstruction.

7.2.2 Identification of a hit

The detector is divided into two halves, one half facing the AD (known as the AD-side) and the other half facing the positron accumulator (known as the POS-side). The enumeration of 72 hybrids is the following: hybrids 1-10 and 37-46 are allocated to the inner layer, the middle layer consists of hybrids 11-22 and 47-58 and the outer layer is comprised of hybrids 23-36 and 59-72. Hybrids 1-36 belong to the AD-side while hybrids 37-72 are assigned to the POS-side, see Fig. 7.5.

In order to identify a hit inside the detector reference frame, every p-side signal strip is coupled with all the n-side signal strips of a hybrid. A hit is then defined as a p- and n-side signal strip intersecting each other in the hybrid reference frame, see Fig. 6.12. For every p-side strip encountering a charged pion on the front of a hybrid, two n-side strips on the rear register a signal. Therefore, grouping n-side and p-side signal strips separately allows one to determine the total number of hits on a hybrid. For signal clusters of an ASIC, the weighted average strip is a value between

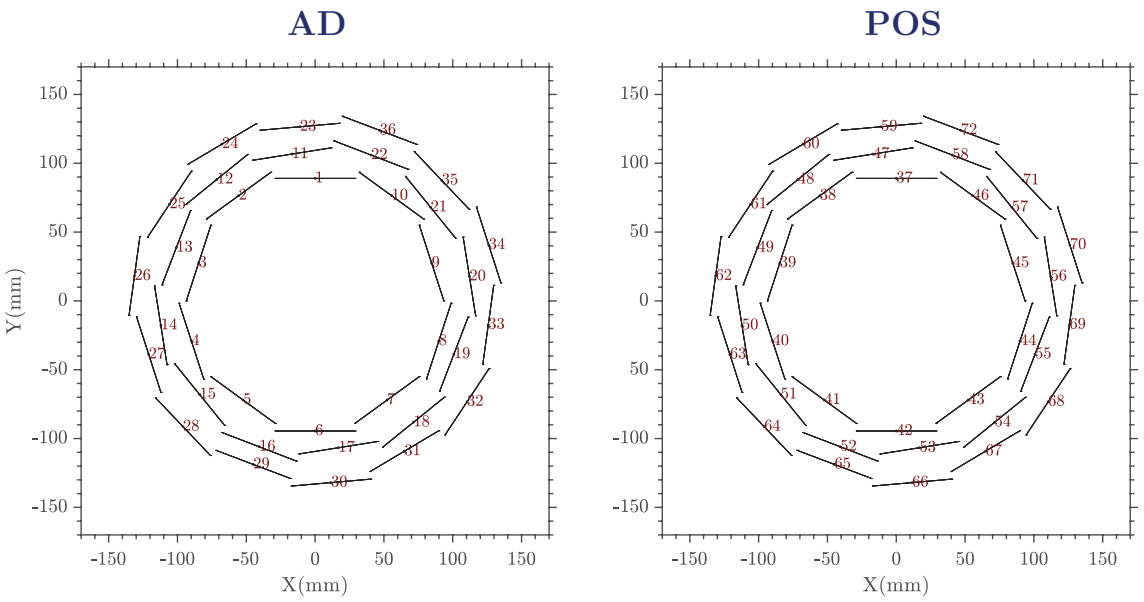

Figure 7.5: Left: the distribution of hybrids on the AD-side. Right: the distribution of hybrids on the POS-side.

0 and 128. As stated in the previous chapter, the total number of strips in a module is enumerated with 1-512, where n-side strips 1-256 corresponds to ASICs 1 and 2 while p-side strips 257-512 is assigned with ASICs 3 and 4. Accordingly, the weighted average strip value of an ASIC is translated to the corresponding hybrid strip number and the signal strips are grouped based on n and p sides. Each grouped signal strips are subsequently allocated with their corresponding pulse heights. With regards to the generated hits, two thresholds are defined for which any events exceeding these two thresholds will not be further considered for vertex reconstruction: threshold on the maximum number of hits on all the 72 hybrids per event - set to 100 - and threshold on the maximum number of hits per layer - set to 20.

7.2.2.1 Distribution of hits on detector layers

Once a hit has been identified as a paired n- and p-side signal strips, the n- and p-side weighted average strip numbers of a hit are converted to a (y, z) coordinate in the hybrid reference frame. The zero-reference (0,0) of the hybrid frame is defined as the black circle on the PCB support in Fig. 5.6. Since the (x, y, z) coordinates of the zero-reference of hybrid is known in the reference frame of the detector,

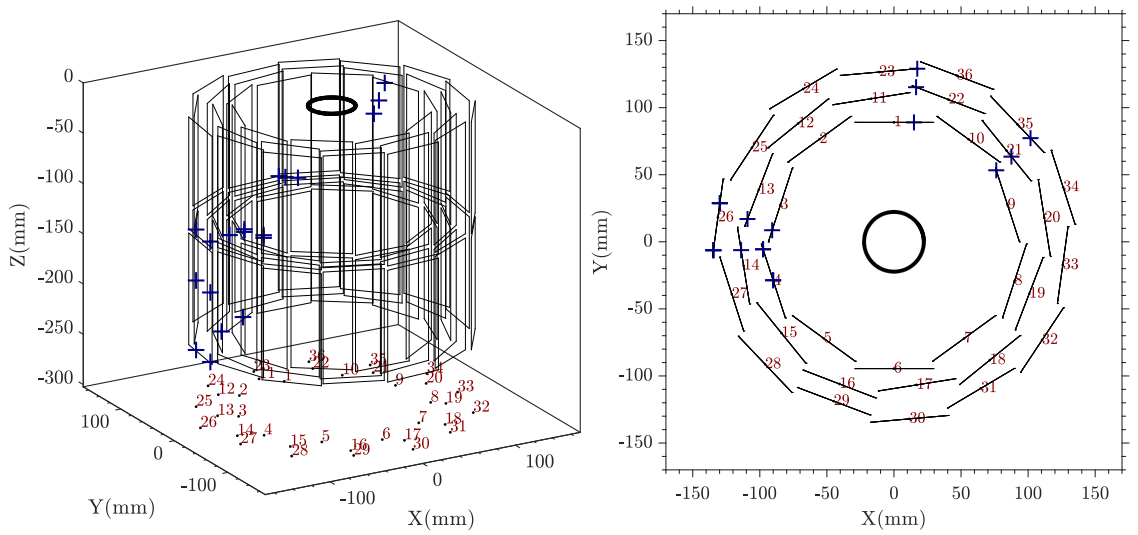

(a) 3-D projection (b) $x - y$ projection

Figure 7.6: Two projections illustrating the AD-side of the detector containing all the 19 hits generated during the mixing event illustrated in Fig. 7.4.

the (y, z) coordinate of the hit in the hybrid reference frame is translated into the corresponding (x, y, z) coordinates in the detector reference frame.

The example mixing event considered for the reconstruction of the vertex in Fig. 7.4 results in a total of 19 hits generated by the intersection of the n- and p-side signal strips. A single hit can now be fully characterized in the reference frame of the detector by determining the following parameters:

- Index : The index number of the hit.
- X : The x-coordinate of the hit in the detector's reference frame (measured in mm).
- Y : The y-coordinate of the hit in the detector's reference frame (measured in mm).
- Z : The z-coordinate of the hit in the detector's reference frame (measured in mm).
- R : The radial distance of the hit from the centre of the detector (measured in mm).

Table 7.1: Tabulated data representing the parameters characterizing the hits on hybrids 1 and 4 of Fig. 7.6.

Index	**X**	**Y**	**Z**	**R**	ϕ	**L**	**H**	n**-PH**	p**-PH**
1	14.923	89	-102.54	90.242	1.4047	1	1	209.02	275.21
4	-90.049	-28.667	-106.04	94.502	-2.8334	1	4	97.341	188.17

- ϕ : The angle (measured in radians) of the hit from $+x$ axis. Any ϕ values within $0 < \phi < +\pi$ and $0 < \phi <$ -π represent a hit in the upper and lower sections of the detector when viewed in the $x - y$ plane, respectively.
- L : The detector layer which the hybrid containing the hit resides on.
- H : The hybrid containing the hit.
- n-PH : The pulse height of the n-side signal strip of the hit.
- p-PH : The pulse height of the p-side signal strip of the hit.

As an example, Table 7.1 tabulates the data for the hits on hybrids 1 and 4 of the inner layer.

Equipped with hits characterizing parameters, Fig. 7.6 provides the visual representation of the AD-side of the detector containing all the hits generated during the mixing event shown in Fig. 7.4.

7.2.3 Selection criteria

Identifying a track candidate, and therefore reconstructing a track, relies on how well three hits on three different layers of the detector are grouped together. A set of selection criteria has been devised to identify valid 3-hit combinations (known as track candidates) for track reconstruction.

In order to visualize the criteria used for selecting hits which would ultimately constitute part of a valid track, the entire 19 hits of the example mixing event is divided into two sets, A and B. Set A is assigned with the collection of hits (a total of 10) on hybrids 4, 13, 14 and 26 and will be the prime tool in providing a visual

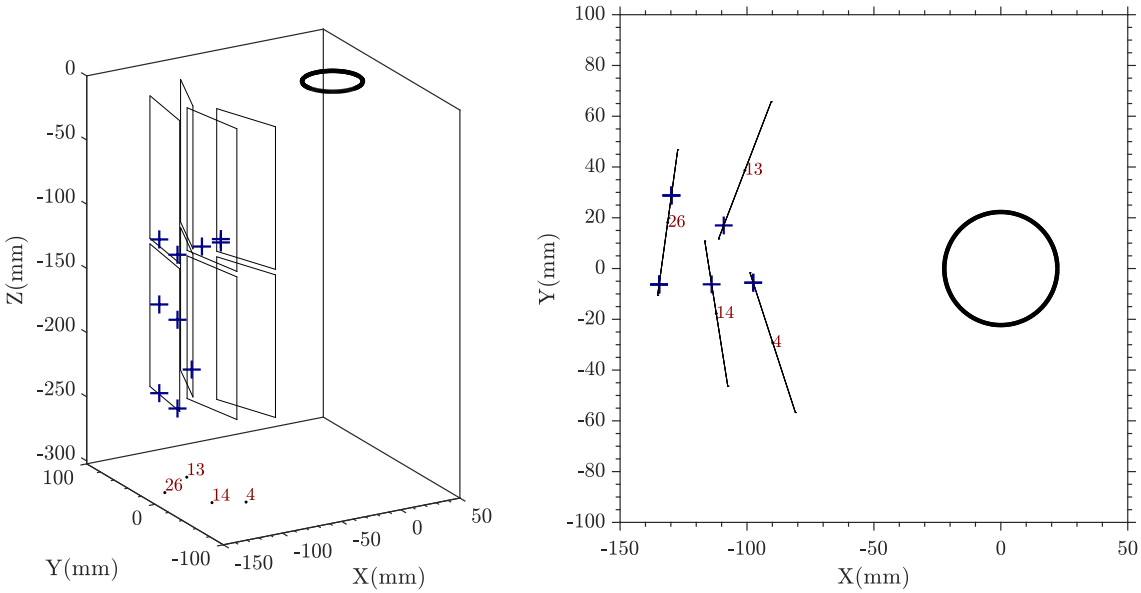

(a) 3-D projection

(b) $x - y$ projection

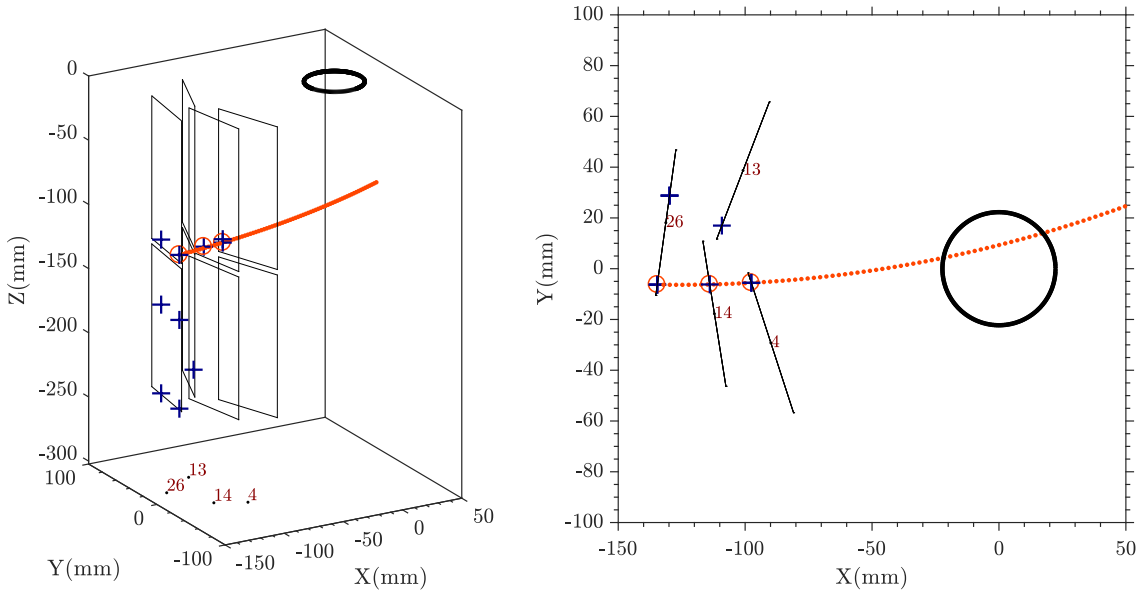

(c) 3-D projection

(d) $x - y$ projection

Figure 7.7: (a-b) Two different projections of set A hits utilized for visualizing various selection criteria aimed at identifying a track candidate consisting of only three hits. (c-d) The final outcome of the selection criteria applied to set A hits where a track has been reconstructed from the track candidate (the best 3-hit combination) meeting all the filtering conditions.

representation of the selection criteria while Set B is allocated to the remainder of the hits of the mixing event.

Figures 7.7(a) and 7.7(b) illustrate set A hits and the corresponding hybrids they are located on. Each hybrid consists of two silicon wafers (see Fig. 5.6), upper and lower. Features of hybrids' hits include: upper wafer of hybrid 4 has two hits at very

close proximity of each other (one selection criterion will focus on identifying track candidates arising from such hits), hybrids 13 and 14 each has one hit on lower and upper wafers, respectively, and hybrid 26 contains 6 hits distributed on both upper and lower wafers. The objective of this section is to quantitatively define filtering mechanisms in order to identify valid 3-hit combinations (track candidates) leading to a reconstructed track. Figures 7.7(c) and 7.7(d) reveal two different projections of the final reconstructed track comprising the best 3-hit combination surviving all the filtering conditions applied to the 10 hits in set A.

7.2.3.1 Cone angle

The deviations of three hits on three different layers of the detector can be described in two ways. Firstly, the angular deviation (a measure of the angular separation of two hits on two different layers) and secondly the translational deviation (a measure of the difference in the z-coordinates of two hits on two different layers).

One way of characterizing the angular deviation is to project all the hits onto the $x-y$ plane. Subsequently, a cone with a vertex at the centre of the detector and subtending a cone angle of 35° (the cone angle threshold) relative to an inner hit is constructed on each side of the inner layer hit, see Fig. 7.8 (35° is set as an arbitrary initial value. A scan of various cone angles will be provided in Sec. 7.5). Any middle layer hit that deviates from the inner layer hit by an angle less than 35° is considered to have met the cone angle selection criterion. Implementing this criterion on the middle layer hits of set A imply that all the middle layer hits meet the criterion. A further utilization of this mechanism on the outer layer hits of set A relative to those middle layer hits which have passed the criterion provides further filtering of the hits. The outer layer hits of set A all meet the cone selection criterion. The final outcome of the cone angle selection criterion applied to both sets of hits consists of 3-hit combinations such that the $x-y$ projection of the outer layer hit is within a cone angle of 35° or smaller of the middle layer hit and the middle layer hit, in turn, is located within a cone angle of 35° or smaller of the inner layer hit.

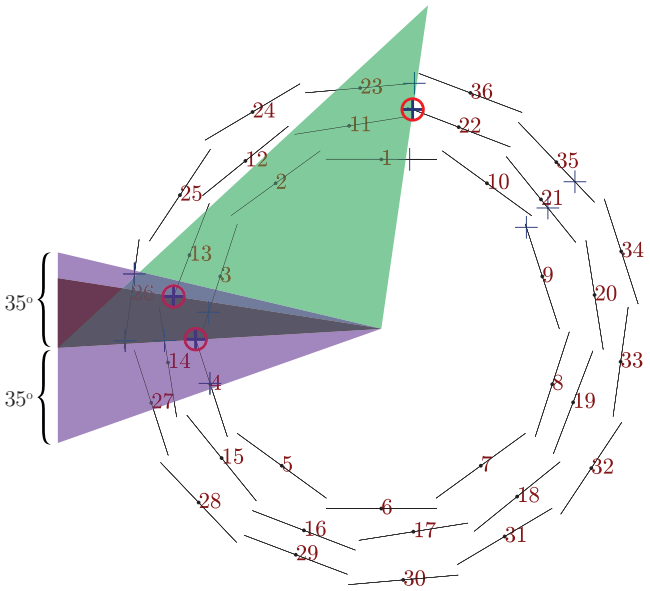

Figure 7.8: The purple cone with a vertex at the centre of the detector and subtending a cone angle of 35° on each side of the inner layer hit on hybrid 4 (the dark blue cross and the red circle marker). Any middle layer hits residing within the purple cone have passed the cone angle selection criterion. The angular separations of the two middle layer hits on hybrids 13 and 22 relative to the inner layer hit on hybrid 4 are represented by the corresponding dark-brown and green projected cones. The middle layer hit on hybrid 13 meets the cone angle filtering condition while the one on hybrid 22 fails.

Fig. 7.8 demonstrates the purple projected cone acting as a filtering angle. The cone has a vertex at the centre of the detector and subtends a cone angle of 35° on each side of the inner layer hit on hybrid 4 (the dark blue cross and the red circle marker). The middle layer hit on hybrid 13 has an angular separation (represented by the dark-brown projected cone) of less than 35° with respect to the inner layer hit and therefore is a hit candidate meeting the cone angle selection criterion. The middle layer hit on hybrid 22 subtends an angle much greater than 35° (represented by the green projected cone) with respect to the inner layer hit and consequently filtered out as a valid hit for a track candidate.

7.2.3.2 $r - z$ normal

Despite the fact that the two middle layer hits on hybrids 13 and 14 of set A have met the cone angle selection criterion relative to the inner layer hit on hybrid 4, it is evident from Fig. 7.7(a) these two hits possess different z-translational deviations

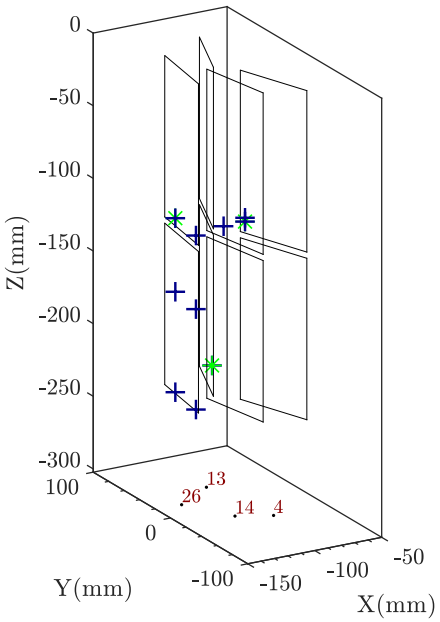

(a) 3-D projection

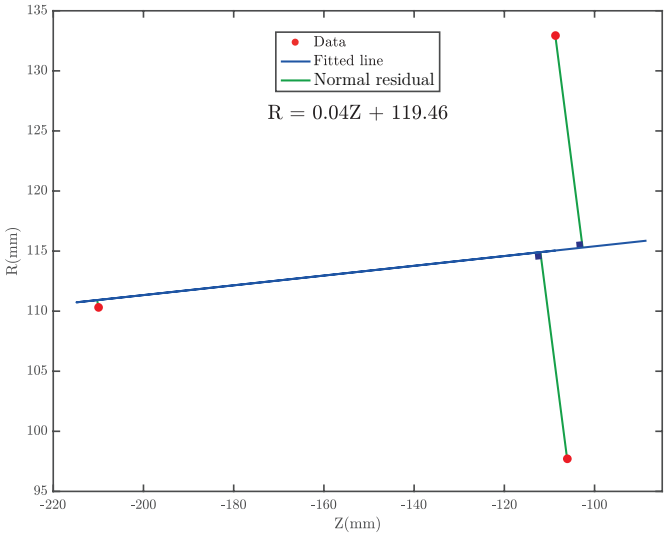

(b) $z - r$ projection

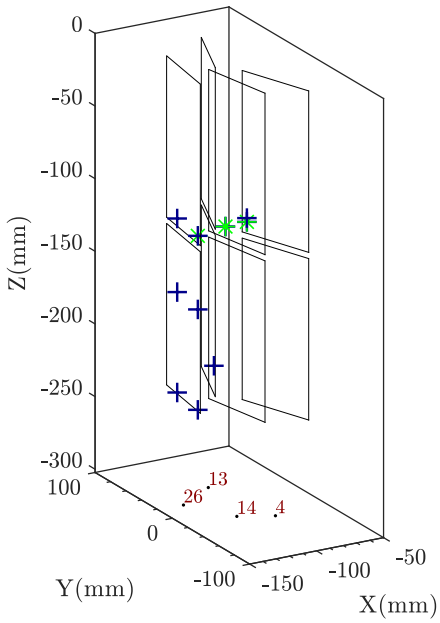

(c) 3-D projection

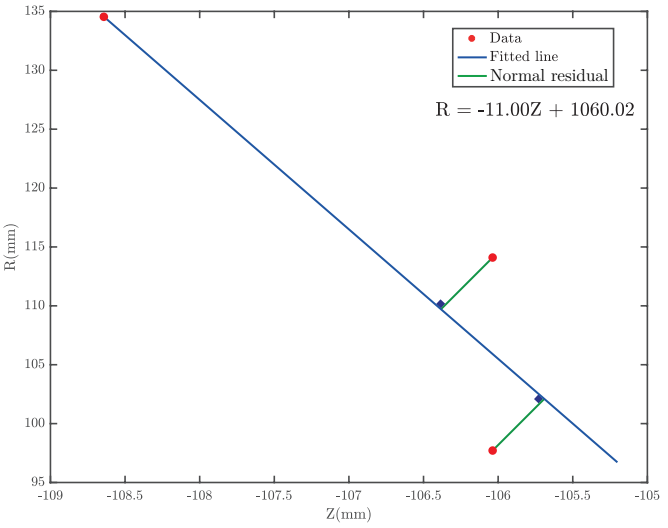

(d) $z - r$ projection

Figure 7.9: (a-b) A 3-hit combination in set A failing to meet the $z - r$ normal filtering mechanism. (c-d) A different 3-hit combination in set A meeting the $z - r$ normal filtering condition.

relative to any of the inner layer hits on hybrid 4. Similar argument applies to the outer layer hits on hybrids 26 where those on the lower silicon wafter of this hybrid are, relative to the middle layer hits, distributed significantly different along the z axis. To account for this translational deviation, a further selection criterion known

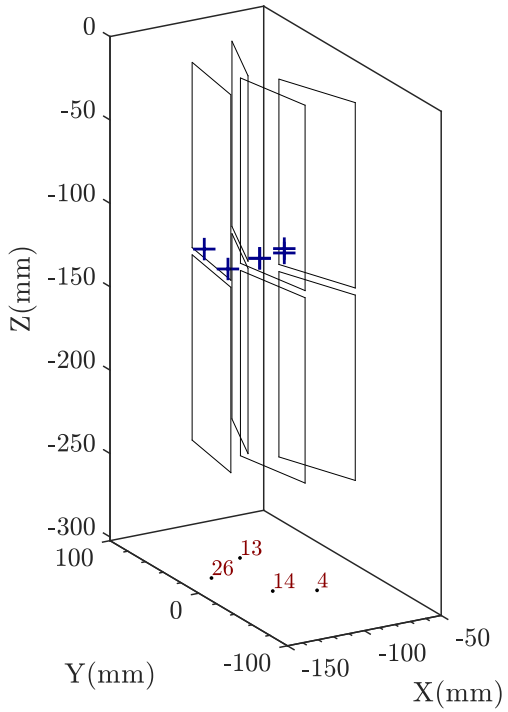

Figure 7.10: Hits of set A surviving cone angle and $z-r$ normal filtration mechanisms.

as $z-r$ normal is defined. Firstly, a plot of $z-r$ coordinates of every 3-hit combination is obtained, see Fig. 7.9. A line of best fit is drawn along the three hits and both the slope (m) and the intercept (c) are determined. For each hit with a (Z, R) coordinate, the perpendicular distance (also known as normal residual (d)) from the line of best fit is defined as

$$d \equiv \frac{\Big| -mZ + R - c \Big|}{\sqrt{(m^2+1)}}. \tag{7.1}$$

For any 3-hit combination, a total normal residual D is defined such that $D = d_1 + d_2 + d_3$ where d_1, d_2, and d_3 are the normal residuals for the first, second and third hits, respectively. Subsequently, an arbitrary $r-z$ normal threshold of 3 is adapted such than any 3-hit combination with a total normal residual D less than this threshold has passed the $r-z$ normal filtering mechanism.

Fig. 7.9 depicts a visual representation of the $z-r$ normal selection criterion whereby (a-b) represents a 3-hit combination failing the criterion due the significant z-deviations between the hits on three different layers of the detector. Figures 7.9(c)

and 7.9(d) represent a different 3-hit combination meeting the filtering condition where the three hits on each layer have significantly smaller z-deviations. Fig. 7.10 contains those hits of set A which have survived the filtering criteria outlined thus far and, as a result, any further criteria to be discussed will only be applicable to these hits of set A.

7.2.3.3 Dot product

The cone angle selection criterion acted as an angular filtering mechanism to accept 3-hit combinations projected onto the $x-y$ plane. The dot product criterion provides a more refined version of the cone angle filtering mechanism since it investigates the angular separation of hits in 3-D.

Two unit vectors are defined for any 3-hit combinations surviving the previously outlined criteria. One vector is defined from the inner layer hit to the middle layer hit and the second from the middle layer hit to the outer layer hit. Since the constructed 3-D vectors are unit vectors, Eq. 7.2 shows that the dot product of the two unit vectors is a representation of the angular separation of the two vectors. Consequently, a new cone angle with an initial arbitrary value of 45° (0.7854 rad) is defined such that any 3-hit combinations with a dot product greater than cos(0.7854) (or equivalently with unit-vectors angular deviation of less than 45°) is considered a valid combination resulting in a track candidate. This filtering condition is the final scheme in filtering the 3-hit combinations.

$$\begin{gathered}\vec{\hat{R}}_1 \cdot \vec{\hat{R}}_2 = \hat{R}_{1x}\hat{R}_{2x} + \hat{R}_{1y}\hat{R}_{2y} + \hat{R}_{1z}\hat{R}_{2z} = \hat{R}_1\hat{R}_2\cos(\theta), \\ \vec{\hat{R}}_1 \cdot \vec{\hat{R}}_2 = \cos(\theta).\end{gathered} \tag{7.2}$$

Fig. 7.11 is a visual representation of dot product selection criterion implemented on set A hits where (a-b) demonstrates a 3-hit combination failing the criterion since the two unit vectors' angular separation is greater than 45° while (c-d) is a different 3-hit combination meeting the dot product filtering condition due to having a smaller angular separation.

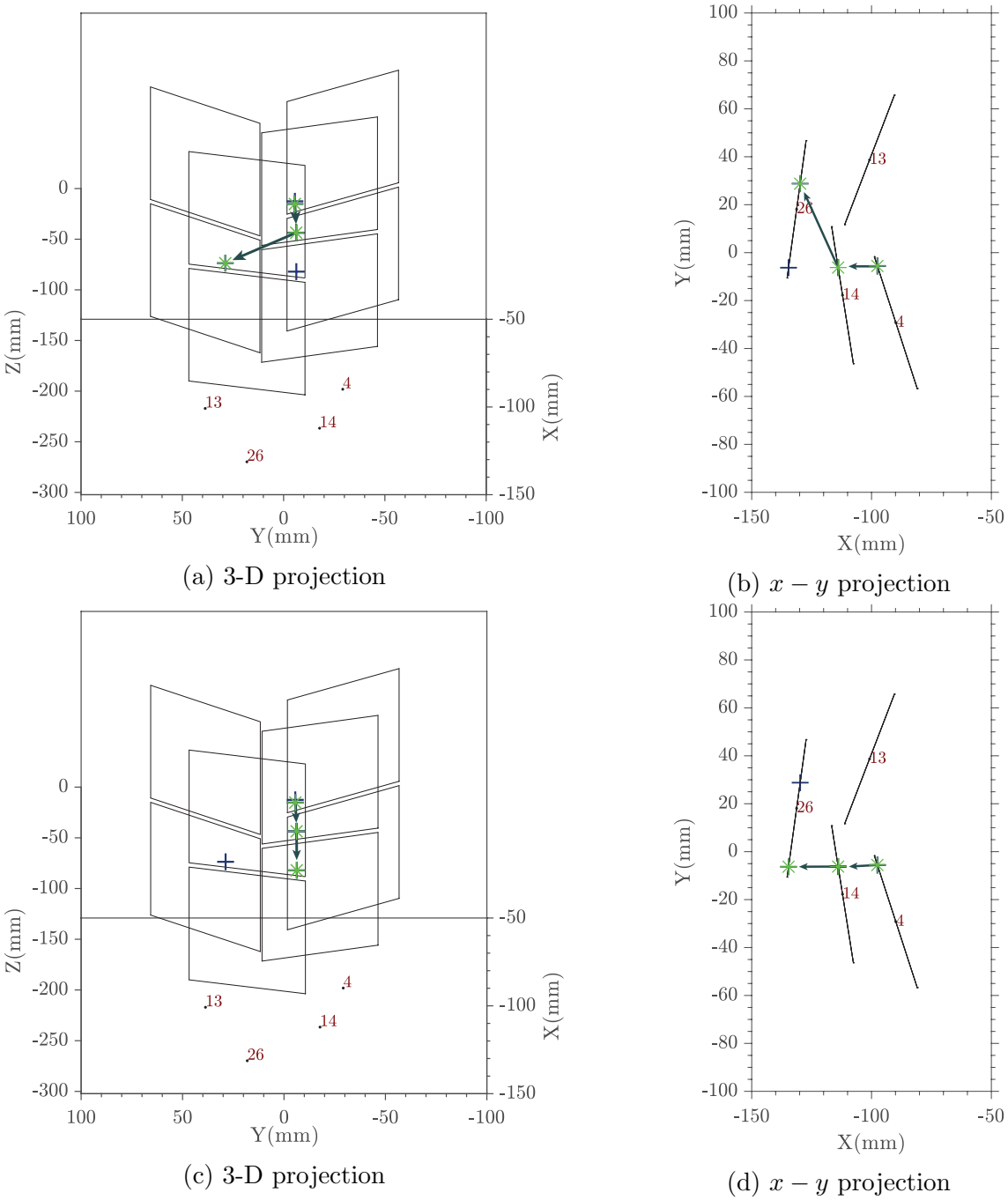

(a) 3-D projection

(b) $x - y$ projection

(c) 3-D projection

(d) $x - y$ projection

Figure 7.11: Illustration of the dot product filtering mechanism applied to the 3-hit combinations of set A where two unit vectors are created from hits on three different layers of the detector. (a-b) A 3-hit combination failing the dot product selection criterion. (c-d) A 3-hit combination meeting the dot product filtering condition. The unit vectors have been scaled for clarity.

7.2.4 Tuning track candidates

Subsequent to the various filtering criteria applied to the all 19 hits (sets A and B hits) of the example mixing event, each 3-hit combination represented with a specific

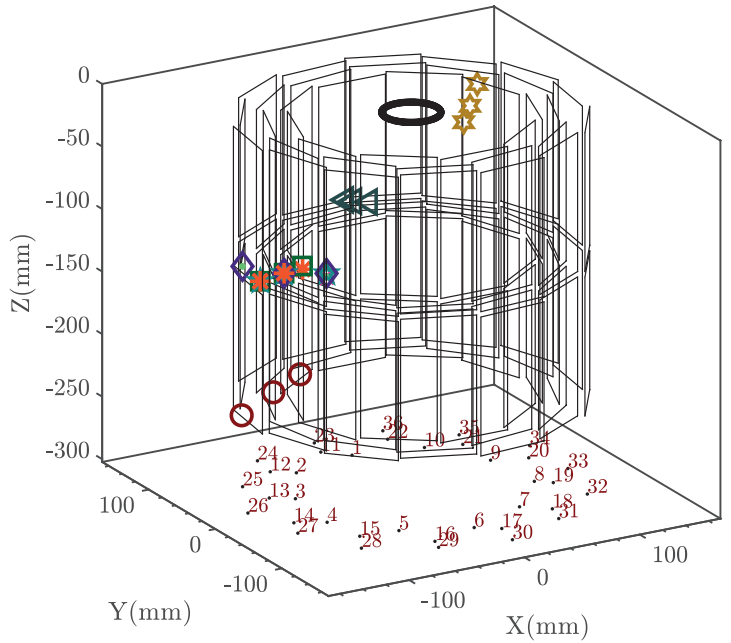

(a) Track candidates in 3-D projection

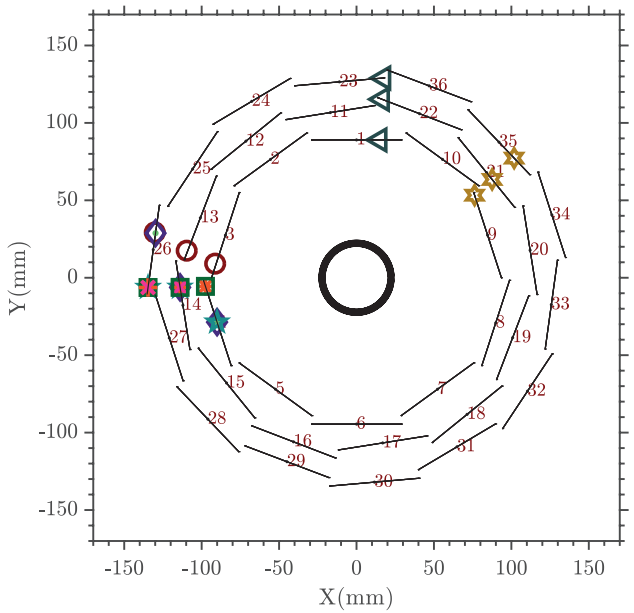

(b) Track candidates in $x - y$ projection

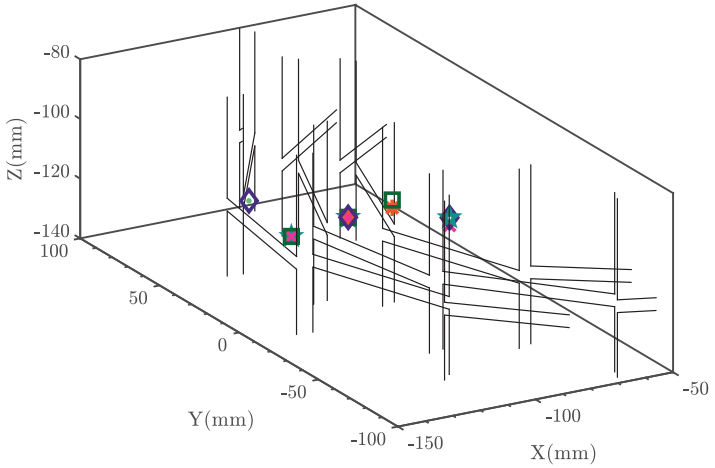

(c) Hybrid 4 track candidates

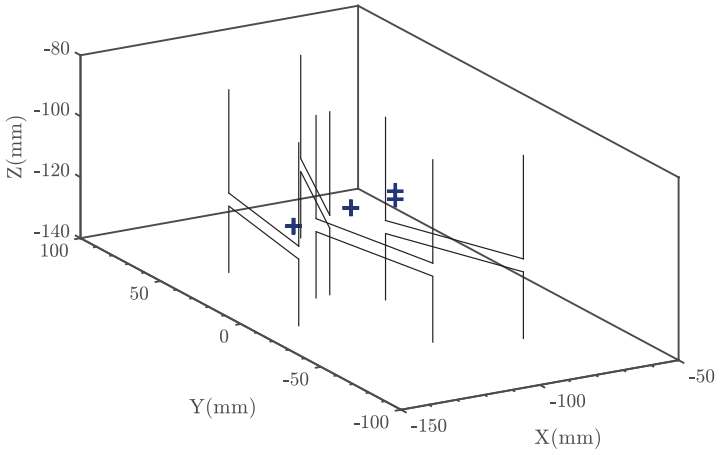

(d) Set A track candidates

Figure 7.12: Outcome of the various selection criteria applied to all the 19 hits (both sets of A and B) of the example mixing event. (a-b) All the 3-hit combinations meeting the selection criteria (track candidates) in 3-D and projected $x - y$ plane views, respectively. (c) An expanded view of the track candidates arising from hits on hybrid 4. (d) Final hits of set A meeting all the selection criteria. See the text for the explanation of the usage of various markers and colours for the 3-hit combinations.

marker in Figures 7.12(a) and 7.12(b) is a track candidate for a reconstructed track. However, there exist some combinations that merit further investigation. For instance, Fig. 7.12(d) demonstrates set A hits subsequent to all the selection criteria. As stated earlier, set A inner layer hits are located on hybrid 4 and are at very close proximity of each other. This implies that set A has two track candidates with their inner layer hits shared by a single hybrid (hybrid 4), resulting in two reconstructed tracks which, when projected onto the $x - y$ plane, are indistinguishable from each other. Hence, as a first step in tuning the track candidates, it is vital to determine which 3-hit combinations have shared hits on any of the detector layers.

An array of colours and markers is used to differentiate all the 3-hit combinations, see Figures 7.12(a)-7.12(c). It can be seen in Figures 7.12(b) and 7.12(c) that all of the four inner layer hits of hybrid 4, when combined with hits on the second and third layers, constitute six different 3-hit combinations. In total, the example mixing event has nine different track candidates which are capable of producing nine reconstructed tracks.

7.2.4.1 Helix construction

A charged particle traversing a solenoidal magnetic field will follow a helical path, assuming there are no ionization energy losses and no interactions due to multiple scattering. As a result, the track the particle follows through the apparatus and the detector can be approximated by a helix which, in turn, allows the reconstruction of the particle trajectory, vital for the determination of the vertex position. In addition, the construction of a helix allows further tuning of the track candidates.

The projection of a helix onto the $x - y$ plane is a circle. A helix to a 3-hit combination can be constructed by firstly projecting the hits onto the $x-y$ plane and subsequently assigning a circle such that it crosses the three hits on three different layers of the detector. Fig. 7.13 depicts all the reconstructed circles representing the $x - y$ projections of the helical tracks of the nine track candidates. The radius of curvature of a circle is a measure of how well the three hits of a helical track are

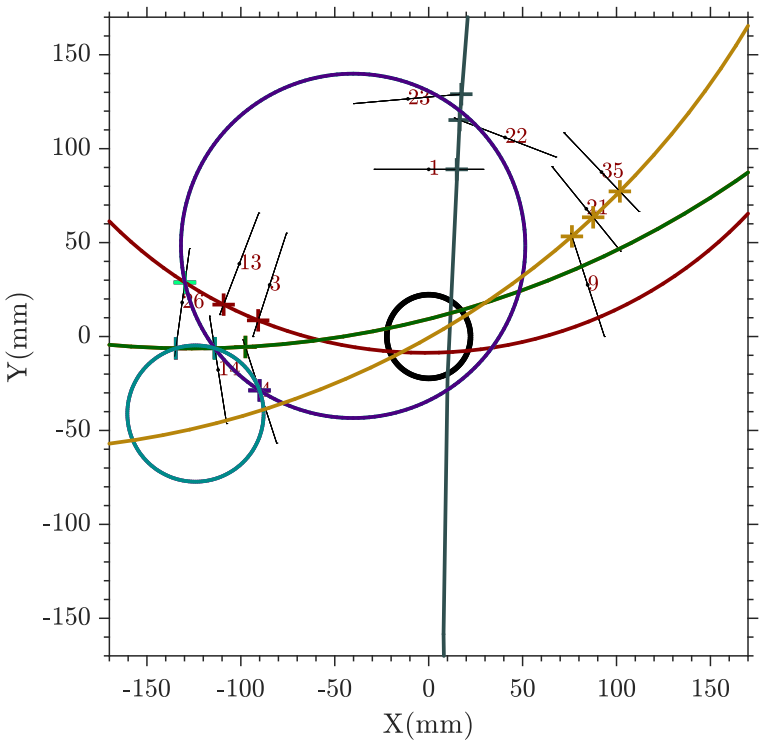

Figure 7.13: The $x-y$ projections of the helical tracks for the nine track candidates of the example mixing event. Only six circles are visible since some of the 3-hit combinations have shared hits and their reconstructed circles are superimposed when projected onto the $x-y$ plane.

aligned along a straight line. The dark slate grey and spring green circles represent the least and highest curved circles. As stated earlier, only six circles are visible since some of the 3-hit combinations have shared hits and therefore their reconstructed circles are superimposed when projected onto the $x-y$ plane.

Fig. 7.14 demonstrates the nine track candidates with part of their reconstructed circles. Each sub-figure's caption represents the track number and the hybrid containing the inner layer hit of that track. It is evident that hits on hybrid 4 result in six track candidates and therefore the corresponding six $x-y$ projected helices. Tracks 3 and 6, tracks 4 and 7, tracks 5 and 8 have shared hits on hybrid 4 and accordingly their $x-y$ projected helices are indistinguishable.

When a charged pion traverses the detector, it leaves only one distinct hit on each layer of the detector. Therefore, only one track candidate arising from the inner layer hybrid 4 is acceptable. The curvature of a circle passing through three hits on three different layers of the detector is a measure of the straightness or the

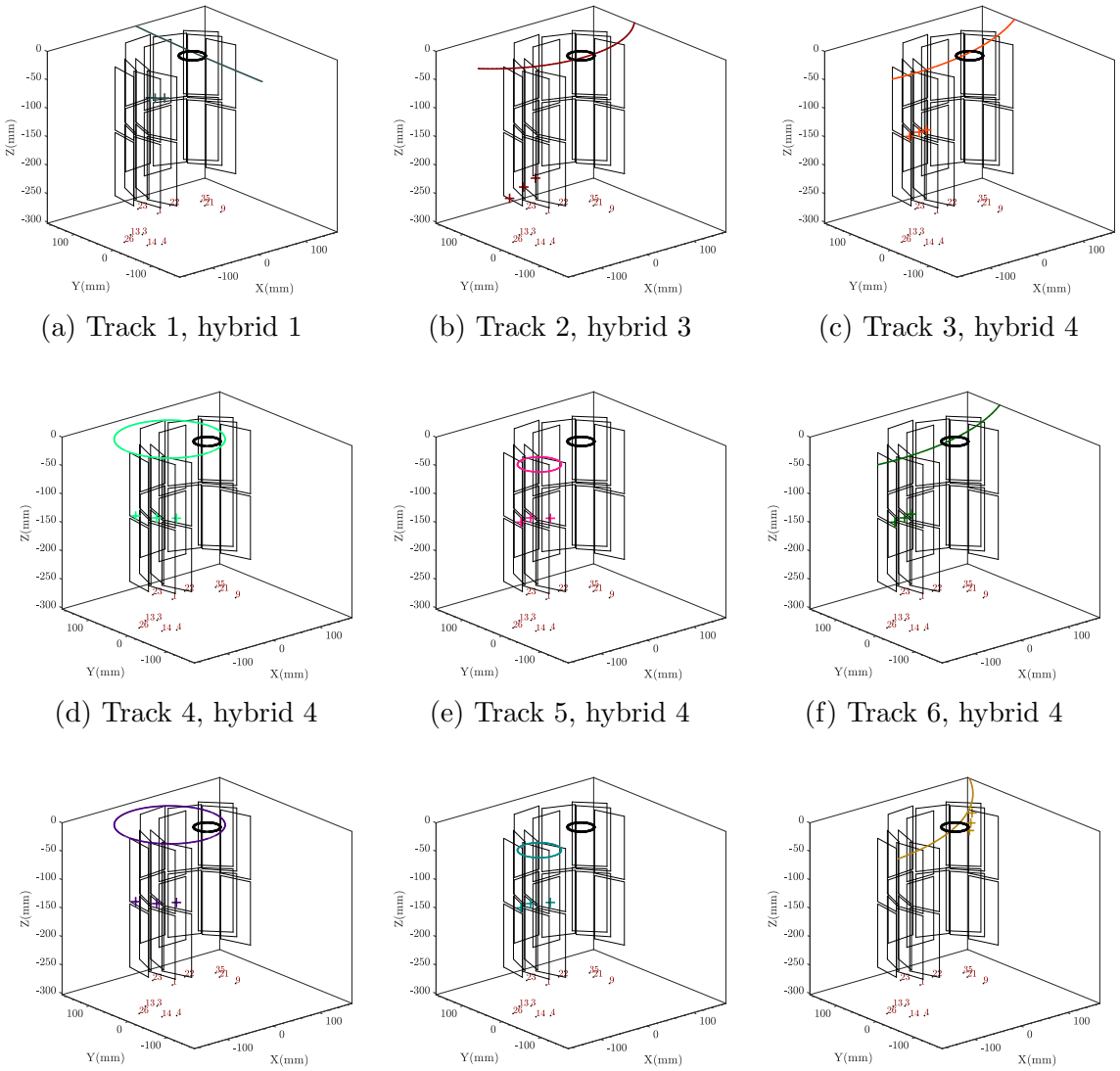

(a) Track 1, hybrid 1 (b) Track 2, hybrid 3 (c) Track 3, hybrid 4

(d) Track 4, hybrid 4 (e) Track 5, hybrid 4 (f) Track 6, hybrid 4

(g) Track 7, hybrid 4 (h) Track 8, hybrid 4 (i) Track 9, hybrid 9

Figure 7.14: Nine track candidates with part of their reconstructed circles. The label in each caption corresponds to the track number and the hybrid containing the inner layer hit of that track. Tracks 3 and 6, tracks 4 and 7, tracks 5 and 8 have shared hits on hybrid 4 and accordingly their $x - y$ projected helices are indistinguishable.

"stiffness" of the track reconstructed from the hits. Therefore, in order to determine the one acceptable track candidate from the six possible candidates of hybrid 4, any 3-hit combination with the least curvature (or equivalently the highest radius of curvature and therefore a more straight track) is selected. Referring to Fig. 7.14, of the six possible track candidates resulting from hybrid 4 (track 3 - track 8), tracks 3 and 6 have the least curvatures. Therefore, the remaining four tracks are filtered out. Tracks 3 and 6 have the same radius of curvature since they share those inner layer hits of hybrid 4 which are at very close proximity to each other. Hence, any

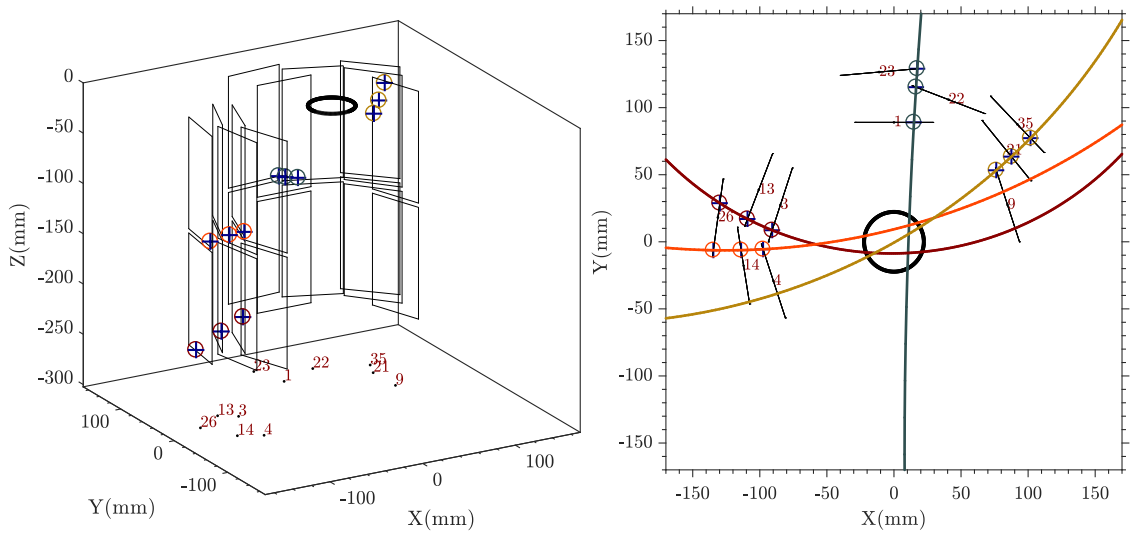

(a) 3-D projection (b) $x-y$ projection

Figure 7.15: (a) The final four best 3-hit combinations (track candidates). (b) Four circles constructed by the $x-y$ projections of the helices to the best three-hit combinations. The best 3-hit combination of Set A is shown by the hits having orange markers and reconstructed circle.

one of these two tracks can be considered as the best track candidate resulted from the passage of the charged pion through hybrid 4.

For the example mixing event considered, the outcome of the selection criteria and track tuning schemes indicate that there are four best track candidates which will contribute to the reconstruction of the tracks and consequently the determination of the vertex for this event. These four best 3-hit combinations along with their $x-y$ projected helices are presented in Fig. 7.15.

7.2.5 Pairing track candidates

Having identified the best track candidates and assigning an $x-y$ projected helical track (circle) to each candidate, further examinations of each track pair will proceed. For a set with n elements, the number of k-combinations is given by the binomial coefficient

$$\binom{n}{k} = \frac{n(n-1)...(n-k+1)}{k(k-1)...1} = \frac{n!}{k!(n-k)!}. \tag{7.3}$$

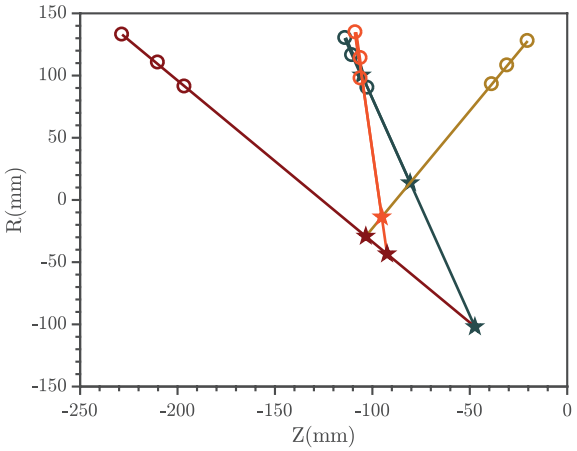

(a) $z-r$ projection

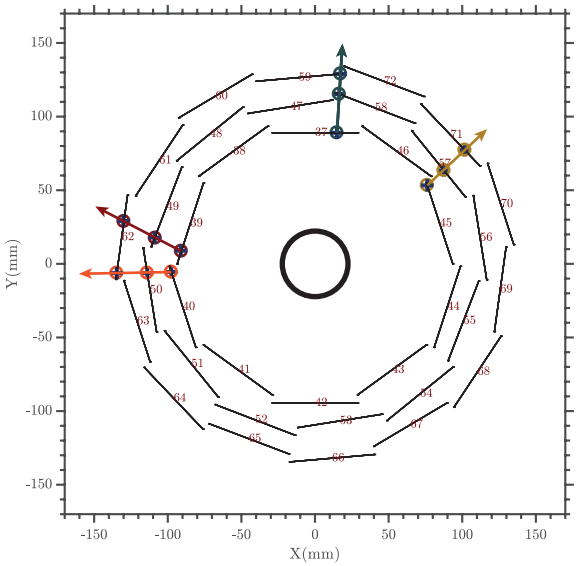

(a) $x-y$ projection of best lines of fit unit vectors

Figure 7.16: (a) $z-r$ projections of the best four track candidates. Each circle marker represents the (z,r) coordinate of a hit of a particular track candidate. A star is the (z,r) coordinate of the intersection of the two-paired tracks. (b) Unit vectors of the 3-D best lines of fit projected onto the $x-y$ plane. The unit vectors have been scaled for clarity.

Eq. 7.3 implies that for a set with 4 track candidates, the number of ways the tracks can be paired is $\frac{4!}{2!(4-2)!} = 6$.

Fig. 7.16(a) is the $z-r$ projections of the best four track candidates. Each circle marker denotes the (z,r) coordinate of a hit of a particular track candidate and the $z-r$ best lines of fit for a paired-track have been extrapolated in order to determine the intersection, indicated by a star, of the two fit lines. As an example, track 1, represented by dark slate grey, has three intersections shown by dark slate grey stars, which implies that the track has been paired with tracks 2 (dark red), 3 (orange red) and 4 (dark gold).

7.2.6 Normalization of pulse heights

Fig. 6.10 is a 2-D representation of the passage of a charged particle through the silicon bulk. The green solid line depicts a charged particle depositing its charge on one strip due to its small incident angle of θ_1 while the pink solid line is the repre-

sentation of a charged particle entering the detector module with a large incident angle of θ_2 and therefore crossing several strips.

A charged particle with an incident angle of 0° (relative to the normal of the hybrid) will have the minimum path length through the silicon bulk. This implies that minimum number of electron-hole pairs will be generated and therefore the two single strips at the front and rear of the module will have the minimum amount of deposited charged (pulse height). On the other hand, a charged particle with an incident angle close to 90° will have the maximum path length, creating the highest number of electron-hole pairs. The corresponding maximum generated charge will be deposited on several adjacent strips giving rise to signal clusters. It can be concluded that the incident angle of a charged particle can be utilized as a parameter to characterize the deposited charge (or equivalent energy) onto the hybrid.

The 2-D representation in Fig. 6.10 can be translated into 3-D by defining two unit vectors, see Fig. 7.17. For any track candidate, one unit vector acting as the directional vector is the normal vector pointing outwards from the hit on the inner layer hybrid (black arrows in Fig. 7.17). The other unit vector is represented by the 3-D best line of fit to the three hits of each track candidate (see Fig. 7.16(b) and red arrows in Fig. 7.17).

A charged particle with a zero incident angle corresponds to the two unit vectors subtending an angle of 0° while a particle with an incident angle of 90° results in a subtended angle of 90° between the two unit vectors. The dot product of two unit vectors is a scalar value which can be used as a normalization factor for the deposited energy of a charged particle. Dividing the deposited energy (the pulse height) by the dot product of the unit vectors provides the normalization of the collected charged and therefore reflecting the deposited energy.

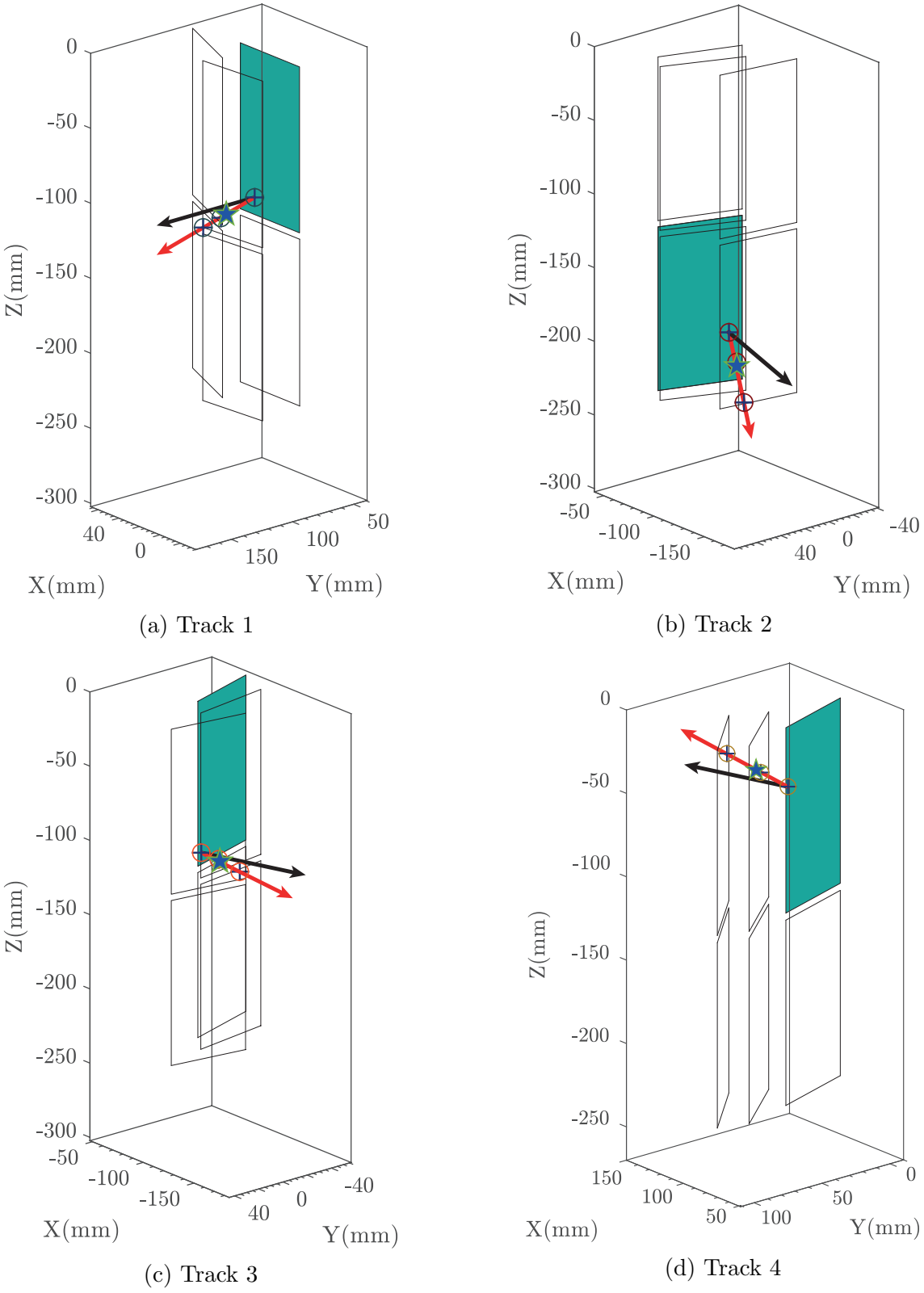

(a) Track 1

(b) Track 2

(c) Track 3

(d) Track 4

Figure 7.17: Visual representation of the dot product between the unit vectors of the inner hybrids' normal (black arrows) and the line of best fit to the 3-hit combinations (red arrows) for the best four track candidates. Also included on each line of best fit is the position of the centroid (blue star with green outline). The unit vectors have been scaled for clarity.

7.3 Track reconstruction

The determination of the position of an antiproton annihilation relies on reconstructing the trajectories of charged particles. As opposed to the Standard Reconstruction Method whereby the tracks are reconstructed using the analytical solution of helices produced by the motion of charged pions in the magnetic field of the external solenoid, the Alternative Reconstruction Method utilizes a numerical scheme to reconstruct the tracks. The following paragraphs provide a detailed description and a visual representation of the track reconstruction using the Alternative Reconstruction Method. These paragraphs, used in conjunction with Fig. 7.18, focus on the reconstruction of the track corresponding to $x-y$ projected helix of the dark red track candidate in Fig. 7.15(b).

Fig. 7.18 is a schematic diagram for visual representation of the three hits (dark blue crosses and the circle markers) of the track candidate and the $x-y$ projected helix (dark red circle) employed to reconstruct the track through these hits. The angular positions of the outer and inner layer hits (θ_{out} and θ_{in}) in the reference frame of the circle are determined. It is noted that these two variables are different to the ϕ angles, presented in Table 7.1, where the angular position of a hit is measured in the reference frame of the detector.

When an annihilation occurs, the charged particle traces a helical path along the direction of the magnetic field lines (or equivalently the detector axis) as it traverses the three layers of the detector. Reconstructing tracks employs the reverse process whereby it is attempted to construct the helical path of the charged particle towards the annihilation origin and subsequently along the magnetic field lines, see Fig. 7.19. However, the vertex reconstruction deploys only the part of the reconstructed track within the inner layer volume of the detector. Therefore, each track is segmented into s parts, each containing n dots amounting to a total of $N = s \times n$ track dots for each track. The first segment corresponds to the angular displacement between the outer and inner hits in the circle reference frame ($\Delta\theta$) as illustrated in the bottom

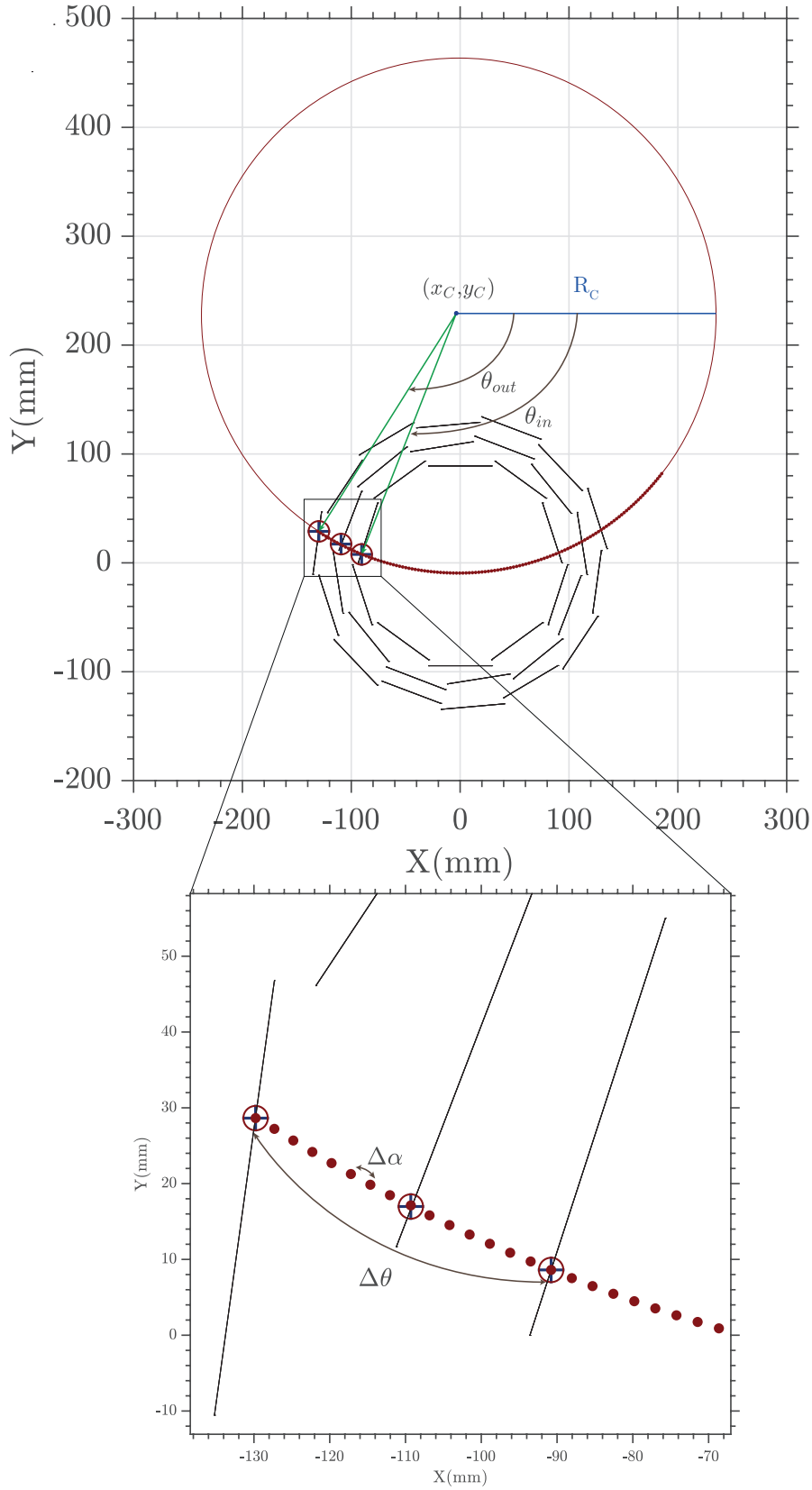

Figure 7.18: The visual representation of reconstructing a track resulted from a track candidate. Top: the three hits (dark blue crosses and the circle markers) of the track candidate and the $x - y$ projected helix (dark red circle) employed to reconstruct the track through these hits. Bottom: an expanded view of the three hits and the track dots. See the text for descriptions of the parameters.

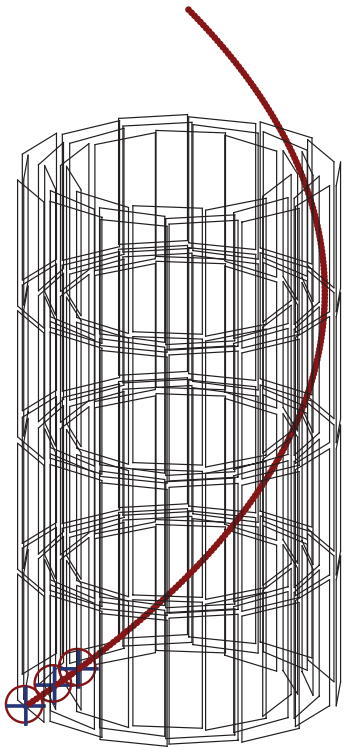

Figure 7.19: Reversed process of the helical motion of the charged particle giving rise to the track candidate.

part of Fig. 7.18. The spacing between dots ($\Delta\alpha$) of a segment is calculated by dividing the angular displacement by the total number of dots in that segment ($\Delta\alpha = \Delta\theta/n$). For convenience, the first dot is assigned to coincide on the outer layer hit. Therefore, the angular position of a given dot is determined by

$$\alpha_i = \theta_{out} + i \times \Delta\alpha, \tag{7.4}$$

where $i = 0...N$-1 and α_i are the dot index and the angular position of a dot with index i in the circle reference frame, respectively. Eq. 7.4 allows α_0 (the angular position of the first dot of the reconstructed track) to be equivalent to the angular position of the outer layer hit.

In order to draw a track dot, its (x, y, z) coordinates must be determined. In the reference frame of the circle, the x and y positions of a track dot are calculated as

$$\begin{aligned} x'_i &= R_C \times \cos\alpha_i, \\ y'_i &= R_C \times \sin\alpha_i, \end{aligned} \tag{7.5}$$

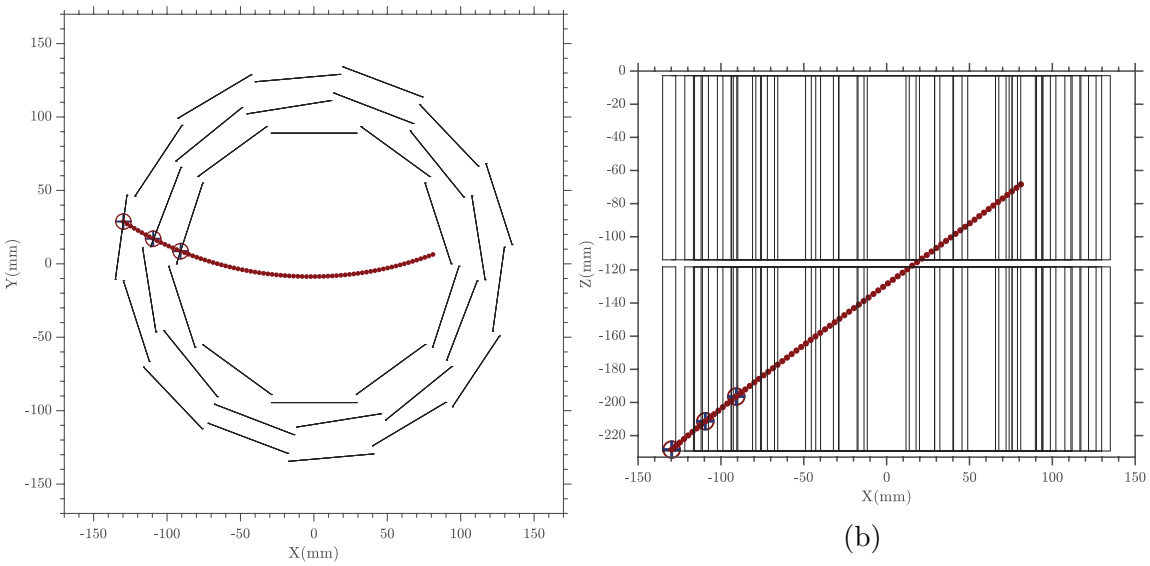

(a) (b)

Figure 7.20: (a) $x-y$ and (b) $x-z$ projections of the reconstructed track subsequent to being subjected to the track length cut.

where R_C is the radius of the $x-y$ projected helix of the track candidate (circle). The z locations of the outer and inner layer hits (z_{out} and z_{in}) are the same in both the circle and detector reference frames. Therefore, the z-coordinate of a hit can be obtained from Table 7.1. The corresponding track dot z-coordinate in the circle reference frame is given by Eq. 7.6 where z'_i and Δz are the z-coordinate of the dot with index i and the z-axial displacement between the outer and inner layer hits, respectively.

$$\begin{aligned} \Delta z &= z_{out} - z_{in}, \\ z'_i &= z_{out} + i \times \frac{\Delta z}{n}, \end{aligned} \tag{7.6}$$

The (x, y, z) coordinates of the track dots in the reference frame of the circle (x'_i, y'_i, z'_i) can be readily converted into the detector reference frame (x_i, y_i, z_i) by

$$\begin{aligned} x_i &= x_C + x'_i, \\ y_i &= y_C + y'_i, \\ z_i &= z'_i, \end{aligned} \tag{7.7}$$

where x_C and y_C are x and y coordinates of the centre of the circle in the detector reference frame.

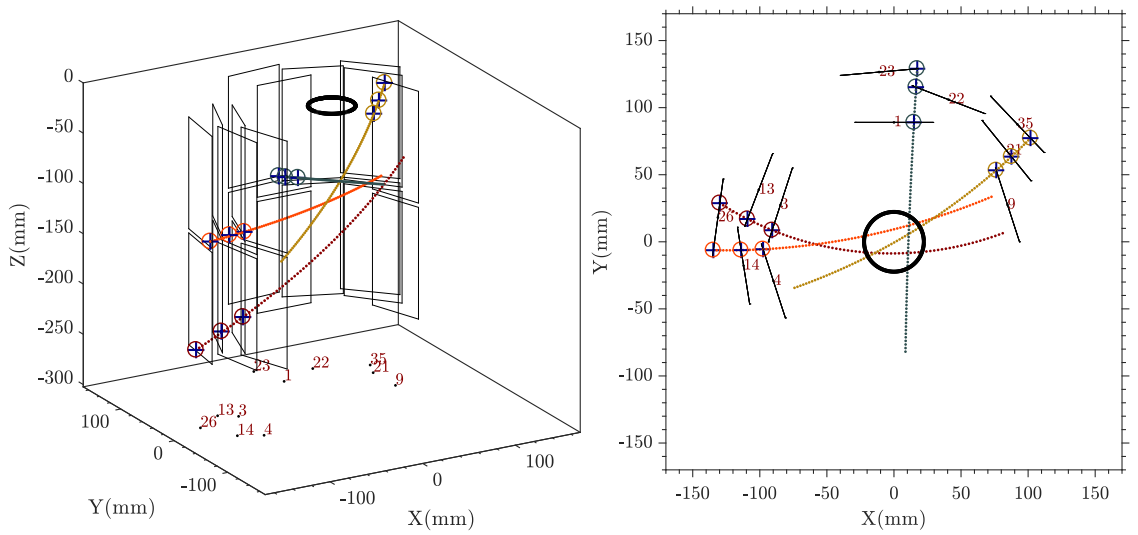

(a) 3-D projection (b) $x - y$ projection

Figure 7.21: The reconstructed tracks of the best four track candidates presented in (a) 3-D and (b) $x - y$ projection views.

Equipped with x_i, y_i, z_i and $N = 15 \times 8 = 120$, the extrapolated track is reconstructed and shown as 120 dark red dots superimposed on the $x - y$ projected helical path in the top part of Fig. 7.18. It can be seen that the reconstructed track has exited the detector volume. A cut variable can be employed to control the length of a track, or equivalently the number of dots. For the track extrapolation to terminate within the detector inner layer with a radius of 89 mm, firstly the index of the track dot with minimum radius is determined. Secondly, for any subsequent dot from the dot with minimum radius, as long as the dot radius is smaller than 89 mm (i.e. the dot is within the detector volume) and not exceeding the dot index of N, it will be drawn. Fig. 7.20 is the outcome of implementing such cut variable where $x - y$ and $x - z$ projections of the reconstructed track are illustrated.

Fig. 7.21 is the illustration of the 3-D and $x - y$ projection views of the reconstructed tracks for the best four track candidates.

7.4 Vertex reconstruction

The tracks identified and reconstructed in Sec. 7.3 form the inputs into the method for the determination of the position of an antiproton annihilation (the vertex),

which is the principal objective of the event reconstruction algorithm. The vertex position is determined as the Point Of Closest Approach (POCA) between the tracks.

Multiple scattering leads to divergence of the reconstructed tracks from the true annihilation position and accordingly the intersection of reconstructed tracks will not be generally a single fixed point. This explains the requirement for the identification of the vertex coordinates (x_v,y_v,z_v) as the point where the tracks pass closest to each other.

7.4.1 Distance of closest approach

The point of closest approach between paired reconstructed tracks is illustrated in Fig. 7.22. The minimum distance between a paired track is indicated by the dark blue line. In addition, the midpoint of the blue line is denoted by the asterisk enclosed by the circle and is the representation of the point of closest approach between the paired extrapolated trajectories.

The point of closest approach between any paired reconstructed tracks is determined by the function *'fminsearch'* (see Appendix C), devised to conduct local searches with the aim of minimizing the distance between the paired tracks in the 3-D reference frame of the detector. For any paired tracks, the function accepts an initial guess ($V_0 = x_0, y_0, z_0$) and the residual for one track of the paired combination is defined as

$$\begin{aligned} \delta_{xi} &= (x_i - x_0)^2, \\ \delta_{yi} &= (y_i - y_0)^2, \\ \delta_{zi} &= (z_i - z_0)^2, \\ \delta_1 &= \min\Big\{(\delta_{xi} + \delta_{yi} + \delta_{zi})\Big\}, \end{aligned} \tag{7.8}$$

where $i = 1...N_{\text{cut}}$ is the index of the dot constituting the reconstructed track, N_{cut} is the total number of dots of the reconstructed track determined by the track length cut and δ_1 represents the minimum residual of the reconstructed track of the

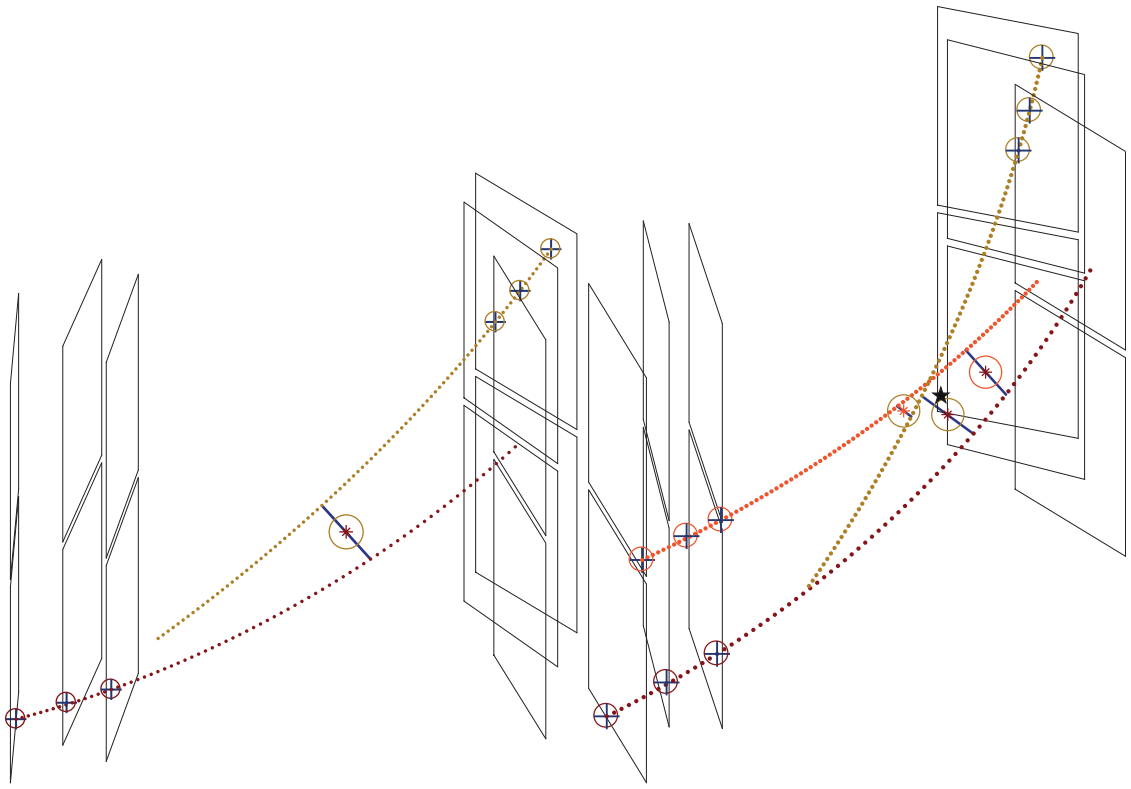

(a) Two-track event (b) Three-track event

Figure 7.22: Spatial illustration of the Point Of Closest Approach (POCA) between (a) two tracks and (b) three tracks. The dotted curves represent the reconstructed tracks. The midpoint along the dark blue line, the smallest distance between two helices, is indicated by the asterisk enclosed by the circle and corresponds to the point two tracks pass closest to each other, the POCA. The POCA is the vertex position in the case of a two-track event as in (a). The vertex position in the case of the three-track event in (b) is represented with a black star. The colour choice for the circle and the asterisk representing a POCA matches that of the paired tracks resulting in the POCA.

paired combination, i.e. the residual of the dot closest to the guessed point V_0. The combined residual for a paired track is therefore defined as

$$\delta = \delta_1 + \delta_2, \tag{7.9}$$

where δ_2 is the minimum residual for the second track. For the two paired tracks, the *'fminsearch'* proceeds with its local search until a point with a minimum value of δ is attained and this point is subsequently considered as the POCA ($d = (d_x, d_y, d_z)$) for the pair. The remaining paired tracks of the annihilation event follow the same scheme and the outcome is the assignment of a POCA and the corresponding mini-

mum residual to any paired combinations.

7.4.2 Vertexing

Combining the points of closest approach for all the paired helices allows one to obtain an estimate for the vertex. In addition, the δ value can be interpreted as a measure of how close the two paired tracks pass each other. A small value of δ indicates that the two paired tracks converge well in the proximity of the POCA, whereas a large value implies otherwise, i.e. the tracks do not extrapolate to a common point. Therefore, the δ value can be incorporated as a quality (weighting) factor in determining the vertex position. This weighting factor takes into account the sensitivity of the vertex to outliers such as any inadequately reconstructed track or a track not extrapolated to the annihilation point that could have shifted the vertex position significantly. The steps in determining an estimate for the vertex is as follows:

- For a particular annihilation event, the total number of paired reconstructed tracks (N_{paired}) is determined.
- For any paired tracks, the POCA ($d = (d_x, d_y, d_z)$) and a corresponding average residual (δ_{ave}), defined by Eq. 7.10, are obtained.

$$\delta_{ave} = \sqrt{(\frac{\delta}{2})}. \tag{7.10}$$

- A weighting (quality) factor for each POCA is determined by

$$w = \sum_{t=1}^{N_{paired}} (\delta_{ave})_t - \delta_{ave} + \epsilon, \tag{7.11}$$

  where the first term on the right is the combined residual due to all the paired tracks. The addition of ϵ to 7.11 is intended as an offset for events with only two tracks.

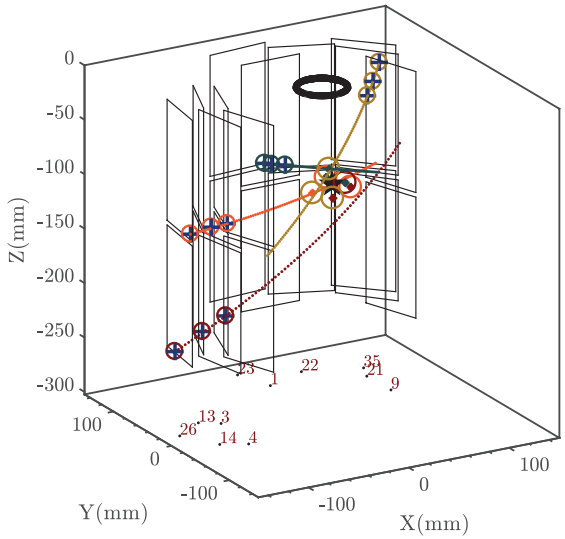

(a) Partial 3-D projection

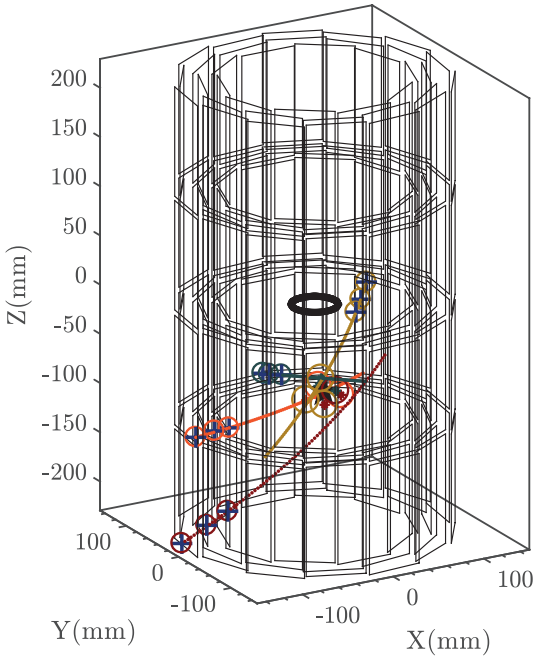

(b) Full 3-D projection

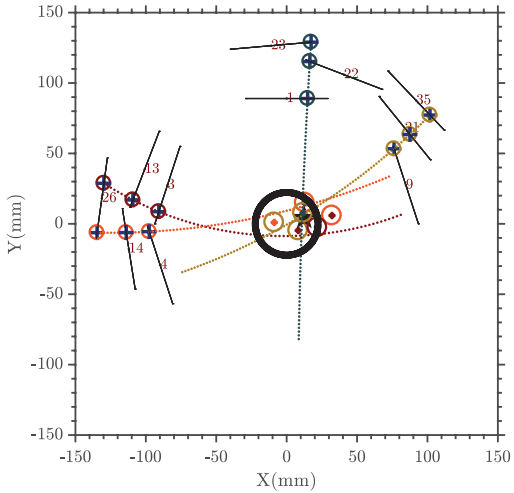

(d) x - y projection

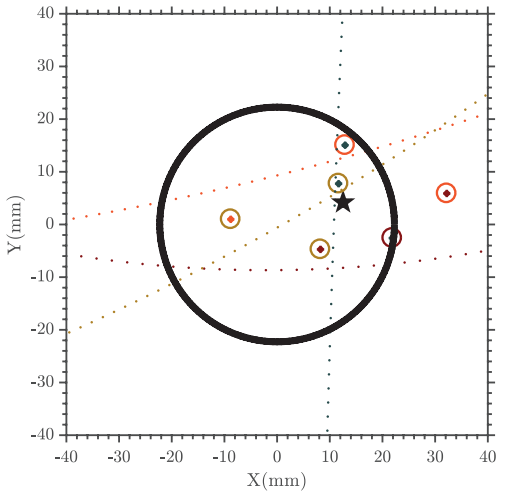

(d) Expanded x - y projection

Figure 7.23: Visual representation of the reconstructed vertex (black star) shown in four different views, (a) partial view only illustrating the hybrids containing the hits, (b) full detector view of all the hybrids, (c) $x-y$ projection of hybrids containing the hits and (d) the expanded view of the reconstructed vertex.

- The x, y and z coordinates of the vertex in the detector reference frame (x_v, y_v, z_v) are determined by Eq. 7.12. As illustrated in Fig. 7.22(a), in the case of a two-track event, $N_{paired} = 1$ and therefore $\sum_{t=1}^{1}(\delta_{ave})_t = \delta_{ave}$. This implies that Eq. 7.11 results in $w = \epsilon$, an infinitesimal residual contribution to the estimation of the vertex position. Equivalently, it is evident from Eq. 7.12 that when $N_{paired} = 1$, the weighting factor cancels out from the numerator and denominator and accordingly the 3-D annihilation vertex of the two tracks is the point of closes approach, i.e. the common point of origin. For higher track events, such as a three-track event in Fig. 7.22(b), the estimation of the vertex position will be affected by the contribution from the residual of the paired tracks.

$$
\begin{aligned}
x_v &= \frac{\sum_{t=1}^{N_{paired}} w_t (d_x)_t}{\sum_{t=1}^{N_{paired}} w_t}, \\
y_v &= \frac{\sum_{t=1}^{N_{paired}} w_t (d_y)_t}{\sum_{t=1}^{N_{paired}} w_t}, \\
z_v &= \frac{\sum_{t=1}^{N_{paired}} w_t (d_z)_t}{\sum_{t=1}^{N_{paired}} w_t}.
\end{aligned}
\tag{7.12}
$$

Fig. 7.23 is the final outcome of the event vertex reconstruction algorithm. It depicts four different views of a reconstructed vertex (black star) corresponding to the same mixing event presented in Fig. 7.4. It demonstrates the capability of Alternative Reconstruction Method (ARM) in reconstructing a vertex compared to that of the Standard Reconstruction Method (SRM) in Fig. 7.3. It is evident that the ARM produces the same output as the SRM for this particular event, a verification of the validity of both methods.

7.5 Results

7.5.1 Vertex reconstruction enhancement

Having identified a vertex arising from the annihilation of an antiproton, this section describes the vertex reconstruction enhancement resulting from the ARM. The two

filtering angles (the cone angle, see Sec. 7.2.3.1, and the dot product, see Sec. 7.2.3.3) for selecting the best track candidates are the prime parameters having the most significant contribution to the vertex reconstruction. The cone angle filtering aimed at selecting hits residing within the $x - y$ projected cone on three different layers of the detector while the dot product filtering angle was defined such that any 3-hit combinations with a dot product greater than the cosine of the corresponding angle was considered a valid combination for track reconstruction.

A scan of the two combined cone and dot product filtering-angle parameters of the Alternative Reconstruction Method for investigating the vertex efficiency is illustrated in Fig. 7.24(a). Utilizing a total of 29,965 mixing events, the vertical red plane depicts an absolute vertex efficiency of 83.5% for the Standard Reconstruction Method (η_{SRM}), an indication that out of the 29,965 mixing events, 25017 events have resulted in 2 or higher reconstructed tracks (see Table. 6.1) and therefore the attainment of a vertex for each of those events. The ARM with a filtering-angle scan parameter of 40°-50° results in a vertex efficiency of 84.8% (η_{ARM}). The relative vertex efficiency comparing the Standard and Alternative Reconstruction Methods is defined by

$$\eta_{\text{rel.}} = \frac{\eta_{\text{ARM}} - \eta_{\text{SRM}}}{\eta_{\text{SRM}}}, \tag{7.13}$$

and is shown in Fig. 7.24(b). The filtering-angle scan parameter of 40°-50° leads to a vertex efficiency enhancement of 1.5%. Furthermore, as each filtering angle is increased, the number of reconstructed vertices also increases, consistent with the fact that more hits will pass the selection criteria and more tracks are reconstructed from the 3-hit combinations. An increase in the reconstructed tracks, in turn, leads to further enhancement of reconstructed vertices. It is noted that filtering angles exceeding the 40°-50° parameter have led to insignificant enhancements of the vertex reconstruction and consequently are not shown in the plot. Attributing a physical process as to why the vertex reconstruction enhancement ceases beyond 40°-50° parameter is challenging since they are several parameters, such as the $r - z$ normal

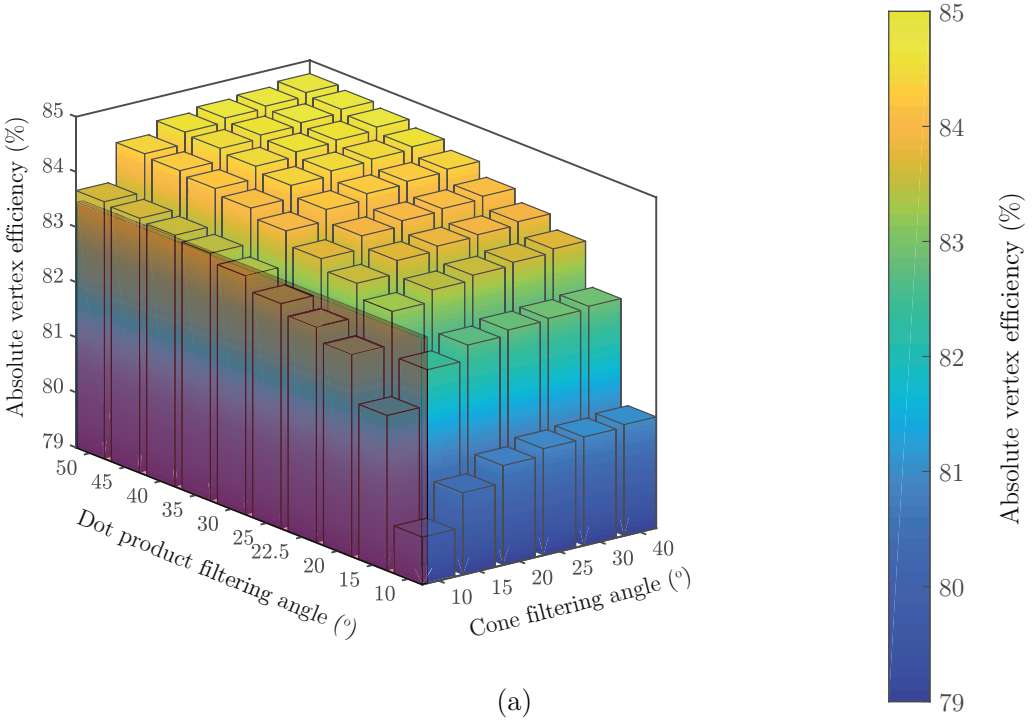

(a)

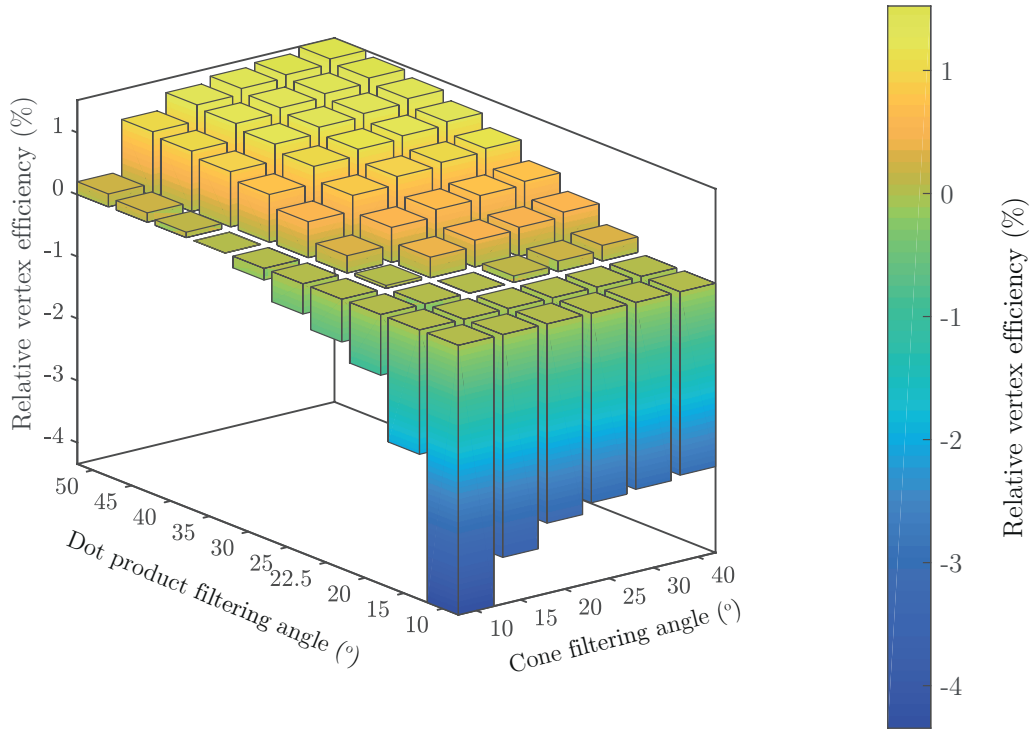

(b)

Figure 7.24: (a) Absolute values of vertex efficiency for the Standard Reconstructed Method (SRM) (red plane) and various filtering-angle scan parameters of the Alternative Reconstruction Method (ARM). The SRM has an absolute vertex efficiency of 83.5% while the ARM with a filtering-angle scan parameter of 40°-50° results in a vertex efficiency of 84.8%. (b) Relative vertex efficiency comparing the Standard and Alternative Reconstruction Methods. The filtering-angle scan parameter of 40°-50° leads to a vertex efficiency enhancement of 1.5%.

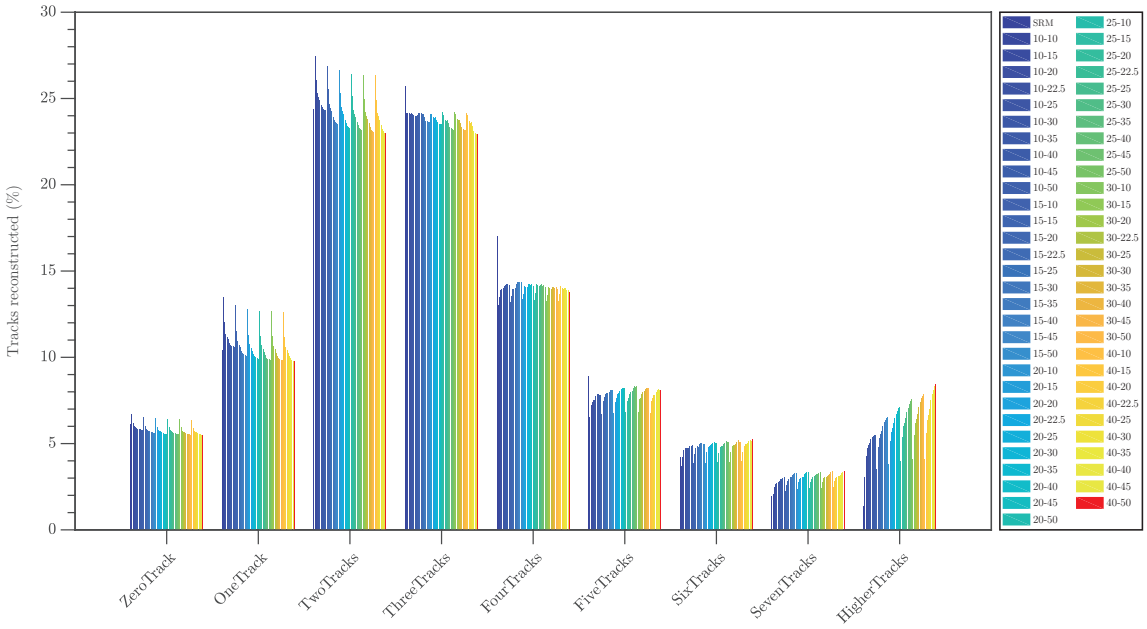

Figure 7.25: Reconstructed tracks comparison between the Standard Reconstruction Method (SRM) and various combined filtering angles scan parameters of the Alternative Reconstruction Method. The two-number combinations of the legend correspond to the cone angle and the dot product filtering angles (in degrees). The red indicates the filtering-angles scan parameter resulting in the highest vertex reconstruction efficiency. The ARM performs superior to the SRM for vertex reconstruction of six, seven and higher-tracks events.

threshold, which simultaneously contribute to the reconstruction of a vertex.

Fig. 7.25 is an illustration of the distribution of the number of tracks reconstructed for both the SRM and various ARM scanning parameters. The parameter with the highest reconstruction efficiency is shown in red. It is evident from this plot that the ARM is superior to the SRM for vertex reconstruction of six, seven and higher-tracks events.

7.5.2 The APA plus ARM enhancement

Combining the enhancements due to the Alternative Pedestal Analysis and the Alternative Reconstruction Method, Fig. 7.26(a) is the demonstration of the absolute vertex efficiencies of the Standard Pedestal and Reconstruction methods (SPA + SRM) as well as the Alternative Pedestal and Reconstruction methods (APA + ARM). This figure indicates that combining the best pedestal parameter, namely $3.5\sigma_0$-$2.5\sigma_1$-$1.5\sigma_0$ combined with the n- and p-side strip signal thresholds of $3.6\sigma_3$,

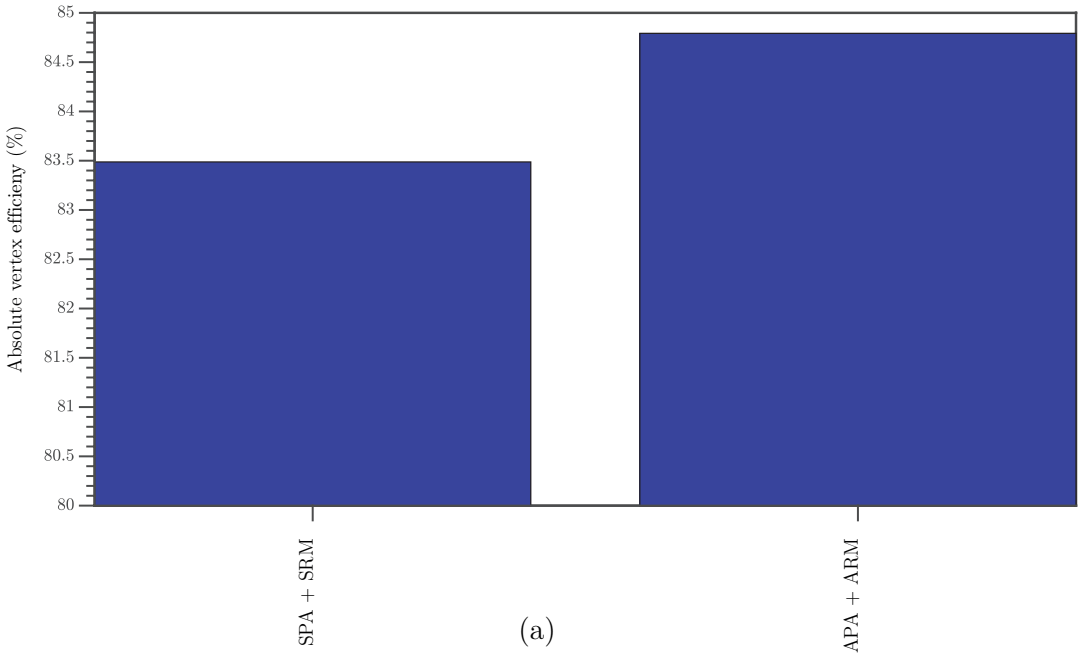

(a)

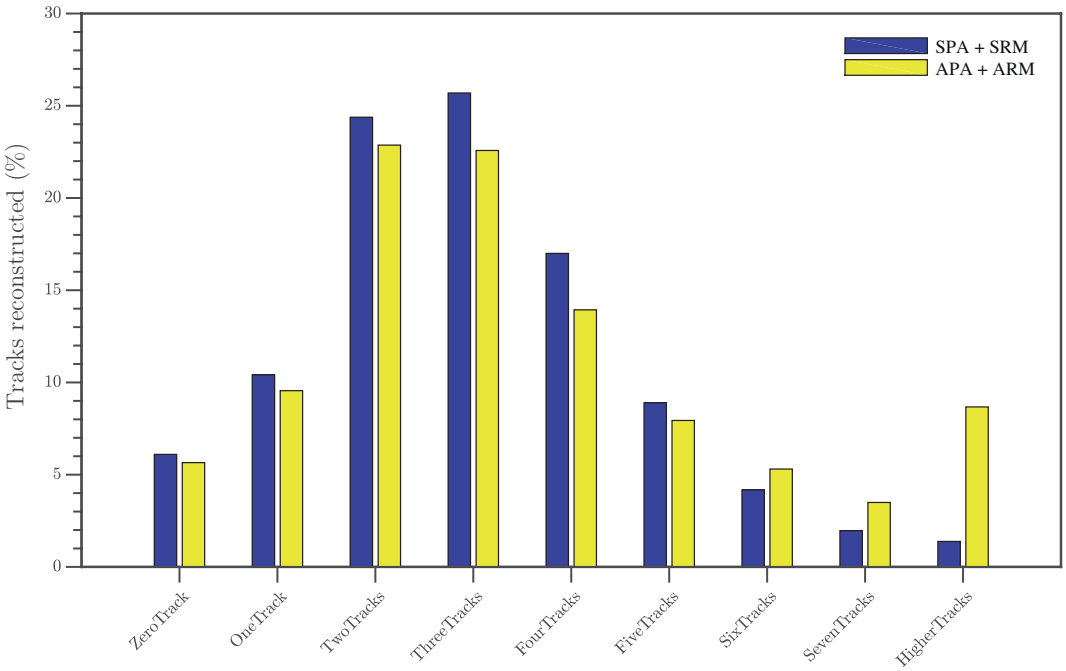

(b)

Figure 7.26: (a) Absolute vertex efficiency comparison between the Standard Pedestal and Reconstruction methods (SPA + SRM) as well as the Alternative Pedestal and Reconstruction methods (APA + ARM). Combining the best pedestal parameter, namely $3.5\sigma_0$-$2.5\sigma_1$-$1.5\sigma_0$ combined with the n- and p-side strip signal thresholds of $3.6\sigma_3$, with the best vertex reconstruction parameter of 40°-50° (corresponding to the cone and dot product filtering angles, respectively) leads to an overall increase in the vertex reconstruction efficiency by 1.5% compared with the combined SPA and the SRM. (b) Reconstructed tracks comparison between the Standard and Alternative Methods. Alternative Pedestal and Reconstruction methods reconstruct vertices more efficiently for events with six, seven and higher tracks.

with the best vertex reconstruction parameter of 40°-50° (corresponding to the cone and dot product filtering angles, respectively) leads to an overall increase in the vertex reconstruction efficiency by 1.5% compared with the combined SPA and the SRM.

Consistent with the distribution of the percentage of tracks reconstructed in Fig. 7.25, Fig. 7.26(b) clearly illustrates the superiority of the Alternative Pedestal and Reconstruction Methods in reconstructing vertices for mixing events resulting in six or higher tracks.

7.5.3 Vertex distribution

7.5.3.1 Bare antiproton

The radial confinement of the antihydrogen atoms is achieved by integrating an octupole magnet into the atom trap which gives rise to the radially increasing magnetic field. However, this integration results in the disturbance of the azimuthal symmetry of the Penning trap field required for the confinement of the charged particles. Figures 7.27(a) and 7.27(b), resulting from 6 experimental cycles where a total of 22.8×10^4 antiprotons were subjected to the octupole fields during the operation of the ALPHA-I SVD, demonstrate the bare antiproton annihilation distributions in the octupole magnetic field. The radius of the antiproton cloud was increased by the corresponding prompt change (on the order of microseconds) in the electrostatic well confining the antiprotons. Subsequently, the ramp-up of the octupole current allows the antiprotons with radius greater than the critical loss radius [81] to be guided towards the electrode wall by the octupole field lines.

Fig. 7.27(a) shows the z-integrated $x-y$ projection, where eight octupole-induced annihilation points are apparent. The eight spots correspond to the antiprotons in the octupolar field following the field lines and meeting the electrode wall. Fig. 7.27(b) is the vertex distribution along the z axis where the electrostatic confining potential determines the locations of the two peaks at approximately $\pm$ 3 cm [31].

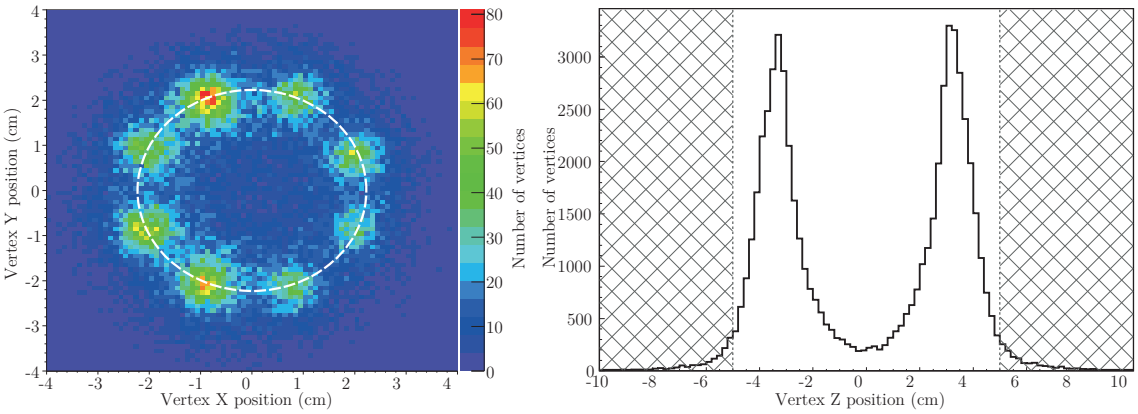

(a) $x - y$ projection (b) z projection

Figure 7.27: Vertex distribution of bare antiproton annihilations during the mixing phase where antihydrogen atoms are formed while the neutral trap magnets are energized. (a) The $x - y$ projection of the vertex distribution, with the colour palette indicating the number of vertices in each bin. The dashed white circle shows the position of the electrode wall. (b) The z distribution of vertices with the unhatched region representing the extent of the electrodes producing the confining electric potential. The zero position corresponds to the centre of the atom trap. The plots have been obtained from the Standard Reconstruction Method during the operation of the ALPHA-I SVD. Image adapted from [31].

7.5.3.2 Bound antiproton

The antihydrogen atoms are formed during the mixing phase where antiprotons are mixed with positrons in the magnetic field of the neutral-atom trap. During this phase, as the charged plasmas interact, there are no manipulating magnetic or electric fields present and most of the reconstructed vertices are due to the annihilation of the bound antiprotons of unconfined antihydrogen atoms formed above the atom trap depth and reaching the trap wall. Figures 7.28(a)-(b) show the z-integrated $x - y$ projection and the z distribution, respectively, of the vertices reconstructed by the Standard Reconstruction Method of the ALPHA-II SVD and correspond to the mixing sampling data in Table 6.1.

Although the reconstruction of bare and bound antiprotons events employs the same method, the overall spatial vertex distribution differs considerably, see Figures 7.27(b) and 7.28(b). The distribution in Fig. 7.28(b) contains a contribution due to the bare antiprotons following the magnetic field lines of the octupole. The positions of the two peaks due to the antiprotons resulting in weakly-formed bound

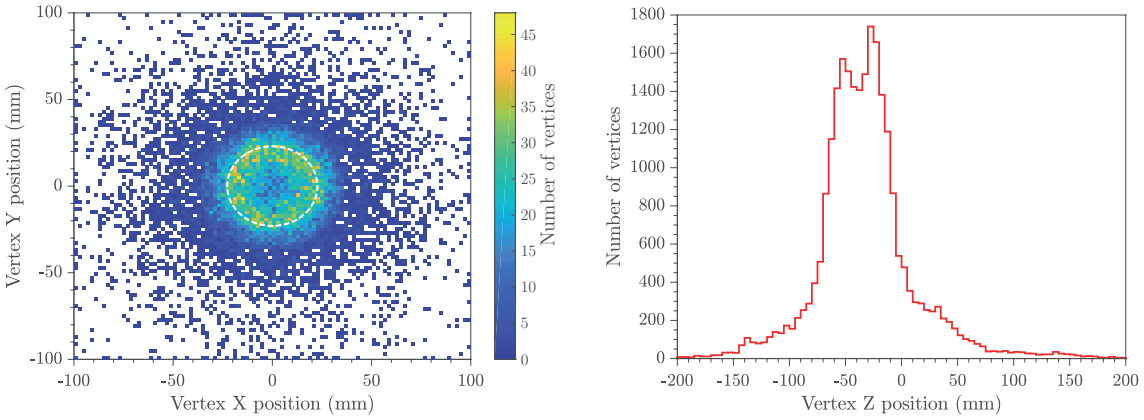

(a) $x-y$ projection (b) z projection

Standard Reconstruction Method

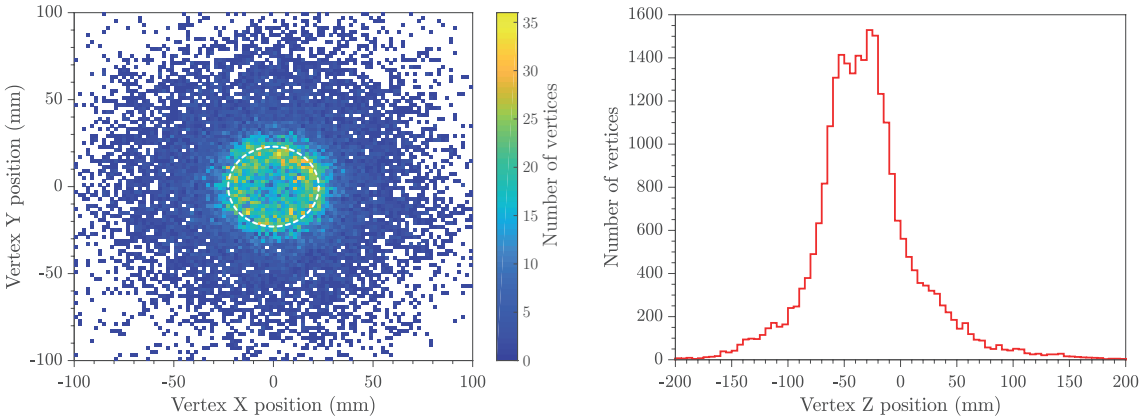

(c) $x-y$ projection (d) z projection

Alternative Reconstruction Method

Figure 7.28: Vertex distribution of both bound and bare antiproton annihilations during the mixing phase where antihydrogen atoms are formed while the neutral trap magnets are activated. The data for these distributions corresponds to mixing sample in Table. 6.1 and has been acquired during the operation of the ALPHA-II SVD. (a-b) The $x-y$ projections of the vertex distributions and the z distribution of vertices obtained from the SRM and (c-d) the ARM, with the colour palette indicating the number of vertices in each bin and the dashed white circle showing the position of the electrode wall.

antihydrogen are clear. These antihydrogen atoms travel to large radii and since the trap field is stronger at larger radii, they become ionized. Valuable information about the initial antihydrogen conditions such as positions, velocities and binding energies can be extracted from vertex distributions such as the one shown in Fig. 7.28(b).

Figures 7.28(c) and 7.28(d) are the z-integrated $x-y$ projection and the z distribution, respectively, of the vertices reconstructed by the Alternative Reconstruction

Method and correspond to the mixing sampling data in Table 6.1. The projected distribution and the z distribution serve as a comparison between the Standard and the Alternative Reconstruction Methods. One key difference is that the two peaks in Fig. 7.28(d) are not as pronounced as those in the distribution obtained from the Standard Reconstruction Method in Fig. 7.28(b).

7.5.3.3 Cosmics

Cosmic rays are high-energy particles (predominately protons), primarily originating outside the Solar System and even from distant galaxies. Upon impact with the Earth's atmosphere, cosmic rays can produce showers of secondary particles that sometimes reach the surface. The majority of cosmic rays that reach the surface are muons (μ^+/μ^-). For the ALPHA SVD, the rate the cosmic muons are detected is ~ 10 Hz (see Table. 6.1). Obtained by the Alternative Reconstruction Method, Fig. 2.23(c) shows the reconstruction of two tracks with very large radius of curvature and the vertex due to passage of a charged cosmic muon through the ALPHA apparatus.

Fig. 7.29 illustrates the distributions of the vertices reconstructed from the cosmic sampling data presented in Table 6.1. In addition to providing a visual comparison between the Standard Reconstruction and the Alternative Reconstruction Methods, these distributions highlight a key difference between a mixing and cosmic event leading to a reconstructed vertex. The cosmic distribution lacks any symmetries, consistent with the fact that cosmic rays can enter the detector at random directions.

The vertex radial position distribution of the mixing sampling data of Table 6.1 is illustrated in Fig. 7.30. The radial position of a mixing event vertex must be smaller than the inner radius of the trap wall electrode. However, the width of the vertex radial position distributions are broadened because of the finite resolution of the SVD as well as the physical processes such as the multiple scattering and the energy loss of the annihilation products as they traverse the apparatus material. This spread provides a statistical measure of how well the reconstructed vertex position is expected to determine the actual position of an annihilation. Therefore, the reso-

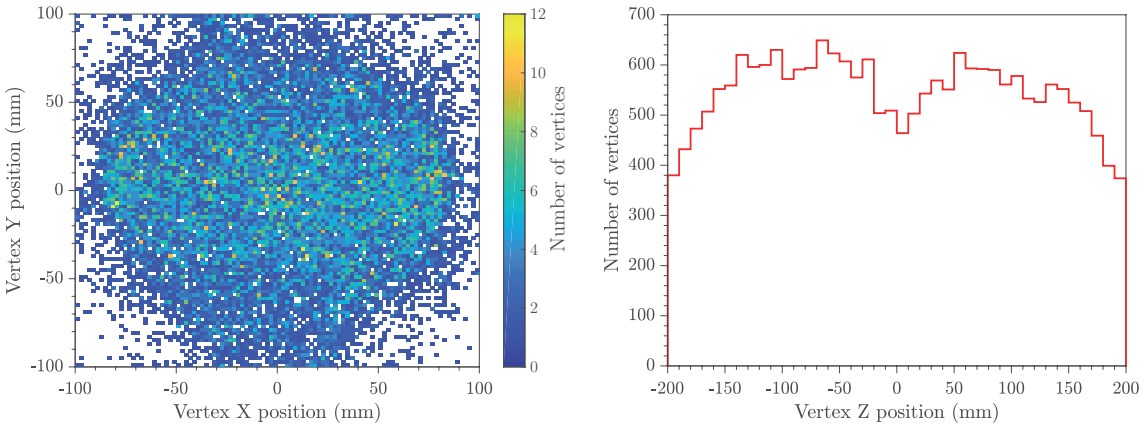

(a) $x - y$ projection (b) z projection

Standard Reconstruction Method

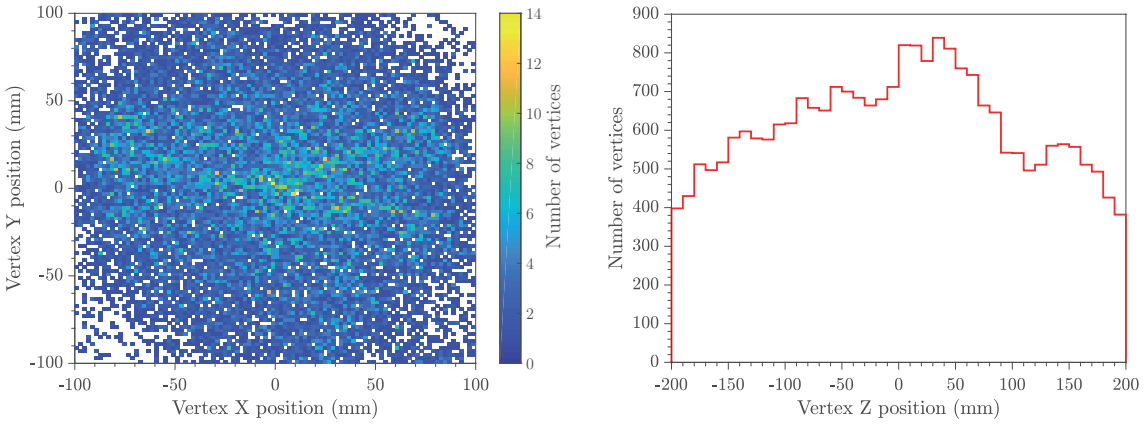

(c) $x - y$ projection (d) z projection

Alternative Reconstruction Method

Figure 7.29: Vertex distribution of the cosmic sampling data in Table 6.1. (a-b) The $x - y$ projections of the vertex distributions and the z distribution of vertices obtained from the SRM and (c-d) the ARM. The colour palette indicates the number of vertices in each bin.

lution of the radial position distribution of the vertices (the width of distributions in Fig. 7.30) can be regarded as the determining factor for evaluating the performance of both the Standard and Alternative Reconstruction Methods.

It is evident from Fig. 7.30 that there exist reconstructed vertices at radii greater than 35 mm for both the SRM and the ARM. However, the numbers seem to be greater for the ARM. This is because the SRM utilizes a pre-defined radial cut at a radius of approximately 35 mm, and therefore the reason behind the sharp decline in the SRM histogram at that radius (see Fig. 7.30(a)). The ARM in Fig. 7.30(b),

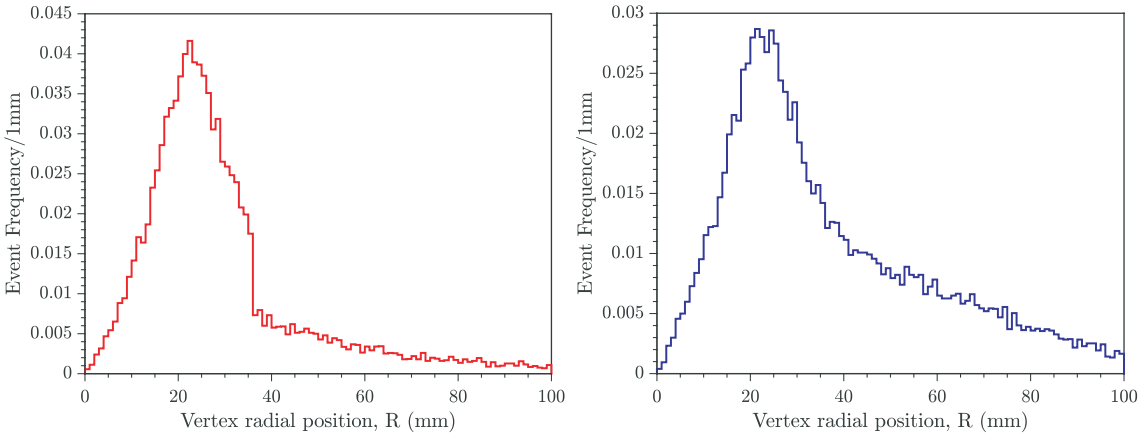

(a) Standard Reconstruction Method (b) Alternative Reconstruction Method

Figure 7.30: Distributions of vertex radial position for (a) the Standard Reconstruction Method and (b) the Alternative Reconstruction Method.

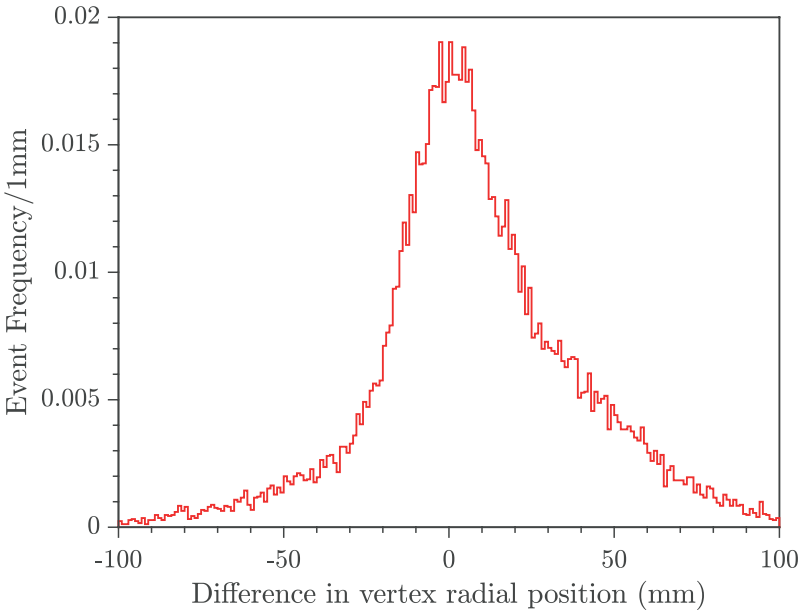

Figure 7.31: Histogram depicting the difference between the radial position of the reconstructed vertices by the SRM and the ARM.

on the other hand, has no pre-defined cut and accordantly its histogram undergoes a steady decline. The ARM algorithm's objective is to provide various types of variable cut studies, not just one single radial cut, subsequent to the reconstruction procedure. Consequently, as opposed to the SRM, no pre-defined cut has been included in devising the ARM. Acquiring a quantitative statistical comparison of the two methods would have been plausible if both methods employed the same reconstruction scheme, i.e. with no variable cut scheme included.

Fig. 7.31 is a plot showing the difference between the radial positions of the vertices reconstructed by the SRM and the ARM. It is neither symmetric nor Gaussian, and there are significant numbers of events for which the two methods differ in radial position by greater than 35 mm. As stated earlier, this asymmetry has arisen as the SRM algorithm uses a pre-defined radial cut at 35 mm. Moreover, the plot does not depict a Guassian curve since the central peak is not well-defined, a consequence of the double peaks in Fig. 7.30(b). Acquiring a well-defined Gaussian curve relies on analysing a greater number of mixing events, an approach which could be attempted in the future studies.

A cosmic vertex radial position can, in principle, be any value since the cosmic rays can enter the apparatus at any random directions and therefore no physical significance can be attributed to the radial position of a cosmic vertex. This is clear from the cosmic vertex distributions shown in Figures 7.29. The distributions of the reconstructed vertices of the Alternative Reconstruction Method clearly demonstrates that it has immense capability in resolving intriguing physical attributes associated with annihilation or cosmic events occurring inside the apparatus.

7.6 Summary

As well as the significant technical challenges facing antimatter scientists, there are only a few trapped anti-atoms trapped, $\sim$ 10, for experimental investigations in comparison with that of the hydrogen atoms (10^{12}), demonstrating the importance of a reliable detection mechanism. The ARM algorithm (see Appendix C) is an alternative vertex reconstruction scheme which results in an improved reconstruction of vertices and has the followings features:

- By dividing the reconstruction algorithm into twenty-one sub-functions, it is devised to be extremely modular, allowing the main script to be the pivot of the physics processes leading to the reconstruction of a vertex.

- For every annihilation/cosmic event, the reconstruction algorithm outputs 18

parameters, which include: the event number, the number of tracks reconstructed, a table showing hybrids containing the hits, a table of the number and indices of the generated hits, the paired-tracks, the POCA coordinates and the corresponding residual of each paired track, the coordinates of the vertex, the directional cosines of the 3-D best-line-of-fit, the dot product of each paired track, the $z-r$ intersection and the corresponding $z-r$ fit, the radius of curvature of each track, the normalized n- and p-side pulse heights, the equations of $z-r$ lines and their corresponding residuals, a table specifying a colour for each track and a table characterizing each hit (see Table 7.1). This comprehensive list allows all the possible investigations related to a particular annihilation/comic event. For instance, combining the colour index table with the table of hit indices allows one to investigate a specific track by extracting all the data related to the 3 hits constituting that track, most importantly the hybrid and the ASICs the charged particle traversed. Consequently, the hits information from the event reconstruction script can be coupled with the output of pedestal analysis script to acquire a visual representation of the pedestal behaviour of the 6 strips (2 strips per hit) generating the hits. This extensive and detailed level of data extraction establishes the Alternative Reconstruction Method as a robust and superior script.

- On average, each mixing experimental cycle contains approximately 5,000 events, where $\sim 85\%$ of them leads into the reconstruction of a vertex and for each event having a vertex, the script saves 18 parameters. However, similar to the Alternative Pedestal Analysis, the Alternative Reconstruction Method is extremely fast and analyses a mixing experimental cycle in less than 3 minutes, on average. Therefore, an entire mixing experimental cycle can take up to 4 minutes (1 minute for pedestal analysis and 3 minutes for event reconstruction).

- The author has attempted to acquire conclusive verification of the performance of the Alternative Reconstruction algorithm by devising a script (see

event-reconstruction-visualization.m script in Appendix D) capable of providing visual comparisons (see Figures 7.3 and 7.4) of several annihilation and cosmic events analysed by both the Standard and Alternative Reconstruction Methods.

Chapter 8

Conclusion & Future Outlook

The CPT theorem is an underlying property of quantum field theories. A direct verification of this theorem is the comparison of the 1S-2S two-photon Doppler-free quantum transition of hydrogen (measured with a precision of 4 parts in 10^{15}) with its corresponding anti-atom (antihydrogen). The long-term objective of the ALPHA collaboration is to apply spectroscopic techniques to probe the atomic structure of antihydrogen atoms with the same accuracy as that of the hydrogen atom.

Probing antihydrogen with laser light poses non-trivial technological challenges since firstly the antihydrogen atoms do not occur naturally and as a result they must be synthesized. Secondly, antihydrogen annihilations with normal matter must be prevented by confining anti-atoms in a vacuum. Furthermore, compared to spectroscopy on 10^{12} atoms of trapped hydrogen, due to the very small trapping rate (the number of trapped anti-atoms per attempt) of ~ 10, working with only a few anti-atoms at a time is a further challenge that needs to be addressed. To meet these technological challenges, ALPHA has devised various experimental and computational techniques that aim to both enhance the antihydrogen formation and trapping rates, as well as increase the detection efficiency of antihydrogen atoms. The prime diagnostic tool for the detection of antihydrogen in the ALPHA experiment is the Silicon Vertex Detector. It is the key component for identifying antihydrogen by its annihilation.

The detection efficiency and spatial resolution of the SVD is determined by how

effectively the statistical, pattern recognition and track reconstruction methods are implemented. Currently, the ALPHA experiment employs a set of software algorithms which both examine the generation of electric pulses due to the passage of charged pions resulting from the annihilation of an antiproton (Standard Pedestal Analysis (SPA)), and estimate the annihilation location (the vertex) whereby the tracks of charged particles are identified and reconstructed using the analytical solution of helices (Standard Reconstruction Method (SRM)). The SPA in conjunction with the SRM result in a vertex reconstruction efficiency of 83.4%.

This thesis has presented both a new method for identifying signal pulses from the background electric pulses of the silicon strips (Alternative Pedestal Analysis, see Appendix A) as well as a completely new, different and enhanced vertex reconstruction method (Alternative Reconstruction Method, see Appendix C). The ARM is based on implementing a set of different filtration mechanisms, compared to the SRM, to identify the track candidates. Moreover, the reconstruction of the tracks is accomplished by adapting a numerical approach, as opposed to the SRM where the reconstruction of tracks are achieved using the analytical solution of helices. Combining the APA and the ARM schemes has led to a vertex reconstruction efficiency of 84.7%, an increase in the vertex reconstruction efficiency by 1.5%.

The new approaches for pedestal analysis and vertex reconstruction utilize a considerably more versatile algorithm. This feature allows significant control over variables and selection parameters employed for the reconstruction of vertices. In terms of algorithmic efficiency, firstly, the enhanced algorithm has been devised to be extremely modular, allowing the main script to be the pivot of the physics processes. Secondly, the extensive and detailed level of data extraction concerning an annihilation event is acquired significantly fast (< 0.04 s). The conclusive verification of the performances of the new approaches are based on their visualization capabilities, the key aspect in devising the APA and the ARM, see Appendices B and D.

The implementation of the enhanced pedestal analysis and vertex reconstruc-

tion methods include: the rejection of cosmic background, the comparison with the simulation of reconstructed vertices, the determination of the correlations between the n- and p-side pulse heights of the hits associated with the tracks contributing to the vertex reconstruction, and the analyses of the extant data from past experiments (1S-2S laser spectroscopy) and data to be acquired from future experiments (Lyman-alpha spectroscopy).

The future of antimatter experiments at CERN relies heavily on acquiring low-energy antiprotons. The Extra-Low ENergy Antiproton (ELENA) ring with a circumference of 30 m is a synchrotron decelerator designed and built to reduce the energy of the beam extracted from the AD to 100 keV, see Fig. 2.7. The machine is currently in its final testing phase and is expected to increase the number of trappable antiprotons in the AD experiments by a factor of between 10 and 100 [82].

Weak Equivalence Principle (WEP), one of the foundations of Einstein's theory of General Relativity (GR), asserts that the composition of a falling body has no effect on its gravitational acceleration. This principle has been verified by Eötvös-Dicke experiments in which various composite objects of normal matter have experienced equal gravitational acceleration with a precision of 10^{-12} [83]. With regard to the gravitational acceleration of atomic and subatomic particles, hardly any non-quantitative measurements such as the neutron interferometric measurements and free electrons exist.

Notwithstanding that propositions for experimental test of the WEP on an elementary particle and its corresponding antiparticle have been suggested, as of yet, no such tests have been carried out. This is primarily due to the fact that shielding the antimatter particles, such as the antiproton, from electromagnetic forces is an extremely formidable business. Nevertheless, due to its neutrality, antihydrogen atoms are unaffected by the presence of electric fields and therefore prove to be an ideal system for the direct verification of the WEP. Significant ongoing attempts are currently being made to combine quantum mechanics and gravity into so-called

quantum gravity theory. However, these attempts have met with no success, an indication that our current understanding of nature is incomplete. Accordingly, the WEP verification using antihydrogen could have significant implications for better understanding of current and future theories, such as quantum gravity and experiments at the AD are currently being developed with such an objective.

A proof-of-principle study for the measurement of antimatter gravitation was first proposed by the ALPHA collaboration in 2013 [84] and a novel apparatus, known as ALPHA-g, with its design devised from several experiences on the simulation and verification of magnetically confined antihydrogen orbits is currently being built alongside the ALPHA-II machine (see Fig. 2.2). The ALPHA-g aims at performing a precise measurement of the antihydrogen gravitational acceleration to test the weak equivalence principle at the 1% level [85].

8.1 Conclusion

ALPHA has established itself as the leading collaboration in conducting laser spectroscopy of antihydrogen atoms, paving the way for shedding light on the current observed matter-antimatter asymmetry in our Universe. In addition, the technological advances in the AD have allowed the field of antihydrogen research to make the transition from proof-of-principle studies of antihydrogen to performing experimental investigations of antihydrogen atoms, making it feasible to verify the CPT theorem by direct comparison of matter and antimatter.

Bibliography

[1] Arthur Schuster. Potential matter.—a holiday dream. *Nature*, 58:367, (1898).

[2] Mea Amoretti, Claude Amsler, G Bonomi, A Bouchta, P Bowe, C Carraro, CL Cesar, M Charlton, MJT Collier, M Doser, et al. Production and detection of cold antihydrogen atoms. *Nature*, 419(6906):456–459, (2002).

[3] G Gabrielse, NS Bowden, P Oxley, A Speck, CH Storry, JN Tan, M Wessels, D Grzonka, W Oelert, G Schepers, et al. Driven production of cold antihydrogen and the first measured distribution of antihydrogen states. *Physical review letters*, 89(23):233401, (2002).

[4] GB Andresen, MD Ashkezari, M Baquero-Ruiz, W Bertsche, Paul David Bowe, E Butler, CL Cesar, S Chapman, M Charlton, A Deller, et al. Trapped antihydrogen. *Nature*, 468(7324):673–676, (2010).

[5] Alpha Collaboration et al. Confinement of antihydrogen for 1,000 seconds. *Nature Physics*, 7(7):558–564, (2011).

[6] C Amole, MD Ashkezari, M Baquero-Ruiz, W Bertsche, PD Bowe, E Butler, A Capra, CL Cesar, M Charlton, A Deller, et al. Resonant quantum transitions in trapped antihydrogen atoms. *Nature*, 483(7390):439, (2012).

[7] Mostafa Ahmadi, M Baquero-Ruiz, W Bertsche, E Butler, A Capra, C Carruth, CL Cesar, M Charlton, AE Charman, S Eriksson, et al. An improved limit on the charge of antihydrogen from stochastic acceleration. *Nature*, 529(7586):373, (2016).

[8] Mostafa Ahmadi, Bruno Ximenez Rodrigues Alves, CJ Baker, W Bertsche, E Butler, A Capra, C Carruth, CL Cesar, M Charlton, S Cohen, et al. Observation of the 1s–2s transition in trapped antihydrogen. *Nature*, 541(7638):506, (2017).

[9] M Ahmadi, BXR Alves, CJ Baker, W Bertsche, E Butler, A Capra, C Carruth, CL Cesar, M Charlton, S Cohen, et al. Observation of the hyperfine spectrum of antihydrogen. *Nature*, 548(7665):66, (2017).

[10] M Ahmadi, BXR Alves, CJ Baker, W Bertsche, E Butler, A Capra, C Carruth, CL Cesar, M Charlton, S Cohen, et al. Antihydrogen accumulation for fundamental symmetry tests. *Nature communications*, 8(1):681, (2017).

[11] M Ahmadi, BXR Alves, CJ Baker, W Bertsche, A Capra, C Carruth, CL Cesar, M Charlton, S Cohen, R Collister, et al. Enhanced control and reproducibility of non-neutral plasmas. *Physical review letters*, 120(2):025001, (2018).

[12] M Ahmadi, BXR Alves, CJ Baker, W Bertsche, A Capra, C Carruth, CL Cesar, M Charlton, S Cohen, R Collister, et al. Characterization of the 1s–2s transition in antihydrogen. *Nature*, page 1, (2018).

[13] Paul AM Dirac. Quantised singularities in the electromagnetic field. In *Proceedings of the Royal Society of London A: Mathematical, Physical and Engineering Sciences*, volume 133, pages 60–72. The Royal Society, (1931).

[14] Carl D Anderson. The positive electron. *Physical Review*, 43(6):491, (1933).

[15] Patrick MS Blackett and Giuseppe PS Occhialini. Some photographs of the tracks of penetrating radiation. *Proceedings of the Royal Society of London. Series A, Containing Papers of a Mathematical and Physical Character*, 139 (839):699–726, (1933).

[16] G Gabrielse, D Phillips, W Quint, H Kalinowsky, G Rouleau, and W Jhe. Special relativity and the single antiproton: Fortyfold improved comparison of p and p charge-to-mass ratios. *Physical review letters*, 74(18):3544, (1995).

[17] Robert S Van Dyck Jr, Paul B Schwinberg, and Hans G Dehmelt. New high-precision comparison of electron and positron g factors. *Physical Review Letters*, 59(1):26, (1987).

[18] L Essen, RW Donaldson, MJ Bangham, and EG Hope. Frequency of the hydrogen maser. *Nature*, 229(5280):110, 1971.

[19] Christian G Parthey, Arthur Matveev, Janis Alnis, Birgitta Bernhardt, Axel Beyer, Ronald Holzwarth, Aliaksei Maistrou, Randolf Pohl, Katharina Predehl, Thomas Udem, et al. Improved measurement of the hydrogen 1 s–2 s transition frequency. *Physical review letters*, 107(20):203001, (2011).

[20] TJ Murphy and CM Surko. Positron trapping in an electrostatic well by inelastic collisions with nitrogen molecules. *Physical Review A*, 46(9):5696, (1992).

[21] GB Andresen, W Bertsche, Paul David Bowe, CC Bray, E Butler, CL Cesar, S Chapman, M Charlton, J Fajans, MC Fujiwara, et al. Compression of antiproton clouds for antihydrogen trapping. *Physical review letters*, 100(20):203401, (2008).

[22] C Amole, GB Andresen, MD Ashkezari, M Baquero-Ruiz, W Bertsche, PD Bowe, E Butler, A Capra, PT Carpenter, CL Cesar, et al. The alpha antihydrogen trapping apparatus. *Nuclear Instruments and Methods in Physics Research Section A: Accelerators, Spectrometers, Detectors and Associated Equipment*, 735:319–340, (2014).

[23] D Möhl. Production of low-energy antiprotons. *Hyperfine Interactions*, 109(1): 33–41, (1997).

[24] FM Bieniosek and K Anderson. Lithium lens for focusing protons on target in the fermilab antiproton source. In *Particle Accelerator Conference, 1993., Proceedings of the 1993*, pages 3163–3165. IEEE, 1993.

[25] D Möhl, G Petrucci, L Thorndahl, and Simon Van Der Meer. Physics and technique of stochastic cooling. *Physics Reports*, 58(2):73–102, (1980).

[26] S Van der Meer. Stochastic cooling in the cern antiproton accumulator. *IEEE Transactions on Nuclear Science*, 28(3):1994–1998, (1981).

[27] Gersh Itskovich Budker and Aleksandr N Skrinskiĭ. Electron cooling and new possibilities in elementary particle physics. *Soviet Physics Uspekhi*, 21(4):277, (1978).

[28] Anke A Wagner. *The g-factor of the valence electron bound in lithiumlike silicon 28Si11+: The most stringent test of relativistic many-electron calculations in a magnetic field*. PhD thesis, (2013).

[29] Lowell S Brown and Gerald Gabrielse. Geonium theory: Physics of a single electron or ion in a penning trap. *Reviews of Modern Physics*, 58(1):233, (1986).

[30] William H Wing. On neutral particle trapping in quasistatic electromagnetic fields. *Progress in Quantum Electronics*, 8(3-4):181–199, (1984).

[31] Richard Hydomako. *Detection of trapped antihydrogen*. Springer Science & Business Media, (2012).

[32] Eoin Butler. Antihydrogen formation, trapping and dynamics. *arXiv preprint arXiv:1107.3860*, (2011).

[33] J Fajans, N Madsen, and F Robicheaux. Critical loss radius in a penning trap subject to multipole fields. *Physics of Plasmas*, 15(3):032108, (2008).

[34] Chukman So. *Antiproton and positron dynamics in antihydrogen production*. PhD thesis, (2014).

[35] A Gutierrez. *submitter: Cold antihydrogen experiments and radial compression of antiproton clouds in the ALPHA apparatus at CERN*. PhD thesis.

[36] Timothy Peter Friesen. *Probing Trapped Antihydrogen. In Situ Diagnostics and Observations of Quantum Transitions*. PhD thesis, University of Calgary, (2014).

[37] GB Andresen, W Bertsche, Paul David Bowe, CC Bray, E Butler, CL Cesar, S Chapman, M Charlton, S Seif El Nasr, J Fajans, et al. Antiproton, positron, and electron imaging with a microchannel plate/phosphor detector. *Review of Scientific Instruments*, 80(12):123701, (2009).

[38] Ronald C Davidson. *Physics of nonneutral plasmas*. World Scientific Publishing Company, (2001).

[39] X-P Huang, JJ Bollinger, TB Mitchell, WM Itano, and DHE Dubin. Precise control of the global rotation of strongly coupled ion plasmas in a penning trap. *Physics of Plasmas*, 5(5):1656–1663, (1998).

[40] TM O'neil. A confinement theorem for nonneutral plasmas. *The Physics of Fluids*, 23(11):2216–2218, (1980).

[41] DL Eggleston, CF Driscoll, BR Beck, AW Hyatt, and JH Malmberg. Parallel energy analyzer for pure electron plasma devices. *Physics of Fluids B: Plasma Physics*, 4(10):3432–3439, (1992).

[42] GB Andresen, MD Ashkezari, M Baquero-Ruiz, W Bertsche, Paul David Bowe, E Butler, CL Cesar, S Chapman, M Charlton, J Fajans, et al. Evaporative cooling of antiprotons to cryogenic temperatures. *Physical review letters*, 105 (1):013003, (2010).

[43] Gerald Gabrielse, X Fei, LA Orozco, RL Tjoelker, J Haas, H Kalinowsky, TA Trainor, and W Kells. Cooling and slowing of trapped antiprotons below 100 mev. *Physical review letters*, 63(13):1360, (1989).

[44] John David Jackson. *Classical electrodynamics*. Wiley, (1999).

[45] G Gabrielse. Comparing the antiproton and proton, and opening the way to cold antihydrogen. *Advances in Atomic, Molecular, and Optical Physics*, 45: 1–39, (2001).

[46] SL Rolston and G Gabrielse. Cooling antiprotons in an ion trap. *Hyperfine Interactions*, 44(1-4):233–245, (1989).

[47] M Amoretti, C Amsler, G Bonomi, A Bouchta, Paul David Bowe, C Carraro, M Charlton, MJT Collier, M Doser, V Filippini, et al. The athena antihydrogen apparatus. *Nuclear Instruments and Methods in Physics Research Section A: Accelerators, Spectrometers, Detectors and Associated Equipment*, 518(3):679–711, (2004).

[48] Gorm B Andresen, Mohammad D Ashkezari, Marcelo Baquero-Ruiz, William Bertsche, Paul D Bowe, Crystal C Bray, Eoin Butler, Claudio L Cesar, Steven Chapman, Michael Charlton, et al. Search for trapped antihydrogen. *Physics Letters B*, 695(1):95–104, (2011).

[49] GB Andresen, W Bertsche, A Boston, Paul David Bowe, CL Cesar, S Chapman, M Charlton, M Chartier, A Deutsch, J Fajans, et al. Production of antihydrogen at reduced magnetic field for anti-atom trapping. *Journal of Physics B: Atomic, Molecular and Optical Physics*, 41(1):011001, (2007).

[50] JR Danielson and CM Surko. Radial compression and torque-balanced steady states of single-component plasmas in penning-malmberg traps. *Physics of Plasmas*, 13(5):055706, (2006).

[51] Gorm Bruun Andresen, MD Ashkezari, M Baquero-Ruiz, W Bertsche, Paul David Bowe, E Butler, CL Cesar, S Chapman, M Charlton, A Deller, et al. Centrifugal separation and equilibration dynamics in an electron-antiproton plasma. *Physical review letters*, 106(14):145001, (2011).

[52] Wolfgang Ketterle and NJ Van Druten. Evaporative cooling of trapped atoms. In *Advances in atomic, molecular, and optical physics*, volume 37, pages 181–236. Elsevier, (1996).

[53] Celeste Carruth, Joel Fajans, Alpha Collaboration, et al. Combining the strong drive regime with evaporative cooling to control plasma parameters in the alpha experiment. In *APS Meeting Abstracts*, (2016).

[54] TM O'Neil and PG Hjorth. Collisional dynamics of a strongly magnetized pure electron plasma. *The Physics of fluids*, 28(11):3241–3252, (1985).

[55] AW Hyatt, CF Driscoll, and JH Malmberg. Measurement of the anisotropic temperature relaxation rate in a pure electron plasma. *Physical review letters*, 59(26):2975, (1987).

[56] Giovanni Manfredi and Paul-Antoine Hervieux. Adiabatic cooling of trapped non-neutral plasmas. *Physical review letters*, 109(25):255005, (2012).

[57] G Gabrielse, WS Kolthammer, R McConnell, P Richerme, R Kalra, E Novitski, D Grzonka, W Oelert, T Sefzick, M Zielinski, et al. Adiabatic cooling of antiprotons. *Physical review letters*, 106(7):073002, (2011).

[58] Muhammed Sameed. *Laser-Ablated Beryllium Ions for Cold Antihydrogen in ALPHA*. PhD thesis, Swansea University, (2017).

[59] Gerald Gabrielse, SL Rolston, L Haarsma, and W Kells. Possible antihydrogen production using trapped plasmas. *Hyperfine Interactions*, 44(1-4):287–293, (1989).

[60] Francis Robicheaux. Three-body recombination for electrons in a strong magnetic field: Magnetic moment. *Physical Review A*, 73(3):033401, (2006).

[61] F Robicheaux. Atomic processes in antihydrogen experiments: a theoretical and computational perspective. *Journal of Physics B: Atomic, Molecular and Optical Physics*, 41(19):192001, (2008).

[62] G Gabrielse, SL Rolston, L Haarsma, and W Kells. Antihydrogen production using trapped plasmas. *Physics Letters A*, 129(1):38–42, (1988).

[63] Gorm Bruun Andresen, MD Ashkezari, M Baquero-Ruiz, W Bertsche, Paul David Bowe, E Butler, PT Carpenter, CL Cesar, S Chapman, M Charlton, et al. Autoresonant excitation of antiproton plasmas. *Physical review letters*, 106(2):025002, (2011).

[64] C. Carruth et al. (ALPHA Collaboration). Evaporative cooling in the strong drive regime to produce stable plasmas for antihydrogen production. Manuscript in preparation.

[65] Steven Jones. *Observation of the 1S-2S Transition in Trapped Antihydrogen*. PhD thesis, (2017).

[66] C Amole, GB Andresen, MD Ashkezari, M Baquero-Ruiz, W Bertsche, E Butler, CL Cesar, S Chapman, M Charlton, A Deller, et al. Discriminating between antihydrogen and mirror-trapped antiprotons in a minimum-b trap. *New Journal of Physics*, 14(1):015010, (2012).

[67] Gorm Bruun Andresen, MD Ashkezari, M Baquero-Ruiz, W Bertsche, Paul David Bowe, E Butler, CL Cesar, M Charlton, A Deller, S Eriksson, et al. Confinement of antihydrogen for 1,000 seconds. *Nature Physics*, 7(7):558, (2011).

[68] Michael Charlton and John W Humberston. *Positron physics*, volume 11. Cambridge University Press, (2001).

[69] C. Ghesquiere. An inclusive view on $\overline{p}p \to n\pi$ at rest. *Symposium on NucleonAntinucleon Interactions, Liblice-Prague, Czech Republic, L. Montanet (ed.); CERN Yellow report CERN-74-018*, (25-28 June 1974).

[70] SJ Orfanidis and V Rittenberg. Nucleon-antinucleon annihilation into pions. *Nuclear Physics B*, 59(2):570–582, (1973).

[71] Robert F Pierret and Gerold W Neudeck. *Advanced semiconductor fundamentals*, volume 6. Addison-Wesley Reading, MA, (1987).

[72] John R Taylor, Michael A Dubson, and Chris D Zafiratos. *Modern physics for scientists and engineers*. Prentice-Hall, (2004).

[73] C Patrignani, Particle Data Group, et al. Review of particle physics. *Chinese physics C*, 40(10):100001, (2016).

[74] G Lütz. Semiconductor radiation detectors: Device physics, (2007).

[75] GB Andresen, MD Ashkezari, M Baquero-Ruiz, W Bertsche, PD Bowe, E Butler, CL Cesar, S Chapman, M Charlton, A Deller, et al. The alpha–detector: Module production and assembly. *Journal of Instrumentation*, 7(01):C01051, (2012).

[76] C Amole, MD Ashkezari, M Baquero-Ruiz, W Bertsche, E Butler, A Capra, CL Cesar, M Charlton, A Deller, S Eriksson, et al. Experimental and computational study of the injection of antiprotons into a positron plasma for antihydrogen production. *Physics of Plasmas*, 20(4):043510, (2013).

[77] C Amole, GB Andresen, MD Ashkezari, M Baquero-Ruiz, W Bertsche, C Burrows, E Butler, A Capra, CL Cesar, S Chapman, et al. Silicon vertex detector upgrade in the alpha experiment. *Nuclear Instruments and Methods in Physics Research Section A: Accelerators, Spectrometers, Detectors and Associated Equipment*, 732:134–136, (2013).

[78] VA1TA Manual. *Ideas ASA*. Hovik, Norway, (2001).

[79] Andrea Capra. *Testing CPT and antigravity with trapped antihydrogen at ALPHA*. PhD thesis, (2015).

[80] GB Andresen, MD Ashkezari, W Bertsche, PD Bowe, E Butler, CL Cesar, S Chapman, M Charlton, A Deller, S Eriksson, et al. Antihydrogen annihilation reconstruction with the alpha silicon detector. *Nuclear Instruments and Methods in Physics Research Section A: Accelerators, Spectrometers, Detectors and Associated Equipment*, 684:73–81, (2012).

[81] GB Andresen, W Bertsche, Paul David Bowe, CC Bray, E Butler, CL Cesar, S Chapman, M Charlton, J Fajans, MC Fujiwara, et al. A novel antiproton radial diagnostic based on octupole induced ballistic loss. *Physics of Plasmas*, 15(3):032107, (2008).

[82] Walter Oelert, Tommy Eriksson, Pavel Belochitskii, and Gerard Tranquille. Ad performance and its extension towards elena. *Hyperfine Interactions*, 213(1-3): 227–236, (2012).

[83] VB Braginskii and VI Panov. Verification of equivalency of inertial and gravitational masses. Technical report, Moscow State Univ., (1971).

[84] C Amole, MD Ashkezari, M Baquero-Ruiz, W Bertsche, E Butler, A Capra, CL Cesar, M Charlton, S Eriksson, J Fajans, et al. Description and first application of a new technique to measure the gravitational mass of antihydrogen. *Nature communications*, 4:1785, (2013).

[85] WA Bertsche. Prospects for comparison of matter and antimatter gravitation with alpha-g. *Phil. Trans. R. Soc. A*, 376(2116):20170265, (2018).

[86] Masaki Hori, Anna Sótér, Daniel Barna, Andreas Dax, Ryugo Hayano, Susanne Friedreich, Bertalan Juhász, Thomas Pask, Eberhard Widmann, Dezső Horváth, et al. Two-photon laser spectroscopy of antiprotonic helium and the antiproton-to-electron mass ratio. *Nature*, 475(7357):484–488, (2011).

[87] Y Bylinsky, AM Lombardi, and W Pirkl. Rfqd-a decelerating radio frequency quadrupole for the cern antiproton facility. *arXiv preprint hep-ex/0008030*, (2000).

[88] RS Hayano. Precision spectroscopy of antiprotonic helium atoms and ions–weighing the antiproton. In *Precision Physics of Simple Atoms and Molecules*, pages 187–201. Springer, (2008).

[89] Michael H Holzscheiter, Niels Bassler, Nzhde Agazaryan, Gerd Beyer, Ewart Blackmore, John J DeMarco, Michael Doser, Ralph E Durand, Oliver Hartley, Keisuke S Iwamoto, et al. The biological effectiveness of antiproton irradiation. *Radiotherapy and Oncology*, 81(3):233–242, (2006).

[90] D Fabris, AS Belov, G Bonomi, I Boscolo, N Brambilla, RS Brusa, VM Byakov, L Cabaret, C Canali, C Carraro, et al. The aegis detection system for gravity measurements. *Nuclear Physics A*, 834(1):751c–753c, (2010).

[91] S Aghion, O Ahlén, C Amsler, A Ariga, T Ariga, AS Belov, G Bonomi, P Bräunig, J Bremer, RS Brusa, et al. Prospects for measuring the gravitational free-fall of antihydrogen with emulsion detectors. *Journal of Instrumentation*, 8(08):P08013, (2013).

[92] P Perez and Y Sacquin. The gbar experiment: gravitational behaviour of antihydrogen at rest. *Classical and Quantum Gravity*, 29(18):184008, (2012).

[93] S Ulmer, C Smorra, A Mooser, Kurt Franke, H Nagahama, G Schneider, T Higuchi, S Van Gorp, Klaus Blaum, Y Matsuda, et al. High-precision comparison of the antiproton-to-proton charge-to-mass ratio. *Nature*, 524(7564): 196–199, (2015).

[94] RG Greaves, MD Tinkle, and CM Surko. Creation and uses of positron plasmas. *Physics of Plasmas (1994-present)*, 1(5):1439–1446, (1994).

[95] TM Squires, P Yesley, and G Gabrielse. Stability of a charged particle in a combined penning-ioffe trap. *Physical review letters*, 86(23):5266, (2001).

Appendices

Appendix A

Pedestal-Analysis.m

Listing A.1: Pedestal-Analysis.m Script

```
clc, clear, close all
tic
% Mixing:

% Windows
% userpath = regexprep(userpath,';','');% Removes ; at the end of the path

userpath = '/Users/Mosi/Dropbox/Business/Public_Sharing/Antimatter';
cd([userpath '/Antimatter_Detection/DATA/MatlabMatFiles/Mixings'])

% command = 'dir /b'; % Windows
command = 'ls -1v'; % Linux
[status, cmdout] = system(command);
runNumbers = str2double(regexp(cmdout, '\d+(\.\d+)?|\.\d+', 'match'));
MIXING = runNumbers;

cd ([userpath '/Antimatter_Detection/Pedestal_Analysis'])

SIGMAF = {[3 2.5 1.5]};

for moji = 1:length(runNumbers)
    if find(runNumbers(moji) == MIXING(1))

        filename = ['R' num2str(runNumbers(moji))];
        Run = num2str(runNumbers(moji));
        clc, close all, clearvars - except userpath filename runNumbers Run tic ↩
            moji Cone MIXING SIGMA SIGMAF INTLIM

        cd([userpath '/Antimatter_Detection/DATA/MatlabMatFiles/Mixings/' Run])

        matFilename = [filename '.mat'];
        mat_object = matfile(matFilename);

        a = cell(1, 4);
        b = cell (1, 4);
        C = cell (1, 72);
        for m = 1:72
            for A = 1:4

                cd([userpath '/Antimatter_Detection/DATA/MatlabObjectModules/↩
                    Mixings/' ...
                  Run '/Module' num2str(m) '/ASIC' num2str(A)])
                load('DATA.mat')

                TotalEvents = size(DATA, 1);

                cd ([userpath '/Antimatter_Detection/DATA/Gains/Module_' num2str(↩
                    m)])
                GFN = ['Gain_' num2str(m) '_' num2str(A) '.mat'];
                load (GFN);
```

```
48
49                  cd([userpath '/Antimatter_Detection/Pedestal_Analysis'])
50                  if (A == 1) || (A == 2)
51                      P = + 1; % NSIDE
52                      RAW_IN = DATA * P;
53                  else
54                      P = - 1; % PSIDE
55                      RAW_IN = DATA * P;
56                      RAW_IN = RAW_IN + 1024;
57                  end
58
59                  [a{:}] = LevelPedestal(RAW_IN, P, SIGMAF{:});
60
61                  for ii = 1:TotalEvents
62                      DATA = a{2}(ii, :);
63                      MOD = DATA ./ G;
64                      a{2}(ii, :) = MOD;
65                  end
66                  b{A} = {a{1} a{2} a{3} a{4}};
67
68              end
69
70              C{m} = b;
71
72          end
73
74      end
75      end
76
77      clc, close all, clearvars - except userpath C filename runNumbers Run tic ↩
            moji Cone MIXING SIGMA SIGMAF INTLIM
78      format short g
79
80      cd([userpath '/Antimatter_Detection/DATA/MatlabMatFiles/Mixings/' Run])
81      load (['R' Run 'VF48.mat']);
82
83      cd([userpath '/Antimatter_Detection/Pedestal_Analysis'])
84
85      INTLIM = 0;
86      PARAMETER = INTLIM;
87
88      TotalEvents = size(C{1}{1}{1}, 1);
89      DIWS50 = cell(1, 72);
90      SA = cell(1, 4);
91      SR = cell(1, TotalEvents);
92      VEC = cell(1, TotalEvents);
93      SUM = zeros(1, TotalEvents);
94
95      SIGMA = {[3.6  3.6]};
96
97      for m = 1:72
98          for A = 1:4
99              if (A == 1) || (A == 2)
100                 sigma = SIGMA{1}(1);
101             else
102                 sigma = SIGMA{1}(2);
103             end
104             for r = 1:TotalEvents
105
106                 SUB = C{m}{A}{2}(r, :);
107
108                 THR = sigma * C{m}{A}{4};
109
110                 S = find(SUB > THR);
111
112                 NOS = length(S);
113
114                 PH = SUB(S);
115
116                 if (NOS > 0)
117
118                     NIC = loc_clus(S);
119
```

```
120                     AIN = [];
121                     ['Intergration: ' num2str(PARAMETER) ' strip(s)'];
122
123                     for jj = 1:length(NIC)
124                         MIN = min(NIC{jj});
125                         MAX = max(NIC{jj});
126                         V = [(MIN - PARAMETER) : (MAX + PARAMETER)];
127                         AIN = [AIN V];
128                     end
129
130                     INZ = AIN(find((AIN > 0) & (AIN < 129)));
131                     SIN = unique(INZ);
132                     Cluster = cell (1, length(NIC));
133                     if length(NIC) == 1
134                         Cluster{:} = SIN;
135                     else
136
137                         for jj = 1:length(NIC)
138
139                             if (jj <= length(NIC) - 1)
140
141                                 if jj == 1
142
143                                     MIN = find(ismember(SIN, min(NIC{jj})));
144                                     MAX = find(ismember(SIN, max(NIC{jj})));
145
146                                     EFR = find(ismember(SIN, (min(NIC{jj + 1}) - ↩
                                            1)));
147
148                                     E = find(ismember(SIN, max(NIC{jj}) + 1));
149
150                                     length(SIN(E:EFR));
151                                     HALF = floor(length(SIN(E:EFR)) / 2);
152                                     if length(SIN(E:EFR)) >= 2 * PARAMETER
153                                         Right = (MAX:MAX + PARAMETER);
154                                     else
155                                         Right = (MAX:MAX + HALF);
156                                     end
157
158                                     Left = find(SIN(1)):MAX;
159
160                                     INDX = [Left Right];
161                                     Cluster{jj} = SIN(INDX);
162                                     Cluster{jj} = unique(Cluster{jj});
163
164                                 else
165
166                                     MIN = find(ismember(SIN, (min(NIC{jj}))));
167                                     MAX = find(ismember(SIN, (max(NIC{jj}))));
168
169                                     ELL = find(ismember(SIN, (max(NIC{jj - 1}) + ↩
                                            1)));
170
171                                     HALF = floor(length(SIN(ELL:MIN - 1)) / 2);
172
173                                     if length(SIN(ELL:MIN - 1)) >= 2 * PARAMETER
174                                         Left = (MIN - PARAMETER:MAX);
175                                     else
176                                         Left = (MIN - HALF:MAX);
177                                     end
178
179                                     EFR = find(ismember(SIN, (min(NIC{jj + 1}) - ↩
                                            1)));
180                                     E = find(ismember(SIN, max(NIC{jj}) + 1));
181
182                                     HALF = floor(length(SIN(E:EFR)) / 2);
183                                     if length(SIN(E:EFR)) >= 2 * PARAMETER
184                                         Right = (MAX:MAX + PARAMETER);
185                                     else
186                                         Right = (MAX:MAX + HALF);
187                                     end
188
189                                     INDX = [Left Right];
```

```
190                                     Cluster{jj} = SIN(INDX);
191                                     Cluster{jj} = unique(Cluster{jj});
192                                 end
193
194                             else
195
196                                 MIN = find(ismember(SIN, (min(NIC{jj}))));
197                                 MAX = find(ismember(SIN, (max(NIC{jj}))));
198
199                                 ELL = find(ismember(SIN, (max(NIC{jj - 1}) + 1)))↩
                                        ;
200
201                                 HALF = floor(length(SIN(ELL:MIN - 1)) / 2);
202                                 if length(SIN(ELL:MIN - 1)) >= 2 * PARAMETER
203                                     Left = (MIN - PARAMETER:MAX);
204                                 else
205                                     Left = (MIN - HALF:MAX);
206                                 end
207
208                                 Right = (MAX + 1:length(SIN));
209
210                                 INDX = [Left Right];
211                                 Cluster{jj} = SIN(INDX);
212                                 Cluster{jj} = unique(Cluster{jj});
213
214                             end
215                         end
216                     end
217
218                     CC = loc_clus([Cluster{:}]);
219                     for kk = 1:length(CC)
220
221                         CSN = CC{kk};
222
223                         PPH = SUB(CSN);
224
225                         PPH(PPH < 0) = PPH(PPH < 0) * - 1;
226
227                         WS = (sum(CSN .* PPH)) / (sum(PPH));
228
229                         if WS > 128
230                             WS = 128;
231                         elseif WS < 1
232                             WS = WS * - 1;
233                         end
234
235                         PUHI = sum(PPH);
236
237                         if PUHI < 0
238                             PUHI = - 1 * PUHI;
239                         end
240
241                         STRIP = WS;
242                         PHS = PUHI;
243
244                         FullDATA_new{r, m, A}{kk} = [r m A STRIP PHS];
245                     end
246                 else
247                     FullDATA_new{r, m, A} = [];
248                 end
249
250             end
251         end
252     end
253
254     clc, close all, clearvars - except userpath C DIWS50 FullDATA_new filename ↩
        runNumbers Run tic TotalEvents replace moji ConeL2 ConeL3 MIXING SIGMA ↩
        SIGMAF INTLIM
255
256     cd ([userpath '/Antimatter_Detection/Pedestal_Analysis'])
257     load('replace.mat')
258
259     RUN = [filename '_Mixing_APA'];
```

```
260     SUM = 0;
261     NoLines = 0;
262     readouts = [];
263     for r = 1:size(FullDATA_new, 1)
264         SUM = SUM + 1;
265         testm = [];
266 
267         for m = 1:size(FullDATA_new, 2)
268 
269             for A = 1:size(FullDATA_new, 3)
270                 if ~ isempty(FullDATA_new{r, m, A})
271                     Z = [FullDATA_new{r, m, A}{:}];
272                     Z = reshape(Z, [5, length(FullDATA_new{r, m, A})]);
273                     Z(1, :) = [];
274                     Z = Z(:);
275                     Z = Z';
276                     testm = [testm Z];
277                 end
278             end
279         end
280 
281         if length(testm) ~= 0
282             NoLines = NoLines + 1;
283         else
284             readouts = [readouts r];
285             testm = replace;
286         end
287 
288         if SUM == 1
289             dlmwrite([RUN '.txt'], testm, 'delimiter', ' ');
290         else
291             dlmwrite([RUN '.txt'], testm, '-append', 'delimiter', ' ');
292         end
293 
294     end
295     toc
296 
297     %{
298     % ======================================================================
299     FUNCTIONS
300     % ======================================================================
301     1: function [RAW_IN FINAL_SUB FINAL_PED FINAL_STD] = LevelPedestal2_v5(RAW_IN↩
            , P, SIGMAF)
302 
303     MOD_IN = RAW_IN;
304     N = length(SIGMAF);
305 
306     for ii = 1:N
307         SIGMAFI = SIGMAF(ii);
308         IPED = nanmean(MOD_IN);
309         ISTD = nanstd(MOD_IN);
310         ISUB = bsxfun(@minus, MOD_IN, IPED);
311         ISUB2 = ISUB;
312         ISUB = bsxfun(@minus, ISUB, nanmean(ISUB, 2));
313 
314         RIND = find(bsxfun(@gt, ISUB, SIGMAFI * ISTD));
315         MOD_IN(RIND) = nan;
316     end
317 
318     FINAL_PED = nanmean(MOD_IN);
319     FINAL_STD = nanstd(MOD_IN);
320     FINAL_SUB = bsxfun(@minus, RAW_IN, FINAL_PED);
321     FINAL_SUB = bsxfun(@minus, FINAL_SUB, (nanmean(ISUB2, 2)));
322 
323     2: function CLUSTER = loc_clus(a)
324     k = [true; diff(a(:)) ~= 1];
325     s = cumsum(k);
326     x = histc(s, 1:s(end));
327     idx = find(k);
328 
329     for i = 1:(length(idx))
330         if i <= length(idx) - 1
331             A = a(idx(i):idx(i + 1) - 1);
```

```
332             else
333                 A = a(idx(length(idx)):end);
334             end
335             CLUSTER{i} = A;
336         end
337         %}
```

Appendix B

Pedestal-Analysis-Visualization.m

Listing B.1: Pedestal-Analysis-Visualization.m Script

```
clc, clear, close all
tic
% Mixing:

% Windows
% userpath = regexprep(userpath,';','');% Removes ; at the end of the path

userpath = '/Users/Mosi/Dropbox/Business/Public_Sharing/Antimatter';
cd([userpath '/Antimatter_Detection/DATA/MatlabMatFiles/Mixings'])

% command = 'dir /b'; % Windows
command = 'ls -1v'; % Linux
[status, cmdout] = system(command);
runNumbers = str2double(regexp(cmdout, '\d+(\.\d+)?|\.\d+', 'match'));
MIXING = runNumbers;

cd ([userpath '/Antimatter_Detection/Pedestal_Analysis'])

SIGMAF = {[3 2.5 1.5]};

for moji = 1:length(runNumbers)
    if find(runNumbers(moji) == MIXING(1))

        filename = ['R' num2str(runNumbers(moji))];
        Run = num2str(runNumbers(moji));
        clc, close all, clearvars - except userpath filename runNumbers Run tic ↩
            moji Cone MIXING SIGMA SIGMAF INTLIM

        cd([userpath '/Antimatter_Detection/DATA/MatlabMatFiles/Mixings/' Run])

        matFilename = [filename '.mat'];
        mat_object = matfile(matFilename);

        a = cell(1, 4);
        b = cell (1, 4);
        C = cell (1, 72);
        for m = 1:72
            for A = 1:4

                cd([userpath '/Antimatter_Detection/DATA/MatlabObjectModules/↩
                    Mixings/' ...
                  Run '/Module' num2str(m) '/ASIC' num2str(A)])
                load('DATA.mat')

                TotalEvents = size(DATA, 1);

                cd ([userpath '/Antimatter_Detection/DATA/Gains/Module_' num2str(↩
                    m)])
                GFN = ['Gain_' num2str(m) '_' num2str(A) '.mat'];
                load (GFN);
```

```
48
49                  cd([userpath '/Antimatter_Detection/Pedestal_Analysis'])
50                  if (A == 1) || (A == 2)
51                      P = + 1; % NSIDE
52                      RAW_IN = DATA * P;
53                  else
54                      P = - 1; % PSIDE
55                      RAW_IN = DATA * P;
56                      RAW_IN = RAW_IN + 1024;
57                  end
58
59                  [a{:}] = LevelPedestal(RAW_IN, P, SIGMAF{:});
60
61                  for ii = 1:TotalEvents
62                      DATA = a{2}(ii, :);
63                      MOD = DATA ./ G;
64                      a{2}(ii, :) = MOD;
65                  end
66                  b{A} = {a{1} a{2} a{3} a{4}};
67
68              end
69
70              C{m} = b;
71
72          end
73
74      end
75  end
76
77  %%
78  clc, close all, clearvars - except C userpath
79
80  Run = '50008';
81  cd ([userpath '/Antimatter_Detection/DATA/MatlabMatFiles/Mixings/' Run])
82  load (['R' Run 'VF48.mat']);
83
84  cd ([userpath '/Antimatter_Detection/Pedestal_Analysis'])
85  figure
86  SZ = size(C{1}{1}{2});
87  N = SZ(1);
88
89  % ii = 3837;
90  ii = 4611;
91
92  % HYB = 11;
93  HYB = 1;
94
95  YSCALE = [- 350 350];
96  SIGMA = 3.6;
97  subplot(2, 2, 1)
98  stairs(C{HYB}{1}{2}(ii, :))
99  hold on
100 stairs(C{HYB}{1}{4} * SIGMA)
101 S1 = find(C{HYB}{1}{2}(ii, :) > C{HYB}{1}{4} * SIGMA);
102 set(gca, 'XLim', [1 128], 'YLim', YSCALE)
103 title(['HYB:' num2str(HYB) ', ASIC:1, EV:' num2str(ii) ', Strips:' num2str(length↩
        (S1)) ', Mean:' num2str(mean(C{HYB}{1}{2}(ii, :)))])
104 grid on
105 beautifulPlot
106 hold off
107
108 subplot(2, 2, 2)
109 stairs(C{HYB}{2}{2}(ii, :))
110 hold on
111 stairs(C{HYB}{2}{4} * SIGMA)
112 S2 = find(C{HYB}{2}{2}(ii, :) > C{HYB}{2}{4} * SIGMA);
113 set(gca, 'XLim', [1 128], 'YLim', YSCALE)
114 title(['HYB:' num2str(HYB) ', ASIC:2, EV:' num2str(ii) ', Strips:' num2str(length↩
        (S2)) ', Mean:' num2str(mean(C{HYB}{1}{2}(ii, :)))])
115 grid on
116 beautifulPlot
117 hold off
118
```

```
119 subplot(2, 2, 3)
120 stairs(C{HYB}{3}{2}(ii, :))
121 hold on
122 stairs(C{HYB}{3}{4} * SIGMA)
123 S3 = find(C{HYB}{3}{2}(ii, :) > C{HYB}{3}{4} * SIGMA);
124 set(gca, 'XLim', [1 128], 'YLim', YSCALE)
125 title(['HYB:' num2str(HYB) ', ASIC:3, EV:' num2str(ii) ', Strips:' num2str(length↩
        (S3)) ', Mean:' num2str(mean(C{HYB}{1}{2}(ii, :)))])
126 grid on
127 beautifulPlot
128 hold off
129
130 subplot(2, 2, 4)
131 stairs(C{HYB}{4}{2}(ii, :))
132 hold on
133 stairs(C{HYB}{4}{4} * SIGMA)
134 S4 = find(C{HYB}{4}{2}(ii, :) > C{HYB}{4}{4} * SIGMA);
135 set(gca, 'XLim', [1 128], 'YLim', YSCALE)
136 title(['HYB:' num2str(HYB) ', ASIC:4, EV:' num2str(ii) ', Strips:' num2str(length↩
        (S4)) ', Mean:' num2str(mean(C{HYB}{1}{2}(ii, :)))])
137 grid on
138 beautifulPlot
139 hold off
140 set(gcf, 'Position', get(0, 'Screensize'));
141
142 cd ([userpath '/Antimatter_Detection/Pedestal_Analysis'])
```

Appendix C

Event-Vertex-Reconstruction.m

Listing C.1: Event-Vertex-Reconstruction.m Script

```
clc, clear, close all

% Windows
% userpath = regexprep(userpath,';','');% Removes ; at the end of the path

userpath = '/Users/Mosi/Dropbox/Business/Public_Sharing/Antimatter';
cd([userpath '/Antimatter_Detection/Event_Vertex_Reconstruction'])
NN = [];
TABLE_HYB = [];
TABLE = [];
HIT_NUMBER = [];
PAIRS = [];
REC_TABLE = [];
AP = [];
T_DCOS = [];
DOT_TR = [];
NORMR_TABLE = [];
ZRINT = [];
R_C = [];
N_TABLE = [];
P_TABLE = [];
ZRLINES = [];
COLR = [];
TR_ARR = [];

% INPUTS:
RUN_NO = 50008;
EVENT_NO = 4611;
TimeStamp = 0;
ConeL2 = 35;
ConeL3 = 45;

% FLAGS:
DRAW = 1;
DRAW_TRACKS = 1;
DRAW_MULTIPLE_VIEWS = 1;

DRAW_ZR_PROJECTION = 0;
STATS = 0;
OUTPUT = 0;

%%%%%%%%%%%%%%%%%%%%%%%%%%% Tabulating pedestal analysis outcome %%%%%%%%%%%%%%
% =========% =========% =========% =========% =========% =========% ========
IN = hittableMixingSPA(RUN_NO, EVENT_NO);
% IN    = hittableMixingAPA(RUN_NO,EVENT_NO);
HITS = IN.HITS;
PHE = IN.PHE;

% ***************************** RESET VALUES ***************************
HIT_NUMBER = 0;
```

```
REC_TABLE = [nan nan nan nan];
NN = 0;
T_DCOS = [nan nan nan];
T_X0 = [nan nan nan];
AP = [nan nan nan];
TABLE = [nan nan nan];
DOT_TR = nan;

% ************************  Simultaneous Triggering ******************
N_THR = 1480;
P_THR = 1480;

THROUGH = 0;
for ii = 1:72
    % for n-side (A1/A2)
    for jj = 1:2
        VECTH = PHE{ii, jj};
        CHS = HITS{ii, jj};
        INDS = find(VECTH > 0 & VECTH < N_THR);
        BACK = VECTH(INDS);
        PHE{ii, jj} = BACK;
        BACK = CHS(INDS);
        HITS{ii, jj} = BACK;
    end
    % for p-side (A3/A4)
    for jj = 3:4
        VECTH = PHE{ii, jj};
        CHS = HITS{ii, jj};
        INDS = find(VECTH > 0 & VECTH < P_THR);
        BACK = VECTH(INDS);
        PHE{ii, jj} = BACK;
        BACK = CHS(INDS);
        HITS{ii, jj} = BACK;
    end

    THROUGH = and(length(PHE{ii, 1}) + length(PHE{ii, 2}), ...
    length(PHE{ii, 3}) + length(PHE{ii, 4}));

    if ~ THROUGH
        PHE{ii, 1} = [];
        PHE{ii, 2} = [];
        PHE{ii, 3} = [];
        PHE{ii, 4} = [];
        HITS{ii, 1} = [];
        HITS{ii, 2} = [];
        HITS{ii, 3} = [];
        HITS{ii, 4} = [];
    end
end

%%%%%%%%%%%%%%%%%%%% Identification of a hit %%%%%%%%%%%%%%%%
% ========%========%========%========%========%========%=======
L1 = [1:10  37:46];
L2 = [11:22  47:58];
L3 = [23:36  59:72];

TRIG_ALL = zeros(1, 72);

NSIDE = cell(72, 1);
PSIDE = cell(72, 1);

NSIDEPH = cell(72, 1);
PSIDEPH = cell(72, 1);

% **********************  Grouping n&p-side fired strips ***************
for ii = 1:72
    % N-side
    % ASIC1:
    N1 = [];
    N1P = [];
    CN1 = HITS{ii, 1};
    PN1 = PHE{ii, 1};
    CLS = loc_clusters(CN1);
```

```
124     for jj = 1:length(CLS)
125         CIND = CLS{jj};
126         N1(jj) = CN1(CIND);
127         N1P(jj) = PN1(CIND);
128     end
129 
130     % ASIC2:
131     N2 = [];
132     N2P = [];
133     CN2 = HITS{ii, 2};
134     PN2 = PHE{ii, 2};
135     CLS = loc_clusters(CN2);
136     for jj = 1:length(CLS)
137         CIND = CLS{jj};
138         N2(jj) = CN2(CIND);
139         N2P(jj) = PN2(CIND);
140     end
141 
142     % P-side
143     % ASIC3
144     P1 = [];
145     P1P = [];
146     CP1 = HITS{ii, 3};
147     PP1 = PHE{ii, 3};
148     CLS = loc_clusters(CP1);
149     for jj = 1:length(CLS)
150         CIND = CLS{jj};
151         P1(jj) = CP1(CIND);
152         P1P(jj) = PP1(CIND);
153     end
154 
155     % ASIC4
156     P2 = [];
157     P2P = [];
158     CP2 = HITS{ii, 4};
159     PP2 = PHE{ii, 4};
160     CLS = loc_clusters(CP2);
161     for jj = 1:length(CLS)
162         CIND = CLS{jj};
163         P2(jj) = CP2(CIND);
164         P2P(jj) = PP2(CIND);
165     end
166 
167     NSIDE{ii} = [(N1) (N2 + 128)];
168     PSIDE{ii} = [(P1 + 256) (P2 + 384)];
169 
170     NSIDEPH{ii} = [N1P N2P];
171     PSIDEPH{ii} = [P1P P2P];
172 
173     TRIG_ALL(ii) = length(NSIDE{ii}) * length(PSIDE{ii});
174 end
175 
176 LAYER1 = sum(TRIG_ALL(L1));
177 LAYER2 = sum(TRIG_ALL(L2));
178 LAYER3 = sum(TRIG_ALL(L3));
179 
180 TRACK_THR = 20;
181 HITN_THR = 100;
182 LTHRESH = 20;
183 
184 if LAYER1 > LTHRESH || LAYER2 > LTHRESH || LAYER3 > LTHRESH
185     disp('MESS')
186 end
187 
188 %%%%%%%%%%%%%%%%%%%%%%%%%%%%%% Distribution of hits on detector layers ↩
        %%%%%%%%%%%%%%%%%%%%%%%%%%%%%
189 %% ========%% ========%% ========%% ========%% ========%% ========%% ======
190 
191 % ********************** Paing n&p side hits of a hybrid ****************
192 VCHANN_PAIRS = cell(72, 1);
193 VCHANN_PAIRSPH = cell(72, 1);
194 TRIG_INDS = find(TRIG_ALL > 0);
195 if isempty(TRIG_INDS)
```

```
196     return
197 end
198 
199 for ii = TRIG_INDS
200     ind = 0;
201     VEC = [];
202     VECPH = [];
203     NNS = NSIDE{ii};
204     PPS = PSIDE{ii};
205     NNSPH = NSIDEPH{ii};
206     PPSPH = PSIDEPH{ii};
207     for jj = 1:length(NNS)
208         for kk = 1:length(PPS)
209             ind = ind + 1;
210             VEC(ind, :) = [NNS(jj) PPS(kk)];
211             VECPH(ind, :) = [NNSPH(jj) PPSPH(kk)];
212             VCHANN_PAIRS{ii} = VEC;
213             VCHANN_PAIRSPH{ii} = VECPH;
214         end
215     end
216 end
217 
218 % ******* Converting hit strip number to hybrid position coordinate *******
219 CPAIRS = cell(72, 1);
220 for ii = TRIG_INDS
221     PAIR_VEC = VCHANN_PAIRS{ii};
222     S = size(PAIR_VEC);
223     N = S(1);
224     for jj = 1:N
225         [Z(jj), Y(jj)] = strip_zy_h(PAIR_VEC(jj, :));
226         Z(jj) = - Z(jj) * sign(36.5 - ii);
227         Y(jj) = - Y(jj) * sign(36.5 - ii);
228     end
229     VEC = [Z' Y'];
230     CPAIRS{ii} = VEC;
231     Z = [];
232     Y = [];
233 end
234 
235 % **** Converting the Z Y hybrid coordinate of the hit into detector reference ↩
        frame ****
236 kk = 0;
237 OFFS = 0;
238 for ii = TRIG_INDS
239     V = CPAIRS{ii};
240     ARR = rot_hyb2(ii, V, OFFS);
241     X = ARR(1, :, 1);
242     Y = ARR(1, :, 2);
243     Z = ARR(1, :, 3);
244     PHEIGHTS = VCHANN_PAIRSPH{ii};
245     N = PHEIGHTS(:, 1);
246     P = PHEIGHTS(:, 2);
247     for jj = 1:length(X)
248         kk = kk + 1;
249         XX(kk) = X(jj);
250         YY(kk) = Y(jj);
251         ZZ(kk) = Z(jj);
252         RR(kk) = sqrt(XX(kk) ^ 2 + YY(kk) ^ 2);
253 
254         PHI(kk) = sign(YY(kk)) * acos(XX(kk) / RR(kk));
255         LAYER(kk) = 1 * ismember(ii, L1) + 2 * ismember(ii, L2) + 3 * ismember(ii↩
                , L3);
256         HYBRID(kk) = ii;
257         N_PH(kk) = N(jj);
258         P_PH(kk) = P(jj);
259     end
260 end
261 
262 % ************************** Constructing TR_ARR ***********************
263 TR_ARR = [XX' YY' ZZ' RR' PHI' LAYER' HYBRID' N_PH' P_PH'];
264 
265 % ***************************** Drawing Detector ************************
266 if DRAW
```

```
267     F1 = figure;
268     hold on
269 
270     dr_AD_r
271     dr_POS_r
272 
273     CENT = [0 0];
274     RAD = 22.275;
275     % viscircles(CENT,RAD,'Color','k','Linewidth',2);
276     view(-30, 20)
277 end
278 
279 %%%%%%%%%%%%%%%%%%%%%%%%%%%%%%%% Identification of track candidates ↩
        %%%%%%%%%%%%%%%%%%%%%%%%
280 %=========%=========%=========%=========%=========%=========%=======
281 
282 %%%%%%%%%%%%%%%%%%%%%%%% Cone Angle Hit Selection Criteria %%%%%%%%%%%%%%%%
283 %=========%=========%=========%=========%=========%=========%=======
284 S = size(TR_ARR);
285 HIT_NUMBER = S(1);
286 
287 if HIT_NUMBER > HITN_THR
288     disp(['MORE THAN ' num2str(HITN_THR) ' HITS ; ' num2str(HIT_NUMBER)])
289     return
290 end
291 
292 IL1 = find(TR_ARR(:, 6) == 1);
293 IL2 = find(TR_ARR(:, 6) == 2);
294 IL3 = find(TR_ARR(:, 6) == 3);
295 
296 DPHI_THR = ConeL2 / 180 * pi;
297 
298 MID_I = [];
299 OUT_I = [];
300 
301 for ii = 1:length(IL1)
302     DA = dangle(PHI(IL1(ii)), PHI(IL2));
303     INDS = find(abs(DA) < DPHI_THR);
304     MID_I = IL2(INDS);
305 
306     OUT_I = [];
307     for jj = 1:length(MID_I)
308         DA = dangle(PHI(MID_I(jj)), PHI(IL3));
309         INDS2 = find(abs(DA) < DPHI_THR);
310         OUT_I = [OUT_I; IL3(INDS2)];
311     end
312     RAW_MID{ii} = unique(MID_I);
313     RAW_OUT{ii} = unique(OUT_I);
314 end
315 
316 %%%%%%%%%%%%%%%%%%%%%%%% Z-R Normal Selection Criteria %%%%%%%%%%%%%%%%
317 %=========%=========%=========%=========%=========%=========%=======
318 
319 TABLE = [];
320 TABLE_HYB = [];
321 
322 NORMR_THR = 3;
323 NORMR_TABLE = [];
324 
325 ll = 0;
326 mm = 0;
327 
328 for ii = 1:length(IL1)
329     MINDS = RAW_MID{ii};
330     OINDS = RAW_OUT{ii};
331 
332     if not(isempty(MINDS) & isempty(OINDS))
333         for jj = 1:length(MINDS)
334             for kk = 1:length(OINDS)
335                 ll = ll + 1;
336 
337                 POINTS_Z = [ZZ(IL1(ii)) ZZ(MINDS(jj)) ZZ(OINDS(kk))];
338                 POINTS_R = [RR(IL1(ii)) RR(MINDS(jj)) RR(OINDS(kk))];
```

```
339
340                 [P S] = polyfit(POINTS_Z, POINTS_R, 1);
341
342                 LineDistance = abs (- P(1) * POINTS_Z + POINTS_R - P(2)) / sqrt ↩
                        ((P(1)) ^ 2 + 1);
343                 d1 = LineDistance(1);
344                 d2 = LineDistance(2);
345                 d3 = LineDistance(3);
346
347                 NORM_R(ll) = d1 + d2 + d3;
348
349                 if NORM_R(ll) < NORMR_THR
350                     mm = mm + 1;
351                     TABLE(mm, :) = [IL1(ii) MINDS(jj) OINDS(kk)];
352                     TABLE_HYB(mm, :) = TR_ARR(TABLE(mm, :), 7)';
353                     NORMR_TABLE(mm) = NORM_R(ll);
354                 end
355             end
356         end
357     end
358 end
359
360 %%%%%%%%%%%%%%%%%%%%%%%%%% Dot-Product Seletion Criteria %%%%%%%%%%%%%%%%%
361 % =========% =========% =========% =========% =========% =========% ========
362 DPHI_THR2 = cos(ConeL3 * (pi / 180));
363
364 NN = size(TABLE);
365 NN = NN(1);
366
367 if NN == 0
368     disp('NO TRACKS')
369     return
370 end
371
372 for ii = 1:NN
373     I1 = TABLE(ii, 1);
374     I2 = TABLE(ii, 2);
375     I3 = TABLE(ii, 3);
376
377     R1 = [XX(I2) - XX(I1) YY(I2) - YY(I1) ZZ(I2) - ZZ(I1)];
378     R2 = [XX(I3) - XX(I2) YY(I3) - YY(I2) ZZ(I3) - ZZ(I2)];
379
380     R1 = R1 / norm(R1);
381     R2 = R2 / norm(R2);
382
383     DPR(ii) = dot(R1, R2);
384     Theta(ii) = acos(DPR(ii));
385
386     if DPR(ii) < DPHI_THR2
387         TABLE(ii, :) = nan;
388         TABLE_HYB(ii, :) = nan;
389         NORMR_TABLE(ii) = nan;
390     end
391 end
392
393 % ************************** Final Track Selection **********************
394 TABLE = TABLE(find(~ isnan(TABLE)));
395 TABLE = reshape(TABLE, length(TABLE) / 3, 3);
396 TABLE_HYB = TABLE_HYB(find(~ isnan(TABLE_HYB)));
397 TABLE_HYB = reshape(TABLE_HYB, length(TABLE_HYB) / 3, 3);
398 NORMR_TABLE = NORMR_TABLE(find(~ isnan(NORMR_TABLE)));
399 NORMR_TABLE = NORMR_TABLE(:);
400
401 NN = size(TABLE);
402 NN = NN(1);
403
404 % ************ Are there more than zero track No candidate left? **********
405 if NN == 0
406     disp('NO TRACKS')
407     return
408 end
409
410 % ***************************** Drawing all hits ************************
```

```
411 if DRAW
412     for ii = 1:size(TABLE, 1)
413         ILX = TR_ARR(TABLE(ii, 1), 1);
414         MLX = TR_ARR(TABLE(ii, 2), 1);
415         OLX = TR_ARR(TABLE(ii, 3), 1);
416         TRACKX = [ILX MLX OLX];
417 
418         ILY = TR_ARR(TABLE(ii, 1), 2);
419         MLY = TR_ARR(TABLE(ii, 2), 2);
420         OLY = TR_ARR(TABLE(ii, 3), 2);
421         TRACKY = [ILY MLY OLY];
422 
423         ILZ = TR_ARR(TABLE(ii, 1), 3);
424         MLZ = TR_ARR(TABLE(ii, 2), 3);
425         OLZ = TR_ARR(TABLE(ii, 3), 3);
426         TRACKZ = [ILZ MLZ OLZ];
427 
428         randCOL = rand(1, 3);
429         if DRAW
430             plot3(TRACKX, TRACKY, TRACKZ, '+', 'Markersize', 12, 'Color', rgb('↩
                    DarkBlue'), 'Linewidth', 1.5), ...
431               set(gca, 'XGrid', 'off', 'YGrid', 'off', ...
432               'XGrid', 'off', 'YGrid', 'off', 'ZGrid', 'off')
433             view(0, 90)
434         end
435     end
436 end
437 
438 %%%%%%%%%%%%%%%%%%%%%%%%%%%%%%%% Track Tunning %%%%%%%%%%%%%%%%%%%%%%%%%%%%
439 % ========% ========% ========% ========% ========% ========% ========
440 
441 IN = TABLE(:, 1);
442 MID = TABLE(:, 2);
443 OUT = TABLE(:, 3);
444 
445 IN_HYB = TABLE_HYB(:, 1);
446 MID_HYB = TABLE_HYB(:, 2);
447 OUT_HYB = TABLE_HYB(:, 3);
448 
449 IN_U = unique(IN);
450 MID_U = unique(MID);
451 OUT_U = unique(OUT);
452 MAX = size(TABLE);
453 MAX = MAX(1);
454 
455 CENTER = zeros(NN, 2);
456 R_C = zeros(NN, 1);
457 
458 % ****** Determine the radius of curvature for the track candidate ********
459 for ii = 1:NN
460     POINTS = [XX(TABLE(ii, 1)) YY(TABLE(ii, 1)); ...
461     XX(TABLE(ii, 2)) YY(TABLE(ii, 2)); ...
462     XX(TABLE(ii, 3)) YY(TABLE(ii, 3))];
463     [CENTER(ii, :), R_C(ii)] = points2circle(POINTS);
464 end
465 
466 % **** Choosing circle (track) with greatest radii of of two tracks with shared ↩
        hits ****
467 ISSAME = loc_same(TABLE);
468 PICKS = [];
469 for ii = 1:length(ISSAME)
470     INDS = ISSAME{ii};
471     BEST = find(R_C == max(R_C(INDS)));
472     BEST = intersect(BEST, INDS);
473     BEST = BEST(1);
474     PICKS = [PICKS BEST];
475 end
476 
477 TABLE = TABLE(PICKS, :);
478 TABLE_HYB = TABLE_HYB(PICKS, :);
479 NORMR_TABLE = NORMR_TABLE(PICKS);
480 R_C = R_C(PICKS);
481 
```

```
ISSAME = loc_same(TABLE);
PICKS = [];
for ii = 1:length(ISSAME)
    INDS = ISSAME{ii};
    BEST = find(R_C == max(R_C(INDS)));
    BEST = intersect(BEST, INDS);
    BEST = BEST(1);
    PICKS = [PICKS BEST];
end

TABLE = TABLE(PICKS, :);
TABLE_HYB = TABLE_HYB(PICKS, :);
NORMR_TABLE = NORMR_TABLE(PICKS);
R_C = R_C(PICKS);

% **** Drawing tiny markers(circles) around the track hits & plot Z-R projection ****
NN = size(TABLE);
NN = NN(1);

TITLE_TXT = ['MATLAB =>' 'R = ' num2str(RUN_NO) ', E = ' num2str(EVENT_NO) ', T = ' num2str(TimeStamp) ', TRA = ' num2str(NN) ', HIT = ' num2str(HIT_NUMBER)];

ranC = {'DarkSlateGray', 'DarkRed', 'OrangeRed', 'DarkGoldenrod', 'SpringGreen', 'DeepPink', 'DarkGreen', 'Indigo', 'DarkCyan'};
if DRAW
    for ii = 1:NN
        I1 = TABLE(ii, 1);
        I2 = TABLE(ii, 2);
        I3 = TABLE(ii, 3);

        COL = rgb(ranC{cycle(ii, 4)});
        plot3(XX(I1), YY(I1), ZZ(I1), 'o', 'Color', COL, 'Markersize', 11, 'Linewidth', 1)
        plot3(XX(I2), YY(I2), ZZ(I2), 'o', 'Color', COL, 'Markersize', 11, 'Linewidth', 1)
        plot3(XX(I3), YY(I3), ZZ(I3), 'o', 'Color', COL, 'Markersize', 11, 'Linewidth', 1)
        set(gcf, 'Units', 'inches', ...
          'Position', [0 0 8.65 8.65])
        set(gca, 'XGrid', 'off', 'YGrid', 'off', 'ZGrid', 'off');
    end
end

if DRAW_ZR_PROJECTION
    F2 = figure; hold on
    for ii = 1:NN
        I1 = TABLE(ii, 1);
        I2 = TABLE(ii, 2);
        I3 = TABLE(ii, 3);

        COL = rgb(ranC{cycle(ii, 4)});
        plot(ZZ(I1), RR(I1), 'o', 'Color', COL, 'Markersize', 11, 'Linewidth', 1)
        plot(ZZ(I2), RR(I2), 'o', 'Color', COL, 'Markersize', 11, 'Linewidth', 1)
        plot(ZZ(I3), RR(I3), 'o', 'Color', COL, 'Markersize', 11, 'Linewidth', 1)
        set(gca, 'XGrid', 'off', 'YGrid', 'off', 'ZGrid', 'off');
    end
    xlabel('Z(mm)', 'Interpreter', 'Latex')
    ylabel('R(mm)', 'Interpreter', 'Latex')
    beautifulPlot2D
end

%%%%%%%%%%%%%%%%%%%%%%%%%%%% Track Pairs Examinations %%%%%%%%%%%%%%%%%%%%%%%%
% ==========% ==========% ==========% ==========% ==========% ==========% ========

if NN > TRACK_THR
    disp(['MORE THAN ' num2str(NN) ' TRACKS'])
    return
end

if NN == 1
    return
end
```

```
549
550 if NN > 2
551     N_POINTS = factorial(NN) / 2 / factorial(NN - 2);
552 end
553
554 if NN == 2
555     N_POINTS = 1;
556 end
557
558 if NN == 0
559     return
560 end
561
562 N_POINTS = round (N_POINTS);
563 PAIRS = zeros(N_POINTS, 2);
564
565 ZINT = zeros(N_POINTS, 1);
566 RINT = zeros(N_POINTS, 1);
567
568 % ********************** Z-R projection of paird-tracks *****************
569 kk = 0;
570 for ii = 1:NN
571     for jj = ii + 1:NN
572
573         kk = kk + 1;
574
575         PAIRS(kk, :) = [ii jj];
576
577         POINTS_Z1 = [ZZ(TABLE(ii, 1)) ZZ(TABLE(ii, 2)) ZZ(TABLE(ii, 3))];
578         POINTS_R1 = [RR(TABLE(ii, 1)) RR(TABLE(ii, 2)) RR(TABLE(ii, 3))];
579
580         [P1 S1] = polyfit(POINTS_Z1, POINTS_R1, 1);
581
582         POINTS_Z2 = [ZZ(TABLE(jj, 1)) ZZ(TABLE(jj, 2)) ZZ(TABLE(jj, 3))];
583         POINTS_R2 = [RR(TABLE(jj, 1)) RR(TABLE(jj, 2)) RR(TABLE(jj, 3))];
584
585         [P2 S2] = polyfit(POINTS_Z2, POINTS_R2, 1);
586
587         ZINT(kk) = (P2(2) - P1(2)) / (P1(1) - P2(1));
588         RINT(kk) = P1(1) * ZINT(kk) + P1(2);
589
590         if DRAW_ZR_PROJECTION
591             COL = [rgb(ranC{cycle(ii, 4)})];
592             a = line([ZINT(kk) ZZ(TABLE(ii, 3))], [RINT(kk) RR(TABLE(ii, 3))]);
593             b = line([ZINT(kk) ZZ(TABLE(jj, 3))], [RINT(kk) RR(TABLE(jj, 3))]);
594             hold on
595             plot(ZINT(kk), RINT(kk), 'Marker', 'p', 'Markersize', 12, '↩
                    MarkerFaceColor', COL, 'MarkerEdgeColor', COL);
596             set(a, 'Color', COL, 'Linewidth', 1.5)
597             COL = [rgb(ranC{cycle(jj, 4)})];
598             set(b, 'Color', COL, 'Linewidth', 1.5)
599         end
600     end
601 end
602
603 ZRINT = {ZINT RINT};
604
605 % ******* Slope, intercept and residual of every track lines in Z-R *******
606 LINES = zeros(NN, 2);
607 ZR_RES = zeros(NN, 1);
608
609 for ii = 1:NN
610     POINTS_Z1 = [ZZ(TABLE(ii, 1)) ZZ(TABLE(ii, 2)) ZZ(TABLE(ii, 3))];
611     POINTS_R1 = [RR(TABLE(ii, 1)) RR(TABLE(ii, 2)) RR(TABLE(ii, 3))];
612     [P1 S1] = polyfit(POINTS_Z1, POINTS_R1, 1);
613     LINES(ii, :) = P1;
614     ZR_RES(ii) = S1.normr;
615 end
616
617 ZRLINES = {LINES ZR_RES};
618
619 CENTER = zeros(NN, 2);
620 R_C = zeros(NN, 1);
```

```
for ii = 1:NN
    POINTS = [XX(TABLE(ii, 1)) YY(TABLE(ii, 1)); ...
    XX(TABLE(ii, 2)) YY(TABLE(ii, 2)); ...
    XX(TABLE(ii, 3)) YY(TABLE(ii, 3))
    ];
    [CENTER(ii, :), R_C(ii)] = points2circle(POINTS);
end

%%%%%%%%%%%%%%%%%%%%%%%%%%%%%% Angle Of Incident %%%%%%%%%%%%%%%%%%%%%%%%%%
% =========% =========% =========% =========% =========% =========% ========

% **** Fit straight lines to 3 hits (Points) for weightedning & angle of incident↩
     approximation ****
T_DCOS = zeros(NN, 3);
T_X0 = zeros(NN, 3);

for ii = 1:NN
    POINTS = [...
    XX(TABLE(ii, 1)) YY(TABLE(ii, 1)) ZZ(TABLE(ii, 1))
    XX(TABLE(ii, 2)) YY(TABLE(ii, 2)) ZZ(TABLE(ii, 2))
    XX(TABLE(ii, 3)) YY(TABLE(ii, 3)) ZZ(TABLE(ii, 3))
    ];

    [x0, a, d, NORMD] = ls3dline_2(POINTS);

    T_DCOS(ii, :) = a;
    T_X0(ii, :) = x0;
end

% *************************** Track Dot-Products ************************
DOT_TR = zeros(N_POINTS, 1);
kk = 0;

for ii = 1:NN
    for jj = ii + 1:NN
        kk = kk + 1;
        DOT_TR(kk) = dot(T_DCOS(ii, :), T_DCOS(jj, :));
    end
end

% ******* Dot-product between the hybrid's normal and best-fit line *******
HA_PHI = hyb_pos2;
HYB_ANGLE = HA_PHI(:, 4);
CA_HYB = [cos(HYB_ANGLE) sin(HYB_ANGLE) zeros(72, 1)];

for ii = 1:NN
    for jj = 1:3
        INDEX = TABLE(ii, jj);

        HYB_NO = HYBRID(INDEX);

        CA_HYB(HYB_NO, :);

        DOT_INC(ii, jj) = dot(CA_HYB(HYB_NO, :), T_DCOS(ii, :));
    end
end

% ******** Normalizing the PH of each hit on a track using DOT_INC ********
N_TABLE_NN = N_PH(TABLE);
P_TABLE_NN = P_PH(TABLE);
N_TABLE = N_TABLE_NN ./ DOT_INC;
P_TABLE = P_TABLE_NN ./ DOT_INC;

%%%%%%%%%%%%%%%%%%%%%%%%%%%%%% Track Reconstruction  %%%%%%%%%%%%%%%%%%%%%%
% =========% =========% =========% =========% =========% =========% ========

% ***************************** Draw 3D tracks ************************
PHI_DIV = 15;
MAX_N = 8 * PHI_DIV;
N_VEC = 0:MAX_N;
X = cell(NN, 1);
Y = cell(NN, 1);
Z = cell(NN, 1);
```

```
693
694 if DRAW
695     figure(F1)
696 end
697
698 SUM = 0;
699 for ii = 1:NN
700     PHI_OUT = sign(YY(TABLE(ii, 3)) - CENTER(ii, 2)) * acos((XX(TABLE(ii, 3)) - ↩
        CENTER(ii, 1)) / R_C(ii));
701     PHI_IN = sign(YY(TABLE(ii, 1)) - CENTER(ii, 2)) * acos((XX(TABLE(ii, 1)) - ↩
        CENTER(ii, 1)) / R_C(ii));
702
703     D_PHI = dangle(PHI_IN, PHI_OUT) / PHI_DIV;
704
705     R_OUT = sqrt(XX(TABLE(ii, 3)) ^ 2 + YY(TABLE(ii, 3)) ^ 2);
706     R_IN = sqrt(XX(TABLE(ii, 1)) ^ 2 + YY(TABLE(ii, 1)) ^ 2);
707
708     Z_OUT = TR_ARR(TABLE(ii, 3), 3);
709     Z_IN = TR_ARR(TABLE(ii, 1), 3);
710
711     D_Z = (Z_IN - Z_OUT) / PHI_DIV;
712
713     X_XY = CENTER(ii, 1) + R_C(ii) * cos(PHI_OUT + N_VEC * D_PHI);
714     Y_XY = CENTER(ii, 2) + R_C(ii) * sin(PHI_OUT + N_VEC * D_PHI);
715
716     R_XY = sqrt(X_XY .^ 2 + Y_XY .^ 2);
717
718     MIN_IND = find(R_XY == min(R_XY));
719     MIN_IND = MIN_IND(1);
720
721     R0 = R_XY(MIN_IND);
722     II = MIN_IND;
723
724     while R_XY(II) < 89 && II < (length(R_XY) - 2)
725         II = II + 1;
726     end
727
728     CUT_IND2 = II;
729
730     X_XY = X_XY(1:CUT_IND2);
731     Y_XY = Y_XY(1:CUT_IND2);
732     Z_XY = Z_OUT + ([1:CUT_IND2] - 1) * D_Z;
733     R_XY = R_XY(1:CUT_IND2);
734
735     COL = rgb(ranC{cycle(ii, 4)});
736     if DRAW_TRACKS
737         plot3(X_XY, Y_XY, Z_XY, '.', 'Color', COL, 'Markersize', 7, 'Linewidth', ↩
                0.5)
738         view(- 30, 20)
739     end
740     % COLR{ii} = COL;
741     COLR{ii} = ranC{cycle(ii, 4)};
742
743     X{ii} = X_XY;
744     Y{ii} = Y_XY;
745     Z{ii} = Z_XY;
746
747 end
748
749 %%%%%%%%%%%%%%%%%%%%%%%%%%%% Vertex Reconstruction %%%%%%%%%%%%%%%%%%%%%%%
750 % ==========% ==========% ==========% ==========% ==========% ==========% =======
751
752 % **** Determing and drawing the DOCA (Distance Of Closest Approach) ******
753 REC_TABLE = zeros(N_POINTS, 4);
754 kk = 0;
755 for ii = 1:NN
756     for jj = ii + 1:NN
757         kk = kk + 1;
758
759         [X0, Y0, Z0, RES] = min_3d(X{ii}, Y{ii}, Z{ii}, X{jj}, Y{jj}, Z{jj});
760         REC_TABLE(kk, :) = [X0 Y0 Z0 RES];
761
762         COL1 = [rgb(ranC{cycle(PAIRS(kk, 1), 7)})];
```

```
763         COL2 = [rgb(ranC{cycle(PAIRS(kk, 2), 7)})];
764 
765         if DRAW
766             plot3(X0, Y0, Z0, '*', 'Color', COL1, 'MarkerSize', 5)
767             plot3(X0, Y0, Z0, 'o', 'Color', COL2, 'MarkerSize', 15)
768         end
769     end
770 end
771 
772 % ********************** Drawing Vertex (black star) ********************
773 Average_RES = sqrt(REC_TABLE(:, 4) / 2);
774 WeightedFactor = sum(Average_RES) - Average_RES;
775 WeightedFactor = WeightedFactor + eps;
776 XR = sum(REC_TABLE(:, 1) .* WeightedFactor) ./ sum(WeightedFactor);
777 YR = sum(REC_TABLE(:, 2) .* WeightedFactor) ./ sum(WeightedFactor);
778 ZR = sum(REC_TABLE(:, 3) .* WeightedFactor) ./ sum(WeightedFactor);
779 
780 AP = [XR YR ZR];
781 
782 if DRAW
783     plot3(XR, YR, ZR, 'kp', 'Markersize', 15, 'MarkerFaceColor', 'k')
784     h = gca(F1);
785     h.View = [- 30 20];
786     set(F1, 'Units', 'inches', 'Position', [3.5 0 10 10])
787 end
788 % FullScree Position => 0 0 17.3750 9.7917
789 
790 if DRAW_MULTIPLE_VIEWS
791     % 3D
792     h0 = gca(F1);
793     f0 = figure;
794     newFig = copyobj(h0, f0);
795     newFig.View = [- 30 20];
796     set(f0, 'Units', 'inches', 'Position', [0 5.4028 8.6806 4.3889])
797 
798     % LB => X-Y
799     h1 = gca(F1);
800     f1 = figure;
801     newFig = copyobj(h1, f1);
802     newFig.View = [0 90];
803     set(f1, 'Units', 'inches', 'Position', [0 0 8.6806 4.3889])
804 
805     % RT => X-Z
806     h2 = gca(F1);
807     f2 = figure;
808     newFig = copyobj(h2, f2);
809     newFig.View = [0 0];
810     set(f2, 'Units', 'inches', 'Position', [8.6806 5.4028 8.6806 4.3889])
811 
812     % RB => Y-Z
813     h3 = gca(F1);
814     f3 = figure;
815     newFig = copyobj(h3, f3);
816     newFig.View = [- 90 0];
817     set(f3, 'Units', 'inches', 'Position', [8.6806 0 8.6806 4.3889])
818 end
819 
820 if DRAW
821     figure(F1)
822 end
823 
824 %%%%%%%%%%%%%%%%%%%%%%%%%%%%%STATISTICS %%%%%%%%%%%%%%%%%%%%%%%%%%%%%%%%
825 % ========% ========% ========% ========% ========% ========% ========
826 if STATS
827     disp('---------------')
828     disp(['Event No : ' num2str(EVENT_NO)])
829     disp(' ')
830 
831     disp('Index table :')
832     disp(TABLE)
833 
834     disp('Hit number :')
835     disp(HIT_NUMBER)
```

```
836
837     disp('Pair table (Track #) :')
838     disp(PAIRS)
839
840     disp('Reconstructed annihilation points & residual value')
841     disp(REC_TABLE);
842
843     disp('Annihilation point:')
844     disp([XR YR ZR])
845
846     disp('TRACK DOT PRODUCTS (BY INDEX) :')
847     disp(DOT_TR)
848
849     disp('ZR - Line fits')
850     disp(LINES)
851
852     disp('ZR RESIDUALS')
853     disp(NORMR_TABLE)
854
855     disp('Z and R intersection table by RZ fit :')
856     disp([ZINT RINT])
857
858     disp('Track curvature :');
859     disp(R_C)
860
861     disp('N_PH normalized');
862     disp(N_TABLE)
863
864     disp('P_PH normalized');
865     disp(P_TABLE)
866     disp('---------------')
867 end
868
869 if OUTPUT
870     OUT = {EVENT_NO, NN, TABLE_HYB, TABLE, HIT_NUMBER, ...
871       PAIRS, REC_TABLE, AP, T_DCOS, DOT_TR, NORMR_TABLE, ...
872       ZRINT, R_C, N_TABLE, P_TABLE, ...
873       ZRLINES, COLR, TR_ARR};
874     save (['R' num2str(RUN_NO) 'E' num2str(EVENT_NO) '.mat'], 'OUT', '-v7.3')
875 end
876
877 OUT = {EVENT_NO, NN, TABLE_HYB, TABLE, HIT_NUMBER, ...
878   PAIRS, REC_TABLE, AP, T_DCOS, DOT_TR, NORMR_TABLE, ...
879   ZRINT, R_C, N_TABLE, P_TABLE, ...
880   ZRLINES, COLR, TR_ARR};
881
882 %{
883 1 => EVENT_NO => VF48 Event #
884 2 => NN => # of tracks reconstructed
885 3 => TABLE_HYB => Index of hybrids containing hits
886 4 => TABLE => Track hits index table
887 5 => HIT_NUMBER => Total # of hits
888 6 => PAIRS => Pair table (Track #)
889 7 => REC_TABLE => Reconstructed annihilation points & residual value
890 8 => AP = ([XR YR ZR] => Annihilation point
891 9 => T_DCOS = a;
892 Directional CosineS = Unit vector COMPONENTS
893 "a" = Directional CosineS of the best - fit line to 3 points (hits) of ii_track ↩
      in 3D
894  * a_x = the x - component of the 3D unit vector in the direction of best - fit ↩
       line = cos(alpha)
895  * a_y = the y - component of the 3D unit vector in the direction of best - fit ↩
       line = cos(beta)
896  * a_z = the z - component of the 3D unit vector in the direction of best - fit ↩
       line = cos(gamma)
897 10 => DOT_TR => TRACK DOT PRODUCTS (BY INDEX)
898
899 11 => NORMR_TABLE => ZR RESIDUALS
900 12 => ZRINT = {ZINT RINT}; => Z and R intersection table by RZ fit
901 13 => R_C => Track curvature
902 14 => N_TABLE => N_PH normalized
903 15 => P_TABLE => P_PH normalized
904 16 => ZRLINES = {LINES ZR_RES};
```

```
LINES => ZR - Line fits
17 => COLR
18 => TR_ARR => [XX' YY' ZZ' RR' PHI' LAYER' HYBRID' N_PH' P_PH'] => All the information regarding HIT number
%}

%{
% ================================================================================
FUNCTIONS
% ================================================================================

% 1: ================================================================================
function OUT = a2_coordinates(IN, OFFS)
S = size(IN);
N = S(1);

for ii = 1:N
    HYBRID = IN(ii, 1);
    N_ASIC = IN(ii, 2);
    N_CHANN = IN(ii, 3);
    P_ASIC = IN(ii, 4);
    P_CHANN = IN(ii, 5);

    VATAC = [(128 * N_ASIC + N_CHANN) (128 * P_ASIC + P_CHANN)];
    [Z0, Y0] = strip_zy_h2(VATAC);
    Z0 = - Z0 * sign(36.5 - HYBRID);
    Y0 = - Y0 * sign(36.5 - HYBRID);
    CPAIR = [Z0 Y0];
    ARR = rot_hyb2(HYBRID, CPAIR, OFFS);
    X = ARR(1, :, 1);
    Y = ARR(1, :, 2);
    Z = ARR(1, :, 3);
    OUT(ii, :) = [X Y Z];
end

% 2: ================================================================================
function beautifulPlot2D
str0 = ' ';
[ax, h3] = suplabel(str0, 't');
set(h3, 'FontSize', 18, 'fontweight', 'bold', 'fontname', 'Times')
set(gca, 'TickLabelInterpreter', 'latex')
set(gca, ...
  'linewidth', 0.8, ...
  'fontsize', 17, ...
  'fontname', 'Times');

set(gca, 'XMinorTick', 'on', 'YMinorTick', 'on', 'XGrid', 'off', 'YGrid', 'off', ...
  'TickDir', 'out', 'TickLength', [.015 .015])

set(gca, 'box', 'off', 'color', 'none')
b = axes('Position', get(gca, 'Position'), 'box', 'on', 'xtick', [], 'ytick', [],'linewidth', 1);
axes(gca)
linkaxes([gca b])
str00 = ' ';
[ax, h3] = suplabel(str00, 't');
set(h3, 'FontSize', 18, 'fontname', 'Times');
end

% 3: ================================================================================
function OUT = cycle(M, N)
OUT = rem(M, N);
if OUT == 0, OUT = N; end
    OUT = abs(OUT);

    % 4: ================================================================================
    function OUT = dangle(A1, A2)
    OUT = angle(exp(i * A1) .* exp(- i * A2));

    % 5: ================================================================================
    function dr_AD_r
    HYB = 1:36;
```

```
975     V = [0  0];
976     OFFS = 0;
977     ARR = rot_hyb2(HYB, V, OFFS);
978     hold on
979     for ii = 1:length(HYB)
980         X = ARR(ii, 1, 1);
981         Y = ARR(ii, 1, 2);
982         Z = ARR(ii, 1, 3);
983         plot3(X, Y, Z, 'k.')
984         a = text(X, Y, Z + 5, num2str(HYB(ii)))
985         set(a, 'Color', rgb('DarkRed'), 'FontSize', 12, 'Interpreter', 'latex')
986         set(gca, 'TickLabelInterpreter', 'latex')
987     end
988
989     clear ARR
990     HYB = 1:36;
991
992     FAR = [ %N_ASIC N_CHANN P_ASIC P_CHANN
993     1 1 4 128
994     1 128 4 128
995     1 128 3 1
996     1 1 3 1];
997
998     CLOSE = [ %N_ASIC N_CHANN P_ASIC P_CHANN
999     2 1 4 128
1000    2 128 4 128
1001    2 128 3 1
1002    2 1 3 1];
1003
1004    N = 36;
1005    for ii = 1:N
1006        MOD = ii * ones(4, 1);
1007        IN1 = [MOD FAR];
1008        OUT = a2_coordinates(IN1, OFFS);
1009        a = fill3(OUT(:, 1), OUT(:, 2), OUT(:, 3), 'r');
1010        set(a, 'FaceColor', 'none')
1011
1012        IN2 = [MOD CLOSE];
1013        OUT = a2_coordinates(IN2, OFFS);
1014        a = fill3(OUT(:, 1), OUT(:, 2), OUT(:, 3), 'r');
1015        set(a, 'FaceColor', 'none')
1016    end
1017    axis equal
1018    xlabel('X(mm)', 'Interpreter', 'Latex');
1019    ylabel('Y(mm)', 'Interpreter', 'Latex');
1020    zlabel('Z(mm)', 'Interpreter', 'Latex');
1021    set(gca, 'Projection', 'Orthographic')
1022    beautifulPlot3D
1023    view(- 22, 37) % => General
1024    %view(90,0) % => For n-side
1025    %view(-90,0) % => For p-side
1026
1027    set(gca, 'XLim', [- 170 170])
1028    set(gca, 'YLim', [- 170 170])
1029
1030    set(gca, 'XGrid', 'off', 'YGrid', 'off', ...
1031      'XGrid', 'off', 'YGrid', 'off', 'ZGrid', 'off')
1032
1033    % 6: ==========================================================================
1034    function dr_POS_r
1035    HYB = 37:72;
1036    V = [0  0];
1037    OFFS = 0;
1038    ARR = rot_hyb2(HYB, V, OFFS);
1039
1040    hold on
1041
1042    for ii = 1:length(HYB)
1043        X = ARR(ii, 1, 1);
1044        Y = ARR(ii, 1, 2);
1045        Z = ARR(ii, 1, 3);
1046        plot3(X, Y, Z, 'k.')
1047        a = text(X, Y, Z + 20, num2str(HYB(ii)));
```

```
        set(a, 'Color', rgb('DarkRed'), 'FontSize', 12, 'Interpreter', 'latex')
        set(gca, 'TickLabelInterpreter', 'latex')
    end

    clear ARR
    HYB = 37:72;

    FAR = [ %N_ASIC N_CHANN P_ASIC P_CHANN
    1 1 4 128
    1 128 4 128
    1 128 3 1
    1 1 3 1];

    CLOSE = [ %N_ASIC N_CHANN P_ASIC P_CHANN
    2 1 4 128
    2 128 4 128
    2 128 3 1
    2 1 3 1];

    N = 72;
    for ii = 37:N
        MOD = ii * ones(4, 1);
        IN1 = [MOD FAR];
        OUT = a2_coordinates(IN1, OFFS);
        a = fill3(OUT(:, 1), OUT(:, 2), OUT(:, 3), 'r');
        set(a, 'FaceColor', 'none')

        IN2 = [MOD CLOSE];
        OUT = a2_coordinates(IN2, OFFS);
        a = fill3(OUT(:, 1), OUT(:, 2), OUT(:, 3), 'r');
        set(a, 'FaceColor', 'none')
    end
    axis equal
    xlabel('X(mm)', 'Interpreter', 'Latex');
    ylabel('Y(mm)', 'Interpreter', 'Latex');
    zlabel('Z(mm)', 'Interpreter', 'Latex');
    set(gca, 'Projection', 'Orthographic')
    beautifulPlot3D

    view(- 22, 37) % => General
    %view(90,0) % => For n-side
    %view(-90,0) % => For p-side

    set(gca, 'XLim', [- 170 170])
    set(gca, 'YLim', [- 170 170])

    % 7: ================================================================
    function OUT = hittableMixingSPA(RUN_NO, EVENT_NO)

    FILE_IN = ['R' num2str(RUN_NO) '_Mixing_SPA.txt'];
    PHE = cell(72, 4);
    HITS = cell(72, 4);

    FID = fopen(FILE_IN, 'r');

    for ii = 1:EVENT_NO - 1
        fgetl(FID);
    end

    LINE_IN = fgetl(FID);
    NUMS = str2num(LINE_IN);
    fclose(FID);

    M = length(NUMS) / 4;
    N = 4;
    EVENTS = reshape(NUMS, N, M)';

    for ii = 1:M
        I = EVENTS(ii, 1);
        J = EVENTS(ii, 2);
        PHE{I, J} = [PHE{I, J} EVENTS(ii, 4)];
        HITS{I, J} = [HITS{I, J} EVENTS(ii, 3)];
    end
```

```
1121
1122        OUT.PHE = PHE;
1123        OUT.HITS = HITS;
1124
1125        % 8: ================================================================
1126        function OUT = hyb_pos2
1127
1128        Z_MOUNT = 302.25;
1129        HA_PHI = zeros(72, 4);
1130
1131        HA_PHI(:, 1) = 1:72;
1132
1133        HA_PHI(1:36, 2) = - Z_MOUNT;
1134        HA_PHI(37:72, 2) = Z_MOUNT;
1135
1136        HA_PHI([1:2:10 37:2:46], 3) = 89;
1137        HA_PHI([2:2:10 38:2:46], 3) = 94.5;
1138
1139        HA_PHI([11:2:22 47:2:58], 3) = 108;
1140        HA_PHI([12:2:22 48:2:60], 3) = 113.5;
1141
1142        HA_PHI([23:2:36 59:2:72], 3) = 127;
1143        HA_PHI([24:2:36 60:2:72], 3) = 132.5;
1144
1145        N = 10;
1146        A = linspace(0, 2 * pi, N + 1) + pi / 2;
1147        A = A(1:N);
1148        A = [A A];
1149        A = A(:);
1150        HA_PHI([1:10 37:46], 4) = A;
1151
1152        N = 12;
1153        A = linspace(0, 2 * pi, N + 1) + pi / 2 + 9 / 180 * pi;
1154        A = A(1:N);
1155        A = [A A];
1156        A = A(:);
1157        HA_PHI([11:22 47:58], 4) = A;
1158
1159        N = 14;
1160        A = linspace(0, 2 * pi, N + 1) + pi / 2 + 5 / 180 * pi;
1161        A = A(1:N);
1162        A = [A A];
1163        A = A(:);
1164        HA_PHI([23:36 59:72], 4) = A;
1165        OUT = HA_PHI;
1166
1167        % 9: ================================================================
1168        function CLS = loc_clusters(VEC)
1169
1170        if isempty(VEC), CLS = []; return, end
1171
1172            N = length(VEC);
1173            DVEC = diff(VEC);
1174            INDS = find(DVEC > 1);
1175            DVEC(INDS) = 0;
1176            DVEC = [0 DVEC 0];
1177            ZEROS = find(DVEC == 0);
1178            M = length(DVEC);
1179            INDLOC = [1:M] - .5;
1180
1181            for ii = 1:length(ZEROS) - 1
1182                MINI = ceil(INDLOC(ZEROS(ii)));
1183                MAXI = floor(INDLOC(ZEROS(ii + 1)));
1184                CLS{ii} = MINI:MAXI;
1185            end
1186
1187            % 10: ↩
                ================================================================↩
1188            function GROUPS = loc_same(VEC)
1189            N = size(VEC);
1190            N = N(1);
1191            BC = [1:N + 1] - .5;
```

```
1192
1193        if isempty(VEC) || N == 1, GROUPS = {1}; return, end
1194
1195            DVEC = [1; abs(prod(diff(VEC), 2)); 1];
1196            BREAKS_I = find(DVEC > 0);
1197
1198            for ii = 1:length(BREAKS_I) - 1
1199                GROUPS{ii} = [ceil(BC(BREAKS_I(ii))):floor(BC(BREAKS_I(ii + 1)))↩
                        ];
1200            end
1201
1202            % 11: ↩
                    ==========================================================================↩

1203            function [x0, a, d, normd] = ls3dline_2(X)
1204            m = size(X, 1);
1205            if m < 3
1206                error('At least 3 data points required: ')
1207            end
1208            x0 = mean(X)';
1209            A = [(X(:, 1) - x0(1)) (X(:, 2) - x0(2)) (X(:, 3) - x0(3))];
1210            [U, S, V] = svd(A, 0);
1211            [s, i] = max(diag(S));
1212            a = V(:, i);
1213            nargout
1214            if nargout > 2
1215                m = size(X, 1);
1216                d = zeros(m, 1);
1217                for i = 1:m
1218                    d(i) = norm(cross((X(i, 1:3)' - x0), a));
1219                end
1220                normd = norm(d);
1221            end
1222
1223            % 12: ↩
                    ==========================================================================↩

1224            function [x0, a, d, normd] = ls3dline_2(X)
1225            m = size(X, 1);
1226            if m < 3
1227                error('At least 3 data points required: ')
1228            end
1229
1230            x0 = mean(X)';
1231            A = [(X(:, 1) - x0(1)) (X(:, 2) - x0(2)) (X(:, 3) - x0(3))];
1232            [U, S, V] = svd(A, 0);
1233            [s, i] = max(diag(S));
1234            a = V(:, i);
1235            if nargout > 2
1236                m = size(X, 1);
1237                d = zeros(m, 1);
1238                for i = 1:m
1239                    d(i) = norm(cross((X(i, 1:3)' - x0), a));
1240                end
1241                normd = norm(d);
1242            end
1243
1244            % 13: ↩
                    ==========================================================================↩

1245            function [X0, Y0, Z0, RES] = min_3d(X1, Y1, Z1, X2, Y2, Z2)
1246
1247            X1 = X1(:);
1248            Y1 = Y1(:);
1249            Z1 = Z1(:);
1250            X2 = X2(:);
1251            Y2 = Y2(:);
1252            Z2 = Z2(:);
1253
1254            V1 = [X1 Y1 Z1];
1255            V2 = [X2 Y2 Z2];
1256
1257            V0 = [0 0 0];
```

```
[V, RES] = fminsearch('min_3d_sfn', V0, [], V1, V2);

SUB1 = bsxfun(@minus, V1, V);
SUB2 = bsxfun(@minus, V2, V);
SUB1 = SUB1 .^ 2;
SUB2 = SUB2 .^ 2;
SUB1 = sum(SUB1, 2);
SUB2 = sum(SUB2, 2);
M1 = unique(min(SUB1));
M2 = unique(min(SUB2));
RES = M1 + M2;
X0 = V(1);
Y0 = V(2);
Z0 = V(3);

% 14: ↩
    ═══════════════════════════════════════════════════════════════════════════↩
```

```
function OUT = min_3d_sfn(V0, V1, V2)
load('min_3d_sfn_data.mat')
A1 = bsxfun(@minus, V1, V0);
A2 = bsxfun(@minus, V2, V0);
A1 = A1 .^ 2;
A1(1:3, :);
A2 = A2 .^ 2;
A2(1:3, :);

S1 = sum(A1, 2);
S2 = sum(A2, 2);
V1 = unique(min(S1));
V2 = unique(min(S2));
OUT = V1 + V2;

load('min_3d_data.mat')

X1 = X{1}; Y1 = Y{1}; Z1 = Z{1};
X2 = X{2}; Y2 = Y{2}; Z2 = Z{2};

X1 = X1(:);
Y1 = Y1(:);
Z1 = Z1(:);
X2 = X2(:);
Y2 = Y2(:);
Z2 = Z2(:);

V1 = [X1 Y1 Z1];
V2 = [X2 Y2 Z2];

V0 = [0 0 0];
[V, RES] = fminsearch('min_3d_sfn', V0, [], V1, V2);
SUB1 = bsxfun(@minus, V1, V);
SUB2 = bsxfun(@minus, V2, V);
SUB1 = SUB1 .^ 2;
SUB2 = SUB2 .^ 2;
SUB1 = sum(SUB1, 2);
SUB2 = sum(SUB2, 2);

M1 = unique(min(SUB1));
M2 = unique(min(SUB2));
RES = M1 + M2;
X0 = V(1);
Y0 = V(2);
Z0 = V(3);

% 15: ↩
    ═══════════════════════════════════════════════════════════════════════════↩
```

```
function [xy, r] = points2circle(A, B, C)

A = [- 94.5 - 8.7552];
B = [- 109.36 0.079473];
C = [- 126.32 13.129];
```

```
            if nargin == 1
                P = A;
                if size(P, 1) ~= 3 || size(P, 2) ~= 2
                    error ('A single input should be a 3-by-2 matrix');
                end
            elseif ~ isequal(numel(A), numel(B), numel(C), 2)
                error('The three points should all have 2 elements.')
            else
                P = [A(:) B(:) C(:)] .' ;
            end

            M = [...
              1 1 1 1; ...
              (P(1, 1) .^ 2 + P(1, 2) .^ 2) P(1, 1) P(1, 2) 1; ...
              (P(2, 1) .^ 2 + P(2, 2) .^ 2) P(2, 1) P(2, 2) 1; ...
              (P(3, 1) .^ 2 + P(3, 2) .^ 2) P(3, 1) P(3, 2) 1 ...
              ];

            M11 = local_minordet(M, 1, 1);
            if M11 == 0
                xy = [];
                r = [];
                warning('No solution! Points may be on a straight line.');
            else
                xy(1) = 0.5 * (local_minordet(M, 1, 2) ./ M11);
                xy(2) = - 0.5 * (local_minordet(M, 1, 3) ./ M11);
                r = sqrt(xy(1) .^ 2 + xy(2) .^ 2 + (local_minordet(M, 1, 4) ./ ↩
                    M11));
            end

            % 16: ↩
                ==========================================================================↩

            function md = local_minordet(M, i, j)
            M(i, :) = [];
            M(:, j) = [];
            md = det(M);
            end
        end

        % 17: ↩
            ==========================================================
        function X = R_alfa(alfa, X0)
        alfa = alfa / 180 * pi;
        R = zeros(2, 2);
        R(1, 1) = cos(alfa);
        R(2, 1) = sin(alfa);
        R(1, 2) = - sin(alfa);
        R(2, 2) = cos(alfa);

        for ii = 1:length(X0(:, 1))
            X01 = X0(ii, :);
            X01 = X01(:);
            XX = R * X01;
            X(ii, :) = XX';
        end

        % 18: ↩
            ==========================================================
        function ARR = rot_hyb2(HYB, V, OFFS)
        HA_PHI = hyb_pos2;
        K = length(HYB);
        L = size(V);
        L = L(1);
        M = 3;
        ARR = zeros(K, L, M);
        for ii = 1:K
            for jj = 1:L
                IND = find(HA_PHI(:, 1) == HYB(ii));
                Z = V(jj, 1) + HA_PHI(IND, 2);
                X0 = HA_PHI(IND, 3);
                Y0 = V(jj, 2);
                ANG = HA_PHI(IND, 4) * 180 / pi + OFFS;
```

```
1395                C0 = [X0 Y0];
1396                C = R_alfa2(ANG, C0);
1397                X = C(1);
1398                Y = C(2);
1399                ARR(ii, jj, :) = [X Y Z];
1400            end
1401        end
1402
1403        % 19: ↩
                ==========================================================================
1404        function OUT = strip_conn2
1405        VATAC = 129:640;
1406        VATAC = VATAC(:);
1407
1408        ASIC(1:128) = 1;
1409        ASIC(129:256) = 2;
1410        ASIC(257:384) = 3;
1411        ASIC(385:512) = 4;
1412        ASIC = ASIC(:);
1413
1414        ASIC_CHANN(1:128) = 1:128;
1415        ASIC_CHANN(129:256) = 1:128;
1416        ASIC_CHANN(257:384) = 1:128;
1417        ASIC_CHANN(385:512) = 1:128;
1418        ASIC_CHANN = ASIC_CHANN(:);
1419
1420        SI_STRIP(1:128) = 128: - 1:1;
1421        SI_STRIP(129:256) = 128: - 1:1;
1422        SI_STRIP(257:512) = 1:256;
1423        SI_STRIP = SI_STRIP(:);
1424
1425        SCAN_STRIP(1:128) = 1:128;
1426        SCAN_STRIP(129:256) = 1:128;
1427        SCAN_STRIP(257:512) = 256 - [1:256] + 1;
1428        SCAN_STRIP = SCAN_STRIP(:);
1429        OUT = [VATAC ASIC ASIC_CHANN SI_STRIP SCAN_STRIP];
1430
1431        % 20: ↩
                ==========================================================================
1432        function [Z, Y] = strip_zy_h2(IN)
1433        VATAC1 = IN(1);
1434        VATAC2 = IN(2);
1435        CH = strip_conn2;
1436        VATAC = CH(:, 1);
1437        ASIC = CH(:, 2);
1438        ASIC_CHANN = CH(:, 3);
1439        SI_STRIP = CH(:, 4);
1440        SCAN_STRIP = CH(:, 5);
1441
1442        ASICX = ASIC(find(VATAC == floor(VATAC1)));
1443        CHANNX = ASIC_CHANN(find(VATAC == floor(VATAC1)));
1444        ASICY = ASIC(find(VATAC == floor(VATAC2)));
1445        CHANNY = ASIC_CHANN(find(VATAC == floor(VATAC2)));
1446
1447        P_PITCH = 0.227;
1448        N_PITCH = 0.875;
1449        P_LENGTH = 226.99;
1450        N_LENGTH = 58.062;
1451
1452        C = [...
1453         - 188.338 - 28.934
1454         - 72.938 - 28.934
1455         - 72.938 28.938
1456         - 72.938 - .1135];
1457
1458        L = [...
1459        0 N_LENGTH
1460        0 N_LENGTH
1461         - P_LENGTH 0
1462         - P_LENGTH 0];
1463
1464        P = [...
1465        N_PITCH 0
```

```
1466        N_PITCH 0
1467        0 P_PITCH
1468        0 P_PITCH];
1469
1470        Z0 = C(ASICX, :) - (CHANNX - 1 + VATAC1 - floor(VATAC1)) * P(ASICX, :);
1471        Y0 = C(ASICY, :) - (CHANNY - 1 + VATAC2 - floor(VATAC2)) * P(ASICY, :);
1472
1473        Z = Z0(1);
1474        Y = Y0(2);
1475
1476        % 21: ↩
                ================================================================
1477        function [Z, Y] = strip_zy_h3(IN)
1478        VATAC1 = IN(1);
1479        VATAC2 = IN(2);
1480
1481        CH = strip_conn3;
1482        VATAC = CH(:, 1);
1483        ASIC = CH(:, 2);
1484        ASIC_CHANN = CH(:, 3);
1485        SI_STRIP = CH(:, 4);
1486        SCAN_STRIP = CH(:, 5);
1487
1488        ASICX = ASIC(find(VATAC == floor(VATAC1)));
1489        CHANNX = ASIC_CHANN(find(VATAC == floor(VATAC1)));
1490        ASICY = ASIC(find(VATAC == floor(VATAC2)));
1491        CHANNY = ASIC_CHANN(find(VATAC == floor(VATAC2)));
1492
1493        P_PITCH = 0.227;
1494        N_PITCH = 0.875;
1495        P_LENGTH = 226.99;
1496        N_LENGTH = 58.062;
1497
1498        C = [...
1499         - 188.338 - 28.934
1500         - 72.938 - 28.934
1501         - 72.938 28.938
1502         - 72.938 - .1135];
1503
1504        L = [...
1505        0 N_LENGTH
1506        0 N_LENGTH
1507         - P_LENGTH 0
1508         - P_LENGTH 0];
1509
1510        P = [...
1511        N_PITCH 0
1512        N_PITCH 0
1513        0 P_PITCH
1514        0 P_PITCH];
1515
1516        Z0 = C(ASICX, :) - (CHANNX - 1 + VATAC1 - floor(VATAC1)) * P(ASICX, :);
1517        Y0 = C(ASICY, :) - (CHANNY - 1 + VATAC2 - floor(VATAC2)) * P(ASICY, :);
1518
1519        Z = Z0(1);
1520        Y = Y0(2);
1521        %}
```

Appendix D

Event-Vertex-Reconstruction-Visualization.m

Listing D.1: Event-Vertex-Reconstruction-Visualization.m Script

```
clc, clear, close all
tic
% Mixing:

% Windows
% userpath = regexprep(userpath,';','');% Removes ; at the end of the path

userpath = '/Users/Mosi/Dropbox/Business/Public_Sharing/Antimatter';
cd([userpath '/Antimatter_Detection/DATA/MatlabMatFiles/Mixings'])

% command = 'dir /b'; % Windows
command = 'ls -1v'; % Linux
[status, cmdout] = system(command);
runNumbers = str2double(regexp(cmdout, '\d+(\.\d+)?|\.\d+', 'match'));
MIXING = runNumbers;

for ii = 1:length(runNumbers)
    if find(runNumbers(ii) == MIXING(1))

        filename = ['R' num2str(runNumbers(ii))];
        Run = num2str(runNumbers(ii));

        cd ([userpath '/Antimatter_Detection/DATA/MatlabMatFiles/Mixings/' Run])
        load ([ 'R' Run 'VF48.mat']);
        load('originalCounts.mat');

        % APA outcome:
        inputFolder_APA = [userpath '/Antimatter_Detection/Pedestal_Analysis'];
        baseFileName_APA = [filename '_Mixing_APA.txt'];
        inputFullFileName_APA = fullfile(inputFolder_APA, baseFileName_APA);

        outputFolder_APA = [userpath '/Antimatter_Detection/↩
            Event_Vertex_Reconstruction'];
        outputFullFileName_APA = fullfile(outputFolder_APA, baseFileName_APA);
        copyfile(inputFullFileName_APA, outputFullFileName_APA);

        % SPA outcome:
        inputFolder_SPA = [userpath '/Antimatter_Detection/Pedestal_Analysis'];
        baseFileName_SPA = [filename '_Mixing_SPA.txt'];
        inputFullFileName_SPA = fullfile(inputFolder_SPA, baseFileName_SPA);

        outputFolder_SPA = [userpath '/Antimatter_Detection/↩
            Event_Vertex_Reconstruction'];
        outputFullFileName_SPA = fullfile(outputFolder_SPA, baseFileName_SPA);
        copyfile(inputFullFileName_SPA, outputFullFileName_SPA);

        RUN = runNumbers(ii);
```

```
        SUM = 0;
        format short g
        for Event = 4611

            % APA
            cd ([userpath '/Antimatter_Detection/Event_Vertex_Reconstruction'])
            ConeL2 = 35; ConeL3 = 45;
            [OUT{1:17}] = APA(RUN, Event, ConeL2, ConeL3);
            APA_Vertex_Position = OUT{7} % => 12.525       4.3575      -92.675
            view(0, 90)
            set(gcf, 'Position', [0, 0, 9, 10])

            % SPA
            ConeL2 = 35; ConeL3 = 45;
            [OUT{1:17}] = SPA(RUN, Event, ConeL2, ConeL3);
            SPA_Vertex_Position = OUT{7} % => 12.521       4.1903       -92.65
            view(0, 90)
            set(gcf, 'Position', [9, 0, 9, 10])

            % Saving Images:
            h = findobj('type', 'figure');
            n = length(h);
            name = {'Alternative_Pedestal_Analysis', 'Standard_Pedestal_Analysis'};
            for f = 1:n
                cd ([userpath '/Antimatter_Detection/Event_Vertex_Reconstruction/Figures'])
                fig = h(f);
                filename = [num2str(Event) '_' name{f}];

                % set(fig, 'render', 'opengl');
                % print (fig, '-deps', filename, '-r300')

                print(filename, '-depsc')

            end
            % close all
            cd ..

        end
        end
    end
    cd ([userpath '/Antimatter_Detection/Event_Vertex_Reconstruction'])
```